

CHARACTERISATION OF IMPACT DAMAGE IN CARBON  
FIBRE REINFORCED PLASTICS BY 3D X-RAY  
TOMOGRAPHY

A THESIS  
SUBMITTED TO THE UNIVERSITY OF MANCHESTER  
FOR THE DEGREE OF  
DOCTOR OF ENGINEERING (ENGD)  
IN THE FACULTY OF ENGINEERING AND PHYSICAL SCIENCES

2012

**JORDAN ELLIOT ROUSE**

SCHOOL OF MATERIALS

# CONTENTS

<b>Abstract</b>	<b>18</b>
<b>Declaration</b>	<b>19</b>
<b>Copyright</b>	<b>20</b>
<b>1 From Aircraft to X-rays, An Introduction</b>	<b>21</b>
1.1 Aims and Objectives . . . . .	25
<b>2 3D X-ray Tomography: Background and Literature</b>	<b>26</b>
2.1 Overview . . . . .	26
2.2 Process Stages of Computed Tomography . . . . .	27
2.2.1 Acquisition . . . . .	28
2.2.2 Reconstruction . . . . .	28
2.2.3 Visualisation and Analysis . . . . .	28
2.3 The Physics of X-Rays . . . . .	29
2.3.1 Production of X-Rays . . . . .	29
2.3.2 Interaction of X-Rays with Matter . . . . .	32
2.3.2.1 The Photoelectric Effect and Scattering . . . . .	34
2.4 Reconstruction Methods . . . . .	35
2.4.1 Alternative Reconstruction Methods . . . . .	40
2.5 Image Quality . . . . .	42
2.5.1 Contrast . . . . .	43
2.5.2 Noise . . . . .	45
2.5.3 Signal to Noise Ratio . . . . .	46
2.5.4 Contrast to Noise Ratio . . . . .	46
2.5.5 Spatial Resolution . . . . .	47
2.6 Artefacts . . . . .	49
2.6.1 Beam Hardening Artefacts . . . . .	49
2.6.2 Edge Artefacts . . . . .	50
2.6.3 Ring Artefacts . . . . .	51
2.6.4 Centre of Rotation Artefacts . . . . .	51

2.6.5	Insufficient Projection Artefacts . . . . .	52
2.6.6	Cone Beam Artefacts . . . . .	53
2.7	Applications in Imaging CFRP Materials . . . . .	53
2.7.1	Materials Characterisation . . . . .	54
2.7.1.1	Porosity . . . . .	54
2.7.1.2	Fibre Architecture . . . . .	55
2.7.1.3	Impact Damage Characterisation . . . . .	58
2.8	Imaging Large Objects . . . . .	60
2.8.1	Region of Interest CT . . . . .	61
2.8.2	Region of Interest Algorithms . . . . .	64
2.8.3	Computed Laminography . . . . .	67
2.9	Phase Contrast Imaging . . . . .	69
2.10	Chapter Summary . . . . .	73
<b>3</b>	<b>Composite Materials and Impact Damage: Background and Literature</b>	<b>74</b>
3.1	Fibre Reinforced Composite Materials . . . . .	74
3.2	Damage in Fibre Reinforced Plastics . . . . .	76
3.2.1	Static Failure of Fibre Reinforced Plastics . . . . .	76
3.2.2	Impact Damage and Failure Mechanisms . . . . .	79
3.2.2.1	Matrix Damage . . . . .	81
3.2.2.2	Delamination . . . . .	82
3.2.2.3	Fibre Failure . . . . .	83
3.2.2.4	Penetration . . . . .	83
3.2.3	Effect of Component Properties on Impact Performance . . . . .	84
3.2.3.1	Fibres . . . . .	84
3.2.3.2	Matrix . . . . .	85
3.2.3.3	Interface . . . . .	86
3.2.3.4	Stacking Sequence . . . . .	87
3.2.3.5	Geometry . . . . .	88
3.3	The Role of Modelling in Composites Design . . . . .	89
3.3.1	Modelling Low Velocity Impact Damage . . . . .	90
3.4	Chapter Summary and Conclusions . . . . .	93
<b>4</b>	<b>Dual-Energy Imaging of High Aspect Ratio CFRP Panels</b>	<b>95</b>
4.1	Introduction . . . . .	95
4.2	System Overview . . . . .	97
4.2.1	System Calibration . . . . .	101
4.3	Theoretical Background to Dual Energy Imaging . . . . .	102
4.3.1	Optimising Image Quality . . . . .	102
4.3.2	Combining Multiple Projection Sets . . . . .	103
4.4	Manufacture of Step Wedges . . . . .	105

4.4.1	Panel Manufacture . . . . .	105
4.5	Radiographic Imaging of Step Wedges . . . . .	109
4.6	Image Analysis of Step Wedge Radiographs . . . . .	110
4.7	Step-Wedge Imaging Results and Discussion . . . . .	111
4.8	Beam Hardening Correction for CFRP Materials . . . . .	117
4.9	Implementation of a Dual Energy Imaging Technique . . . . .	121
4.9.1	Process Outline and Experimental . . . . .	121
4.9.2	Results and Discussion . . . . .	125
4.9.2.1	Effect of Projection Misalignment . . . . .	130
4.9.2.2	Large Panels . . . . .	131
4.10	Chapter Summary and Conclusions . . . . .	135
<b>5</b>	<b>Characterisation of Low velocity Impact Damage Tolerance of Carbon Fibre Reinforced Plastic</b>	<b>136</b>
5.1	Introduction . . . . .	136
5.2	Materials . . . . .	137
5.3	Panel Manufacture . . . . .	137
5.4	Drop Weight Impact Testing . . . . .	138
5.4.1	Drop Weight Impact Experimental Procedure . . . . .	138
5.4.2	Results and Discussion . . . . .	141
5.4.2.1	Summary . . . . .	147
5.5	Compression After Impact Testing . . . . .	147
5.5.1	Experimental Procedure . . . . .	148
5.5.2	Results and Discussion . . . . .	149
5.5.3	CAI Testing Summary . . . . .	153
5.6	Interlaminar Shear Testing . . . . .	153
5.6.1	Specimen Preparation . . . . .	154
5.6.2	Interlaminar Shear Test Experimental Procedure . . . . .	155
5.6.3	Results and Discussion . . . . .	156
5.7	Imaging Impact Damage in CFRP coupons . . . . .	158
5.7.1	Dual Energy X-ray CT of impacted CFRP coupons . . . . .	158
5.7.1.1	CT Imaging Methodology . . . . .	158
5.7.2	Ultrasonic C-Scan of impacted CFRP coupons . . . . .	161
5.8	Imaging Results and Discussion . . . . .	162
5.8.1	Qualitative X-ray CT Results . . . . .	163
5.8.1.1	Unidirectional Samples . . . . .	163
5.8.1.2	Woven Samples . . . . .	165
5.8.2	Quantitative X-Ray CT Measurements . . . . .	168
5.8.2.1	Image Processing . . . . .	168
5.8.2.2	Quantifying Damage in UD samples . . . . .	172
5.8.2.3	Quantifying Damage in Woven Samples . . . . .	184

5.9	Chapter Summary and Conclusions . . . . .	189
<b>6</b>	<b>Region of Interest Imaging of Impact damage in CFRP</b>	<b>191</b>
6.1	Introduction . . . . .	191
6.2	Background . . . . .	192
6.3	Assessment of ROI data completion methods . . . . .	193
6.3.1	Imaging Experimental Method . . . . .	193
6.3.2	Data Completion Methods . . . . .	194
6.3.3	Results and Discussion . . . . .	199
6.3.3.1	ROI vs. Sectioning . . . . .	199
6.3.3.2	Data Completion Results . . . . .	204
6.4	Effect of Number of Projections on Image quality in ROI Scans . . . . .	210
6.4.1	Experimental Method . . . . .	210
6.4.2	Results and Discussion . . . . .	210
6.5	ROI Imaging of Impact Damage . . . . .	217
6.5.1	Experimental Method . . . . .	217
6.5.2	Results and Discussion . . . . .	218
6.5.2.1	Uni-Directional Material . . . . .	218
6.5.2.2	Woven Material . . . . .	220
6.6	Chapter Summary and Conclusions . . . . .	225
<b>7</b>	<b>Imaging Damage using Grating Interferometry X-Ray Tomography</b>	<b>227</b>
7.1	Introduction . . . . .	227
7.2	Background . . . . .	228
7.3	Experimental Method . . . . .	232
7.4	Results and Discussion . . . . .	237
7.4.1	Projections . . . . .	237
7.4.2	Tomography . . . . .	241
7.4.3	Dark field imaging of CAI Samples . . . . .	247
7.5	Chapter Summary and Conclusions . . . . .	250
<b>8</b>	<b>General Conclusions and Further Work</b>	<b>252</b>
8.1	Commercial Aspects . . . . .	256
8.1.1	Cost . . . . .	256
8.1.2	Supply Chain Position . . . . .	258
8.1.3	Current Limitations and Future Developments . . . . .	258
<b>A</b>	<b>Characterisation of Computed Tomography System</b>	<b>261</b>
A.1	Introduction . . . . .	261
A.2	Objectives . . . . .	261
A.3	Determination of System Resolution . . . . .	262
A.3.1	Resolution Target . . . . .	262

---

A.3.1.1	Results and Discussion . . . . .	263
A.3.2	Spot Size Measurement by Radiography of a Tungsten Wire . . . . .	266
A.3.2.1	Methodology . . . . .	266
A.3.2.2	Results and Discussion . . . . .	266
A.3.3	Reconstructed Volume Resolution . . . . .	268
A.3.3.1	Measurement of Edge Profiles . . . . .	269
A.3.3.2	Results and Discussion . . . . .	269
A.4	Effect of Projection Number on Image Quality . . . . .	271
A.5	Characterisation of Spectral Emission from a Multi-Metal Target . . . . .	273
A.5.1	Experimental Method . . . . .	273
A.5.2	Spectra Results . . . . .	275
A.5.2.1	Cu target . . . . .	275
A.5.2.2	Mo Target . . . . .	276
A.5.2.3	Ag Target . . . . .	278
A.5.2.4	W Target . . . . .	279
A.5.2.5	Comparison of Targets . . . . .	282
A.5.3	X-ray Source Stability . . . . .	284
A.5.4	Beam Transmission Through CFRP . . . . .	286
A.6	Appendix Summary and Conclusions . . . . .	288
<b>B</b>	<b>Matlab code for dual energy CT</b>	<b>289</b>

## LIST OF FIGURES

1.1	The Boeing 787 and section of the 787 composite fuselage . . . . .	22
1.2	Examples in X-Ray imaging . . . . .	23
1.3	Examples of CT applications . . . . .	24
2.1	Schematic of cone beam X-Ray tomography system. . . . .	26
2.2	Illustration of the electromagnetic spectrum . . . . .	29
2.3	Production of Bremsstrahlung X-rays . . . . .	30
2.4	Production of characteristic radiation . . . . .	31
2.5	Illustration of electron interaction with a target material . . . . .	32
2.6	Overview of X-ray interactions with matter . . . . .	33
2.7	Dependance of the mass attenuation coefficient on photon energy for tungsten . . . . .	34
2.8	Relative dominance of the photoelectric affect and Compton Scattering .	35
2.9	Projection intensities from perpendicular directions of a component with three different linear attenuation coefficients . . . . .	36
2.10	Parallel projection geometry . . . . .	37
2.11	Fan beam projection geometry . . . . .	38
2.12	Graphical representation of the Fourier Slice Theorem in two dimensions (Pan and Kak, 1983) . . . . .	39
2.13	Data-space partitions corresponding to various scan configurations or common CT issues in which knowledge of data function within some portions of the data space is missing (Pan <i>et al.</i> , 2009a). . . . .	41
2.14	Relationship between image quality parameters . . . . .	43
2.15	$\Delta\mu$ as a function of photon energy . . . . .	44
2.16	Illustration of contrast . . . . .	45
2.17	Grey value distributions due to noise . . . . .	47
2.18	Process of MTF measurement . . . . .	48
2.19	Example of the cupping effect . . . . .	49
2.20	Streaks at high contrast edges due to edge artefacts . . . . .	50
2.21	Ring artefacts in a CT slice . . . . .	51
2.22	Centre of rotation error . . . . .	52

2.23	Artefacts due to an insufficient number of projections . . . . .	52
2.24	Cone beam artefacts in a stack of discs . . . . .	53
2.25	Cross-sectional image of a CFRP laminate with iodine based contrast agent coated plies . . . . .	55
2.26	Cross-sectional images of CFRP laminate with gadolinium (III) flouride coated plies . . . . .	56
2.27	3D renderings of void content evolution during processing . . . . .	57
2.28	Evolution of macro porosity with processing time. From (Centea and Hubert, 2011). . . . .	57
2.29	CT slices at four different positions in an impacted CFRP laminate . . . .	58
2.30	3D CT renderings of Impact damage in 20 ply laminates under 92J impact energy. (a) CFRP (b) CFRP/ glass hybrid . . . . .	59
2.31	Illustration of the truncated projection . . . . .	60
2.32	CT scans of a 48cm diameter polymer phantom . . . . .	61
2.33	Reconstructions of a contrast phantom . . . . .	62
2.34	Sinogram extension procedure by Kyrieleis <i>et al.</i> . . . . .	63
2.35	ROI cone beam reconstructions of a CFRP coupon with laser drilled defects	64
2.36	Simulated fan beam reconstructions of a 'popeye' phantom with truncated projections. Top: FBP reconstruction. Bottom: BPF with Hilbert filtering (Noo <i>et al.</i> , 2004). . . . .	65
2.37	Reconstructions of a rat leg comparing FBP and BPF methods (Cho <i>et al.</i> , 2006). . . . .	66
2.38	Experimental set-up sketched for synchrotron-radiation computed laminography . . . . .	67
2.39	Geometry of composite samples used by Moffat <i>et al.</i> . . . . .	67
2.40	Comparison of volumes produced using CL (left) and CT (right). From (Moffat <i>et al.</i> , 2010). . . . .	68
2.41	Contrast between a crack and composite material in CT and CL . . . . .	68
2.42	CL images of progressive loading in a CFRP plate . . . . .	69
2.43	Schematic set-up of a diffraction-enhanced X-ray imaging system with a synchrotron beam. In the figure, the crystal analyser is drawn to correspond with the high angle case ( $\theta > 0$ ) of Fig. 2.44 (Zhou and Brahme, 2008). . . . .	70
2.44	Diffraction-enhanced images of a rod showing that X-rays deviated in the object through small angles will be reflected with either a greater or lower efficiency depending on the angle of incidence relative to the rocking curve of the silicon crystal (Zhou and Brahme, 2008). . . . .	71
2.45	Schematics of (a) attenuation-based imaging configuration (b) in-line phase contrast imaging configuration (Zhou and Brahme, 2008) . . . . .	71

2.46	Dependence of in-line phase-contrast images on the distance between object and detector. Here, given numerical data for $R_2$ are only illustrative, which, in practice, will depend on the specific system set-up (Zhou and Brahme, 2008). . . . .	72
3.1	Specific tensile strength (tensile strength divided by density) as a function of specific modulus (modulus divided by density) of composite materials, monolithic metals and ceramics . . . . .	75
3.2	Forms of composite reinforcements . . . . .	76
3.3	Illustration of failure in a composite as a result of stress exceeding critical values of (a) axial tensile stress , (b) transverse tensile stress , and (c) shear stress . . . . .	77
3.4	Nomenclature and orientation of shear stresses acting within an aligned fibre composite . . . . .	77
3.5	(a) Tensile and compressive stresses in a fibre due to in-phase buckling, leading to a kink zone. (b) Two planes of fracture formed with brittle carbon fibres. (c) Unfractured kink zone formed with Kevlar 49 fibres . . .	79
3.6	In-plane buckling of fibres and fibre kink band geometry . . . . .	79
3.7	Initial impact damage in an impacted 0/90/0 composite plate . . . . .	81
3.8	Generic sources of delamination . . . . .	82
3.9	[Residual flexural strength versus impact energy for ballistically impacted surface-treated and untreated carbon fibre composites . . . . .	86
3.10	Residual compressive strengths of 6376/T400H after ring-supported impacts	87
3.11	Low velocity impact energy to initiate damage vs. target thickness for ( $\pm 45^\circ$ ) CFRP composites . . . . .	88
3.12	Examples of composite modelling . . . . .	90
3.13	Matrix compression failure in a GFRP lap joint subject to low velocity impact (Choudhry, 2009). . . . .	91
3.14	Principle behaviour of a cohesive zone model (Borg <i>et al.</i> , 2004) . . . . .	92
3.15	Comparison of impact damage on (0 <sub>2</sub> /45 <sub>2</sub> /90 <sub>2</sub> / - 45 <sub>2</sub> )s laminate at equal displacements (Bouvet <i>et al.</i> , 2009). . . . .	93
4.1	Schematic illustration of dual-source CT using two image detectors (Petersilka <i>et al.</i> , 2008). . . . .	96
4.2	Nikon Metrology Custom CT bay with 225kV X-ray source . . . . .	98
4.3	Cone beam geometry showing origin of magnification and penumbra blurring . . . . .	99
4.4	Effective pixel size vs. magnification . . . . .	100
4.5	Maximum sample size vs. magnification factor . . . . .	100
4.6	Theoretical variation of signal-to-noise ratio with beam transmission. . . .	103
4.7	Vacuum bagging arrangement (Coenen, 2003). . . . .	106

4.8	Cure cycle characteristics. . . . .	107
4.9	UD step-wedge. . . . .	108
4.10	Schematic of step-wedge imaging experiment (not to scale). . . . .	109
4.11	8mm step-wedge section imaged under various voltages. These images are uncorrected, direct from the detector. . . . .	110
4.12	Radiograph of 64mm step section from UD step-wedge . . . . .	111
4.13	Transmittance vs. accelerating voltage for UD step-wedge using Cu target. . . . .	112
4.14	Transmittance vs. accelerating voltage for UD step-wedge using Mo target. . . . .	112
4.15	Transmittance vs. accelerating voltage for UD step-wedge using Ag target. . . . .	113
4.16	Transmittance vs. accelerating voltage for UD step-wedge using W target. . . . .	113
4.17	Variation of transmittance with accelerating voltage through 4mm of ma- terial for different target materials. . . . .	114
4.18	Variation of transmittance with accelerating voltage through 8mm of ma- terial for different target materials. . . . .	115
4.19	Variation of transmittance with accelerating voltage through 16mm of ma- terial for different target materials. . . . .	115
4.20	SNR vs. T for 32mm step-wedge section compared to theoretical prediction. . . . .	116
4.21	Beam hardening correction for Cu target at 100 kV. . . . .	117
4.22	Illustration of beam hardening correction for 32mm step wedge sections. Imaged at 50kV. . . . .	118
4.23	Illustration of beam hardening correction for 64mm step wedge sections. Imaged at 100kV. . . . .	119
4.24	Illustration of beam hardening correction for 128mm step wedge sections. Imaged at 150kV. . . . .	120
4.25	Process flow for combining two CT scans into a single, dual-energy pro- jection set. . . . .	123
4.26	Reconstructed cross sections for the compromised energy scan and the two dual-energy cases. . . . .	126
4.27	Zoomed views of selections A, B and C from 4.26 . . . . .	127
4.28	Line profiles across MM' from figure 4.27. . . . .	128
4.29	Resulting damage threshold when applying a threshold to the object equiv- alent to the background grey level in each case. . . . .	129
4.30	Angular data for two consecutive CT scans under the same imaging con- ditions. . . . .	131
4.31	Photograph of NPL defect panel. . . . .	132
4.32	Reconstructed images of compromised scan of NPL panel. . . . .	133
4.33	Reconstructed cross sections of NPL panel. . . . .	133
4.34	Variation of absorbance with thickness in MTM-45 CFRP and associated third-order polynomial fits for beam hardening correction with the tung- sten target material. . . . .	134

5.1	Instron CEAST 9350 drop weight impact testing machine. . . . .	139
5.2	(a) Schematic showing impact test conditions, adapted from (Prichard and Hogg, 1990). (b) Photograph of sample holder containing a woven plate. .	140
5.3	Typical force-time relationships at an impact energy of 12 J for the UD and woven materials . . . . .	141
5.4	Typical force-displacements curves for a 12 J impact . . . . .	142
5.5	Typical energy-time curves for a 12 J impact . . . . .	142
5.6	Typical force-time curves under various impact energies for the UD material	143
5.7	Typical force-time curves under various impact energies for the woven material. . . . .	143
5.8	Peak impact force for UD and woven materials under various impact energies. . . . .	145
5.9	Comparison of absorbed energy at various impact energies for UD and woven materials. . . . .	146
5.10	Vertical deformation under the impactor for UD and woven materials under various impact energies . . . . .	147
5.11	Schematic of the specimen support conditions in the compression after impact test . . . . .	148
5.12	CAI rig with a sample mounted in the 600 kN hydraulic test machine . . .	149
5.13	Typical load-displacement curves for UD and woven CAI samples after various impact energies . . . . .	150
5.14	Compression after impact strength vs. impact energy for UD and woven materials. . . . .	151
5.15	CAI strength vs. absorbed energy for UD and woven materials. . . . .	153
5.16	Test and sample geometries for the interlaminar shear strength test . . . .	154
5.17	Interlaminar shear strength test rig with a sample in place . . . . .	155
5.18	Schematic load-displacement curve for an interlaminar shear strength sample, showing load at first failure, $P_R$ . . . . .	156
5.19	Typical Force-displacement profiles for UD and woven materials during the ILSS test. . . . .	157
5.20	Schematic of scan setup for CT imaging of impacted samples (not to scale).	160
5.21	Midas NDT Ultrasonic Transmission C-scan equipment . . . . .	162
5.22	Typical reconstructed cross section of impact damage in a UD plate . . .	163
5.23	Typical in-plane damage in a UD plate . . . . .	164
5.24	Exaggerated schematic of how out-of-plane deformation causes damage at multiple ply interfaces to appear in a single CT cross section. . . . .	164
5.25	3D renderings of UD impact samples showing relative damage areas . . .	165
5.26	Typical reconstructed cross section of impact damage in a woven plate . .	166
5.27	Typical in-plane damage in a woven plate . . . . .	167
5.28	3D renderings of woven impact samples showing relative damage areas .	168

5.29	CT slice and associated histograms of an impacted sample. . . . .	169
5.30	Effect of applying a $3 \times 3$ median filter to the image in figure 5.29. . . . .	170
5.31	Example of damage thresholding in a UD plate which was subjected to 12 J impact. Sample is viewed in XY plane. . . . .	171
5.32	Summation of image masks encompassing delaminations with individual CT slices . . . . .	172
5.33	In-plane delamination area under increasing impact energies for UD ma- terial. CT images (left column) are through-thickness summations of total in-plane damage, compared against transmission C-scan data (right col- umn). . . . .	173
5.34	In-plane damage area for UD samples measured with CT and C-scan. . .	174
5.35	Mean damage area as a function of depth for the 3 J impact . . . . .	175
5.36	Mean damage area as a function of depth for the 6 J impact . . . . .	176
5.37	Mean damage area as a function of depth for the 9 J impact . . . . .	176
5.38	Mean damage area as a function of depth for the 12 J impact . . . . .	177
5.39	Interfacial damage area for individual ply interfaces under various impact energies for the UD material. . . . .	178
5.40	Typical damage shapes at ply interfaces in a UD sample impacted at 12 J. .	181
5.41	Distribution of shear stress in a quasi-isotropic laminate . . . . .	182
5.42	Horizontal and vertical damage extent in UD samples under various im- pact energies. . . . .	183
5.43	In-plane damage area under increasing impact energies for woven mate- rial. CT images (left column) are through-thickness summations of total in-plane damage, compared against transmission C-scan data (right col- umn). . . . .	185
5.44	Variation of in-plane damage area with impact energy for woven material. .	186
5.45	Mean damage area as a function of depth for the 3 J impact . . . . .	187
5.46	Mean damage area as a function of depth for the 6 J impact . . . . .	187
5.47	Mean damage area as a function of depth for the 9 J impact . . . . .	188
5.48	Mean damage area as a function of depth for the 12 J impact . . . . .	188
5.49	Horizontal and vertical damage extent in the woven material under vari- ous impact energies. . . . .	189
6.1	Simplified explanation of missing data problem. . . . .	192
6.2	ROI imaging setup . . . . .	194
6.3	Projection and line profiles with no data completion. . . . .	196
6.4	Projection and line profiles with level extension data completion. . . . .	197
6.5	Projection and line profiles with cosine extension data completion. . . . .	198
6.6	Projection and line profiles with object sectioned to fit within ROI field of view. . . . .	199
6.7	Comparison of ROI and sectioned cross-sections of impacted CFRP sample. .	200

6.8	Cropped views of ROI and sectioned scans demonstrating loss in feature contrast. Note that line profiles are slightly offset due to sample not being scanned in exactly same position once it had been sectioned. . . . .	201
6.9	ISO 50 thresholds of ROI and sectioned CT scans . . . . .	202
6.10	ISO 50 image segmentation of original ROI data versus a 3 x 3 pixel noise reduction. . . . .	203
6.11	ROI reconstructions using level extension method . . . . .	205
6.12	ROI reconstructions using cosine extension method . . . . .	206
6.13	Line profiles across the centre of the object using level and cosine extension methods. . . . .	207
6.14	ISO 50 thresholds of original truncated ROI data and extension methods using various tail lengths. . . . .	208
6.15	ROI reconstructions with varying numbers of projections . . . . .	211
6.16	Location of measurements for image quality indicators and line profiles. .	212
6.17	Variation of SNR and CNR with no. of projections . . . . .	213
6.18	Line profile across CC' . . . . .	214
6.19	Line profile across DD' . . . . .	215
6.20	Segmented damage areas as a function of projections used in the reconstruction. . . . .	216
6.21	Reconstructed cross sections in XZ plane of UD material. 3 J impact. . .	218
6.22	Reconstructed cross sections in XZ plane of UD material. 6 J impact. . .	219
6.23	Reconstructed cross sections in XZ plane of UD material. 9 J impact. . .	219
6.24	Reconstructed cross sections in XZ plane of UD material. 12 J impact. . .	220
6.25	Reconstructed cross sections in XZ plane of UD material. 3 J impact. . .	221
6.26	Reconstructed cross sections in XZ plane of UD material. 6 J impact. . .	222
6.27	Reconstructed cross sections in XZ plane of UD material. 9 J impact. . .	222
6.28	Reconstructed cross sections in XZ plane of UD material. 12 J impact. . .	223
6.29	Propagation of a delamination into a fibre tow in plain woven CFRP. . . .	224
6.30	Variation of cross sectional damage area with distance from impactor contact point in plain woven CFRP. . . . .	225
7.1	Set-up of grating interferometer CT . . . . .	229
7.2	Illustration of angular deviation in differential phase imaging (Pfeiffer <i>et al.</i> , 2006) . . . . .	229
7.3	Tomographic reconstruction (a) Projection geometry. (b) Backprojection filter function for absorption line integrals. (c) Backprojection filter function for gradient (DPC) projection integrals (Pfeiffer <i>et al.</i> , 2007). . . . .	231
7.4	Example images of a felt-tip pen. (a) Transmission (b) Differential phase contrast (c) dark field. From Revol <i>et al.</i> (2011b). . . . .	232
7.5	Experimental set-up of grating interferometer tomography equipment at CSEM. . . . .	233

7.6	Photographs of sample Z1. . . . .	233
7.7	Sample co-ordinate system used to describe geometry in the grating experiment. . . . .	234
7.8	Experimental set-up for variation of sample orientation with respect to optical axis. . . . .	235
7.9	Absorption, differential phase contrast (DPC), and scattered projections of sample Z1. Rotation angle specified is around the $Y$ tomographic axis. . . . .	237
7.10	Ultrasonic C-scan of sample Z1, showing delamination area. Spatial resolution approximately 1 mm. . . . .	238
7.11	Absorption, DPC and scattered projections of sample Z1. Rotation angle specified is around optical ( $X$ ) axis. . . . .	240
7.12	Intensity line profiles across damage area (inset) of sample Z1 under various optical axis rotation angles. . . . .	241
7.13	Reconstructed slices of sample Z1 in $XY$ plane. Impacted face on left. . . . .	242
7.14	Reconstructed slices of sample Z1 in $XZ$ plane. Impacted face on left. . . . .	243
7.15	Reconstructed slices of sample Z1 in $YZ$ plane. Impacted face on left. . . . .	245
7.16	Local artefacts in DPC and DF $YZ$ plane images, magnified from figure 7.15 . . . . .	246
7.17	3D renderings of impact damage using grating interferometer tomography. . . . .	247
7.18	Grating Interferometer Projection images of sample B15 which was impacted at 15 J. . . . .	248
7.19	Dark field projections of 5 J impact sample rotated with respect to optical axis. . . . .	248
7.20	Dark field projections of 10 J impact sample rotated with respect to optical axis. . . . .	249
7.21	Dark field projections of 15 J impact sample rotated with respect to optical axis (a-c). Respective damage areas thresholded (d-f). . . . .	249
7.22	Variation of thresholded damage area with rotation about optical axis. . . . .	250
8.1	CT images of fatigue damage in CFRP containing dye penetrant. (a) is a reconstructed cross section, (b)-(d) 3D renderings highlighting the dye penetrant (red). . . . .	254
8.2	Propagation phase contrast image of a CFRP laminate with uni-directional plies. . . . .	255
8.3	Commercial applications of computed tomography . . . . .	256
8.4	Nominal (CAD) actual (CT) comparison of an aluminium valve block (Brunke, 2010). . . . .	260
A.1	Flat field corrected radiograph of resolution plate at 120X magnification . . . . .	263
A.2	Cropped and enhanced view of resolution target illustrating line profiles take across resolution markings. . . . .	264

A.3	Line profiles across resolution scale bars at (a) AA' and (b) BB' from figure A.2. . . . .	265
A.4	Radiograph of tungsten wire, showing line profile . . . . .	267
A.5	Line profile across edge of tungsten wire . . . . .	268
A.6	(a) Reconstructed central slice of tungsten wire (b) Differential image of central slice. . . . .	270
A.7	Line Response Function of the edge of the central reconstructed slice of tungsten wire. The LRF is taken over the line AA' in figure A.6(b). . .	270
A.8	Edge resolution vs. slice number for the reconstructed tungsten wire volume. Slices are numbered from the bottom of the volume upwards relative to the detector. . . . .	271
A.9	Variation of SNR with no of projections for a CFRP which fits inside the detector field of view. . . . .	272
A.10	Reconstructed cross sections of woven MTM-45 coupon with varying numbers of CT projections. . . . .	272
A.11	Amptek XR-100T CdTe detector system. Amplifier (left), detector housing fitted with collimator (right).(Amptek, 2011). . . . .	274
A.12	Linear calibration obtained using a dial source and W spectra peaks. . . .	274
A.13	Cu target spectrum at 225kV at 50 $\mu$ A . . . . .	275
A.14	Cu target spectrum at 50kV, 100kV and 225kV at 50 $\mu$ A . . . . .	276
A.15	Cu target spectrum at 50 $\mu$ A, 100 $\mu$ A and 200 $\mu$ A at 100kV . . . . .	276
A.16	Mo target spectrum at 225kV at 50 $\mu$ A . . . . .	277
A.17	Mo target spectrum at 50kV, 100kV and 225kV at 50 $\mu$ A . . . . .	277
A.18	Mo target spectrum at 50 $\mu$ A, 100 $\mu$ A and 200 $\mu$ A at 100kV . . . . .	278
A.19	Ag target spectrum at 225kV at 50 $\mu$ A . . . . .	278
A.20	Ag target spectrum at 50kV, 100kV and 225kV at 50 $\mu$ A . . . . .	279
A.21	Ag target spectrum at 50 $\mu$ A, 100 $\mu$ A and 200 $\mu$ A at 100kV . . . . .	279
A.22	W target spectrum at 225kV at 50 $\mu$ A . . . . .	280
A.23	W target spectrum at 50kV, 100kV and 225kV at 50 $\mu$ A . . . . .	281
A.24	W target spectrum at 50 $\mu$ A, 100 $\mu$ A and 200 $\mu$ A at 100kV . . . . .	281
A.25	Comparison of spectra produced with each target at 225kV and 50 $\mu$ A. . .	282
A.26	Comparison of spectra produced with each target at 225kV and 50 $\mu$ A, magnified to show relative bremsstrahlung backgrounds. . . . .	282
A.27	Stability of 225kV X-ray source . . . . .	285
A.28	Spectra obtained with and without a CFRP sample obstructing the X-ray beam, and difference between the spectra. . . . .	286
A.29	Transmission profile of a CFRP sample at 225kV and 80 $\mu$ A . . . . .	287

## LIST OF TABLES

4.1	Step-wedge imaging conditions. . . . .	110
4.2	Image quality results for the compromise and dual-energy cases. . . . .	127
4.3	CT settings for dual-energy imaging of NPL panel. . . . .	132
5.1	Selected material properties for MTM-45 from material supplier's data sheet. . . . .	137
5.2	p-values for first failure loads in UD materials under various impact energies	144
5.3	p-values for absorbed energies in UD and woven materials . . . . .	146
5.4	p-values for CAI strength in UD samples under various impact energies .	152
5.5	p-values for CAI strength in woven samples under various impact energies	152
5.6	Interlaminar shear test symbols . . . . .	154
5.7	Interlaminar Shear Measured Sample Dimensions . . . . .	155
5.8	ILSS values for UD and woven materials . . . . .	157
5.9	Sample batches for CT imaging . . . . .	159
5.10	Imaging parameters for dual energy scanning of impacted samples. . . . .	161
5.11	P-values for interfacial damage areas after 3 J impact. . . . .	179
5.12	P-values for interfacial damage areas after 6 J impact. . . . .	179
5.13	P-values for interfacial damage areas after 6 J impact. . . . .	179
5.14	P-values for interfacial damage areas after 12 J impact. . . . .	180
6.1	Image conditions for ROI imaging of impact test coupon . . . . .	194
6.2	Image quality indicators for sectioned and ROI scans. . . . .	200
6.3	Image quality indicators within the object for level and cosine data completion methods . . . . .	209
6.4	Image conditions for ROI imaging of impact test coupon using varying projection numbers . . . . .	210
6.5	Image conditions for ROI imaging UD and woven impacted coupons . . .	217
7.1	Imaging parameters for grating interferometer tomography of sample Z1.	234
7.2	Imaging parameters for tomography of sample Z1 at HMXIF. . . . .	236
8.1	Costs associated with industrial tomography systems. . . . .	257

8.2	Rates to access CT equipment at University of Manchester. . . . .	257
A.1	Image conditions for radiograph of resolution target . . . . .	262
A.2	Image conditions for radiograph of tungsten wire . . . . .	266
A.3	Image conditions for CT scan of tungsten Wire . . . . .	269
A.4	Comparison of total counts, and percentage of total counts in fluorescence peaks for each target material at 225kV . . . . .	283

# ABSTRACT

The University of Manchester

Jordan Elliot Rouse

Engineering Doctorate (EngD)

Characterisation of Impact Damage in Carbon Fibre Reinforced Plastics by 3D X-Ray Tomography

5<sup>th</sup> July 2012

Carbon fibre reinforced plastics (CFRP's) are finding increased use as structural materials in many transport applications, particularly next generation commercial aircraft. The impact damage tolerance of these materials is relatively poor compared to conventional aircraft materials such as aluminium. As a result there is a concerted research effort to improve the damage tolerance of these materials. Understanding the microstructural mechanisms of damage can help to design improved materials. Three-dimensional X-Ray computed tomography (CT) allows these damage mechanisms to be identified and quantified non-destructively. However, a lack of published work in the field means no consistent methodologies for imaging or quantifying damage in CFRP's using X-Ray tomography exist. This thesis provides several novel methodologies for imaging and quantifying impact damage using X-Ray CT. A dual energy imaging methodology was developed to overcome the reduction in CT image quality caused by the high aspect ratio of CFRP structures. This approach resulted in a 66% increase in signal-to-noise ratio, and a 109% increase in contrast-to-noise ratio. The development of a methodology for quantifying impact damage in CFRP based on thresholding the in-plane damage area showed good agreement with ultrasonic C-scan results, and allowed correlations between impact energy, damage area and compression-after-strength to be made. Region of interest (ROI) algorithms for high magnification imaging of impact damage in CFRP plates were investigated. These algorithms were not developed by the author, but further understanding of their effectiveness and practical applications is presented in this work. Finally, a novel X-Ray tomographic imaging technique using interferometry was applied to imaging impact damage in CFRP's. This method was developed by a research group in Switzerland at the *Centre Suisse d'Electronique et de Microtechnique (CSEM)* in Zurich. The work in this thesis presents the first application of the technique to image impact damage in CFRP.

# DECLARATION

**The University of Manchester**

**Candidate Name:** Jordan Elliot Rouse

**Faculty:** Engineering and Physical Sciences

**Thesis Title:** Characterisation of Impact Damage in Carbon Fibre Reinforced Plastics by 3D X-Ray Tomography

I declare that no portion of this work referred to in this thesis has been submitted in support of an application for another degree or qualification of this or any other university or other institute of learning.

## COPYRIGHT

- i. The author of this thesis (including any appendices and/or schedules to this thesis) owns certain copyright or related rights in it (the "Copyright") and s/he has given The University of Manchester certain rights to use such Copyright, including for administrative purposes.
- ii. Copies of this thesis, either in full or in extracts and whether in hard or electronic copy, may be made only in accordance with the Copyright, Designs and Patents Act 1988 (as amended) and regulations issued under it or, where appropriate, in accordance with licensing agreements which the University has from time to time. This page must form part of any such copies made.
- iii. The ownership of certain Copyright, patents, designs, trade marks and other intellectual property (the "Intellectual Property") and any reproductions of copyright works in the thesis, for example graphs and tables ("Reproductions"), which may be described in this thesis, may not be owned by the author and may be owned by third parties. Such Intellectual Property and Reproductions cannot and must not be made available for use without the prior written permission of the owner(s) of the relevant Intellectual Property and/or Reproductions.
- iv. Further information on the conditions under which disclosure, publication and commercialisation of this thesis, the Copyright and any Intellectual Property and/or Reproductions described in it may take place is available in the University IP Policy (see <http://www.campus.manchester.ac.uk/medialibrary/policies/intellectualproperty.pdf>), in any relevant Thesis restriction declarations deposited in the University Library, The University Library's regulations (see <http://www.manchester.ac.uk/library/aboutus/regulations>) and in The University's policy on presentation of Theses.

## FROM AIRCRAFT TO X-RAYS, AN INTRODUCTION

Composite materials are playing an increasingly important role in today's aerospace industry. One of the reasons for this increasing use of composites is the drive to reduce aircraft weight in order to reduce fuel consumption, as well as the increasing engineering requirements placed on modern aircraft. Composite materials can offer a solution to these problems due to their excellent mechanical properties coupled with low densities. Hence, for a given load carrying requirement, a composite component may be lighter than a conventional metal component.

However, several barriers still present a challenge to increasing the use of composite materials in engineering applications. High raw material costs, difficulties in processing some materials and a lack of understanding of material behaviour are a few of these. Such factors are particularly applicable to the aerospace industry where keeping costs down is vital, but reliability and predictability of materials are vital for safety requirements.

Fibre reinforced composite materials, such as those based on carbon fibres embedded in an epoxy resin matrix, are the most widespread composite materials used in aircraft. These materials are being used in wing skins, engine coverings, and primary structures. As an example, the new Boeing 787 aircraft comprises over 50% by weight of composite materials (Marsh, 2005), as shown in figure 1.1

However, as with all performance issues in engineering, trade-offs are inevitable. The excellent general properties of laminated composites come at the expense of the through-thickness properties. As a result, the ability of composite materials to withstand impact events is often poor. This has led to a concerted research effort into the cause and effects of impact damage in composites materials with aims to improve the damage tolerance.

To help improve the understanding of impact damage in composite materials many non-destructive testing techniques have been utilised. These techniques have included ultrasonic inspection, thermal imaging and X-rays. This thesis takes a focus on using X-rays to image damage in carbon fibre reinforced plastic (CFRP) in three-dimensions using a process known as 3D X-ray computed tomography (CT).



(a)



(b)

Figure 1.1: (a) The Boeing 787(Sizer, 2009) and (b) section of the 787 composite fuselage (Boeing, 2009).

Many people are familiar with the use of X-rays to image damage inside the body, such as broken bones, but this form of radiation can be used to image virtually any object (even those in space!). Figure 1.2 shows some examples of objects imaged using X-rays.

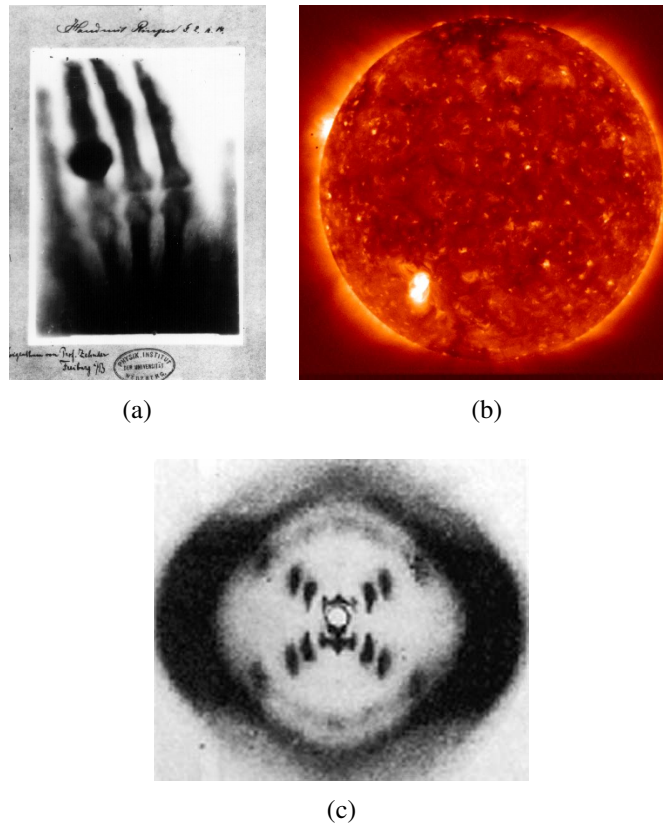
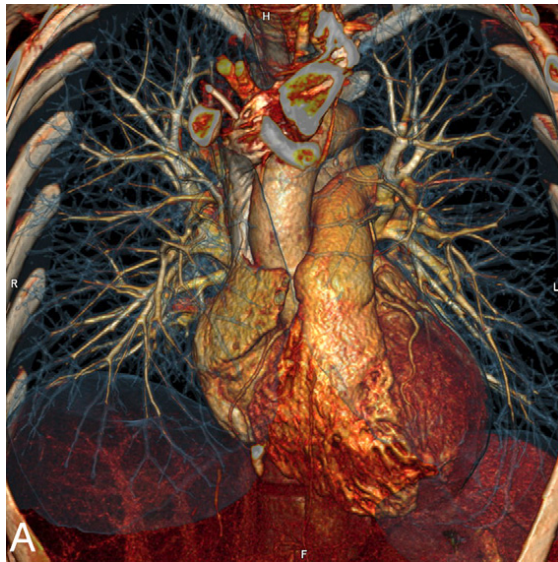


Figure 1.2: Examples in X-ray imaging. (a) The first radiograph taken of a human body part, by Roentgen, the discoverer of X-rays. The hand belonged to his wife (Röntgen, 1895). (b) A false colour X-ray image of our sun (NASA, 2000). (c) 'Photo 51', the X-ray diffraction image which proved the helical structure of DNA (Franklin, 1952).

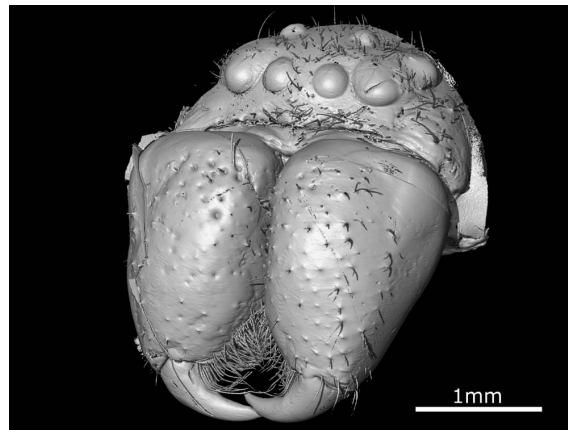
X-ray imaging was further advanced in the 1970s when Hounsfield developed the first X-ray CT system (Hounsfield, 1973), for which he shared the 1979 Nobel Prize for Physiology or Medicine with Allan McLeod Cormack. Hounsfield's CT system allowed the cross sectional imaging of body parts for medical diagnosis by taking radiographs on the object from many different angles. Since these early developments, hardware and software improvements now allow the use of CT to investigate virtually any object on a much larger scale than initially possible. Fully three-dimensional data allows us to 'look inside' objects without having to destructively interfere with them. This has led to the use of CT in medical diagnosis, detection of defects in materials, reverse engineering, and even natural history research. Some examples are shown in figure 1.3.



(a)



(b)



(c)

Figure 1.3: Examples of CT applications (a) Medical diagnosis (Becker and Johnson, 2011) (b) 3D rendering of porosity in a metal casting (Brandmüller, 2008) (c) 3D rendering of a prehistoric Huntsman spider (McNeil).

Although CT has shown to be an effective tool for the characterisation of defects and damage in engineering materials, a review of the literature shows very little published activity specifically related to impact damage in CFRP using CT. This could be due to several reasons; the type of CT equipment needed has only become practical for laboratory sources in the last few years and the shape of structures made from CFRP makes them geometrically difficult to image using CT. These issues are explored further in chapter 2. What data is available shows highly qualitative studies, useful in describing the processes of impact damage, but little quantitative data.

## 1.1 Aims and Objectives

The majority of the experimental work presented in this thesis was performed at the Henry Moseley X-Ray Imaging Facility (University of Manchester) and the National Composites Certification and Evaluation Facility (University of Manchester). The project aimed to achieve the following;

- Develop a methodology to improve the imaging of high aspect ratio CFRP objects for a laboratory cone-beam CT system
- Develop a methodology to allow quantification of impact damage in CFRP objects
- Explore the use of advanced CT techniques to image damage in CFRP objects

These aims were achieved by the following;

- Characterisation of a laboratory CT system in order to optimise imaging of CFRP materials
- Development of a dual-energy imaging method to improve imaging of high aspect ratio CFRP objects
- Application of the dual-energy method to quantify and characterise damage in CFRP objects
- Comparison of CT data with other non-destructive testing methods to qualify CT measurements
- The application of region-of-interest (ROI) imaging techniques
- The use of novel phase-contrast CT equipment to image damage in CFRP objects

Chapters 2 and 3 present background and literature reviews regarding X-ray tomography and impact damage in CFRP respectively. Chapter 4 presents a novel approach to imaging high aspect ratio objects using a dual-energy technique. The work in Chapter 7 investigates the use of grating interferometer CT to image impact damage. This technique is also known as differential phase contrast (DPC). The DPC work was performed at the *Centre Suisse d' Electronique et de Microtechnique* (Swiss Center for Electronics and Microtechnology, CSEM) in Zurich.

## 3D X-RAY TOMOGRAPHY: BACKGROUND AND LITERATURE

This section provides an overview of the computed tomography technique, including a theoretical background to the topic. The different scanning geometries in laboratory based CT scanners are explored, before a brief explanation of the reconstruction method is given. A discussion of artefacts associated with tomography is then presented, followed by an exploration of the applications of CT to imaging composite materials.

### 2.1 Overview

Computed X-Ray Tomography (CT) is non-destructive inspection method which provides cross-sectional information about an object over 2-D cross sections (CT 'slices'), or the whole volume. Hence the method is often referred to as 'Three-dimensional X-Ray Computed Tomography'. Information about the object is acquired from a finite number of radiographic projections taken at various angles as the object is rotated axially. Figure 2.1 illustrates the basic geometry of a modern cone-beam CT system.

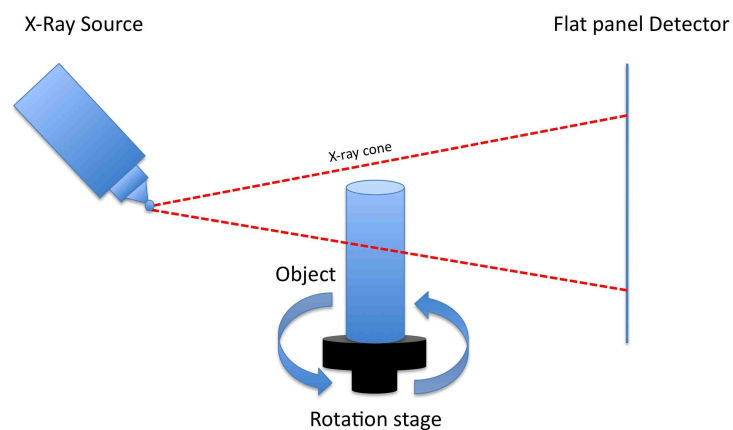


Figure 2.1: Schematic of cone beam X-Ray tomography system.

Because different materials have various X-Ray attenuation coefficients, the spatial distribution of these coefficients through the cross section of the object allows a reconstructed representation of their distribution. The process therefore allows a non-destructive view of the inside of an object.

CT provides an excellent non-destructive imaging technique where the primary goal is to identify, locate and quantify volumetric defects to a high accuracy, and in three-dimensions (British Standards, 2009a). As all materials absorb X-Rays (to varying extents), the technique can be used to image virtually any object. When discussing the field of non-destructive testing, the terms '*non-destructive testing*' (NDT), '*non-destructive evaluation*' (NDE) are often used interchangeably. Strictly speaking NDT is process of acquiring the data (e.g. by acquiring a radiograph or C-scan), while NDE is the process of using that data to evaluate the condition of the object of interest.

Compared to conventional (2D) radiography, whereby overlapping features are superimposed on to each other, CT provides an imaging method where individual features appear separate from each other; i.e. the full spatial information of the sample is preserved. Accurate dimensional measurements in addition to density measurements can be achieved with proper system calibration. As a result, CT is a particularly useful tool in both Non-destructive testing (NDT) for structural integrity measurement and metrology. CT is particularly useful in metrological applications due to;

- Data acquisition without contacting the object
- Internal and external dimensional information
- Export of 3D model data for reverse engineering applications

As with any imaging system, there are inherent limitations. CT can never produce an exact representation of the measured object, and various artefacts are inherent in the procedure (although many can be corrected for). Generally, the effectiveness of the CT imaging process involves a trade-off between spatial resolution, artefacts, and image noise.

## 2.2 Process Stages of Computed Tomography

To generate and obtain useful information from a CT data set (volume), three general steps are required. These steps are referred to as;

1. Acquisition
2. Reconstruction
3. Visualisation and analysis

### 2.2.1 Acquisition

The first stage in the generation of a CT data set is to acquire useful radiographs (or ‘*projections*’). These projections are acquired systematically, from a sequence of increasing viewing angles known as the ‘*projection angle*’. The identification of a particular feature is highly dependant on the number of angles from which projections are taken. Hence, increasing the number of projections will generally improve the quality of a CT scan.

Most imaging systems contain inherent artefacts, and as a result a CT scan must involve image correction parameters which are described before the scan begins. Offset and gain reference images are taken to apply ‘*flat field correction*’. This correction is performed by acquiring projections using black (X-Rays off) and white (X-rays on with no sample in the field of view) reference images to correct for detector variations. These variations may include pixels which give an inflated reading (hot pixels), and to establish the dynamic range of the detector under a given set of imaging conditions. Other corrections such as optical pin-cushion distortion may also be applied. Each projection in the acquisition has these corrections applied by automated software.

### 2.2.2 Reconstruction

Reconstruction is the stage which differentiates computed tomography from traditional radiography, and can therefore be said to be the most important stage. During reconstruction, the projections obtained during image acquisition are passed to a ‘*reconstruction algorithm*’ which may produce a stack of cross-sectional slices, or a single three-dimensional volume, depending on the software used.

### 2.2.3 Visualisation and Analysis

Once a CT volume has been reconstructed, useful information needs to be extracted using *visualisation* and *analysis* techniques. This stage encompasses any actions which involve image viewing and processing, as well as data extraction and processing.

Visualisation can be performed in 2D planes (slices) or in 3D space. The advantage of 3D data visualisation is that the object is represented in a way which corresponds to the natural appearance of the real object, making feature identification simpler.

Digital filters such as noise reduction, edge detection and downsampling among others can be used to process and extract relevant data. This allows visual representation of feature of interest through 3D surfaces, false colour images etc. and also numerical quantification of CT data.

## 2.3 The Physics of X-Rays

To understand how a CT system works, an appreciation of the physics of X-Rays is required in terms of X-Ray generation, propagation, and the interaction of the radiation with matter.

### 2.3.1 Production of X-Rays

X-Rays are a form of electromagnetic wave, with wavelengths which occupy the range of 0.1 to 10nm on the electromagnetic spectrum. Figure 2.2 shows how X-rays compare to other forms of electromagnetic energy in terms of photon energy.

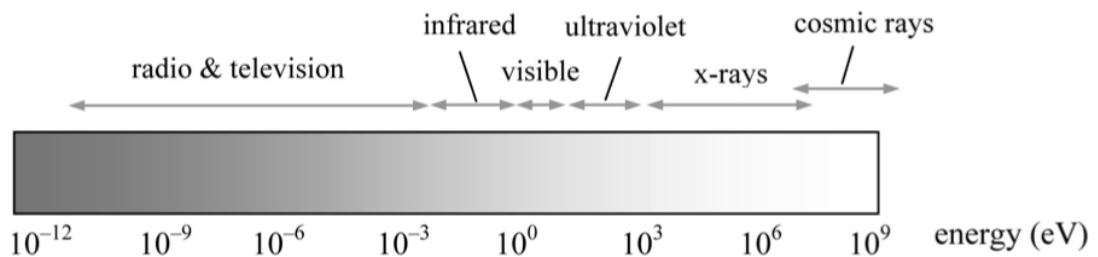


Figure 2.2: Illustration of the electromagnetic spectrum (Hsieh, 2003)

In the context of radiographic imaging using laboratory sources, X-Rays are produced when a target material is bombarded by high speed electrons. The kinetic energy of the incident electrons may be transferred to the target material by several types of collision event, which in turn produce X-rays.

The energy of an X-ray photo,  $E$ , is given by:

$$E = hv = \frac{hc}{\lambda} \quad (2.1)$$

where;

- $h$  is Planck's constant ( $6.63 \times 10^{-34} Js$ )
- $c$  is the speed of light in a vacuum ( $3 \times 10^8 ms^{-1}$ )
- $\lambda$  is the wavelength of the X-ray.

Generally, the energy of an X-ray is described in terms of *electron-volts (eV)*; the amount of kinetic energy obtained by an electron accelerated across an electrical potential of 1V, which equates to a value of  $1.602 \times 10^{-19} J$ . The maximum possible energy of an X-ray photon is the kinetic energy of the incident electron. However, most collisions between the incident electrons and the target material result in low energy transfers, due to interaction between the incident electron and outer shell electrons of the target material.

This process produces heat but no X-rays. Typically 99% of the input energy is converted to heat (Hsieh, 2003).

Several types of interaction between the incident electron and the target atoms do produce X-rays.

The most common type of interaction results in *Bremsstrahlung* radiation. Here, inelastic collisions between the incident electron and the target nucleus cause sudden deceleration of the electron, resulting in the emission of a quantum of energy i.e. an X-ray photon. The energy of this photon varies; it may be small if little energy is lost during the interaction, but can be as large as the total kinetic energy of the incident electron if a direct electron-nucleus collision occurs. The Bremsstrahlung radiation is continuous over the entire x-ray spectrum. A schematic of the production of Bremsstrahlung is given in figure 2.3.

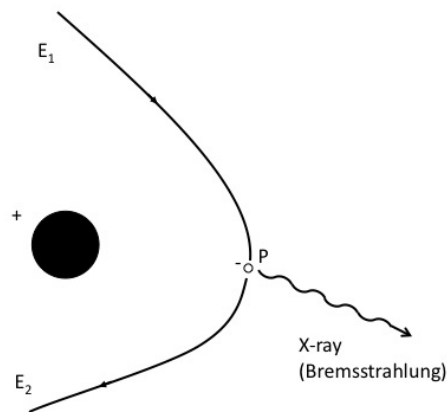


Figure 2.3: Production of Bremsstrahlung X-rays. An electron at point P suddenly loses energy by the emission of an X-ray photon. The electron continues with a reduced energy,  $E_2$ . From (Graham and Cloke, 2003).

The intensity of Bremsstrahlung radiation produced is related to the atomic number of the target material by the relationship:

$$I \propto ZE^2 \quad (2.2)$$

Where  $Z$  is the atomic number of the target material, and  $E$  is the incident electron energy.

A second type of interaction between the incident electrons and the target material superimposes characteristic line spectra over the continuous Bremsstrahlung. This characteristic radiation occurs when high speed electrons directly interact with inner-shell electrons (such as K or L shell electrons) of the target material. The inner shell electron is

ejected by the collision, ionising the atom. An electron from a higher energy shell drops down to fill the vacant position, releasing an X-Ray photon. Figure 2.4 illustrates the production of characteristic radiation.

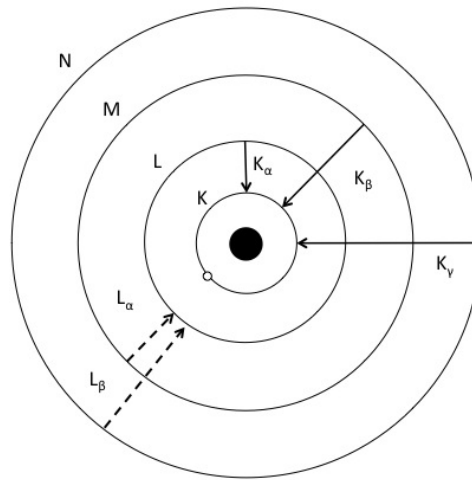


Figure 2.4: Production of characteristic radiation. K-lines are produced by quantum jumps down to the K-shell. From (Graham and Cloke, 2003).

Plotting the intensity versus energy of the X-rays produced from a given target materials, produces a *spectrum*, giving the summation of the Bremsstrahlung and characteristic radiation. Figure 2.5 illustrates a typical spectrum, highlighting the contributions from different radiation events.

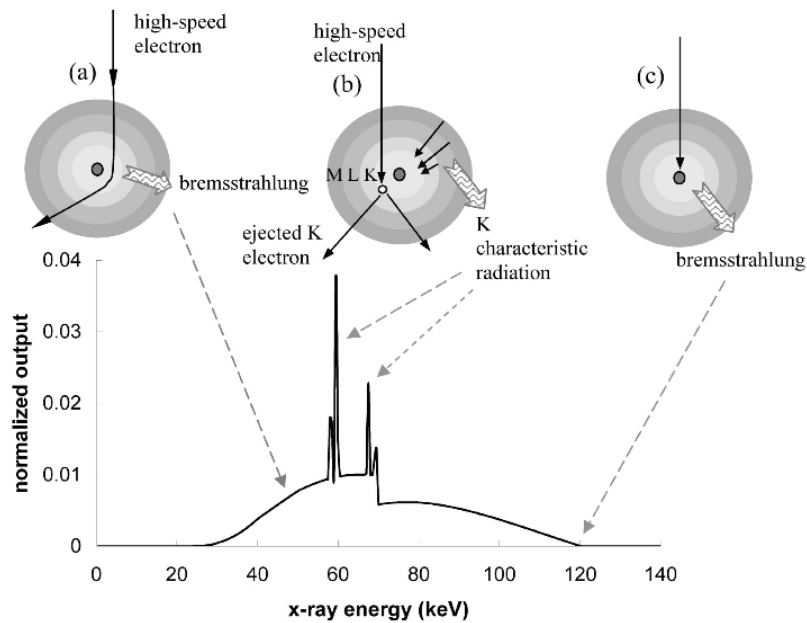


Figure 2.5: Illustration of electron interaction with a target material. (a) Bremsstrahlung radiation, (b) characteristic radiation, and (c) maximum photon energy due to Bremsstrahlung events where entire kinetic energy of the incident electron is transferred to the target atom (Hsieh, 2003).

### 2.3.2 Interaction of X-Rays with Matter

When an sample is illuminated by a beam of X-rays, the radiation may interact with the atoms in the sample in different ways. The possible interaction methods are outlined in figure 2.6. These mechanisms are obviously also applicable to any filtration material used in the CT scan.

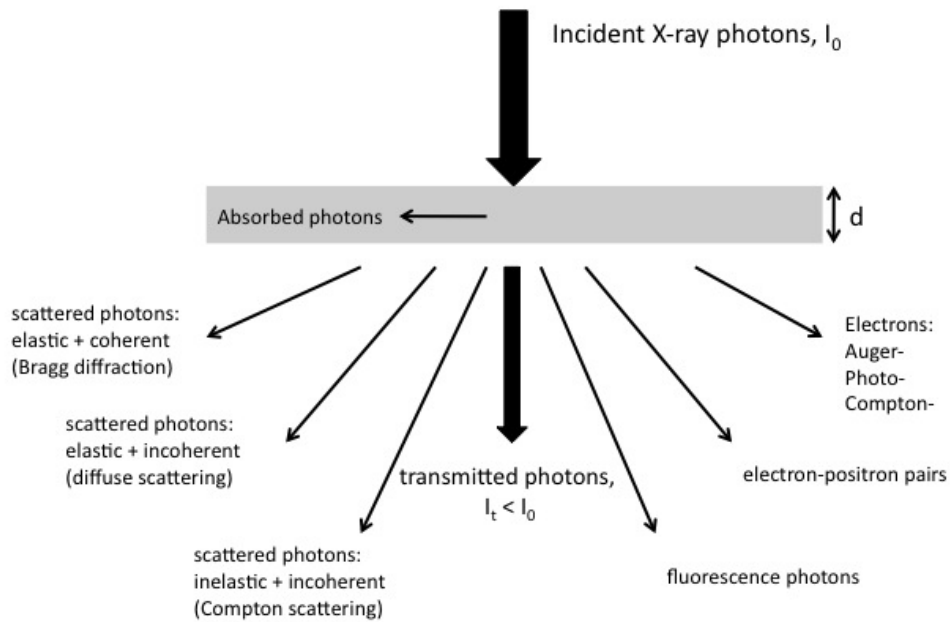


Figure 2.6: Overview of X-ray interactions with matter (Banhart, 2008)

In general, an X-ray photon may interact with a material by *scattering* or *absorption*. A photon may also pass through a material without any interaction. Absorption processes result in energy being transferred to the material from the X-ray photon, whereas scattering causes deflection of the X-ray photon from its original path and may (elastic scattering) or may not (elastic scattering) result in energy transfer to the material. If the intensity of the incident X-ray beam is compared before and after interacting with a material, it is observed that the beam intensity reduces; this process is termed *attenuation* and occurs due to absorption and scattering. The attenuation of the X-ray beam is given by the Beer-Lambert law:

$$I_t = I_0 e^{-\mu x} \quad (2.3)$$

where;

- $I_0$  = incident beam intensity
- $I_t$  = transmitted beam intensity
- $\mu$  = total linear attenuation coefficient
- $x$  = path length through object

The total linear attenuation coefficient,  $\mu$  is defined as the fraction of X-rays removed from a beam per unit thickness of the attenuator (Graham and Cloke, 2003). The term *total* is used because an attenuation coefficient occurs due to each attenuating process (the photoelectric effect and scattering). For transmission tomography, the overall attenuation of the beam is the main concern, the details of the processes contributing to attenuation of the x-ray beam can be found in many references (Banhart, 2008; Graham and Cloke, 2003; Jackson and Hawkes, 1981). However, a brief discussion of the photoelectric effect (an absorption process), and scattering will be presented here as they can strongly effect the set-up and optimisation of a CT scan.

### 2.3.2.1 The Photoelectric Effect and Scattering

When an incident X-ray photon transfers its energy to a bound electron in the sample, this electron is ejected with the energy of the incident photon minus the binding energy of the electron. The newly excited atom will then relax (an electron fills the hole), causing the emission of a photon of characteristic radiation. The X-ray photon has therefore been absorbed. The probability of absorption occurring within a material (the absorption cross-section), depends on the incident X-ray photon energy, and displays rapid changes at energies which correspond to core electron states. This process gives rise to 'absorption edges' of type K, L, or M depending on the electron transitions. Figure 2.7 illustrates the the effect of the photoelectric effect in tungsten.

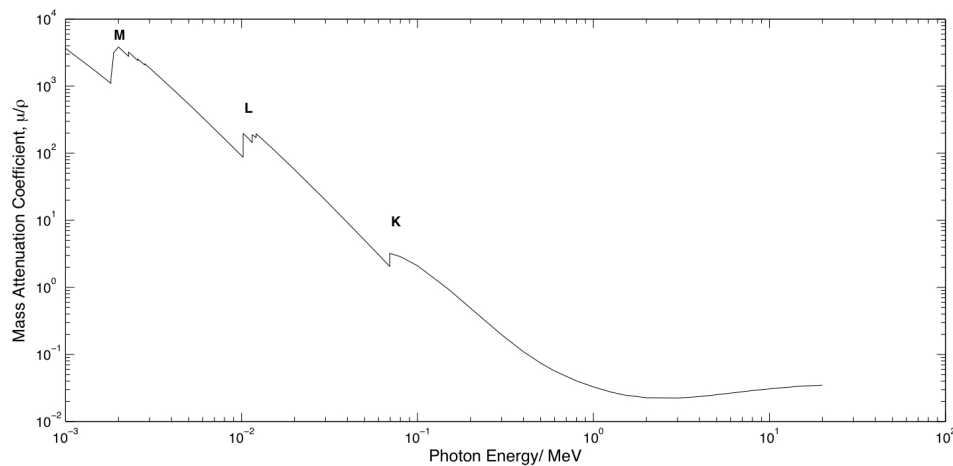


Figure 2.7: Dependence of the mass attenuation coefficient on photon energy for tungsten National Institute of Standards, (2011).

At the energies used in CT scanning, the predominant scattering effect is known as *Compton scattering*, which is an inelastic event. If the incident X-ray photon has an energy much greater than the binding energy of the electron it interacts with, the electron can be regarded as a free electron. In this case, partial absorption of the X-ray photon occurs, causing deflection of the photon from its original path. This attenuation process

becomes significant at high energies and lower atomic number. Figure 2.8 illustrates the relative dominance of the photoelectric effect and Compton scattering at various energies.

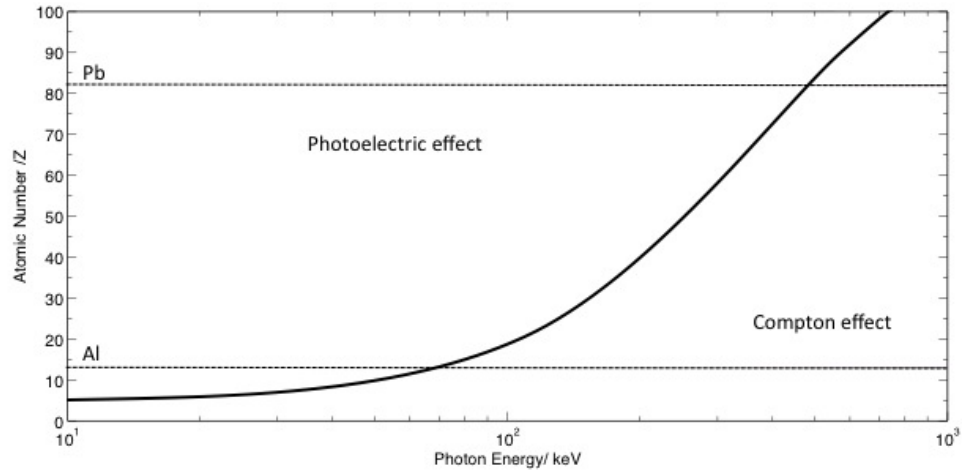


Figure 2.8: Relative dominance of the photoelectric affect and Compton Scattering (Banhart, 2008)

## 2.4 Reconstruction Methods

In section 2.6 the Beer-Lambert law was introduced, which forms the basis of reconstructing a CT image. For each pixel on the imaging detector, the beam intensity for a specific photon energy is given by:

$$I_t = I_0 e^{-\mu x} \quad (2.4)$$

By rearranging the Beer-Lambert equation, the integral of the linear attenuation coefficient,  $\mu$  can be calculated for each ray path:

$$\ln \left( \frac{I_0}{I_t} \right) = \int \mu(x, y) dx \quad (2.5)$$

Where  $\mu(x, y)$  is the value of the linear attenuation coefficient at a point (x,y) along the ray path, illustrated in figure 2.9. In a polychromatic laboratory source, the above integral must be performed for all photon energies in the X-ray spectrum.

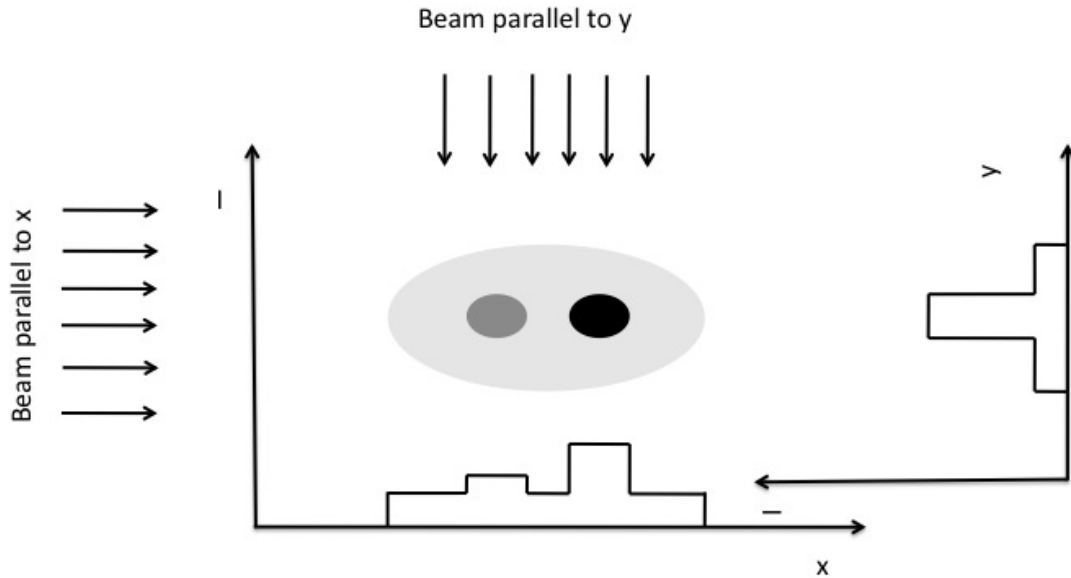


Figure 2.9: Projection intensities from perpendicular directions of a component with three different linear attenuation coefficients,  $I(x)$  is the intensity profile measured behind the sample. Adapted from (Banhart, 2008).

Hence, each projection acquired is composed of a set of line integrals of  $\mu$  for each ray path. Taking projections over multiple angles gives the Radon transform of the object for a given cross section (Radon, 1917, 1986). Radon showed that if the line integrals for all ray paths were known, the value of a function (i.e projection intensity) could be determined. Subsequently he showed that the inverse Radon transform enabled reconstruction of the function  $\mu(x, y)$ .

To accurately reconstruct an object, more advanced mathematical theories were developed using the Beer-Lambert law as a basis. The first reconstructions were based on the parallel beam geometry, illustrated in figure 2.10

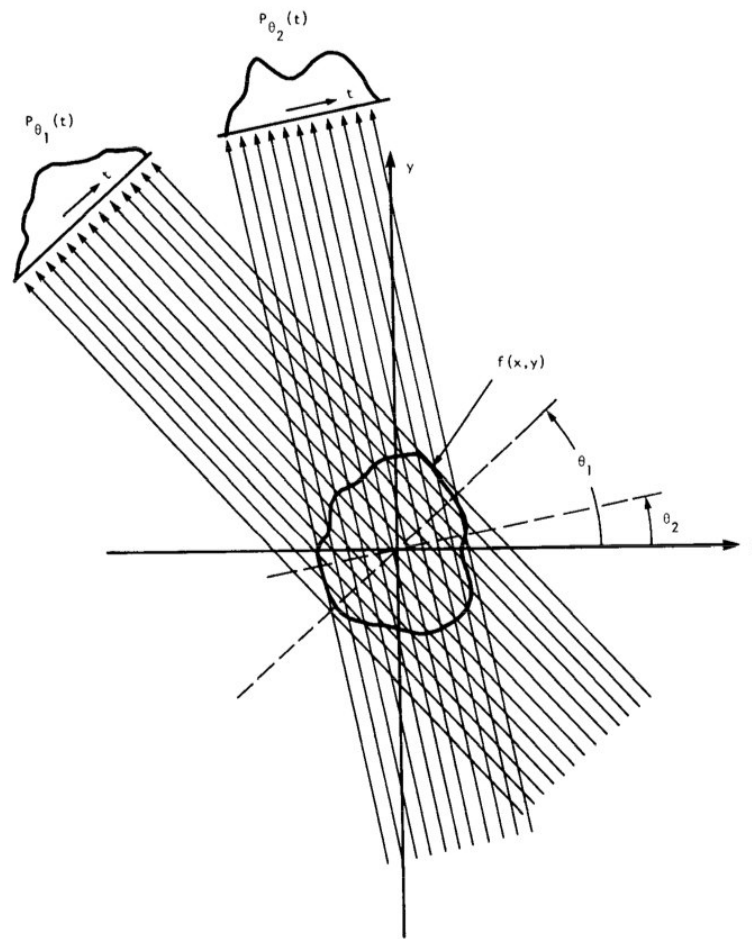


Figure 2.10: Parallel projection geometry. Projections are taken by measuring a set of parallel rays for a number of different angles. From (Rosenfeld and Kak, 1982).

In the parallel beam geometry, all X-rays are parallel resulting in a 1:1 magnification of the object. This type of geometry is often used on synchrotron CT stations, where spatial resolution is determined by detector pixel size.

Fan beam geometry allows for geometrical magnification of the object by use of a point source which is fixed relative to the detector array. Figure 2.11 shows the geometry of this acquisition method.

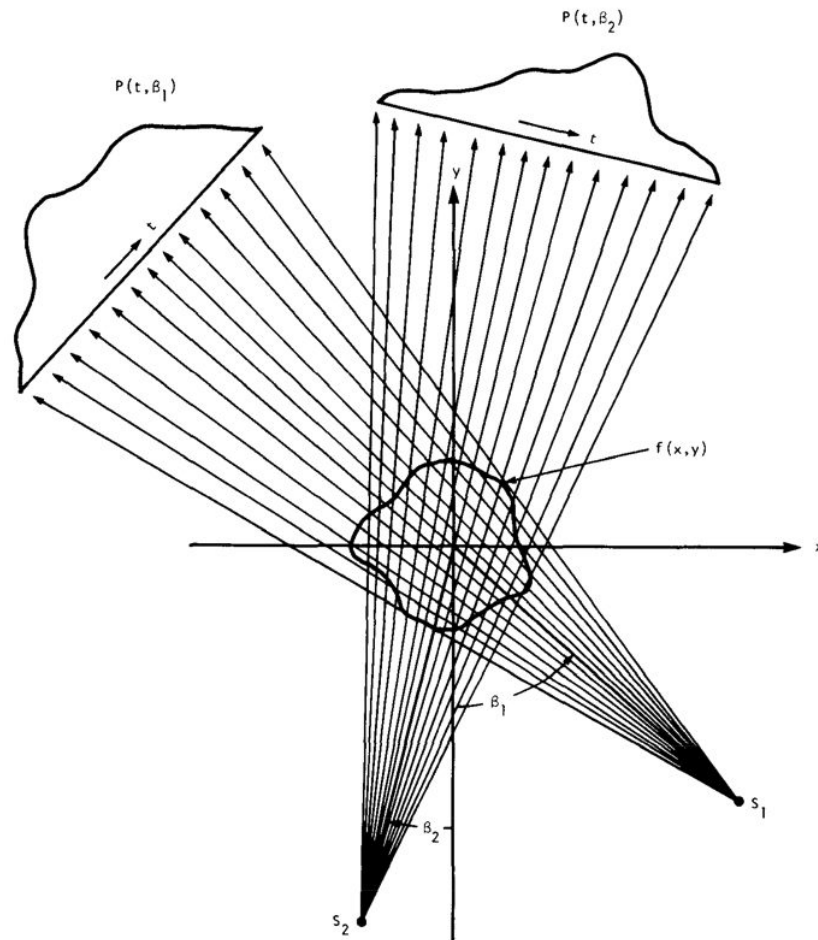


Figure 2.11: Fan beam projection geometry, showing all rays emanate from one location. From (Rosenfeld and Kak, 1982).

Once the projections have been acquired, the object is reconstructed. Most systems implement a form of the filtered back projection (FBK) algorithm, which was initially developed for the parallel beam geometry (Herman, 2009). Back projection effectively involves projecting the ray integrals back through the object, which will then constructively interact in regions which correspond to variations of  $\mu$ . This gives an approximation of the original object, but must be filtered to remove blurring. This stage is typically performed in the frequency domain, using the Fourier Slice Theorem (FST), details of which can be found in (Kak and Slaney, 1988) along with mathematical derivations of the reconstruction process. The FST (often referred to as the Projection, or Central Slice Theorem) is the basis of tomographic reconstruction. The FST states that the Fourier transform of a two-dimensional function,  $f(r)$ , projected onto a one-dimensional line is equal to first performing a Fourier Transfer on the function and the slicing through its origin which is parallel to the projection line (Kak and Slaney, 1988). The concept is shown graphically in figure 2.12

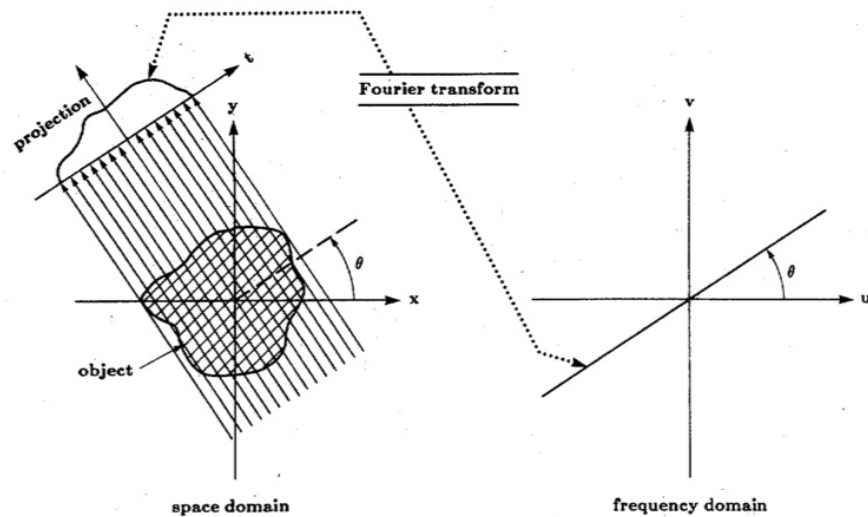


Figure 2.12: Graphical representation of the Fourier Slice Theorem in two dimensions (Pan and Kak, 1983)

From a fundamental perspective, given the Fourier transform of an object from enough angles, simply performing an inverse Fourier transform allows us to reconstruct an estimate of the entire object function,  $f(x, y)$  (Kak and Slaney, 1988).

Each of the rays in a projection has a width determined by factors such as the focal spot size of the X-ray source, detector pixel width and the magnification of the projection (Herman, 2009). The angular increment of each projection should therefore be small enough to allow adequate sampling of features in the object. Early work on CT reconstructions demonstrated that the number of projections to provide a satisfactory Radon transform of an object lies between  $\frac{q\pi}{2}$  and  $\frac{q\pi}{4}$  where  $q$  is the maximum width of the object in pixels (Kak and Slaney, 1988). For example, an object filling the field of view on a 2000-pixel wide detector would require between 3142 and 1570 projections.

The parallel and fan-beam projection methods allow the reconstruction of a single cross-section of an object. Acquiring a 3D CT volume historically involved repeated scans, with the object being translated in the vertical direction to obtain CT slices at various heights. More recently 3D reconstruction algorithms have been implemented which allow CT acquisition of the full object through the use of a magnifying cone-beam system, resulting in a dramatic decrease in full-volume data acquisition time. These reconstructions are mainly based on the Feldkamp, Davis and Kress (FDK) algorithm (Feldkamp *et al.*, 1984), a generalisation of the 2D back-projection algorithms.

No exact solution to the FBK algorithm exists except for the central slice, which represents a fan-beam geometry with a cone beam (Feldkamp *et al.*, 1984). Away from the mid-plane the FBK gives an approximation, although a highly accurate one. The accuracy deteriorates with increasing cone angle (demonstrated in Appendix A). This approximation occurs due to insufficient data for a stable solution to the inverse problem away from the mid-plane. Tuy's sufficiency criteria (Tuy, 1983) details the requirements

for an exact solutions. 3D reconstruction deals with this issue by measuring the tilted projects (i.e. those away from the mid-plane), and projecting back onto the scanning plane and applying the 2D form of fan-beam reconstruction. High cone angles will still produce blurring errors, although some efforts at removing these in medical CT scanners have been demonstrated by using novel scanning geometries such as helical trajectories (Hu and Zhang, 2009; Soimu *et al.*, 2008). It appears that the cost of implementing these systems has so far been prohibitive for industrial CT systems

### 2.4.1 Alternative Reconstruction Methods

Analytical reconstruction techniques based on filtered back projection, such as the FDK algorithm, are dominant in industrial tomography systems due to their ease of implementation and minimal computational requirements. Despite recent advances in hardware and mathematical solutions to inverse problems, FBP techniques have remained widespread Pan *et al.* (2009a). However, alternative reconstruction techniques based on iterative methods are becoming increasingly popular. Algorithms such as the *Algebraic Reconstruction Technique* (ART) begin with an estimate of the object and converge to solution by a series of iterative projection-correction steps (Pan *et al.*, 2009a). These algorithms are reported to have a better tolerance to noise in the acquired projections, along with a greater tolerance of sparse data sets. These sparse data sets may be in form of fewer/ missing projections, limited angle tomography, or non-uniformly spaced projections. Furthermore, iterative reconstruction techniques are more effective at reducing image defects such as those induced by scatter and metal artefacts (Mueller *et al.*, 1998; Subbarao *et al.*, 1997). Figure 2.13 illustrates a variety of imaging problems (in sinogram form) for which ART methods have been shown to be effective.

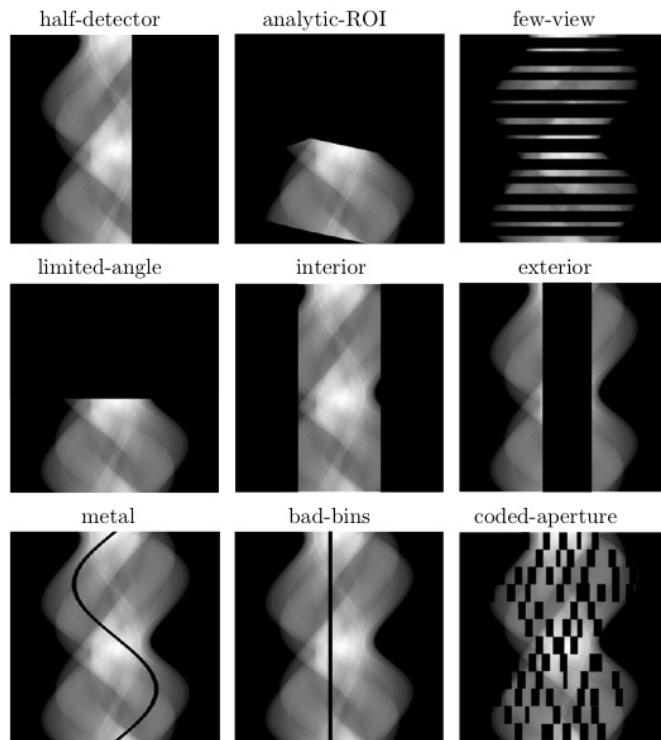


Figure 2.13: Data-space partitions corresponding to various scan configurations or common CT issues in which knowledge of data function within some portions of the data space is missing (Pan *et al.*, 2009a).

Unfortunately, the ART approach has significant computational cost and is relatively slow when compared to traditional approaches (Pan *et al.*, 2009b).

The original iterative reconstruction method was developed by Gordon *et al.* (1970) for medical CT systems, and further research demonstrated that ART could successfully reconstruct images based on only half the number of projections required by back-projection approaches (Guan and Gordon, 1996). This property has clear benefits for medical CT, where reduced patient dose through minimising scanning time is a prime concern. One barrier to the further proliferation of ART, particularly in industrial tomography, was the production of strong aliasing artefacts at high cone angles ( $>20^\circ$ ). Engineering applications of CT with flat-panel detectors often require the cone angle to exceed this limit, in order to achieve high magnification while keeping the field of view reasonably large. Additionally, back-projection methods give better contrast between materials of similar density compared to iterative methods (Ali *et al.*, 2004).

Variations on ART have been developed since the work of Gordon *et al.* (1970), the most popular are as follows:

- Simultaneous Iterative Reconstruction Technique (SIRT,(Gilbert, 1972))
- Simultaneous Algebraic Reconstruction Technique (SART(Andersen and Kak, 1984))
- Multiplicative Algebraic Reconstruction Technique (MART, (Gordon *et al.*, 1970))

A mathematical comparison of the various algorithms can be found in (Subbarao *et al.*, 1997).

It appears that although each variation of ART has led to improvements over FBP in some respect, no version has proved to overcome every weakness of FBP. In fact very few papers in the literature have demonstrated the applicability of ART techniques to real data, many simply demonstrate the effectiveness on phantom projections. The predictable nature of FBP algorithms in terms of computational cost and reconstruction times will likely prevent the uptake of ART in industrial CT systems in the short-term (Mueller *et al.*, 1998). Relatively recent work (Pan *et al.*, 2009b) did however show effective use of SART on a clinical CT system which could reconstruct phantom data in reasonable times. The incremental increase in image quality is also a limiting factor, whereby the cost-performance trade-off is not yet a worthwhile investment for industrial CT manufacturers. Intellectual property rights concerning algorithm implementation are also a barrier (Pan *et al.*, 2009a). Pan *et al.* (2009a) also commented on the fact that a large number of papers are published concerning iterative techniques applied to phantom data, with little or no follow up in terms of application to real data. The knowledge transfer between algorithm developers and CT engineers is therefore poor, and is detrimental to the uptake of alternative reconstruction techniques in commercial practise.

## 2.5 Image Quality

Although reconstructions of an objects cross section can never exactly replicate the original, the image quality is mainly determined by the competing influences of noise, contrast, spatial resolution and artefacts (Dainty and Shaw, 1974; Hammersberg and Mangard, 1999; Maans, 2000).

Laboratory CT systems generally employ polychromatic X-ray sources, resulting in non-optimal energy settings for virtually any imaging task (Hammersberg and Mangard, 1999). This feature is made worse by the complex interaction of various imaging parameters (such as beam energy and exposure time) and their relationship with final image quality. Figure 2.14 illustrates the competing influences in obtaining a high quality image, and the measurements which relate them.

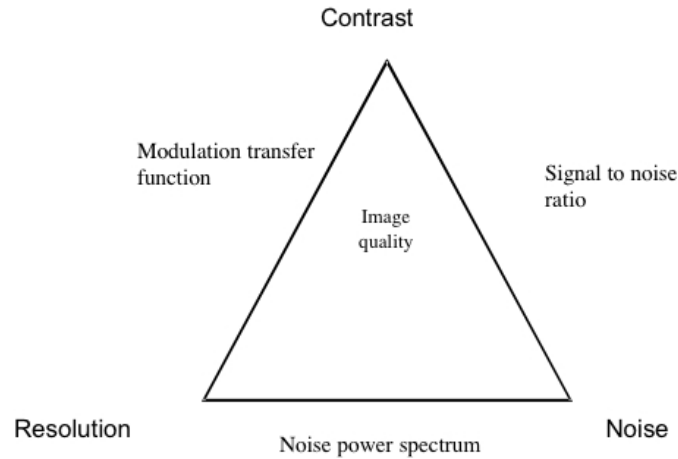


Figure 2.14: Relationship between image quality parameters (corners) and the measurements used to relate them (sides of the triangle)(Stenstrom, 2001).

### 2.5.1 Contrast

As previously described, the process of CT imaging comprises reconstructing the linear attenuation coefficient,  $\mu$ . To be distinguishable, a feature such as a pore or inclusion needs a linear attenuation coefficient which differs sufficiently from the linear attenuation coefficient of its background (British Standards, 2009b).

Section 2.3.2.1 described how  $\mu$  varies with photon energy. Figure 2.15 illustrates the variation of  $\mu$  for a background material ( $\mu_b$ ) and foreground material ( $\mu_f$ ), where  $\Delta\mu$  is the difference in attenuation between the materials:

$$\Delta\mu = |\mu_b - \mu_f| \quad (2.6)$$

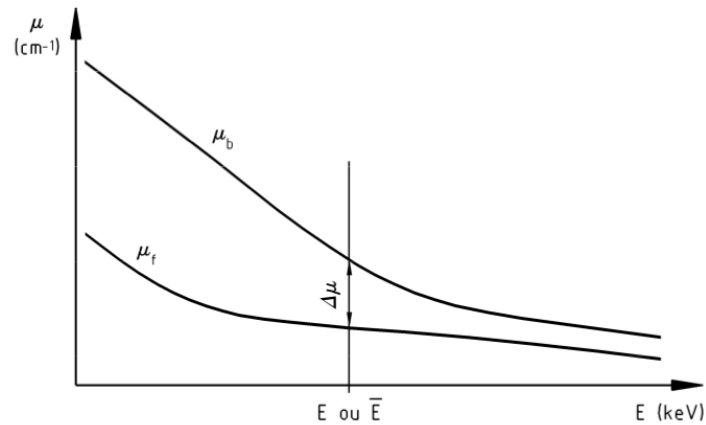


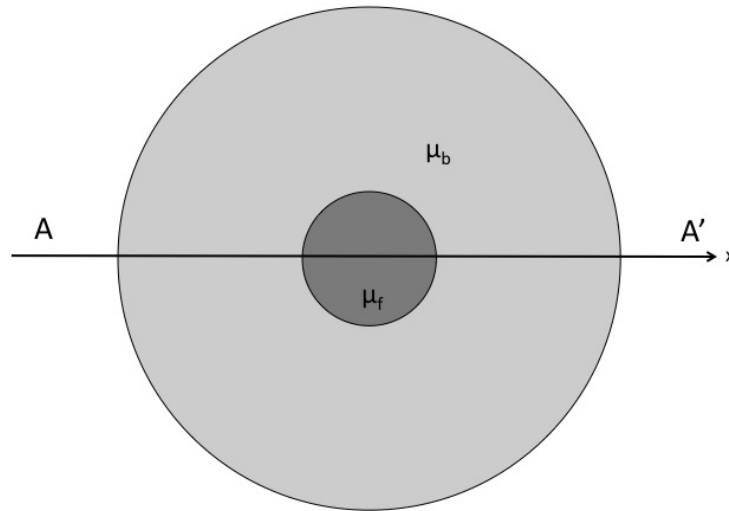
Figure 2.15:  $\Delta\mu$  as a function of photon energy, from (British Standards, 2009b).

The image contrast is then typically defined as the percent difference in attenuation of a material from its background (British Standards, 2009b):

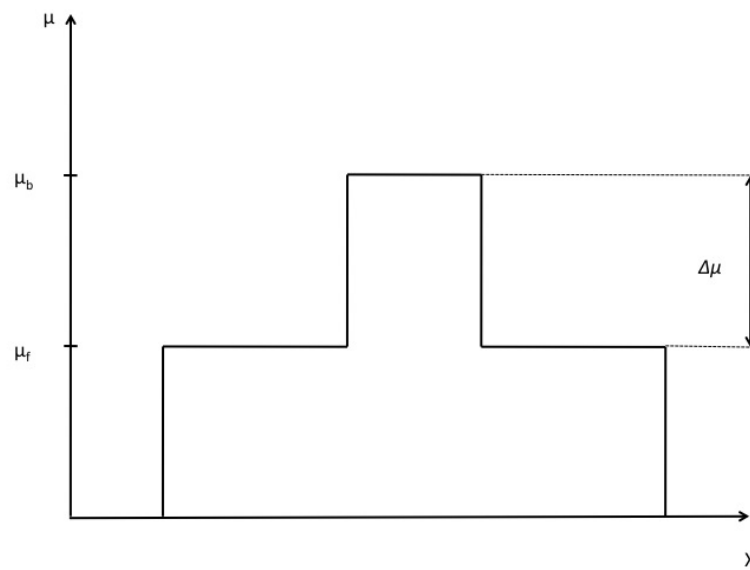
$$\Delta\mu(\%) = \frac{|\mu_b - \mu_f|}{\mu_b} \times 100 \quad (2.7)$$

As  $\Delta\mu$  decreases with higher photon energies, choosing the correct beam energy is a very important factor in maximising image contrast.

Contrast is manifest in a reconstructed slice by a difference in grey value between an object and background. If no image degradation was introduced by the system, a line profile across an object in a reconstructed slice, figure 2.16a would be that shown in figure 2.16b. The sharpness of the edge, i.e. the gradient of the line between  $\mu_b$  and  $\mu_f$ , decreases with decreasing contrast.



(a) Reconstructed slice of an object containing a foreground defect with attenuation coefficient  $\mu_f$ , in a background with an attenuation coefficient  $\mu_b$



(b) Signal line profile plot through the object in (a) along the line AA'

Figure 2.16: Illustration of contrast, from (British Standards, 2009b).

## 2.5.2 Noise

Due to statistical fluctuations in the photon flux generated from the X-ray source, the number of photons arriving at the detector per unit time varies. The fluctuations have well defined characteristics, obeying a Poisson Distribution (British Standards, 2009b). These fluctuations are termed *photon-* or *shot- noise*. Due to the Poisson statistical nature of photon noise, it can be characterised by the fact that the variance of the signal is equal to

its mean. Hence, noise is often specified as the standard deviation,  $\sigma$ , the square root of the variance.

If an average of  $N$  photons are detected over a given sampling time (i.e. image exposure time), the number of photons actually recorded in the exposure will vary by  $\pm\sqrt{N}$  68% of the time (British Standards, 2009b).

Further noise can be added to the image through detector noise and scattered radiation.

To experimentally quantify the noise in a CT scan,  $\sigma$  is usually found for a homogeneous area containing  $m$  pixels within a reconstructed slice. Each of these pixels has some value,  $\mu_i$ , and a mean given by:

$$\bar{\mu} = \frac{1}{m} \sum_{i=1}^m \mu_i \quad (2.8)$$

The standard deviation is then calculated as:

$$\sigma = \sqrt{\frac{\sum_{i=1}^m (\mu_i - \bar{\mu})^2}{m - 1}} \quad (2.9)$$

If  $m$  is in the range  $25 \leq m \leq 100$ ,  $\sigma$  is not particularly sensitive to the number of pixels average (British Standards, 2009b), but does have a positional dependence over the whole of a reconstructed slice.

### 2.5.3 Signal to Noise Ratio

The signal-to-noise ratio (SNR) is given by:

$$SNR = \frac{\bar{\mu}}{\sigma} \quad (2.10)$$

The SNR is therefore related to the degree of attenuation by an object, and can therefore vary significantly across a reconstructed slice if several objects are present in the background object, such as porosity in a matrix. The SNR will increase with increasing photon counts (a higher signal), therefore improving the image (British Standards, 2009b). This can be achieved for example, by using longer acquisition times for each radiographic project, or using a higher filament current to generate more X-ray photons per unit time.

### 2.5.4 Contrast to Noise Ratio

Increasing image noise,  $\sigma$  will cause an increase in the distribution of CT grey values,  $\mu$ , present in a material. This grey value spread may lead to an overlap in grey values for different materials, as shown in figure 2.17

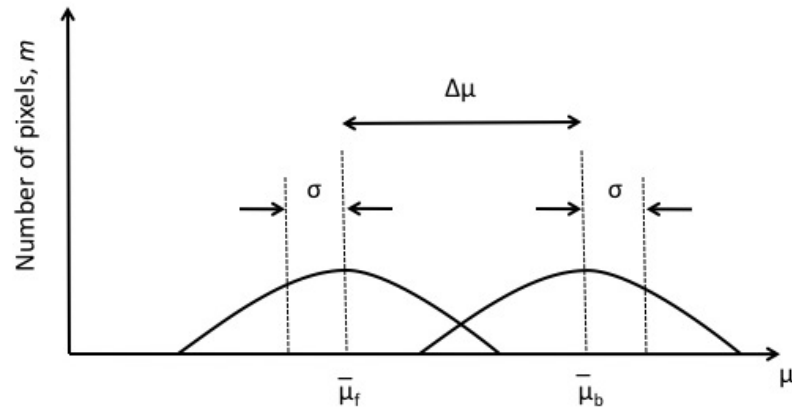


Figure 2.17: Grey value distributions in foreground ( $\bar{\mu}_f$ ) and background ( $\bar{\mu}_b$ ) due to noise. From (British Standards, 2009b).

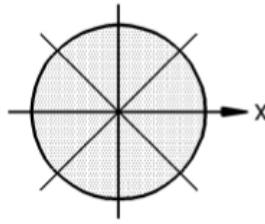
The contrast-to-noise ratio (CNR) describes whether the attenuation difference between a feature and its background is greater than the background noise level. Good detectability is said to occur at CNR values of 3 and above (British Standards, 2009b). The CNR is given by:

$$CNR = \frac{|\mu_f - \mu_b|}{\sigma_b} \quad (2.11)$$

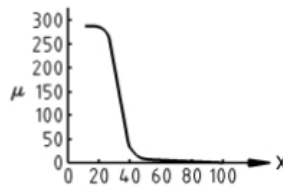
### 2.5.5 Spatial Resolution

The spatial resolution of a CT system is measured from reconstructed cross-sections using the Modulation Transfer Function (MTF). The MTF is ‘the modulus of the one-dimensional Fourier transform of a Dirac profile convolved by the systems point spread function (PSF)’ (British Standards, 2009b). The PSF is the response of the system to an ideal point object. The MTF describes the systems ability to reproduce spatial frequencies. Generally high frequencies, i.e. small features, are not produced as accurately as low frequencies, i.e. large homogenous features.

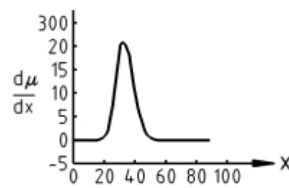
The process of measuring the MTF in the case of a cylinder is presented in figure 2.18. Usually the maximum value of the MTF is normalized to unity, and expressed in line pairs per millimetre (lp/mm).



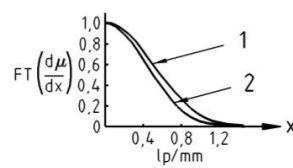
(a) CT cross-section of a cylinder



(b) Profile along edge: Edge Response Function (ERF)



(c) Derivative of the ERF: Line response function (LRF)



(d) Modulus of the LRF: Modulation Transfer Function (MTF), (1) theoretical curve (2) experimental curve

Figure 2.18: Process of MTF measurement, from (British Standards, 2009b).

## 2.6 Artefacts

All imaging systems display some form of artificial features in their images, created by inherent problems in the physics and mathematics of creating the image. These artificial features are known as 'artefacts'. If quantitative measurements are to be made from CT grey values, these artefacts must be accounted for (adn S.G. Azevedo *et al.*, 1990) . Typical errors created by artefacts in CT produce artificial patterns in the image, or cause shifts in grey values.

### 2.6.1 Beam Hardening Artefacts

The type of X-ray source used in laboratory CT systems produce a polychromatic X-ray spectrum. The spectrum consists of characteristic peaks imposed on a Bremsstrahlung background (as shown in section 2.3). The average photon energy of this radiation spectrum increases as it propagates through an object, due to the preferential absorption of low energy photons. As the X-ray beam becomes more penetrating, the linear attenuation coefficient of the object is underestimated away from the edges (British Standards, 2009b). The result is known as the '*cupping effect*', and gives reduced grey values inside the object. Figure 2.19 illustrates the problem.

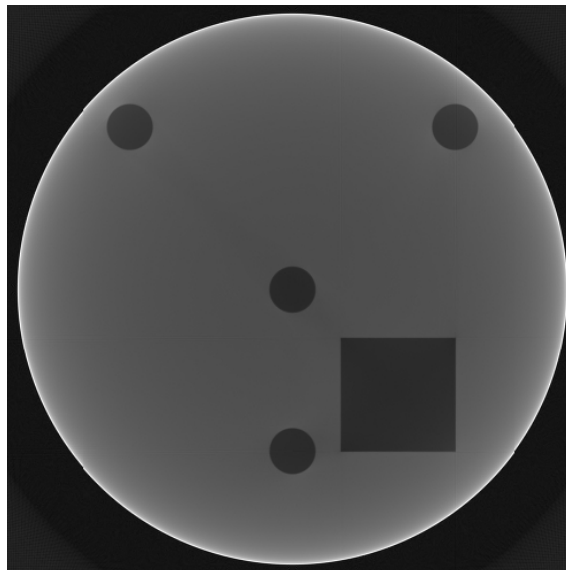


Figure 2.19: Reconstructed CT slice from a test phantom, showing an example of the cupping effect due to beam hardening. From (British Standards, 2009b)

The beam hardening effect can be compensated for in two ways.

Firstly, filtering the beam prior to its interaction with the sample reduces the energy shift through the sample, as the lower energy photons have already been removed by the initial filtration. However, this may be impractical for weakly absorbing materials where sufficient absorption contrast can only be obtained by the use of low energy photons.

Secondly, beam hardening correction can be applied to the CT slices during the reconstruction. By taking projections of a step-wedge of the same material as is being studied over a range of known thicknesses, the grey values in the projection data can be corrected to give a true thickness. Research has shown that third-order correction polynomials often fit step-wedge data well (Gao *et al.*, 2006; Hammersberg and Mangard, 1998; Remeysen and Swennen, 2006; Van de Casteele *et al.*, 2004). Beam hardening correction, however, is specific to a single material. Therefore correction of objects consisting of several materials is unlikely to be valid for all features within an object.

### 2.6.2 Edge Artefacts

The finite width of the X-ray beam, which is defined by the focal spot size and each detector pixel, may produce errors known as *edge artefacts* in the reconstructed slices. Each projection represents a convolution of a particular line integral with the profile of the beam, which results in some loss of spatial information (Kak and Slaney, 1988). Taking many projections (over small angular increments) can reduce this problem. However, when there sharp changes in signal level, this spatial error becomes large enough to produce artefacts which appear as streaks moving away from high contrast edges (British Standards, 2009b). The artefacts appear due to mathematic non-equivalence in the CT process; the measured quantity (logarithm of the line integral convolved with the beam profile) is not equivalent to the required reconstruction quantity (convolution of the beam profile with the logarithm of the line integral) (British Standards, 2009b; Kak and Slaney, 1988). Figure 2.20 illustrates the edge artefact problem.

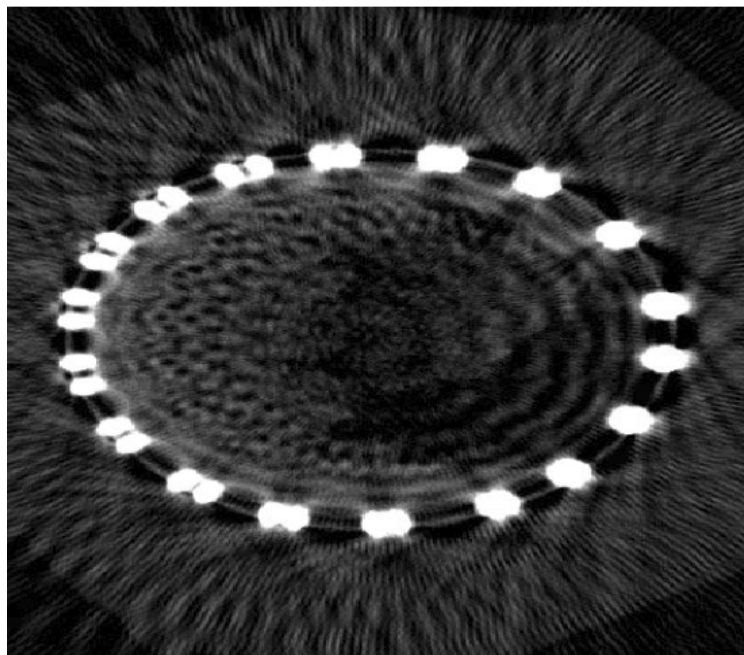


Figure 2.20: Streaks at high contrast edges due to edge artefacts. From (British Standards, 2009b).

Although other types of artefacts can often be corrected by optimised CT conditions, this is not the case for edge artefacts. Trying to eliminate the source of artefacts by reducing the spot size and/or detector pixel size to better approximate the line integrals required for reconstruction causes a large reduction in photon counts (British Standards, 2009b). This photon reduction in turn leads to higher noise levels or longer exposure times to compensate.

### 2.6.3 Ring Artefacts

Ring artefacts are systematic errors which are caused by an error in the detector (British Standards, 2009b). These errors may arise from a faulty pixel, detector non-linearity or ageing of the detector. Ring artefacts appear as concentric rings, centred on the axis of rotation, as shown in figure 2.21.

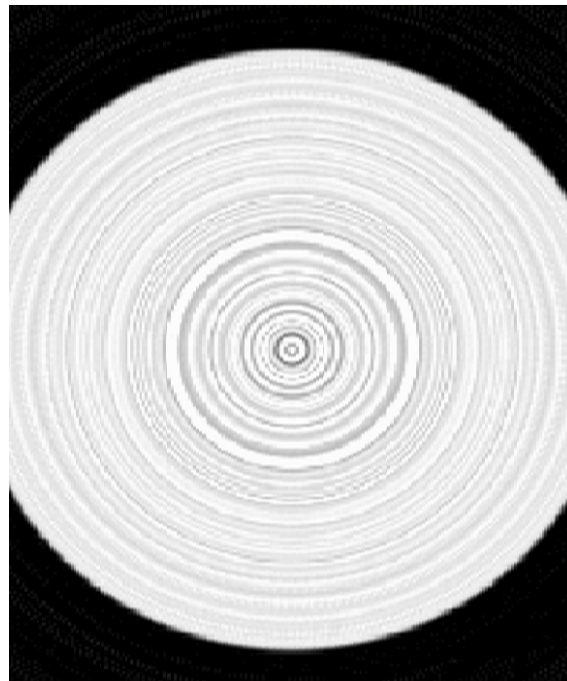


Figure 2.21: Ring artefacts in a CT slice. From (British Standards, 2009b).

Ring artefacts can easily be removed, or sufficiently suppressed by detector calibration (flat field correction) and/ or software post-processing. Hardware compensation can also be used. For example, the Nikon Metrology CT systems are able to shift the sample by small (several pixel) increments between projections to smear out any artefacts from bad pixels.

### 2.6.4 Centre of Rotation Artefacts

If the axis of rotation of an object being scanned is not specified correctly, projections of the object are not backprojected correctly through the volume. This inaccuracy results

in point-like features being reconstructed as circular objects. Features in the plane of reconstruction appear doubled, as shown in figure 2.22.

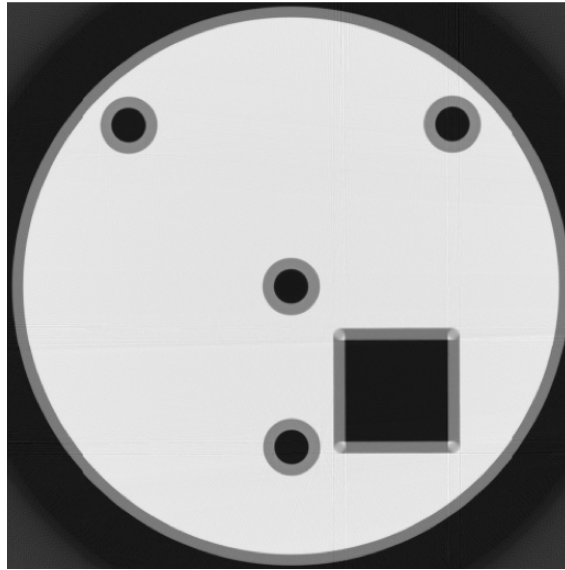


Figure 2.22: Centre of rotation error. From (British Standards, 2009b).

### 2.6.5 Insufficient Projection Artefacts

In section 2.4, the concept of a minimum number of projections being required to reconstruct an object was discussed. If the number of projections is insufficient, streaks may appear in the reconstructed slices which propagate radially from the centre of rotation. This type of artefact is shown in figure 2.23.

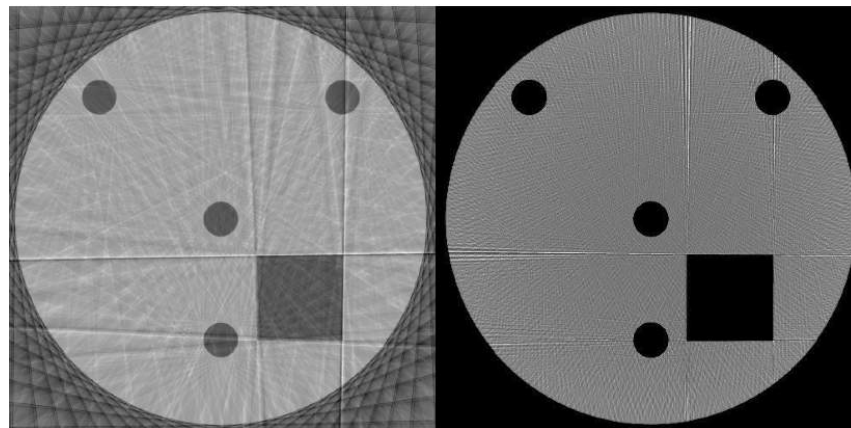


Figure 2.23: Artefacts due to an insufficient number of projections. The left image has 50% fewer projections than the right. From (British Standards, 2009b).

Increasing the number of projections to the correct value (between  $\frac{q\pi}{2}$  and  $\frac{q\pi}{4}$ , section 2.4) will reduce the strength of this type of artefact, but the effect is enhanced at the edges of features where a rapid geometrical change occurs, such as at the corner of a square.

### 2.6.6 Cone Beam Artefacts

Three-dimensional cone-beam reconstruction algorithms, such as the one developed by Feldkamp *et al.* (Feldkamp *et al.*, 1984) are approximations away from the central slice (see section 2.4). This results in incorrect descriptions of geometrical features away from the central slice, as shown in figure 2.24.

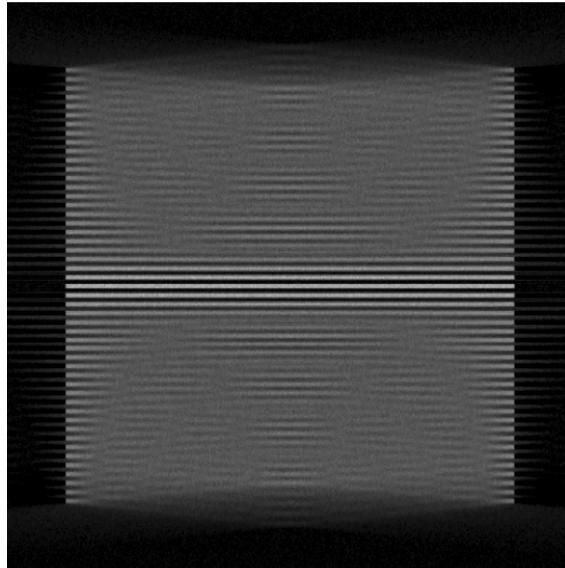


Figure 2.24: Cone beam artefacts in a stack of discs. From (British Standards, 2009b).

## 2.7 Applications in Imaging CFRP Materials

Two-dimensional radiography has been applied to the characterisation of defects and damage in CFRP materials for many years. The range of penetration energies available using X-rays allows the inspection of most composite structures. The technique has been shown to be an effective detection method for non-planar defects such as porosity, voids, solid inclusions (Crane *et al.*, 2000). Changes in material thickness and composition can also be identified. However, many authors have stated contradictory results, observing that 2D radiography is not particularly effective (Prakash, 1980; Salkind, 1976; Scott and Scala, 1982). In fact ultrasonic C-scan methods often remain the main NDT technique used by many companies to qualify materials and components for use on aircraft. Despite this, 2D radiography has proven useful for investigation of large internal voids, such as searching for water ingress in honeycomb structures (Jones *et al.*, 1988).

Because a 2D radiograph relies on significant attenuation of the X-ray beam, defects which are planar and perpendicular to the beam may not be detected. This is also true for defects which have a similar mass absorption coefficient to the component being investigated. Hence, defects such as delaminations may go undetected unless radiographs are taken from multiple angles. Furthermore, as the defects are superimposed onto a 2D surface, any overlapping defects cannot be separated, and depth quantification is impossible.

Three-dimensional X-Ray CT has overcome many of the above problems. As the entire cross section of the component can be imaged through reconstruction processes, the spatial extent of any features of interest can be quantified. For this reason, CT has become an important tool in materials characterisation. However, as with any NDT technique, there are limitations to using CT for inspection of composite materials.

These problems include:

- Low X-ray attenuation contrast between fibres and epoxy resins
- High aspect ratio of many composite structures
- Field of view limitations

Recent developments have allowed the above problems to be overcome to varying extents, as will be discussed in the following sections.

## 2.7.1 Materials Characterisation

CFRP materials used in load bearing structures such as wing skins and spars generally employ toughened epoxy resins. A typical atomic composition for an epoxy resin comprises 76.66% carbon, 22.76% oxygen and 0.59% hydrogen (Crane *et al.*, 2000), resulting in a linear attenuation coefficient of  $0.2028/cm$  compared to  $0.279/cm$  for carbon fibres (at 50keV photon energy). The attenuation contrast between fibres and resin is therefore very low. In terms of microstructural characterisation therefore, a significant proportion of work has focussed on features which provide enough contrast with the composite material to allow their measurement. This typically includes porosity and cracks or foreign object inclusion.

### 2.7.1.1 Porosity

Many research papers have shown successful quantification of porosity in carbon-carbon and glass fibre-epoxy composites (Douarche *et al.*, 2001; Martìn-Herrero and Germain, 2007; Tiseanu *et al.*, 2011; Weber *et al.*, 2010), but few have discussed the problem in carbon fibre reinforced epoxies. In the case of porosity measurement however, the principle of measurement is the same regardless of material; the bulk object simply needs ample attenuation contrast from air (or other entrapped gas) to allow greyscale segmentation of the porosity. In particular, Weber *et al.* (Weber *et al.*, 2010) demonstrated that CT is comparative to mercury porosimetry for porosity measurements in carbon-carbon composites (carbon fibres embedded in a carbon matrix).

Recent work by Centea and Hubert (Centea and Hubert, 2011) demonstrated how X-ray tomography can be used to monitor the evolution of porosity in out-of-autoclave cured CFRP. They used a woven pre-impregnated materials (ACG MTM 45-1, the same used in the experimental parts of this thesis), and interrupted the cure cycle at various time points.

The work showed how the volume and distribution of porosity changes during the cure cycle in terms of macro porosity, dry fibre tow area and ply thickness. Figures 2.27 and 2.28 show examples.

### 2.7.1.2 Fibre Architecture

Due to the small difference in attenuation coefficient between carbon fibres and epoxy resins, resolving fibre architecture for accurate quantification in CFRP materials is very difficult. In fact for uni-directional materials with no macroscopic fibre tow geometry, individual fibres are not resolvable on standard micro-CT cone-beam systems.

In materials such as 2D and 3D woven composites, which are cured out-of-autoclave (i.e. at pressures  $\approx 1$  atmosphere) the relatively low laminate compaction and high porosity makes identification of fibre architecture somewhat easier. Djukic *et al.* (Djukic *et al.*, 2009a,b) demonstrated the use of contrast agents applied to fibre tows and mixed with the resin can help to improve contrast between the material constituents, allowing segmentation of fibre tows, resin, and porosity. While the contrast agents were effective in allowing the measurement of tow dimensions and orientations, along with ply thicknesses they were found to introduce beam hardening artefacts in the reconstructions. Figures 2.25 and 2.26 show examples of the work by Djukic *et al.*

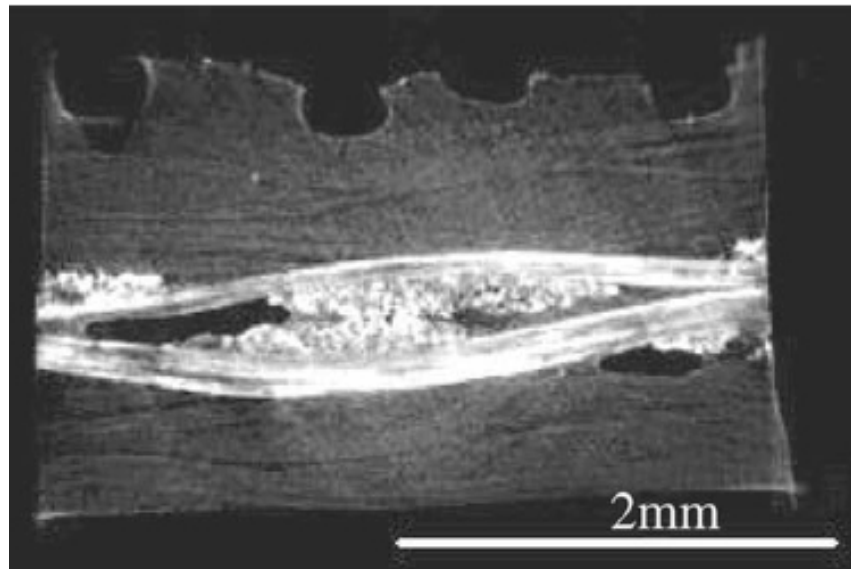


Figure 2.25: Cross-sectional image of a CFRP laminate with iodine based contrast agent coated plies. From (Djukic *et al.*, 2009b).

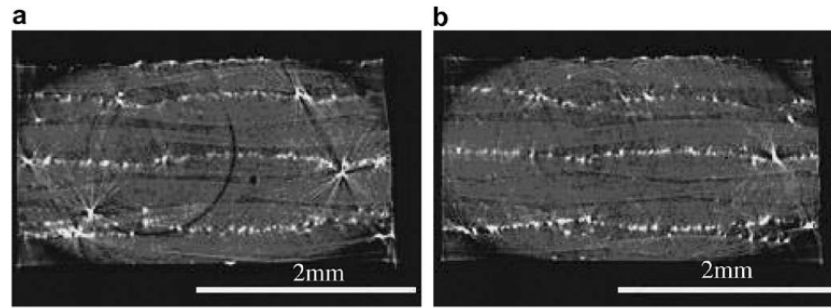
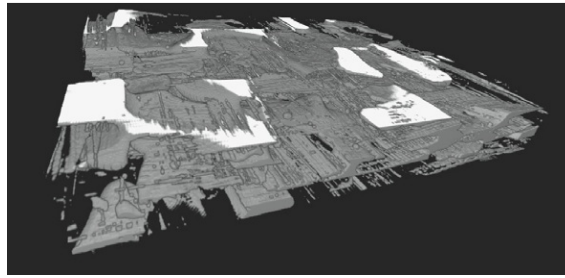
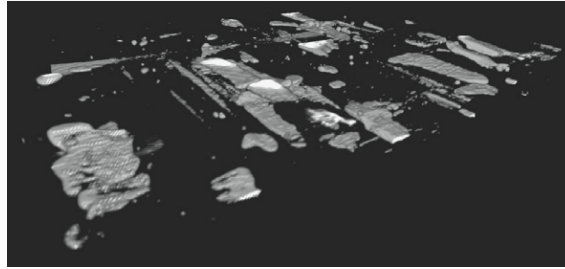


Figure 2.26: Cross-sectional images of CFRP laminate with gadolinium (III) fluoride coated plies. (a) high artefact area (b) lower artefact area. From (Djukic *et al.*, 2009b).

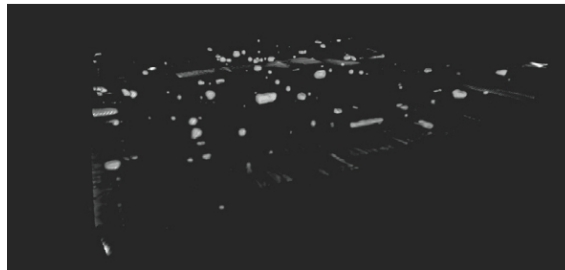
It should also be noted that although contrast enhancements are suitable for identifying microstructural features, in the case of using additives they could potentially cause a change in material properties. Therefore if the aim of using CT to characterise materials is to relate this information to mechanical properties by testing the same samples as are imaged, the use of contrast agents may not be appropriate. This is also true for large field of view imaging, where the resolution is not high enough to resolve microstructural features but is sufficient, for example, to resolve the global spread of delamination damage due to impact.



(a)



(b)



(c)

Figure 2.27: 3D renderings of void content evolution during processing. From (Centea and Hubert, 2011).

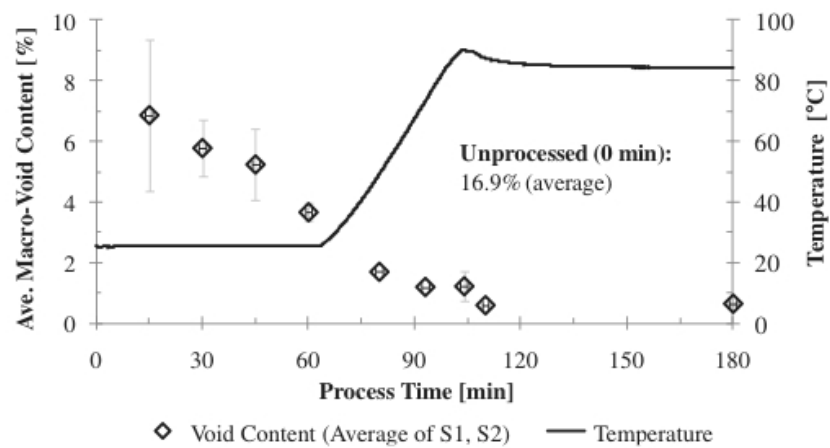


Figure 2.28: Evolution of macro porosity with processing time. From (Centea and Hubert, 2011).

### 2.7.1.3 Impact Damage Characterisation

Some of the earliest studies of impact damage using a laboratory type CT system was performed by Symons (Symons, 2000) in 1999. His work investigated both low and high velocity impact in UD CFRP materials of 0/90° layup. Symons confirmed in three-dimensions how delaminations are distributed throughout the thickness of the panel; increasing in area towards the back face. Figure 2.29 shows an example of the CT slices obtained in Symons' work, illustrating classic delamination and matrix cracking patterns.

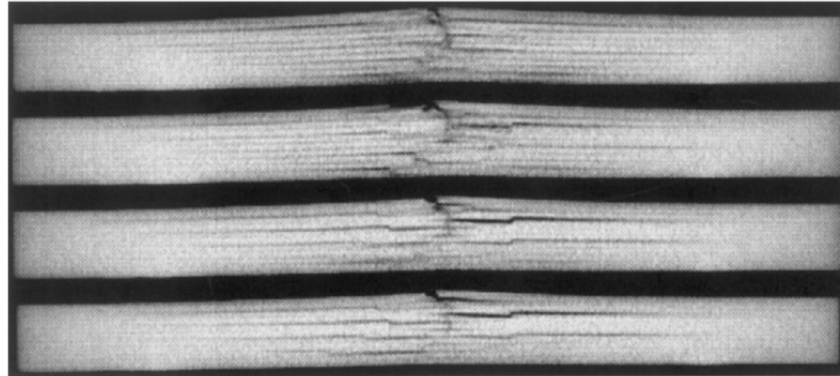


Figure 2.29: CT slices at four different positions in an impacted CFRP laminate. From (Symons, 2000)

The work by Symans using CT led to increases in the understanding of failure processes in CFRP, relating the absorbed energy during impact to fracture energy, frictional work and inelastic matrix behaviour. However, at the time the paper was published, CT scanners were still using linear detectors which could only acquire a single slice of a single projection at once, resulting in extremely long scan times which were often impractical compared to C-scan and optical microscopy.

Very little work employing CT was then published until recently (within the last two years). With the increased focus on improving material properties, particularly with respect to impact tolerance, several researchers have used CT to analyse impact damage in modern hybrid materials. These include CFRP materials which include glass fibre layers (Enfedaque *et al.*, 2010) and the use of through-thickness stitching (Tan *et al.*, 2011a).

Enfedaque *et al.* (Enfedaque *et al.*, 2010) examined the impact behaviour of thick hybrid laminates of woven carbon and glass manufactured by resin transfer moulding (RTM), under 30-245J energies. Their work used CT to qualitatively identify failure mechanisms under impact, were shown to be the same for both plain carbon and hybrid glass/ carbon materials. Examples from this work are shown in figure 2.30

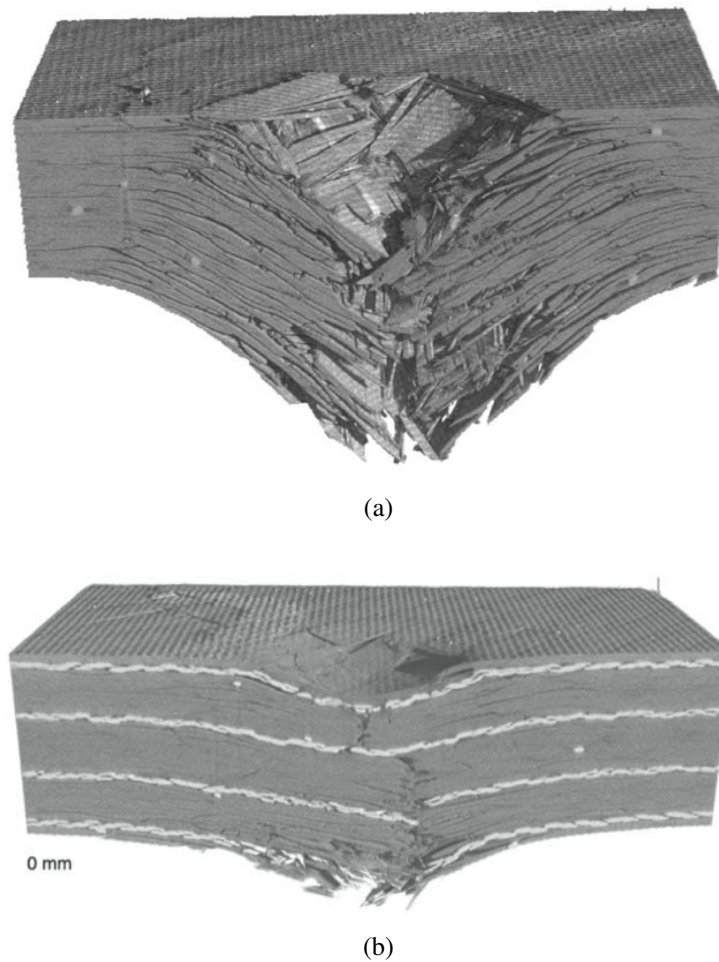


Figure 2.30: 3D CT renderings of Impact damage in 20 ply laminates under 92J impact energy. (a) CFRP (b) CFRP/ glass hybrid. From (Enfedaque *et al.*, 2010).

Tan *et al.* (Tan *et al.*, 2011a) then used CT to illustrate the improved impact damage tolerance of through thickness stitched UD CFRP laminates. The use of CT allowed the demonstration of crack initiation at stitch locations due to the presence of weaker resin rich areas, although overall damage tolerance was improved due to the restriction of delaminations by the stitches. Furthermore, they showed the damage pattern was constrained to a circular region by the stitching, as opposed to a spreading pattern found in conventional laminates.

Although CT is becoming an important tool for the characterisation of impact damage, it is apparent from the literature that the tool is generally being employed to qualitatively described damage. Several reasons may explain this observation; data processing of 3D volumes is relatively time consuming, and extremely demanding computationally. Furthermore, the trade-offs between resolution, sample size and image quality coupled with a complex network of damage make identification, segmentation and measurement of damage difficult.

## 2.8 Imaging Large Objects

Due to their laminated structure, CFRP materials have excellent in plane properties but relatively poor through-thickness behaviour. As a result, CFRP is generally utilised in thin, shell-like structures such as panels and stiffening members. These structures therefore have extremely high aspect ratios, and large surface areas.

Most structural applications of CFRP therefore result in objects which are bigger than the maximum imaging area of typical laboratory based or synchrotron CT imaging systems. Furthermore, the high aspect ratios can result in insufficient penetration of the X-ray beam through the object, which can produce misleading results (Helfen *et al.*, 2006).

In general, when an object is larger than the field of view (FOV) available (i.e. the imaging area of the detector), the projections do not fully encompass the object. These projections are said to be ‘*truncated*’, and the methods of imaging objects larger than the FOV fall into the category of the *truncated data problem*. Figure 2.31 illustrates how a truncated projection is formed.

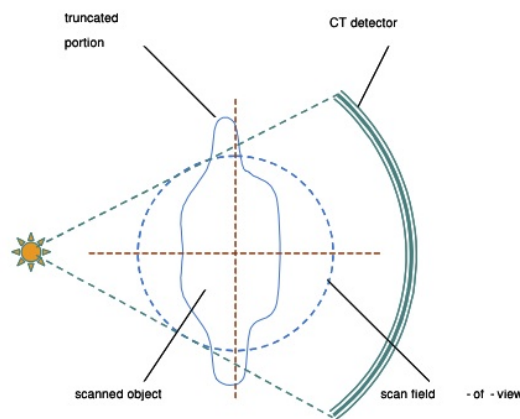


Figure 2.31: Illustration of the truncated projection. From (Li and Hsieh, 2007).

Trying to reconstruct an object from incomplete projections using conventional algorithms results in object inaccuracies and image artefacts. Figure 2.32 illustrates an example of reconstruction artefacts in a truncated data problem.

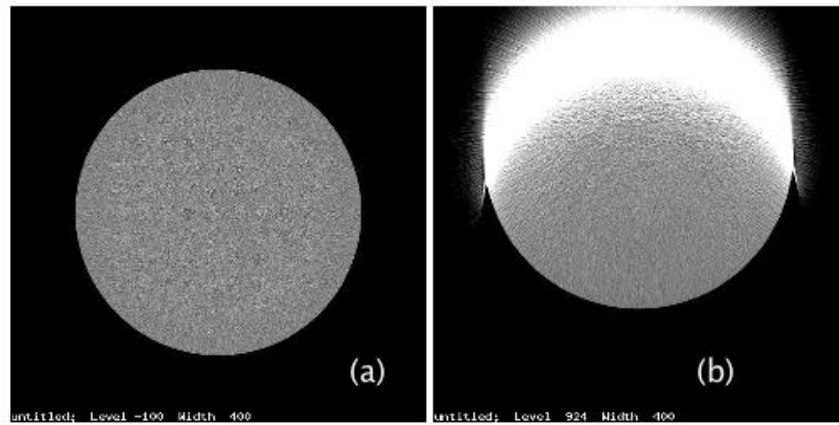


Figure 2.32: CT scans of a 48cm diameter polymer phantom. (a) shows the true object, imaged completely within the FOV, (b) shows artefacts caused by using a regular back-projection reconstruction when the top edge of the phantom is positioned 8cm outside the FOV. From (Li and Hsieh, 2007).

Depending on the desired aims of the imaging experiment, several approaches to the truncated data problem have been devised. These approaches are classified as region-of-interest (ROI) CT, extended field of view methods, and computed laminography (CL).

### 2.8.1 Region of Interest CT

Region of interest CT involves the reconstruction of projection data which comprises a small volume of an object larger than the detector FOV. This allows small volumes of an object to be imaged at high resolution. In the case of 2D cone and fan beam CT geometries, the problem has been investigated widely to varying degrees of success (Anastasio *et al.*, 2007; Chun *et al.*, 2004; Faridani, 1997, 2000, 1992a,b).

The majority of studies on ROI scanning have employed data completion methods to overcome the truncation problem, first implemented in parallel beam geometry. Wiegert *et al.* showed that although these methods cannot provide an exact reconstruction of the ROI, close approximation is possible (Wiegert *et al.*, 2004). The process of data completion involves filling out the truncated projections, and then applying a conventional reconstruction algorithm. Filling out, or estimating, the missing projection data is achieved by extrapolating known information about the object. The estimation method works well for parallel beam geometry as the total attenuation for each projection remains constant over all projection angles. This is not the case for 3D cone beam ROI's, and so the same principles cannot be applied. Although ROI methods for 3D cone beam geometry have been relatively unexplored (Anastasio *et al.*, 2007) some successful implementations have been shown.

Many cone beam ROI's have approached the problem using *a priori* information about the object. These methods are generally referred to as 'zoom-in' tomography. Chun *et al.* (Chun *et al.*, 2004), among others (Gentle, 1990) provided a successful method

whereby two CT scans are performed on the same object, one at high resolution (ROI), and one with the entire object within the FOV. The ROI data is then extended around the edges of the projections by data from the full view scan. Importantly, the data outside the ROI is not reconstructed, the projections are used to provide accurate data of the line integrals outside the ROI which then allows reconstruction using normal FBP methods. Figure 2.33 illustrates the effectiveness of the method.

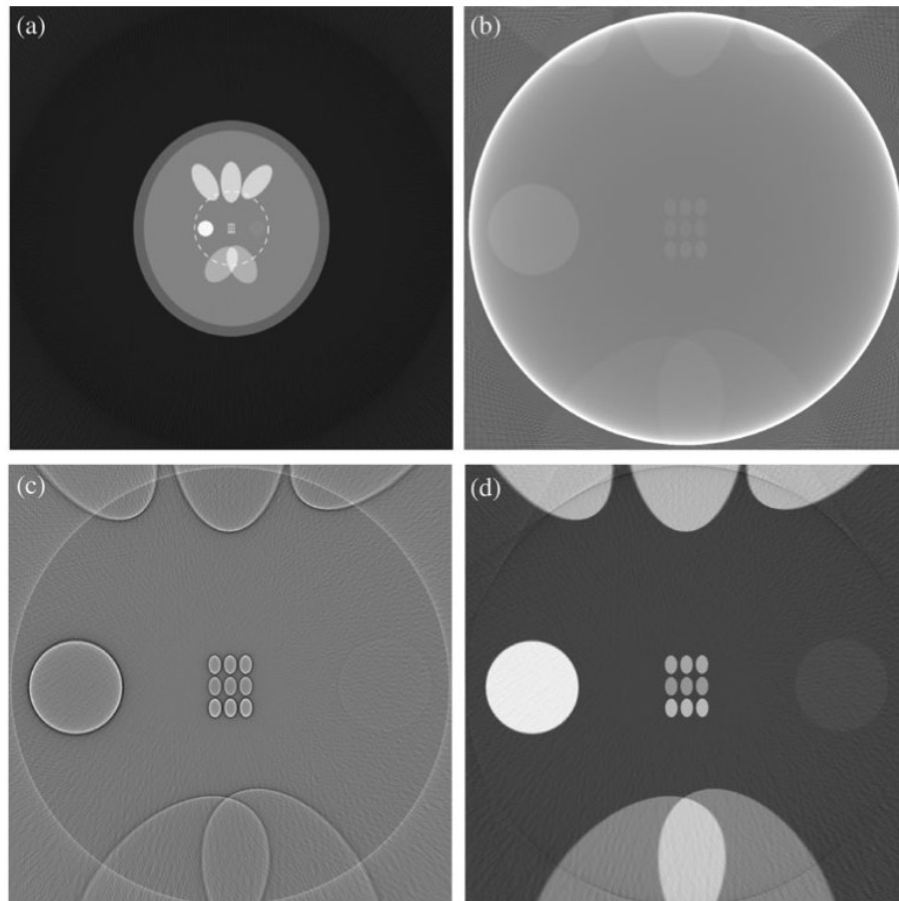


Figure 2.33: Reconstructions of a contrast phantom from (Chun *et al.*, 2004). (a) Full FOV reconstruction from complete projection data (dashed circle represents ROI). (b) ROI reconstructed from incomplete projection data using a conventional fan-beam reconstruction. (c) ROI reconstructed using a local tomography algorithm by Faridani *et al.* (Faridani, 1992b). (d) ROI reconstructed using the zoom-in method.

It can be seen from figure 2.33 that older ROI algorithms (C) preserve high frequency components such as edges well, but suppress lower frequencies. This results in suppressed grey values for objects within the ROI, and bright rings at the edge of the ROI. The zoom-in method provides good edge contrast as well as reduced suppression of grey values within features of interest. A ring artefact is still present at the edge of the ROI, but is greatly reduced. However, the zoom-in method does require two CT scans to be performed, resulting in increased scan time and higher exposure to the object (a problem for biological samples, but not for materials studies).

More recent studies have focused on applying ROI methods to scientific and engi-

neering studies on synchrotron and laboratory CT systems. Kyrieleis *et al.* developed a simpler data completion method, whereby the sinograms in a projection set are extended by a constant value from the edge of the truncated projection, as shown in figure 2.34. They studied a variety of samples including antler, a mouse skull, and a 5.5mm CFRP laminate using a synchrotron imaging system (Station 16.3 at the Synchrotron Radiation Source, Daresbury Laboratory and Beamline B16 at Diamond Light Source).

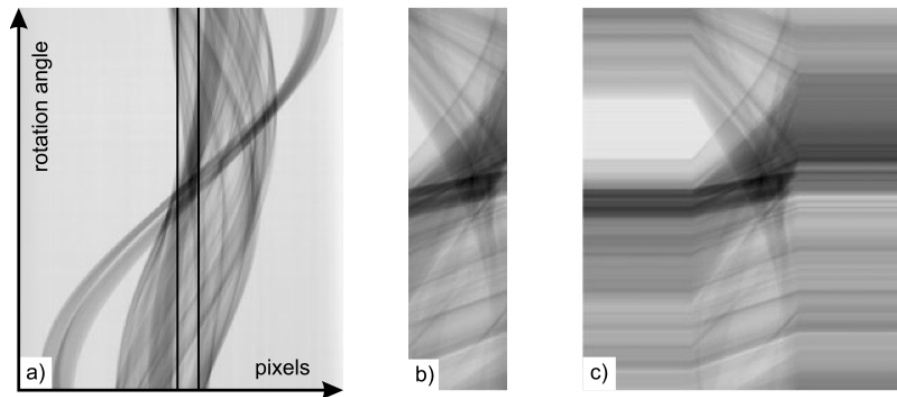


Figure 2.34: Sinogram extension procedure demonstrated using a sinogram of an object 3060 pixels wide. (a) shows a 200 pixel wide ROI cutout represented by the vertical black lines. (b) shows the ROI laterally upsampled to a width of 4000 pixels. (c) using the pixel values at the edges, 4000 pixels are added to the edge of the ROI. (b) and (c) are scaled horizontally by a factor of 3. From (Kyrieleis *et al.*, 2010).

The constant value extension method by Kyrieleis *et al.* was shown to accurately reconstruct ROI's to within 1% of the total sample width. Their method suppressed typical 'glow' artefacts often associated with ROI reconstruction. Furthermore, they showed that the ROI may be located away from the centre of the sample and still give acceptable results. However, artefacts in the form of bright-stripes and ring like artefacts were apparent in a high aspect ratio CFRP sample, attributed to the long path length through the thickest direction. Interestingly, the study demonstrated that the number of projections required using this method of data extension is closer to the limit of  $\frac{q\pi}{2}$  than  $\frac{q\pi}{4}$  to give good image quality.

More recently, Amos *et al.* (Amos, 2011; Amos *et al.*, 2010) followed on from the work demonstrated in (Kyrieleis *et al.*, 2010) by developing a ROI method for a cone-beam industrial CT system. Amos showed that two different methods for extension of the projection data gave very good reconstructions of CFRP coupons. In the first instance, he used a sinogram extension method to tail the truncated data to zero. This gave good suppression of ROI artefacts, but errors from missing data still remained. A second method using model estimation (prior knowledge of the object dimensions and attenuation) was successful in reducing intensity errors and geometrical errors due to missing data, but was more complicated and time consuming to implement. This second method however used a user-generated model of the object, removing the requirement for two scans of the object (as necessary in zoom-in tomography). Figure 2.35 illustrates the effectiveness of ROI scans

in CFRP samples containing small defects using the various extension methods presented in (Amos, 2011).

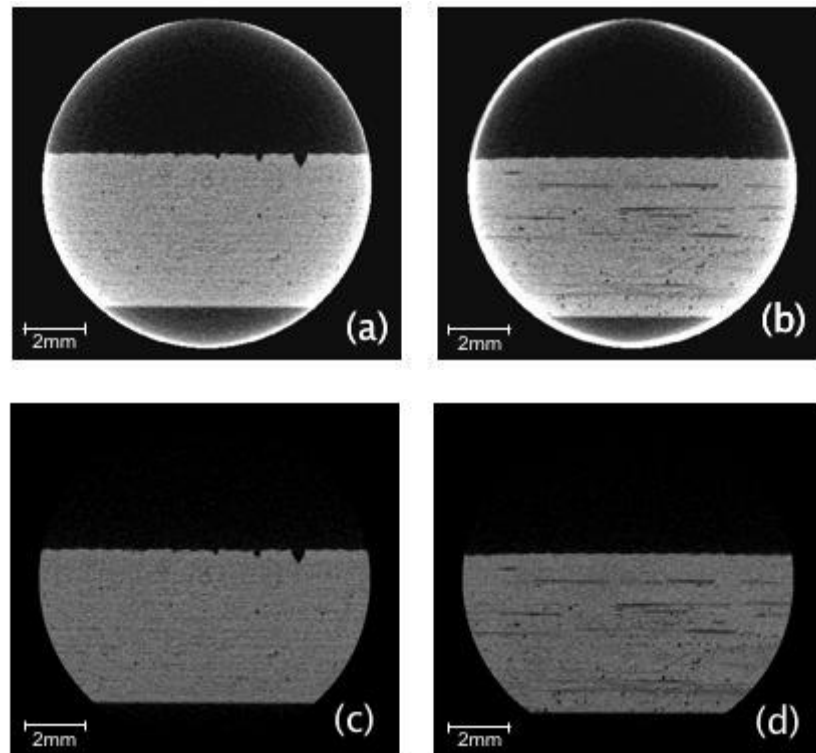


Figure 2.35: ROI cone beam reconstructions of a CFRP coupon with laser drilled defects. (a) Reconstruction from truncated projections using conventional reconstruction at the mid-plane of the detector. (b) Reconstruction of object in (a) at a high cone angle. (c) Reconstruction of the object using data completion method at the mid-plane of the detector. (d) Reconstruction using data completion method at a high cone angle.

## 2.8.2 Region of Interest Algorithms

The approaches to ROI tomography discussed in the previous section are all based on combining data completion methods with traditional filtered back-projection reconstruction. It is clear that these methods have been successful to varying degrees but do not solve the fundamentals of the truncated data problem. Several authors have published significant work in the medical CT field which aims to overcome this fundamental problem through an alternative reconstruction approach. These novel methods are based on the 'Back-Projection Filtration' (BPF) algorithm developed for a helical scanning geometry (Zou and Pan, 2004). The method was initially developed to cope with the vertical truncation problem during translation of the source in helical medical CT. The BPF approach takes the derivatives of each projection before the back projection step. Back-projecting the derivative produces an image corresponding to the 'Hilbert Image', which can be recovered using the 1D Hilbert Transform. Noo *et al.* (2004) developed the BPF approach further by incorporating the method in a circular trajectory fan-beam CT system. They developed a two-step Hilbert transform approach which could also handle transversely

truncated projections. This research therefore paved the way for direct reconstruction of ROI's which are contained within transversely truncated projections. The actual ROI itself however must not be truncated in any projections using this method. It should also be noted that the methods developed by Zou and Pan (2004) and Noo *et al.* (2004) provide exact solutions in the case of helical scanning and circular fan-beam trajectories. Figure 2.36 shows an example reconstruction.

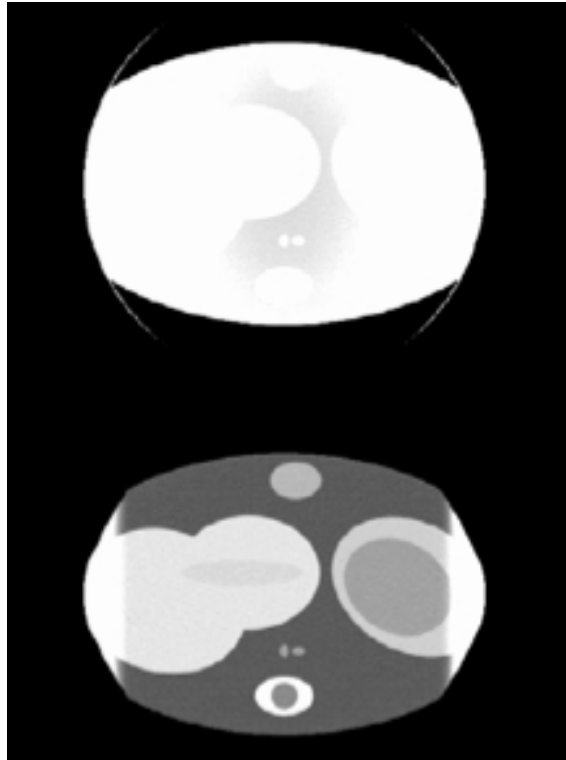


Figure 2.36: Simulated fan beam reconstructions of a 'popeye' phantom with truncated projections. Top: FBP reconstruction. Bottom: BPF with Hilbert filtering (Noo *et al.*, 2004).

Defrise *et al.* (2006) improved upon the data sufficiency criteria required for ROI proposed by earlier researchers (Noo *et al.*, 2004; Zou and Pan, 2004). They showed that stable reconstructions could be performed on more restrictive data than previously thought, such as highly truncated data or limited views. Importantly, they extended the method to give acceptable results for 3D cone beam data. Figure 2.37 gives an applied example of this 3D methodology by Cho *et al.* (2006), published at the same time as the work by Defrise *et al.* (2006). Image quality are shown to be significantly improved, and artefacts reduced in the ROI scan when comparing the BPF to the FBP method.

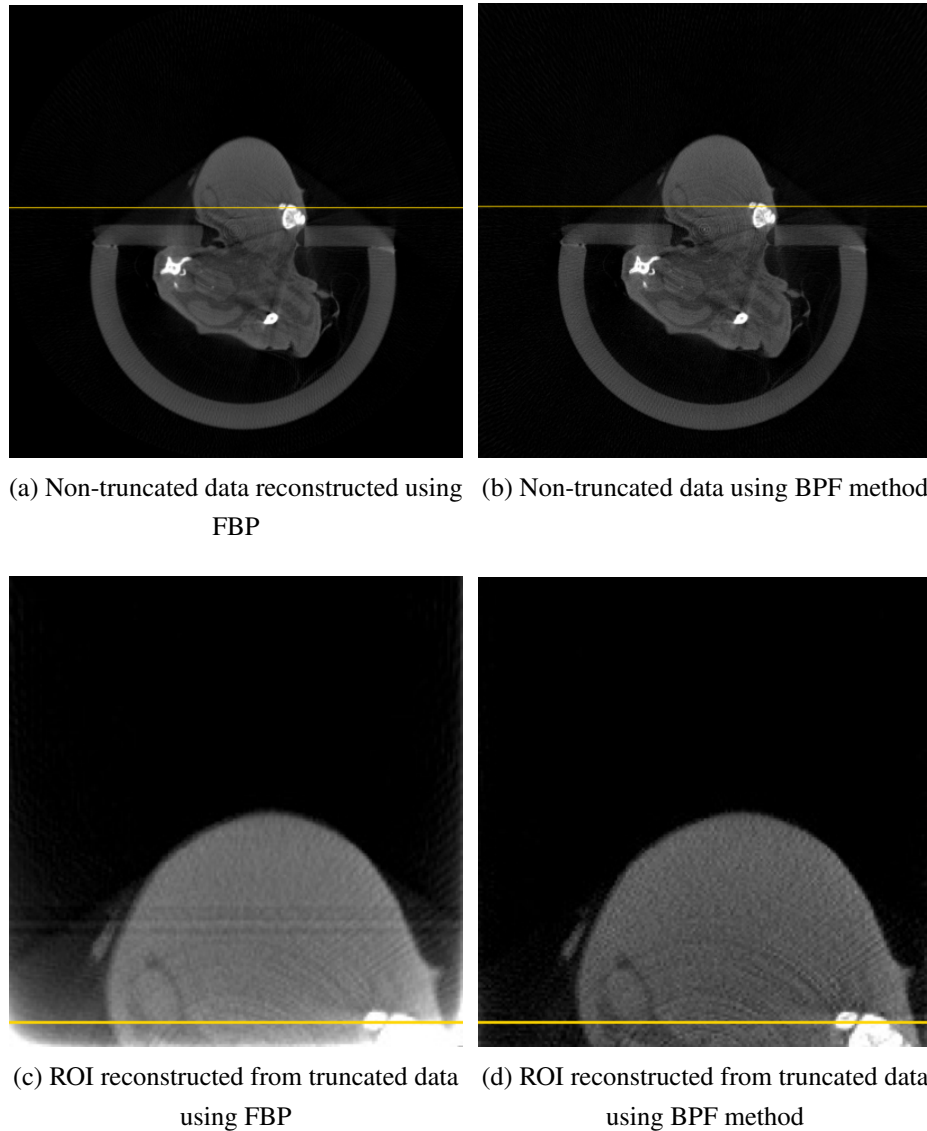


Figure 2.37: Reconstructions of a rat leg comparing FBP and BPF methods (Cho *et al.*, 2006).

Although these specific ROI algorithms (as opposed to data extension/ FBP methods) appear to provide good quality reconstructions on phantom (simulated) data, there is limited evidence of the data applied on real data sets. Many of the authors on the topic note that in reality, the BPF methods can introduce significant noise and require significant computational capacity (Bian *et al.*, 2010) reported a recent advance with the application of the BFP method to a system with a moving source and moving detector which gave reduced noise. As with the reconstruction approaches discussed in section 2.4.1 however, the combination of system complexity and computing resources seem to have prevented the uptake of these methods in industrial tomography.

### 2.8.3 Computed Laminography

Computed laminography (CL) is a technique similar to CT which allows effective imaging of large, flat objects (Fu *et al.*, 2010; Gondrom *et al.*, 1999; Helfen, 2005, 2007). In CL the sample is rotated at an angle,  $\theta$ , relative to the X-ray beam, as illustrated in figure 2.38. This arrangement means that X-ray transmission is similar for all rotation angles.

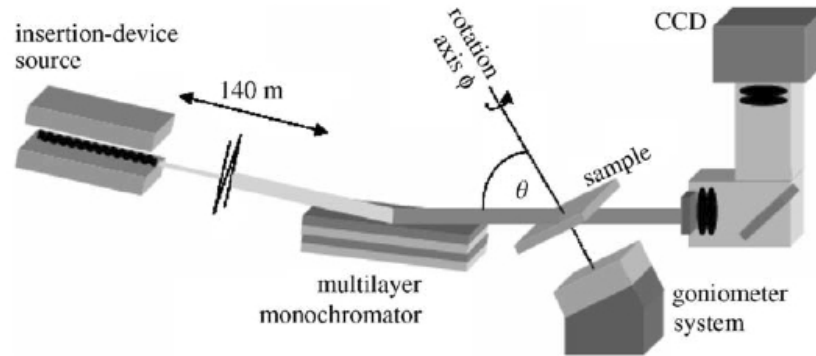


Figure 2.38: Experimental set-up sketched for synchrotron-radiation computed laminography with monochromatic beam at ESRF beamline ID19. The limiting case of  $\theta = 90^\circ$  corresponds to computed tomography (Helfen *et al.*, 2006).

Moffat *et al.* (Moffat *et al.*, 2010) used laminography to image damage in  $[0/90]_s$  laminates successfully in two cases. Firstly they showed that laminography could successfully image microcracks, resin rich regions and single fibres in a small object, comparable in size to typical CT samples used for synchrotron imaging. The sample was a 1mm thick laminate which had been subjected to 70% of its ultimate tensile stress to induce cracking. Figure 2.39 shows the sample dimensions used by Moffat *et al.*, followed by example images of their findings.

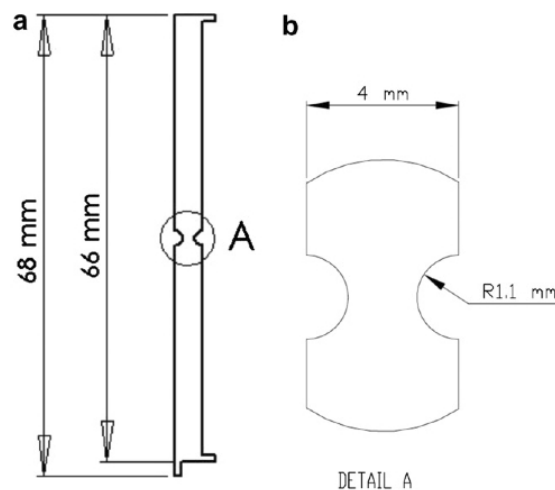


Figure 2.39: Geometry of composite samples used by Moffat *et al.* (Moffat *et al.*, 2010) to demonstrate use of laminography to image damage in CFRP.

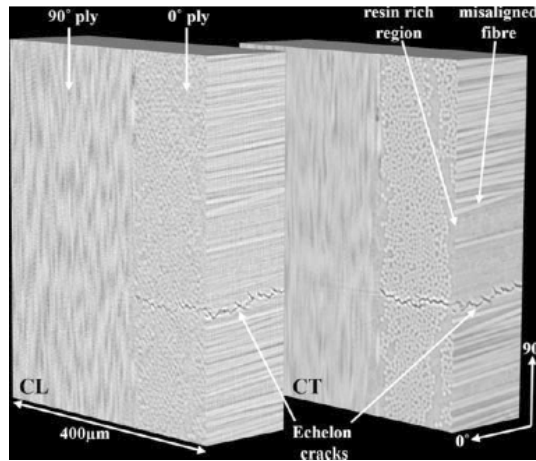


Figure 2.40: Comparison of volumes produced using CL (left) and CT (right). From (Moffat *et al.*, 2010).

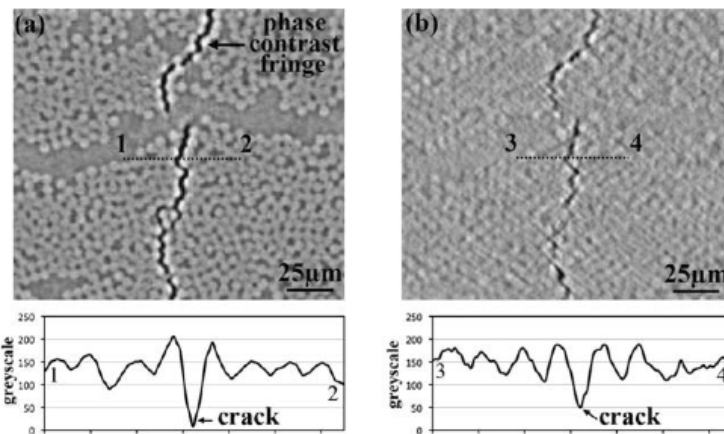


Figure 2.41: Contrast between a crack and composite material in CT (a) and CL (b). From (Moffat *et al.*, 2010).

As can be seen from the previous figures, while CL results in noisier and lower contrast images compared to CT, the technique is still able to resolve adequate detail in conventional geometry samples. Moffat *et al.* also showed the technique is suitable for imaging larger objects by scanning a  $70\text{mm} \times 60\text{mm}$  coupon under in-situ loading. The experiment successfully demonstrated imaging of progressive cracking was possible using CL, as shown in figure 2.42.

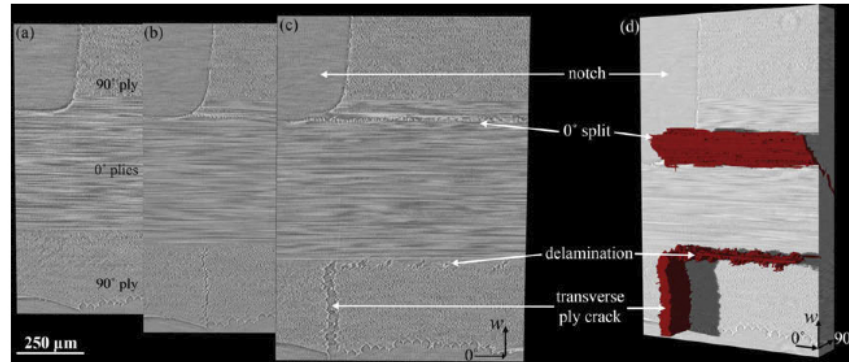


Figure 2.42: CL images of progressive loading in a CFRP plate showing ply splitting, delamination and matrix cracking. From (Moffat *et al.*, 2010).

Other studies have replicated the above results (Xu *et al.*, 2010), but all experiments have been performed on synchrotron imaging beamlines. This is due to the complexity of implementing a laminography reconstruction on cone-beam, polychromatic X-ray spectrum laboratory CT systems. Currently there are no published papers where this methodology has been employed successfully to image large objects on a laboratory system.

## 2.9 Phase Contrast Imaging

When performing CT scans on materials with a low atomic number, the absorption contrast is often not sufficient to provide useful image contrast. Imaging of carbon fibre reinforced polymer composites is a perfect example of this case. Over the last decade, several imaging techniques have been developed which take advantage of the wave properties of X-Rays to improve image contrast. The occurrence of diffraction and refraction, under certain conditions, can give enhanced radiographic contrast due to the presence of *phase contrast*. For example, by passing a 20 kV X-Ray beam through a 50  $\mu\text{m}$  biological sample, the resulting absorption is on the order of a few per cent while the phase shift is on the order of  $\pi$  (Weitkamp *et al.*, 2005). The phase,  $\phi$  of an X-Ray beam is shifted when passing through a material by:

$$\phi = -\frac{2\Pi}{\lambda} \int \sigma(z) dz \quad (2.12)$$

Where  $\bar{\lambda}$  is the mean wavelength of the X-Ray spectrum,  $\delta$  is the refractive index of the sample, and  $z$  is the sample thickness. Recording this phase shift can offer substantial improvements in image contrast.

Three main modes of imaging are used to obtain phase contrast in X-ray imaging;

- Diffraction enhanced
- Propagation (in-line)
- Interferometer methods

These image modes rely in particular on the coherence of the X-Ray beam, as it is this property which determines the occurrence of diffraction and interference. Due to the requirement of beam coherence, initial phase contrast experiments were developed at synchrotron facilities. Recently however, propagation and interferometer based imaging methods have been implemented successfully on laboratory systems.

The first implementation of phase contrast methods were developed for medical applications at synchrotron sources, using diffraction as the method for generating contrast (Harding *et al.* (1987)). A monochromatic beam incident on an object may undergo deviations of the order of micro-radians due to refractive index gradients within the object. The transmitted beam passes through an analyser crystal which acts as a diffraction grating, shown schematically in figure 2.43. X-Rays are therefore diffracted if the Bragg condition is met to produce constructive interference. These rays then impinge upon the image detector (Zhou and Brahme, 2008). An angular acceptance range known as the 'rocking angle', dependant on the analyser crystal, allows tuning of the diffracted beam. Various refraction angles can therefore be recorded, providing information about both absorption and refraction, as illustrated in figure 2.44.

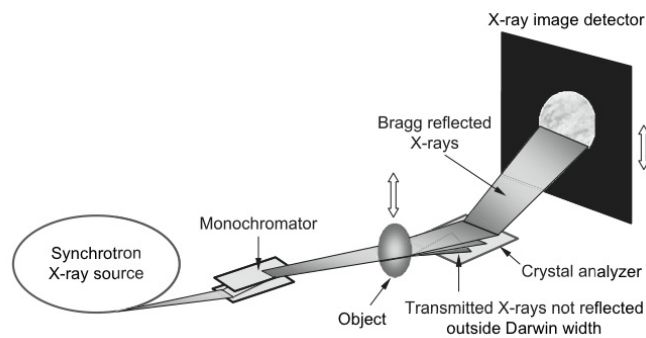


Figure 2.43: Schematic set-up of a diffraction-enhanced X-ray imaging system with a synchrotron beam. In the figure, the crystal analyser is drawn to correspond with the high angle case ( $\theta > 0$ ) of Fig. 2.44 (Zhou and Brahme, 2008).

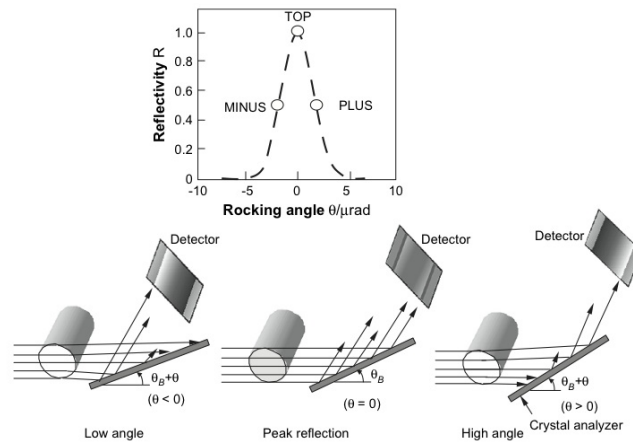


Figure 2.44: Diffraction-enhanced images of a rod showing that X-rays deviated in the object through small angles will be reflected with either a greater or lower efficiency depending on the angle of incidence relative to the rocking curve of the silicon crystal (Zhou and Brahme, 2008).

Propagation, or in-line, imaging exploits *fresnel diffraction* to generate phase contrast and was pioneered by Snigirev *et al.* (1995) and Wilkins *et al.* (1996). When an X-Ray beam passes through an object, the shape of the incident wavefront is modified by variations in the sample refractive index. If this beam is allowed to propagate over a large distance, the wave front variations will result in beam interference, producing intensity variations at material boundaries. If the detector is placed directly behind the object, a conventional absorption image is formed, while increasing the sample-detector distance will cause a gradual increase in the phase contrast. Figure 2.45 shows a schematic of the in-line method.

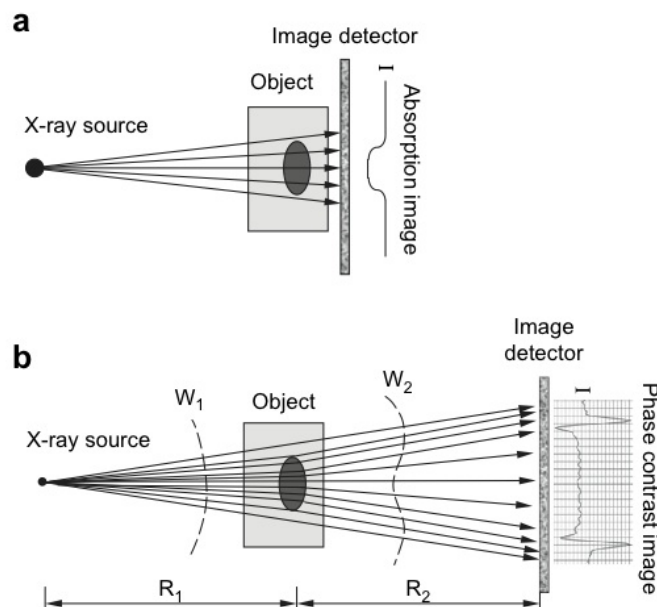


Figure 2.45: Schematics of (a) attenuation-based imaging configuration (b) in-line phase contrast imaging configuration (Zhou and Brahme, 2008)

Polychromatic X-Ray beams can be used to generate in-line phase contrast, meaning the method is suitable for use on laboratory scale X-Ray sources. However, the source must generate a beam with some degree of spatial (lateral) coherence:

$$L_{coh} = \frac{\lambda R_1}{s} \quad (2.13)$$

where  $L_{coh}$  is the spatial coherence length of the source,  $\lambda$  is the wavelength of the X-Ray,  $R_1$  is the source-sample distance, and  $s$  is the focal spot size of the source. Figure 2.46 illustrates the relative dependence of edge enhancement with the sample-detector distance. Due to the limited resolution of laboratory X-Ray detectors, the in-line phase method can take advantage of geometrical magnification, although this may introduce geometric blurring at high magnifications. Systems such as the X-Radia Micro CT system at the Henry Moseley X-Ray Imaging Facility makes use of an optical magnification system to overcome this issue to some extent. In this system, detectors are coupled lenses of various magnifications using imaging intensifiers on a rotating barrel (similar to an optical microscope). This set up allows resolutions of approximately  $1 \mu\text{m}$  to be attained.

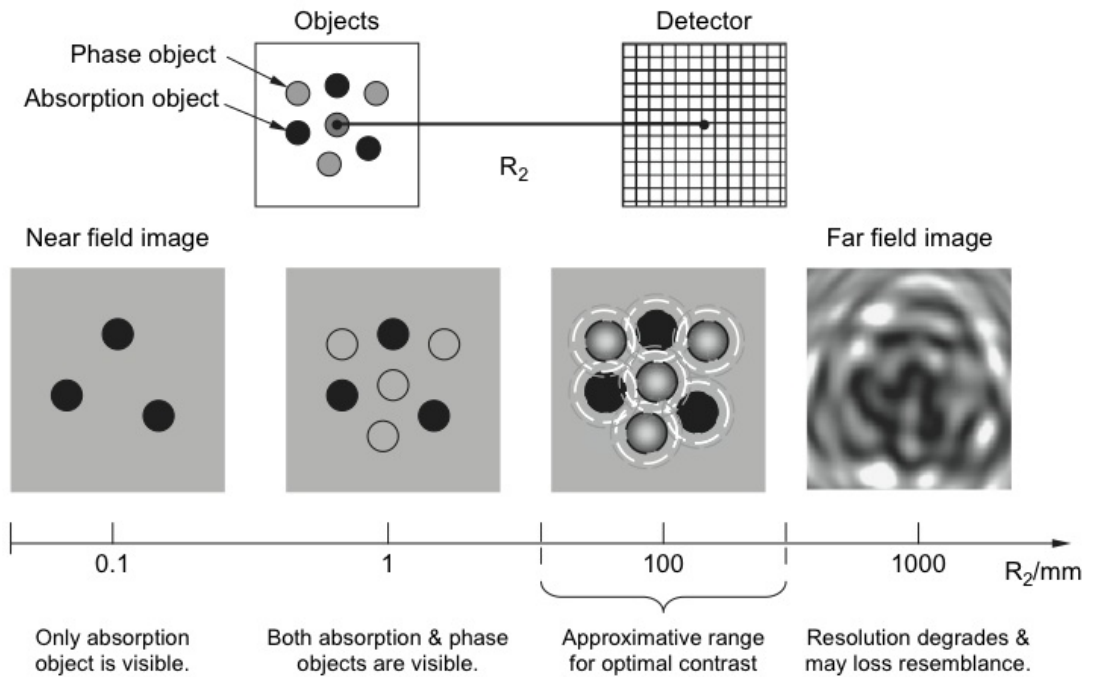


Figure 2.46: Dependence of in-line phase-contrast images on the distance between object and detector. Here, given numerical data for  $R_2$  are only illustrative, which, in practice, will depend on the specific system set-up (Zhou and Brahme, 2008).

Interferometer systems are a relatively novel system of imaging, whereby a set of gratings in the imaging sequence create interference patterns which are dependent on local variations of refractive index within the sample. As such, the method has proved suitable for imaging samples with large internal variations of the refractive index. The method has been employed in work in this thesis, and is therefore covered in detail in Chapter 7.

## **2.10 Chapter Summary**

In summary, CT clearly has significant potential as a characterisation and NDT tool for composite materials. A lack of recent publications regarding the study of impact damage on laboratory CT systems leaves huge scope for novel research, especially with recent hardware advances. These hardware advances include high resolution flat panel detector systems, phase contrast imaging systems and grating interferometry tomography.

## COMPOSITE MATERIALS AND IMPACT DAMAGE: BACKGROUND AND LITERATURE

This chapter provides a brief look at the microstructure of fibre reinforced composites materials and associated mechanics of damage. Initially, an overview of damage in fibre reinforced composites is presented, with a detailed investigation of impact damage and associated research literature.

### 3.1 Fibre Reinforced Composite Materials

A composite material is often described as one in which two or more phases are distributed on a microscopic scale (Hull and Clyne, 1996.). Although there is no universally accepted definition of what a composite material is, the Dictionary of Composite Materials Technology gives the following description:

**Composite:** ‘A multiphase material formed from a combination of materials which differ in composition or form, remain bonded together, and retain their identities and properties’ (Lee, 1989).

It is therefore apparent that composite materials encompass an extremely wide variety of individual materials, ranging from natural composites such as wood and bone, through to man-made materials such as carbon fibre reinforced plastic. Composites were used in the very first aircraft flown by the Wright Brothers in 1903, in the form of a natural composite; wood (Soutis, 2005). Since then, composite materials have become increasingly successful in the aerospace industry due to their high specific strength and stiffness compared to typical aerospace materials (Soutis, 2005). Figure 3.1 compares the specific properties of a range of composite materials and monolithic metals and ceramics. Long-fibre reinforced plastics have been adopted to a greater extent recently, for example the new Boeing B787 will employ at least 50% by weight of fibre-reinforced material (Marsh, 2005). This increased used of composites in aircraft could lead to a possible 40% weight reduction in secondary aero-structures and 20% in primary structures such as wings (Soutis, 2005).

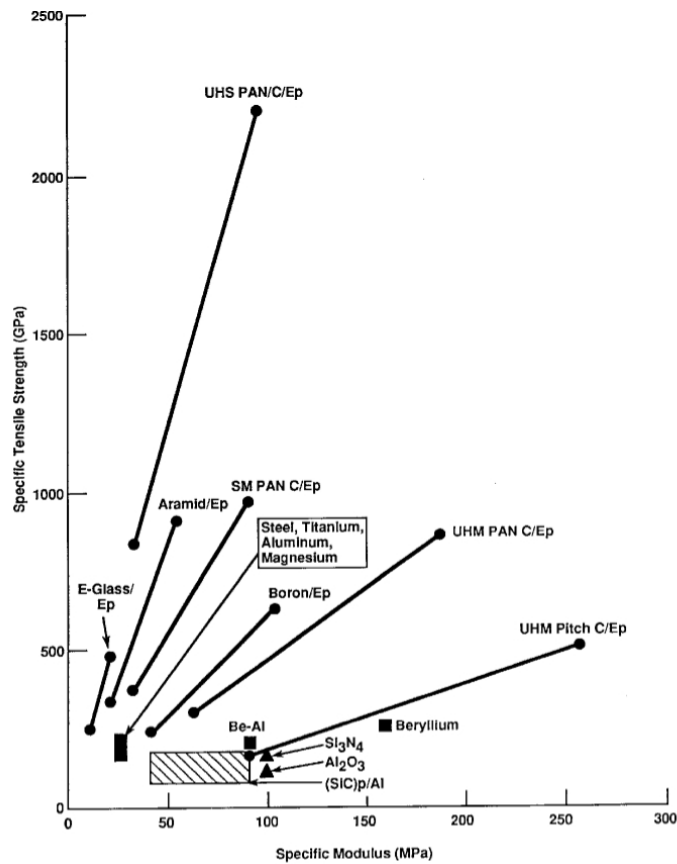


Figure 3.1: Specific tensile strength (tensile strength divided by density) as a function of specific modulus (Young's modulus divided by density) of composite materials, monolithic metals and ceramics (Zwebe, 2002)

Composites as modern engineering materials are generally used in a form whereby a strong, brittle reinforcing phase is dispersed within a tougher and more ductile phase known as the matrix (Hull and Clyne, 1996.). Furthermore, it is generally accepted that the aim of designing a composite material is to obtain properties which are superior to those of the individual phases/materials. Composites are generally classified by whether the composite is naturally occurring or man made, but more often (and more usefully) by the type of matrix and reinforcement materials. However, these classifications can be sub-divided depending on the geometry of the reinforcing phase. With respect to matrix material, composites are classified as polymer-matrix composites (PMCs), metal-matrix composites (MMCs), or ceramic-matrix composites (CMCs). The reinforcing phase(s) may then fall into one of several categories. The most frequently used reinforcing geometry in aerospace composites is a continuous fibre with alignment of the fibres. Figure 3.2 shows the various classifications of composite materials with regards to the geometry of the reinforcing phase.

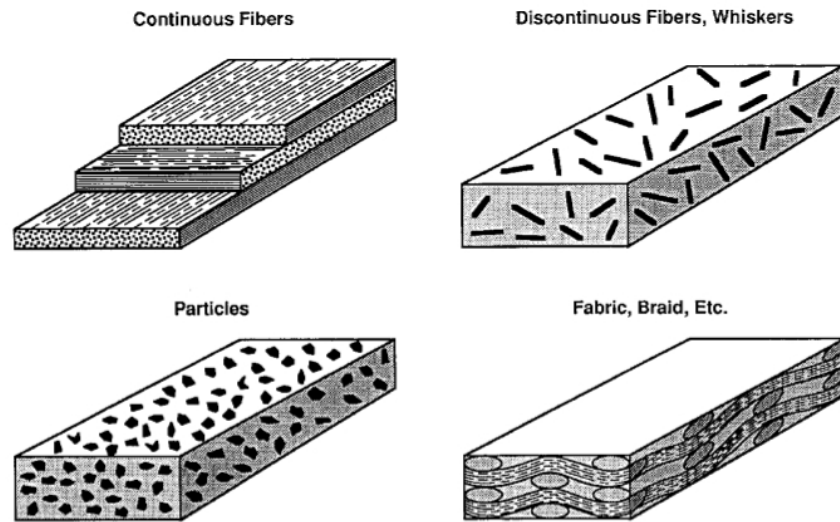


Fig. 1 Reinforcement forms.

Figure 3.2: Forms of composite reinforcements. From (Zwebe, 2002).

## 3.2 Damage in Fibre Reinforced Plastics

### 3.2.1 Static Failure of Fibre Reinforced Plastics

Due to the anisotropic properties of composite materials, and the fact that interfaces exist with the material, the damage and failure modes of these materials are relatively complex. Several mechanisms such as matrix micro-cracking, fibre fracture, fatigue, delamination and environmental factors may all contribute to the failure of a composite structure (Clyne and Withers, 1993) (Hull and Clyne, 1996.). When a high stress is applied to a unidirectional lamina, there are several types of failure which may occur (Hull and Clyne 1996). The failure mode depends upon the type of applied stress, but the three most important types are shown in figure 3.3.

Fracture of the fibres may occur due to very large stresses parallel to the fibre direction. Under this circumstance, the matrix will also fail due to the high stresses and the entire composite will fail. In general, however, fibre reinforced composites are generally more vulnerable to transverse tensile or shear loading. This is because under these circumstances the strength of the composite is reliant on the matrix strength, or the strength of the fibre/matrix interface (Clyne and Withers, 1993). In this case, fracture will occur on surfaces parallel to the fibre direction either entirely within the matrix, at the fibre/matrix interface, or within the fibre (Hull and Clyne, 1996.).

Shear failure of a composite often occurs on planes which are determined by the fibre direction. Figure 3.4 illustrates the six combinations of shearing direction and planes, along with their associated indices.

The shear mode denoted by the pairs  $\tau_{21}$  and  $\tau_{31}$  are unlikely to occur because there is generally a high resistance to shear fracture of the fibres. With regards to the remaining

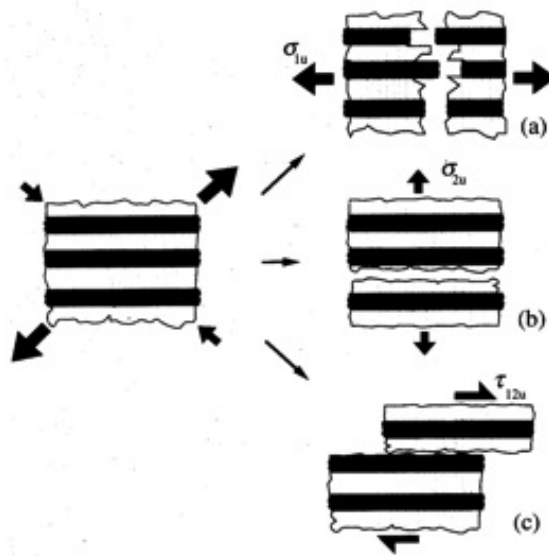


Figure 3.3: Illustration of failure in a composite as a result of stress exceeding critical values of (a) axial tensile stress , (b) transverse tensile stress , and (c) shear stress (Clyne and Withers, 1993)

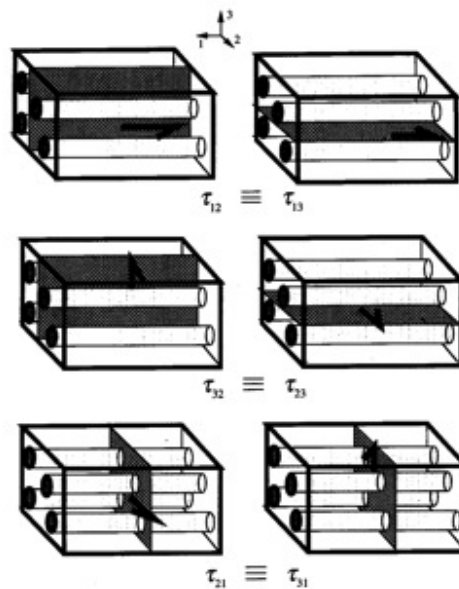


Figure 3.4: Nomenclature and orientation of shear stresses acting within an aligned fibre composite (Hull and Clyne, 1996.)

two shear pairs the magnitude of  $\tau_{12}$  is the most important. This is because during the stressing of a thin lamina in the 1-2 plane stresses of the type  $\tau_{32}$  do not occur. Shear strength is generally affected by the same factors as the transverse tensile strength due to stress concentrations in the matrix between fibres.

The failure of an aligned, long fibre composite in compression depends on how the material is loaded, as well as the degree of lateral constraint. Under axial compression, fibres will tend to buckle according to the Euler equation. In this case, the buckling of the fibres is equated to a cylindrical rod.

$$\sigma_{*b} = \frac{\pi^2 E}{16} \left( \frac{d}{L} \right)^2 \quad (3.1)$$

Where

- $\sigma_{*b}$  is the buckling strength
- $E$  is Young's Modulus
- $d$  is the rod diameter
- $L$  is the rod length

Hence, fibres with a high aspect ratio ( $L/d$ ) will tend to buckle more easily. However, some lateral stability is provided by the matrix, so the Euler equation may provide an under estimate of the actual compression strength. Figure 3.5 illustrates the process of buckling, and how tensile and compressive zones are generated on the respective fibre surfaces. This process leads to fracture in brittle fibres, but in ductile reinforcements, such as Kevlar™, a kink zone may form (Hull and Clyne, 1996.).

In addition to macroscopic buckling described by the Euler equation, a more common failure mechanism known as '0° fibre microbuckling' is the most prevalent failure mechanism in compression (Berbinau *et al.*, 1999). As a consequence of this phenomenon the compressive strength of an aligned, long fibre composite is approximately 60-70% of the tensile strength (Soutis, 1991). This mechanism of buckling is thought to initiate by the elastic bending of fibres near a free edge, loaded by shear transfer from the matrix (Berbinau *et al.*, 1999). This loading then results in rotation and ultimately fracture of the fibres, forming a kink band, as shown in figure 3.6.

Fracture of the fibres takes place on the compressive surface of the fibres, as the tensile stresses generated have been shown to be too low to cause failure (Berbinau *et al.*, 1999). Further loading, and hence fibre rotation may also cause matrix failure, causing the composite to lose its load carrying capability.

Research has shown that in order for a composite to have a high compressive strength, Euler and microbuckling must be inhibited (Berbinau *et al.*, 1999; Soutis, 1991). Soutis suggests that this increase in strength can only be achieved by an increase in shear modulus and shear strength (Soutis, 1997), due to factors such as fibre waviness inducing significantly larger matrix shear stresses.

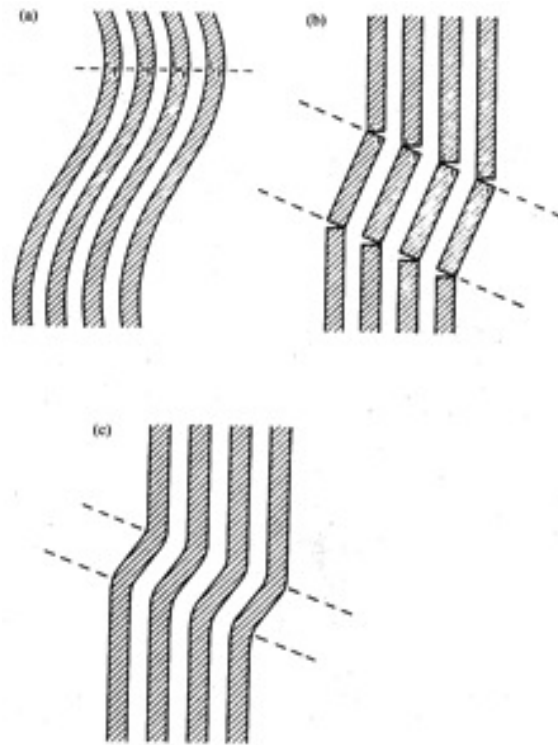


Figure 3.5: (a) Tensile and compressive stresses in a fibre due to in-phase buckling, leading to a kink zone. (b) Two planes of fracture formed with brittle carbon fibres. (c) Unfractured kink zone formed with Kevlar 49 fibres (Hull and Clyne, 1996.)

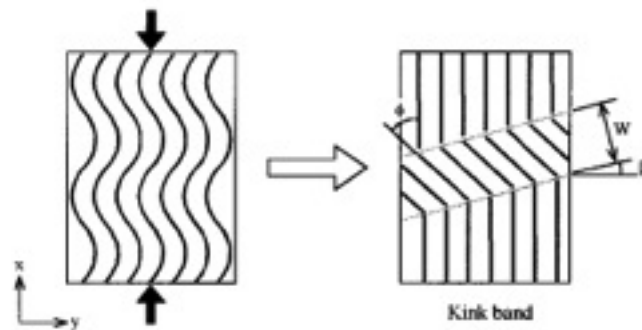


Figure 3.6: In-plane buckling of fibres and fibre kink band geometry (Berbinau *et al.*, 1999)

### 3.2.2 Impact Damage and Failure Mechanisms

One of the most significant limitations facing the use of composites materials is their response to localised impact loading (Cantwell and Morton, 1991). Carbon fibre composites are generally characterised as being vulnerable to impact damage, owing to the brittle properties of the fibre and matrix materials (Caprino *et al.*, 2007). Prediction of impact damage development in composites is difficult in comparison to conventional aerospace materials such as aluminium. At low to medium incident impact energies, metals absorb this energy through elastic and plastic deformation (Shadbolt *et al.*, 1981). While plastic deformation will often cause permanent damage in metallic structures, the effects are not

usually critical (Bradshaw *et al.*, 1973). At higher impact energies, penetration of the metallic component may occur, but the effect on the strength of the component may be predicted using fracture mechanics (Avery, 1981).

However, the ability of a composite material to undergo plastic deformation is minimal (Cantwell and Morton, 1991). As a result energy is often absorbed through the creation of large fracture areas, ensuing in significant losses of strength and stiffness (Rotem, 1988). Furthermore, the damage zone is frequently complex in nature and therefore difficult to characterise (Avery, 1981). Consequently, maximum allowable design strains of only 0.5% are employed in industry to prevent impact failure, and therefore the superior in-plane properties of composites are not fully exploited (Richardson and Wisheart, 1996). Further concern with regards to impact loading arises from the geometry of composite structures, resulting in most impact events causing loading in a transverse direction. Because of the lack of through thickness reinforcement, damage tolerance in this respect is particularly poor (Richardson and Wisheart, 1996).

Impact events are generally classified as low or high velocity (Richardson and Wisheart, 1996). The manner in which the material responds and damage is induced, depends on the chemical and physical characteristics of the three composite constituents (fibre, matrix and interface) and the impact velocity (Cantwell and Morton, 1991). Although much research has been done in the field of impact, there is still a significant amount of disagreement in the literature between the definitions of low/high velocity impact events. Hence the point of transition between the two events is also unclear.

In general, it is reported that high velocity impacts are dominated by stress wave propagation through the material leading to localised damage as the structure does not have time to respond. Conversely, in low velocity impact, the response of the target is highly important. This is because the relatively high contact duration allows elastic energy absorption and the entire structure can respond (Richardson and Wisheart, 1996). Several researchers have defined the two types of impact in terms of the damage which is induced (Joshi and Sun, 1985; Liu and Malvern, 1987). In this context, low velocity is characterised by damage such as matrix cracking and delamination, and high velocity by fibre fracture as a result of penetration. In comparison, Cantwell and Morton (Cantwell and Morton, 1991) considered the testing techniques used to simulate impact events to classify low velocity as being up to  $10\text{ms}^{-1}$ .

Four major modes of failure have been identified in long fibre reinforced composites (Richardson and Wisheart, 1996)

1. Matrix damage
2. Delamination
3. Fibre failure
4. Penetration

The energy absorbing capability of the above fracture processes depends on the constituent (fibre, matrix, interface) properties in addition to the impact mode. In general, failure which involves fibre fracture results in a large amount of energy dissipation, whereas fracture of the matrix or interface results in low fracture energies (Cantwell and Morton, 1991).

### 3.2.2.1 Matrix Damage

Low velocity transverse impact loading of a composite usually initiates matrix damage before other damage modes. This damage is mostly in the form of matrix cracks, although fibre/matrix debonding is also common (Richardson and Wisheart, 1996). Matrix cracks are usually found to be oriented parallel to the fibre direction, and occur as a result of fibre/matrix property mismatch (Joshi and Sun, 1985). The typical crack and delamination pattern found by Joshi and Sun (Joshi and Sun, 1985) is illustrated in figure 3.7.

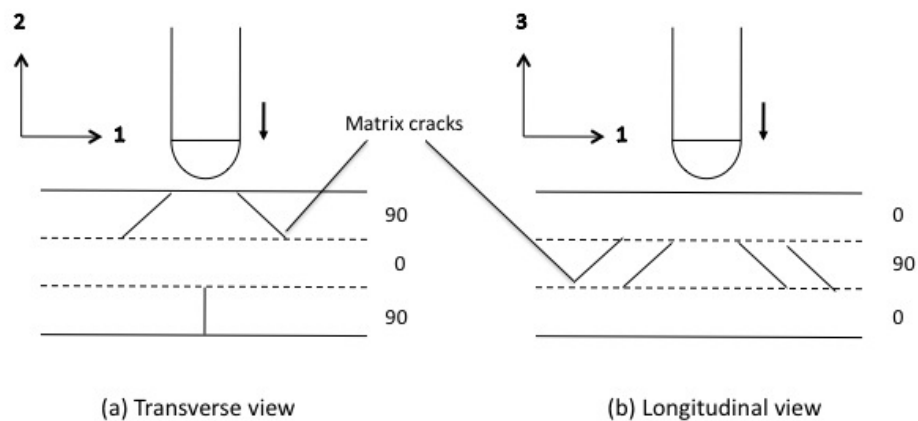


Figure 3.7: Initial impact damage in an impacted 0/90/0 composite plate adapted from (Joshi and Sun, 1985)

The cracks in the upper and middle layers shown in figure 3.7 are known as shear cracks (Choi *et al.*, 1991a). These cracks are inclined at  $45^\circ$  and are formed due to the high transverse shear stress, which is related to the contact force and area. The cracks on the lower surface (figure 3.7 (a)) are induced by a high tensile bending stress and termed a 'bending crack' (Richardson and Wisheart, 1996). The bending stress is related to the flexural deformation of the material, and the cracks are characteristically vertical (Jih and Sun, 1993; Lee and Sun, 1993). Cantwell and Morton deduced that the type of matrix cracking observed after impact is dependant also on the geometry of the specimen. They showed that short thick specimens result in high peak contact loads due to higher

stiffness, leading to transverse shear cracks in the upper plies. Conversely, long thin specimens display bending cracks in the lower plies due to high deflections as a result of lower stiffness (Cantwell and Morton, 1989).

### 3.2.2.2 Delamination

Delamination of a composite laminate can cause significant reductions in strength and stiffness, and as such is a critical failure mode (Pagano and Schoeppner, 2000). Research has shown that delamination may reduce the load bearing capability of a composite by 50% (Cantwell *et al.*, 1983). A delamination is described as a crack running in the matrix between plies of different fibre orientation, but not between lamina of the same ply group (Richardson and Wisheart, 1996; Wang, 1979). Figure 3.8 shows some of the sources of delamination.

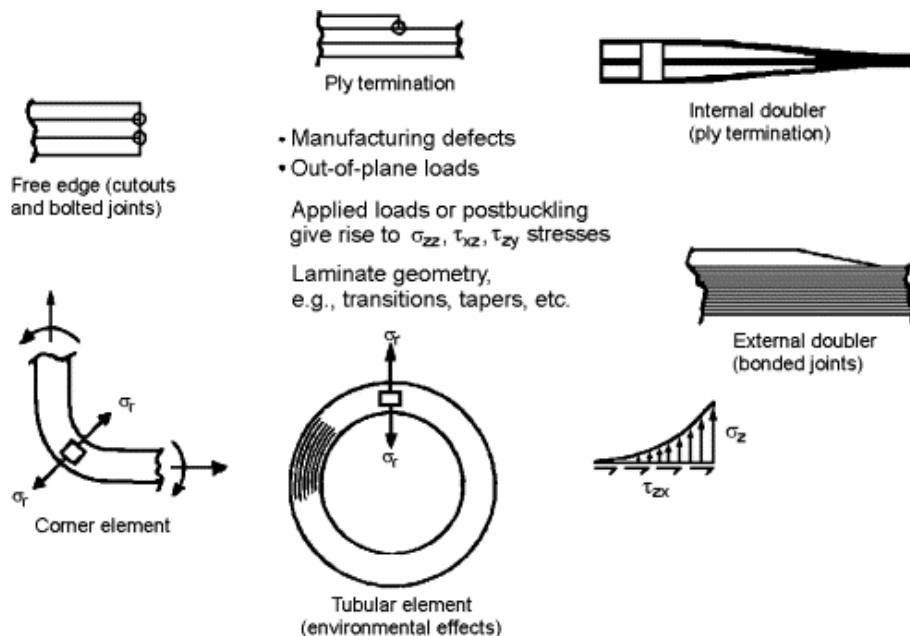


Figure 3.8: Generic sources of delamination (Pagano and Schoeppner, 2000)

Liu demonstrated that delamination occurs due to bending stiffness mismatches between adjacent plies (Liu, 1988). It was found that the level of delamination increases as the angle between adjacent plies increases. Liu defined a coefficient of bending mismatch revealing a 0/90 laminate to be the worst case scenario, hence the larger the mismatch, the larger the delamination area. Schoeppner and Abrate (Schoeppner and Abrate, 2000) demonstrated that a ‘threshold load’ exists for composite materials, below which an impact will not cause delamination damage. This was identified by a sudden load drop in the load-time history during impact testing due to laminate level damage. Furthermore, it has been shown that delamination will only occur where matrix cracks already exist (Choi *et al.*, 1991a,b). Joshi and Sun (Joshi and Sun, 1985) researched this interaction

between matrix cracking and delamination in 0/90/0 laminates. It was found that matrix shear cracks of the type shown in figure 3.7(a) are halted by the change in fibre direction at the laminae interface, and as a result propagate as a delamination between the layers.

### 3.2.2.3 Fibre Failure

Failure of the fibres in a composite is a precursor to catastrophic failure, and generally occurs after other mechanisms such as delamination and matrix cracking (Richardson and Wisheart, 1996). Fibre failure occurs due to locally high stresses (mainly in shear) in proximity to the impactor, whereas high bending stresses on the non-impacted face cause failure in this region. The energy required for fibre failure on the non-impacted surface is given as (Dorey, 1988);

$$Energy = \frac{\sigma^2 wtL}{18E_f} \quad (3.2)$$

Where:

- $\sigma$  = flexural strength
- $E_f$  = flexural modulus
- $w$  = width
- $L$  = unsupported length
- $t$  = specimen thickness

### 3.2.2.4 Penetration

Penetration of a composite occurs when fibre failure has reached a critical level, allowing to impactor to pass through the material (Lee and Sun, 1993). Penetration tends to occur more often in high velocity impacts due to the localised nature of the impact (Cantwell and Morton, 1989).

A simple analytical model for the energy absorbed during penetration is given by Dorey (Dorey, 1988);

$$Energy = \pi \gamma td \quad (3.3)$$

Where:

- $\gamma$  = fracture energy
- $d$  = diameter of impactor
- $t$  = plate thickness

### 3.2.3 Effect of Component Properties on Impact Performance

The properties of the constituents of a composite material determine the 'threshold' energy or stress to activate any particular failure mode during impact (Richardson and Wisheart, 1996). The following sections discuss the effect of each constituent on impact properties.

#### 3.2.3.1 Fibres

A wide range of mechanical properties are currently attainable for different fibre materials. As a result, it is often difficult to separate effects due to mechanical properties from those due to geometrical factors (e.g. fibre diameter), and interfacial properties (e.g. chemical bond strength) (Cantwell and Morton, 1991). Adams (Adams and Miller, 1975) found the impact resistance of S-glass and Kevlar composites to be more than five times that of a Modmor II carbon fibre composite in Charpy tests. Beaumont et al. showed that E-glass and Kevlar composites failed progressively as opposed to carbon fibre reinforced composites which failed catastrophically at maximum load (Beaumont *et al.*, 1974). This was attributed to the ductility index (DI) of the fibres (the ratio of energy associated with crack propagation compared to that during crack initiation). It was shown that carbon fibres have a low DI, and hence a low energy absorbing capability leading to poor impact resistance. Several researchers have also compared the impact performance of different types of carbon fibres. It has been shown that type II fibres (high strength) offer superior impact resistance (Bader and Ellis, 1974; Hancox and Wells, 1973). Izod impact testing by Chamis et al. (Chamis *et al.*, 1972) showed that the main energy absorbing mechanisms in composites are interlaminar shear deformations and flexure. They also found that the area under the linear portion of stress-strain curve gives a good indication of a material's impact resistance, with larger areas under the curve representing a more effective energy absorbing material. Further work by Beaumont took into account the energy absorbing mechanisms during micro-mechanical failure processes, giving equations for the work of de-bonding and fibre pull-out (Beaumont, 1979). Beaumont gives the work of de-bonding as:

$$W_d = \frac{\pi d^2 \sigma_f^2 l_d}{24 E_f} \quad (3.4)$$

Where:

- $l_c = \sigma_f d / 2\pi$ , the critical transfer length
- $\tau =$  constant frictional shear stress

Beaumont went on to state that fibre pull-out is the is the main mechanism responsible for toughness in carbon fibre composites, as opposed to fibre sliding for glass fibre composites (Beaumont, 1979). Equation 3.4 reveals work to pull-out is strongly dependant on the fibre diameter, hence in theory a larger fibre diameter should perhaps improve

the impact properties of carbon fibre composites. In contrast to this theory however, fibre manufacturers have gradually decreased the diameter of fibres as this offers increased failure strains (Bradshaw *et al.*, 1973; Cantwell and Morton, 1991). Current fibre diameters may be around 5 $\mu\text{m}$  compared to 7-8 $\mu\text{m}$  for the first generation of carbon fibres. The improvement in failure strain has increased the strain energy absorbing ability of the fibres, resulting in improved impact properties.

Under low velocity impact, where the specimen response is important, it is clear that reductions in fibre diameter offer a better all-round solution to impact properties as opposed to increasing the fibre diameter. However, under high velocity impact where the specimen response is more localized, it may be that large diameter fibres offer a better solution to impact resistance due to local energy absorbing mechanisms such as fibre pull out becoming more important (Cantwell and Morton, 1991).

### 3.2.3.2 Matrix

The polymer matrix in a fibre-reinforced composite has several functions. The matrix acts to align, stabilise and protect the fibre, as well as ensuring stress transfer between fibres (Cantwell and Morton, 1991; Richardson and Wisheart, 1996). Although the fibres are responsible for carrying most of the load, the properties of the matrix are critical. An example previously mentioned is that impact induced delamination can cause a 50% reduction in strength (Cantwell *et al.*, 1983). Most structural fibre-reinforced plastics employ thermoset polymers, in particular epoxy resins as they meet the hot/wet compressive strength requirements. However, epoxy is brittle and hence has a low toughness leading to problems with delamination (Richardson and Wisheart, 1996). Several methods have been employed in matrix systems to improve interlaminar fracture toughness. These include the use of tough rubber or thermoplastic particles (Bascom *et al.*, 1981; Sela and Ishai, 1989), the addition of thin tough interlayers (C.Ruiz and Xia, 1991; Sun and S.Rechak, 1988), and the use of plasticising modifiers (Sela and Ishai, 1989) among others. However, despite improvements in matrix toughness generally decreases other mechanical properties and the improvements seen in the pure matrix material are never fully transferred to the composite (Cantwell and Morton, 1991). This is thought to be due to restriction of the crack-tip plastic zone by the fibres, hence negating to a certain extent the increased toughness of the matrix (Cantwell and Morton, 1991). Thermoplastic matrices have also been successfully employed to increase the toughness of composite materials, and can give an increase in toughness an order of magnitude greater than thermoset matrix composites (Richardson and Wisheart 1996). However, inferior properties with regards to chemical resistance, thermal stability, creep and fibre/matrix bonding have limited the use of thermoplastic matrices (Sela and Ishai, 1989). Research conducted by Williams and Rhodes (Williams and Rhodes, 1982) showed the impact induced damage and residual properties varied dramatically between modified and unmodified graphite/epoxy composites. They demonstrated that brittle systems generally failed by extensive

delamination, as opposed to tougher systems failing in transverse shear near the impact site. Furthermore, the authors concluded that the tensile performance of the pure matrix has a considerable effect on the impact properties of the composite. Additionally, it was stated that to improve impact properties, the matrix strength should exceed 69MPa and its failure strain should be greater than 4%. The matrix should also have a shear strength exceeding 3.1GPa to provide adequate compressive strength.

### 3.2.3.3 Interface

The surface of the fibres in a composite is often treated to improve the level of adhesion between the fibre and matrix (Cantwell and Morton, 1991) resulting in a three-dimensional layer which has its own distinct properties (Lehmann, 1985). Carbon fibres are treated in an oxidative process, the extent of which determines the bond strength with the matrix. This bond strength has a significant effect on the mechanical performance of the composite (Cantwell and Morton, 1991). Research has shown that fibres with low levels of surface treatment tend to result in failure of the composite at low transverse stresses, leaving smooth fibres at the fracture surface. An increased level of fibre treatment results in failure within the matrix at a higher stress, due to the increased strength of the fibre/matrix bond (Bradshaw *et al.*, 1973; Lehmann, 1985). Rogers *et al.* (Rogers, 1971) demonstrated that a fourfold increase in the energy required to initiate damage during impact could be obtained by increasing the fibre/matrix bond strength. However, at higher energies it was shown that the residual properties of fibre-treated composites decline sharply up to the perforation limit (Dorey, 1980), as shown in figure 3.9. Furthermore, it can be seen that the perforation limit is dramatically lower in a fibre-treated composite compared to one in which the fibres are not treated.

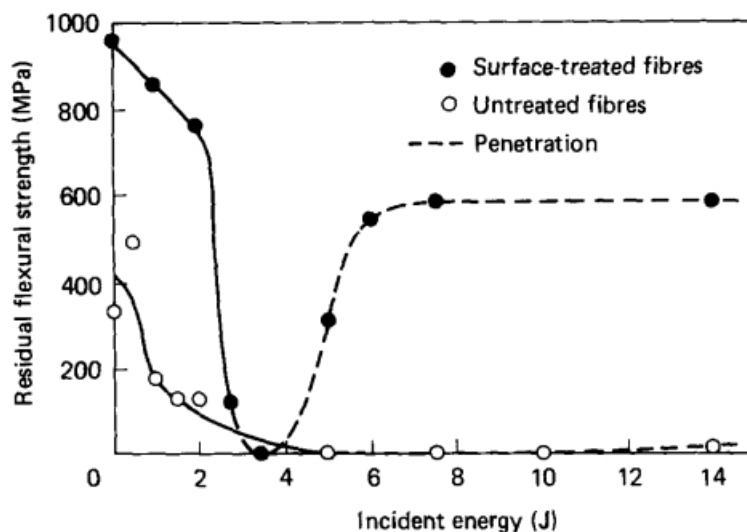


Figure 3.9: Residual flexural strength versus impact energy for ballistically impacted surface-treated and untreated carbon fibre composites (Dorey, 1980)

Dorey explained the above results with regards to the transverse fracture energy of a composite (Dorey, 1980). He stated that the transverse fracture energies for treated and untreated fibre composites are  $20\text{kJm}^{-2}$  and  $60\text{kJm}^{-2}$  respectively. However, despite these fracture energies, figure 3.9 shows that above the energies required to achieve penetration, the residual properties of the treated fibre composites are much better than for the untreated composites. This characteristic is due to the fact that in treated fibre composites, the impact damage is localised around the point of impact, often forming a clean hole (Rogers, 1971).

### 3.2.3.4 Stacking Sequence

In addition to the fibre stacking sequence affecting the mechanical properties of a composite, research has shown that it also significantly affects the impact resistance (Dorey, 1975; Morton and Godwin, 1989). Several researchers have shown that incorporating  $\pm 45^\circ$  surface plies into a composite can offer increased impact resistance and residual strength (Dorey 1975; Morton and Godwin 1989). An example of these results is shown in figure 3.10.

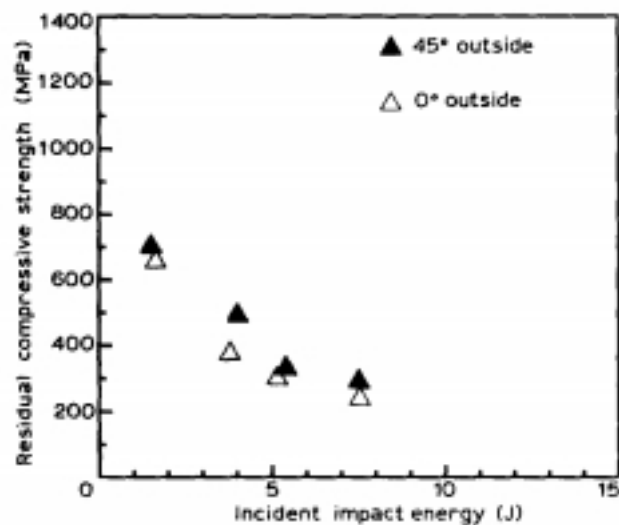


Figure 3.10: Residual compressive strengths of 6376/T400H after ring-supported impacts (Morton and Godwin, 1989)

Dorey later explained that these surface plies increase the flexibility of the composite, improving the elastic energy absorption and therefore improving the impact resistance (Dorey, 1982). Dorey also stated that these  $\pm 45^\circ$  surface plies also act to protect the load bearing  $0^\circ$  fibres from impact induced damage. Cantwell and Morton demonstrated that the low velocity impact damage incurred in  $\pm 45^\circ$  laminates depended upon the thickness, and therefore the stiffness of the structure (Cantwell and Morton, 1989). They showed that failure in thin, flexible targets initiates in the lowermost plies due to the bending induced stresses. Conversely, failure initiates on the top surface of thicker, stiffer composites due

to the contact stress at the impact site. The results are shown in figure 3.11.

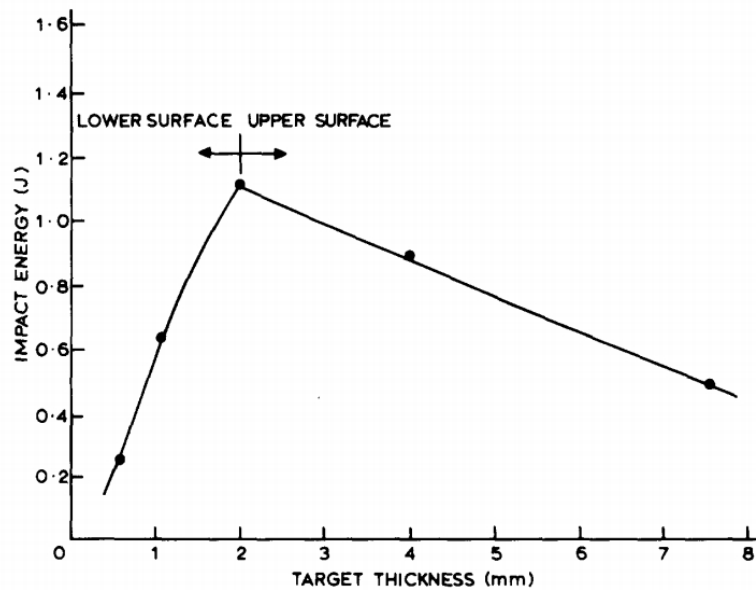


Figure 3.11: Low velocity impact energy to initiate damage vs. target thickness for ( $\pm 45^\circ$ ) CFRP composites (Cantwell and Morton, 1989)

A model developed by Liu proposed that delamination is most likely to occur in a composite when there is a large mismatch in bending stiffness, for example between  $\pm 45^\circ$  plies (Liu, 1988). It was shown by Liu that the level of delamination increased with angle  $q$  in a ( $0^\circ/q^\circ$ ) glass-epoxy laminate. Liu's research suggests therefore, that sudden large changes in fibre direction should be avoided to reduce delamination as a result of bending stiffness mismatch.

### 3.2.3.5 Geometry

Testing of simple CFRP beams has shown that the span-to-depth ratio can determine the mode of failure in low-velocity impact (Cantwell and Morton, 1991), and specimen geometry is fundamental in determining the overall impact response of a composite. In low velocity impact, long thin beams have been shown to fail in flexure, compared to short thick beams failing in an interlaminar mode (Bradshaw *et al.*, 1973; Cantwell and Morton, 1989; Morton and Godwin, 1989). In contrast to low velocity testing however, tests at high velocity (Cantwell, 1988) have shown that specimen geometry becomes less important. Cantwell tested this theory on large and small plates, and found that the damage area was similar in both small and large plates for a given impact energy. This observation suggests therefore, that under high velocity impact, small coupons can be tested to characterise the behaviour of larger structures (Cantwell and Morton, 1991).

### 3.3 The Role of Modelling in Composites Design

The ability to predict how a composite structure will behave under load is becoming an increasingly important tool in composites design. The use of finite element analysis (FEA) to model composites can improve design efficiency, and help to substantially reduce development costs. The spiralling costs involved with large scale testing of structural elements when compared to material coupon tests, also justifies the use of FEA to give an economic advantage.

Many decades of research efforts have been directed towards modelling the various failure mechanisms in composite materials, and as such many different modelling strategies exist. The complex nature of composite materials and structures manufactured from them means that no single modelling approach can account for damage and failure under all possible conditions. This complexity arises due to the range of possible lay-up configurations, geometries, loading conditions and failure mechanisms which may occur. Additional variations such as material choice (e.g. toughened or non-toughened resin systems), fibre architecture, and manufacturing routes all add to the complexity of modelling. Furthermore, FE modelling is only of use when valid material properties are used. This applies equally for modelling materials in terms of linear elastic modelling (e.g. for deflections under load), damage onset, or damage propagation.

It is beyond the scope of this thesis to review all possible modelling approaches, therefore this section will give a brief overview of the available methods with some illustrative examples. The reader is directed to the literature for detailed information on specific modelling strategies. Excellent reviews of failure theories can be found in works such as Hinton *et al.* (2004); Mishnaevsky and Brøndsted (2009); Orifici *et al.* (2008).

Failure criteria are broadly classified into two main categories- strength based, and fracture mechanics based. These fields can then be classified according to whether they consider general failure as opposed to specific failure modes, and whether they consider in-plane (intra-laminar) or out-of-plane (interlaminar failure). When modelling composite materials and structures, one must consider the length scales over which these failure criteria can occur. These length scales include sub-ply, ply, laminate, structural detail and component levels (Orifici *et al.*, 2008). Therefore, the engineer has the option to model the mechanical behaviour and failure of a composite in an extremely wide ranging context. Furthermore, the choice of modelling strategy will strongly depend on the computational resources and material data available, and the complexity of the structure being modelled.

Considering the range of strategies and opportunities for analysing composite structures, modelling has proven successful in applications ranging from predicting the mechanical properties of novel 3D woven composite materials to the crash response of composite helicopter fuselages.

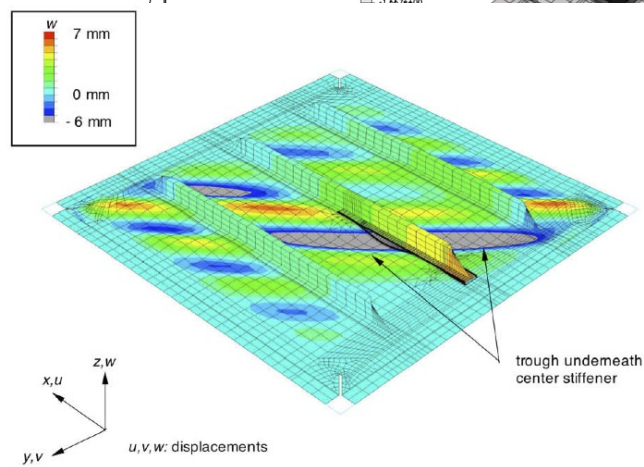
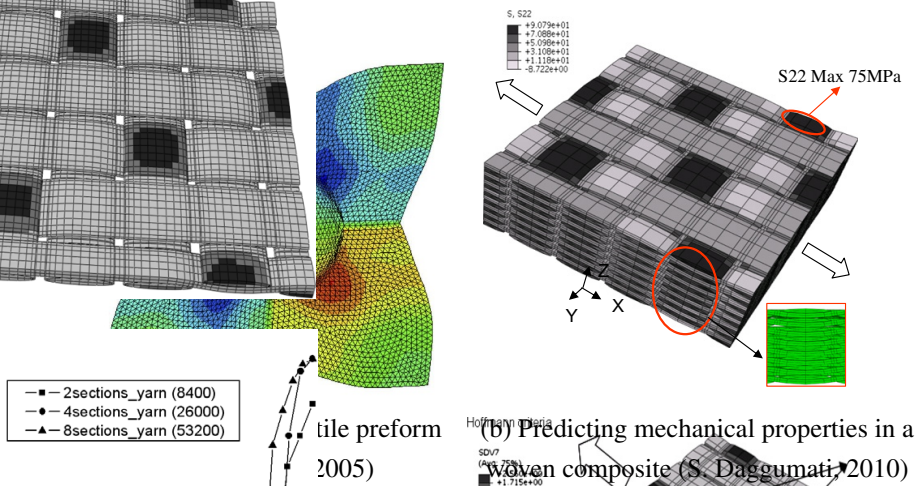


Figure 3.12: Examples of composite modelling

### 3.3.1 Modelling Low Velocity Impact Damage

The modelling of impact damage in carbon fibre composites has been the subject of much research over the last 30-40 years, and a multitude of modelling approaches exist for this specific area of damage analysis. In general, research has approached the problem by considering damage in terms of four main areas (?):

- A failure criteria approach
- A fracture mechanics approach
- A plasticity or yield surface approach
- A damage mechanics approach

All the above approaches generally scrutinise a particular parameter to predict and monitor the onset and progression of damage and failure.

Failure criteria approaches have been employed since the early work on modelling the strength of composite structures. Values such as stress, strain, force, displacement and rotation (among others) have all been used to determine the state of damage. The material is considered to be irreversibly damaged once a particular criteria has been satisfied. The failure criteria approach is therefore suited to applications such as 'first ply failure' of a laminate, or the failure of a structural assembly. While the failure criteria approach is one of the simpler modelling strategies, it is limited to addressing distinct failures and is not suitable for analysing the progression of damage such as delaminations or cracks (?). The method has proved useful for its simplicity, and more complex implementations have been demonstrated whereby several failure criteria can be combined for complex loading cases. The earlier implementations of stress/ strain based criteria can only provide a failure index appropriate to a macro-scale failure, such as the Tsai-Wu (Tsai and Wu, 1971) and Maximum Stress/ Strain theories (Tsai, 1992). Other criteria however, can provide indications of constituent (fibre/ matrix) failure, such as the Hashin (Hashin, 1980) and Puck (Puck and Schürmann, 2002) criteria. The major recent development in this area has been with the introduction of the LaRC03 and LaRC04 criteria (Maimi *et al.*, 2006; Pinho *et al.*, 2005). Choudhry (2009) compared various stress-strain based criteria for lap joints under low velocity impact, and found the physically based LaRC03/04 criteria to give the most realistic results.

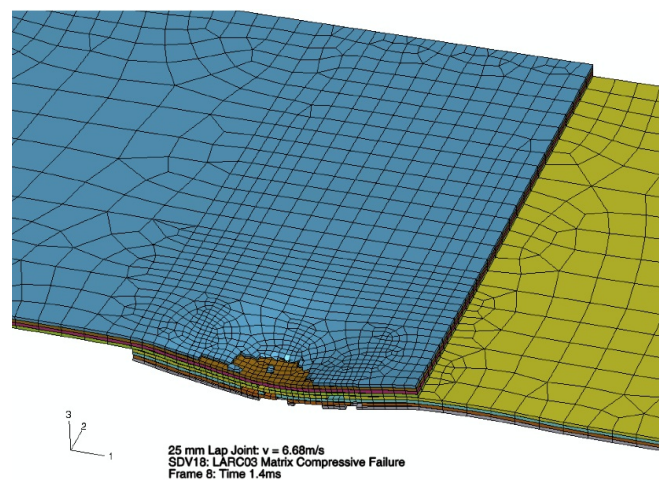


Figure 3.13: Matrix compression failure in a GFRP lap joint subject to low velocity impact (Choudhry, 2009).

Fracture mechanics approaches consider the growth of existing defects. While classical fracture mechanics were developed for metals, and considered the propagation of a single crack based on strain energy release rates, the situation is analogous to propagation of a delamination. This approach has therefore proven useful for predicting the growth of delaminations and their effect of structural integrity, as well as fibre-matrix debonding and the evolution of matrix cracking. The use of classical fracture mechanics has allowed researchers to discover the importance of loading rates, crack growth directions and

ply orientations (among many other factors), on the propagation of damage. One of the most significant advances in modelling since the introduction of fracture mechanics approaches was the development of the Virtual Crack Closure Technique (VCCT) (Rybicki and Kanninen, 1977). While this approach successfully demonstrated realistic delamination propagation in simple geometries and loading conditions, its use has been shown to be inappropriate for modelling low-velocity impact damage due to strict requirements in its implementation. These requirements include prohibitive crack tip element sizes, self-similar crack tip growth, and the existence of a pre-crack with a finite length (Yang and Cox, 2005). These conditions were overcome by significant improvements in composite specific fracture mechanics approaches by authors such as Borg *et al.* (2004) and (Yang and Cox, 2005). These researchers implemented the approach known as cohesive zone modelling, which more accurately captured delamination propagation in transverse loading (e.g. impact) conditions without the restrictions imposed on VCCT. Figure 3.14 gives an example of the geometrical context of cohesive zone modelling.

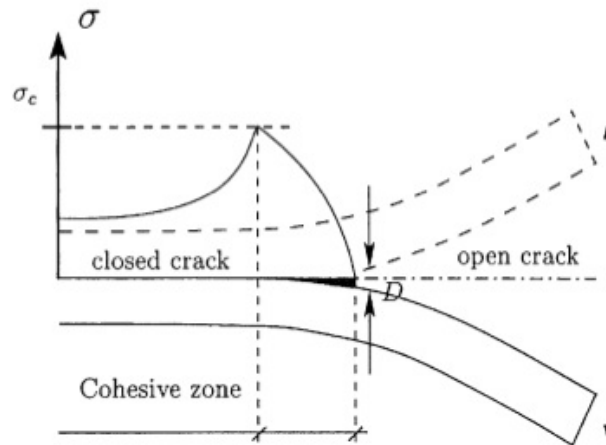


Figure 3.14: Principle behaviour of a cohesive zone model (Borg *et al.*, 2004)

Wisnom (2010) provides an excellent review of cohesive zone modelling, highlighting significant papers in the field. For example, the work by Bouvet *et al.* (2009) showed excellent correlation between predicted and experimental impact damage results for uni-directional carbon laminates, as shown in figure 3.15

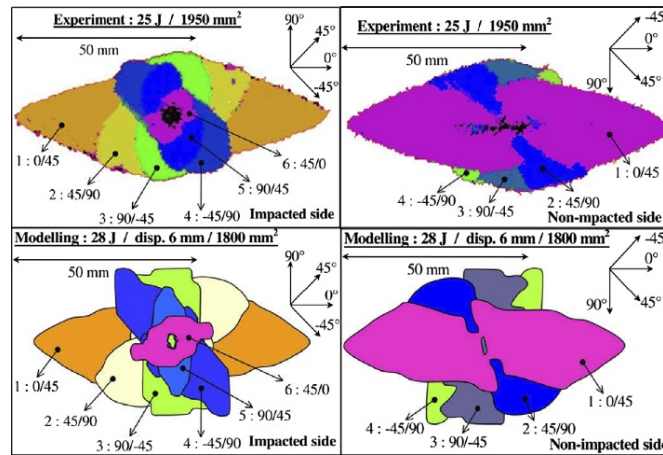


Figure 3.15: Comparison of impact damage on  $(0_2/45_2/90_2/ - 45_2)_s$  laminate at equal displacements (Bouvet *et al.*, 2009).

More recently, researchers have developed the field of continuum damage mechanics (CDM) as an approach to modelling damage. CDM allows the full range of events in the damage sequence to be modelled, from the initiation of various forms of damage in a material, to the progression of this damage and subsequent laminate/ part/ structural failure. This approach effectively combines the approaches of failure criteria models (such as strength based criteria), with fracture mechanics concepts within a single modelling strategy. In order for this behaviour to be modelled, CDM employs material degradation parameters whereby material properties are reduced in response to damage progression. These degradation parameters are defined within the material constitutive behavior. Many different failure modes can therefore be incorporated into the same model, such as fibre fracture, matrix cracking and buckling in compression (Orifici *et al.*, 2008). Furthermore, the CDM approach can be used to model composite materials on the micro- or meso-scale. Unit cells can be modelled to analyse fibre, matrix and interfacial damage explicitly, while averaged properties can be used to define ply failures on the meso-scale. Similarly, structural components such as stiffened panels can be modelled using this approach. Iannucci and Willows (2006) made significant progress in the field of CDM to model low velocity impact damage in woven composites by formulating a coupled damage-strain damage mechanics model. Their approach utilised cohesive zone modelling in conjunction with a stress threshold for damage commence and a critical energy release (fracture mechanics) to allow propagation of delaminations. Many variations on the CDM approach can be found in the literature, for specific materials and loading cases. For example, specialist formulations for 3D woven composites and through-thickness stitched composites exist.

### 3.4 Chapter Summary and Conclusions

Clearly the impact damage response of composite materials is a complex subject area. Advances in materials engineering are of key importance to improving the impact damage

tolerance of CFRP. Understanding the microstructural response of materials can help to improve the materials design through fibre architecture, resin chemistry and processing methods. As will be seen in the following chapters, X-Ray tomography is a particularly useful tool for helping in this improvement process as it allows a three-dimensional non-destructive analysis of the damage inside a component.

## DUAL-ENERGY IMAGING OF HIGH ASPECT RATIO CFRP PANELS

### 4.1 Introduction

Due to the laminated structure and highly anisotropic behaviour of CFRP materials, structures manufactured from these materials are often plate-like in geometry. This geometry results in very high aspect ratio structures (thickness to width ratio). The high aspect ratio of CFRP structures presents a significant challenge when employing non-destructive techniques for the inspection, due to the highly variable attenuation of radiation in the thickness and width directions. In the case of X-Ray tomography, this means that the optimum beam energy to give a good quality projection will not be the same for all projection angles.

Industrial tomography generally approaches this problem in several ways:

- physically cutting the sample to reduce the aspect ratio;
- stacking samples if multiple are available, and the stack will still fit within the detector field of view;
- performing imaging under beam conditions which give acceptable results over the most projection angles, accepting the loss in image quality.

This chapter presents a novel dual-energy method for imaging high aspect ratio CFRP plates using a laboratory X-ray CT system. The procedure involves performing two CT scans at different X-ray accelerating voltages, each optimised for the thinnest and thickest X-ray path lengths through plate respectively. The projections from the two CT scans are then combined into a single set of radiographic projections which can then be reconstructed using conventional algorithms to give an improved CT data set. The procedure involves acquiring attenuation data about the candidate materials, developing beam hardening correction parameters, and combining the two projection sets using a computational method in Matlab. The technique uses conventional reconstruction code, and is therefore easy to implement on any CT system.

Previous applications of dual-energy CT have focused on optimising contrast between materials of different atomic number. This approach is particularly apparent in the medical industry where contrast between various soft tissue structures is important. Authors such as Kalender *et al.* (1990) and Petersilka *et al.* (2008) demonstrated practical implementations of dual-energy medical CT. However, in this context dual energy CT has been implemented through the use of dual X-Ray sources and detectors. Figure 4.1 shows an illustration of a dual-source-detector set up common in many medical CT systems.

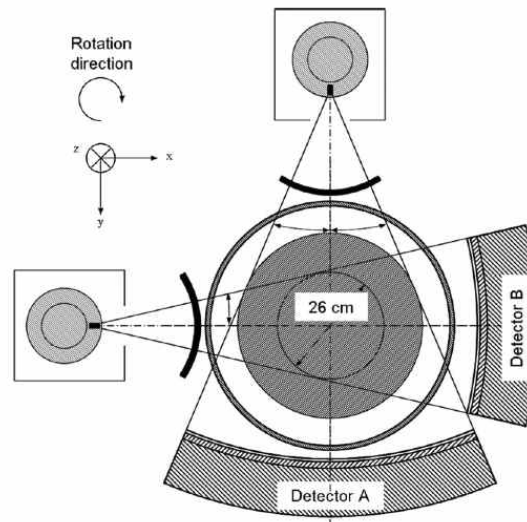


Figure 4.1: Schematic illustration of dual-source CT using two image detectors (Petersilka *et al.*, 2008).

The approach used in medical CT reduces patient dose and prevents the potential problems of image registration when two sequential scans (high and low energy) are performed using a single source-detector setup. Effectively, the dual-source-detector approach results in two separate reconstructed volumes which then have to be decomposed to give the true 'dual-energy' data. The expense of such a system appears to have prevented its uptake in industrial CT.

A similar approach has been used in airport baggage/ security scanners where quantifiable material thickness and chemical identification is required, such as the identification of explosives Singh and Singh (2003); Ying *et al.* (2007).

More recent approaches have attempted to improve the imaging problem by the development of novel imaging sensors. Increased dynamic range detectors, and those with the ability to discriminate particular X-Ray energies have been shown to be effective. For example, Sia *et al.* (2011) have recently developed a hybrid photon counting energy sensitive detector array based on a CdZnTe material. While the detector allows energy selective imaging and can therefore reconstruct specific energy ranges, the detector is too small for most industrial CT applications due to manufacturing costs and scaling issues.

Work by Amos (2011) approached a similar issue to that covered in this thesis to compensate for significant differences in absorption in CFRP- aluminium joints. However,

while his approach gave improved results, a fairly complex thresholding procedure was required to separate low- and high-attenuation regions in the radiographs prior to reconstruction. Nachtrab *et al.* (2011) developed a dual-energy approach based on an original approach by Heismann *et al.* (2003). Their work aimed to quantify density measurements in materials samples using industrial tomography. Their procedure was based on a 1st order linearisation procedure, and again needed calibration. While Nachtrab *et al.* (2011) improved the atomic number range over which the technique could work compared to Heismann *et al.* (2003), again the approach requires two separate reconstructions in addition to calibration against a known object.

While the approach used in this work draws on elements of the above dual energy methods, the implementation is slightly different. While all previous approaches have aimed to improve contrast between different chemical species, the work presented here aims to account for significant variations in material thickness. It is shown that a simpler approach to combining multiple energy data sets can be taken because a material calibration step (as in medical dual energy CT) is not required. Otherwise, a standard back-projection algorithm can be used for reconstruction, as all data processing is performed on the radiographs prior to any reconstruction. As a result, only one reconstructed data set is generated as opposed to two for the examples which are present in the literature.

The aim of the work presented in this chapter was therefore:

- To develop an image processing algorithm which successfully combines multiple CT scans to produce an improved CT data volume compared to a 'compromised' CT scan
- Implementation of this algorithm on an industrial CT scanner

This aim was achieved through the following objectives:

- Manufacture of step-wedges of both uni-directional and woven CFRP materials
- Acquisition of a range of radiographic projections to quantify linear attenuation coefficients of candidate materials
- Acquisition of a range of radiographic projections to quantify the effect of material thickness and accelerating voltage on image quality
- Deduction of beam hardening correction coefficients for both candidate materials
- Development a Matlab script to combine dual-energy projection sets

## 4.2 System Overview

The CT system for all the tomographic imaging in this thesis (except Chapter 7) is the Nikon Metrology 225kV custom bay. This system is based on a commercially available

X-ray system, which has been customised to accommodate large samples and provide expanded beam capabilities up to 320kV by means of an interchangeable source. The general specification of the equipment is as follows:

- Microfocus X-ray source, with a minimum focal spot size of 5-10 $\mu$ m
- Maximum accelerating voltage of 225kV (expandable to 320kV)
- Maximum tube current of 2mA
- A multi-metal target, consisting of Copper, Molybdenum, Silver and Tungsten
- A 5-axis sample manipulator with 50kg load capacity
- Cone beam geometry allowing sample magnification up to 300X
- Walk-in enclosure measuring 2 x 2 x 2m

Radiographs are collected on a Perkin Elmer XRD 1641-AN monolithic amorphous Silicon digital X-ray detector, which has the following specifications:

- 4,000,000 effective pixels in a 2000 x 2000 array
- 100 $\mu$ m pixel pitch
- 16 bit data acquisition, giving 65,535 grey levels
- Image exposure ranging from 250ms to 4000ms

The system is operated via:

- A windows XP control PC operating Nikon Metrology Inspect-X software
- A windows XP acquisition PC operating CT Agent data acquisition software and CT Pro reconstruction software

Figure 4.2 shows the CT system



Figure 4.2: Nikon Metrology Custom CT bay with 225kV X-ray source (left), 5-axis sample manipulator stage (centre) and 2000 x 2000 pixel flat panel detector (right).

The CT system is a cone-beam geometry configuration, which results in geometrical magnification ( $M$ ) of the object as illustrated in figure 4.3, and determined by equation (4.1).

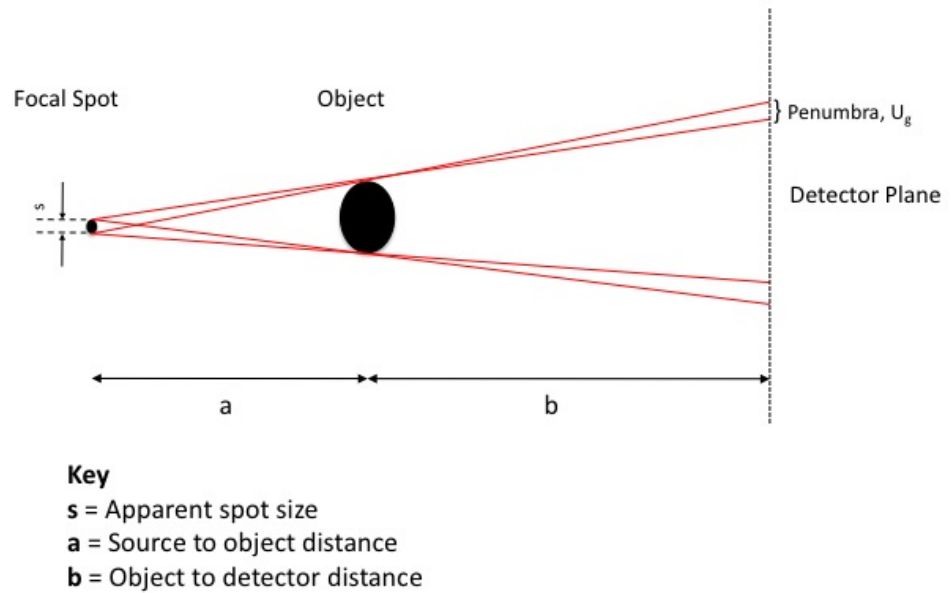


Figure 4.3: Cone beam geometry showing origin of magnification and penumbra blurring.

$$M = \frac{(a + b)}{a} \quad (4.1)$$

As the X-ray focal spot is not infinitely small, a penumbra forms at the edges of the object, as illustrated in figure 4.3. The size of the penumbra, also known as geometric unsharpness ( $U_g$ ) is related to the spot size given by (4.2).

$$U_g = s \times \frac{b}{a} \quad (4.2)$$

Figure 4.4 illustrates the effective pixel size at various magnifications.

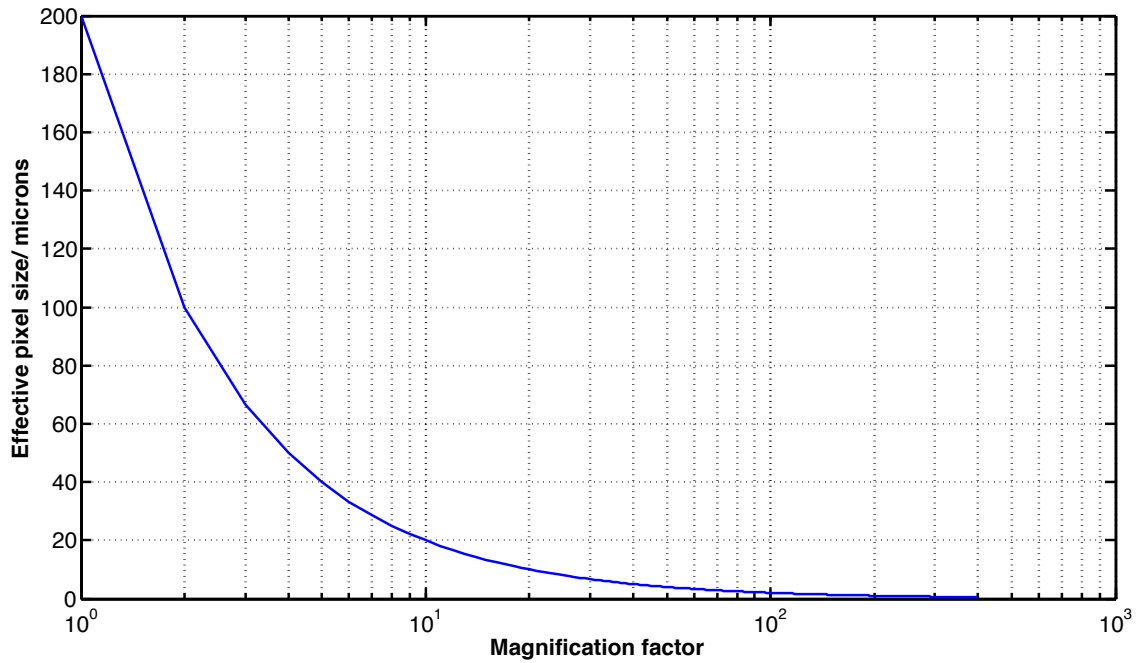


Figure 4.4: Effective pixel size vs. magnification.

Due to the geometrical magnification, the detector field of view decreases with increasing magnification. This relationship means that in general, the sample size must decrease with higher magnifications to stay within the field of view. There is also a practical reason in that the sample must also be able to rotate without hitting the X-ray gun. Figure 4.5 illustrates the maximum sample width which can be imaged within the FOV at various magnifications.

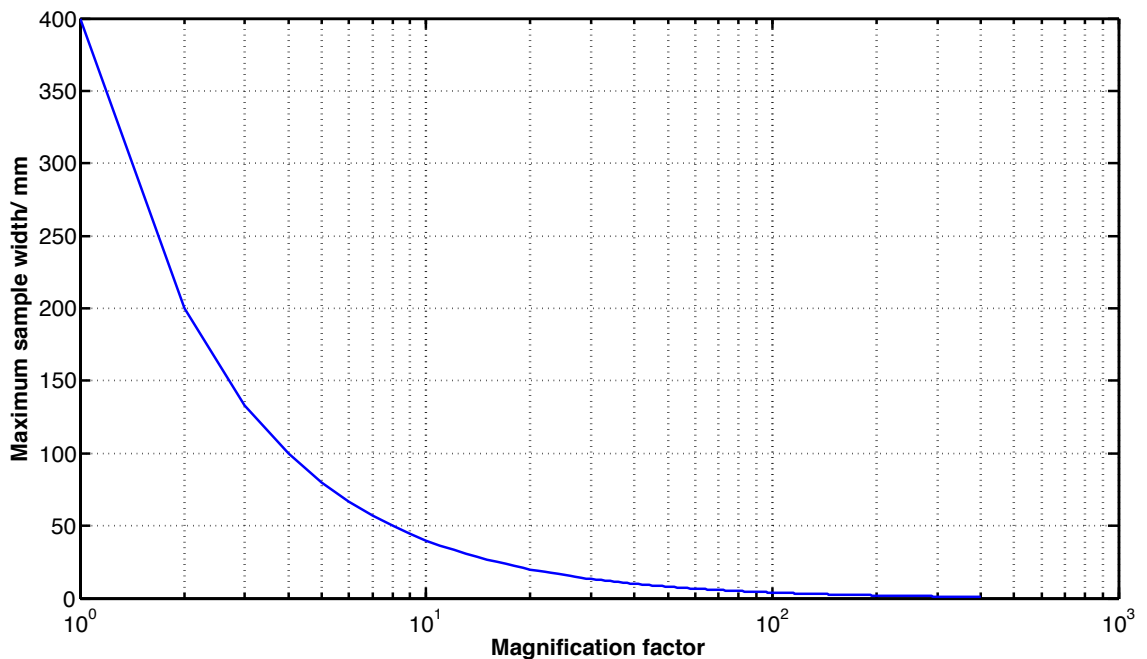


Figure 4.5: Maximum sample size vs. magnification factor.

### 4.2.1 System Calibration

In order to acquire accurate radiographs (and therefore accurate CT scans), several procedures must be carried out in order to ensure precise operation of the system. These are:

- Voltage conditioning
- Source-detector alignment
- focus optimisation

*Voltage conditioning* comprises stabilising the potential difference which generates the X-rays (by accelerating electrons onto the target material). The accelerating voltage is set to the maximum (225kV), and the ‘auto conditioning’ option selected. This generates a potential difference between the anode (X-ray filament) and cathode (target material), but does not apply a current to the filament, hence no X-rays are produced. X-rays can be generated effectively when the actual voltage reaches the maximum voltage and becomes stable.

*Source-detector alignment* involves setting geometrical alignment of the X-ray source and image detector so that the centre of the cone beam aligns with the centre of the detector. This is performed by placing a calibration rod into the sample holder on the sample manipulator, and taking radiographs at low and high magnifications. If the system is aligned correctly in the horizontal and vertical planes, a vertical edge in the centre of the radiograph will remain in the same position. Likewise, a horizontal edge placed at the horizontal centre of the radiograph will remain in the same position.

*Focus optimisation* ensures that the electron beam is focused on the target material correctly, resulting in the smallest possible spot size and sharp images. To carry out this procedure a printed circuit board with fine features (down to 5 $\mu$ m) is imaged at high magnification. Initially, course correction is performed by direct control of the magnetic steering coils inside the gun. Once a reasonable image is obtained, fine control can be used to optimise the focus at low, medium, and high voltages (typically 60, 120 and 225 kV). Interpolation is then applied by the Inspect-X software to apply focus correction at all voltages.

## 4.3 Theoretical Background to Dual Energy Imaging

### 4.3.1 Optimising Image Quality

The derivations in this section are collated from a range of sources and general imaging principles (Chesler *et al.*, 1977; Hughes, 1963) In order to achieve the best image quality in a CT scan, the signal-to-noise ratio of the projections must be maximised. Each spectral component of a polychromatic X-ray beam is exponentially attenuated (see section 2.3.2), resulting in the number of photons,  $N$ , reaching the detector being:

$$N(\lambda) = N_{ref}(\lambda)e^{-\int \mu_{abs}(\lambda,l)dl} \quad (4.3)$$

Where

$\lambda$  is the X-ray wavelength

$N_{ref}$  is the number of photons when no object is present (white reference)

$\mu_{abs}$  is the absorption coefficient

$l$  is the path length through the object

$N_{ref}$  takes into account the source spectrum and the detection efficiency at each wavelength. The number of photons detected at each wavelength can be modelled as a Poisson distribution, and since the sum of independent Poisson distributed random variables also follows the Poisson distribution, so does the total detected counts summed over all wavelengths:

$$N^{tot} = \int_0^{\infty} N(\lambda)d(\lambda) = \int_0^{\infty} d\lambda N_{ref}(\lambda)e^{-\int \mu_{abs}(\lambda,l)dl} \quad (4.4)$$

For a Poisson distribution with a mean  $N^{tot}$ , the standard deviation is given by the square root of  $N^{tot}$ , and the probability tends to a normal distribution.

The transmittance,  $T$ , of a polychromatic beam is given by:

$$T = \frac{N^{tot}}{N^{tot ref}} \quad (4.5)$$

The standard deviation for  $T$  can be calculated by combining the  $N^{tot}$  and  $N_{ref}$ , which for large photon counts is given by:

$$\sigma_T = \frac{T}{\sqrt{N^{tot ref}}} \sqrt{\frac{1}{T} + \frac{\sigma^{tot ref^2}}{N^{tot ref}}} \quad (4.6)$$

The reference image is taken as an average of multiple exposures to reduce the image noise in  $\sigma^{tot ref}$ . Next, the polychromatic absorbance,  $A$  is:

$$A = -\ln(T) \quad (4.7)$$

and has the standard deviation:

$$\sigma_A = \frac{\sigma_T}{T} = \frac{1}{\sqrt{N^{tot ref}}} \sqrt{\frac{1}{T} + \frac{\sigma^{tot ref^2}}{N^{tot ref}}} \quad (4.8)$$

The signal to noise ratio in a projection is therefore given by:

$$\frac{A}{\sigma_A} = -\sqrt{T} \ln T \frac{N^{tot ref}}{\sqrt{N^{tot ref} + T \sigma^{tot ref^2}}} \quad (4.9)$$

Using the FDK cone-beam reconstruction algorithm (Feldkamp *et al.*, 1984) involves the summation of absorbances after applying a Fourier filter, resulting in the reconstruction noise being highly dependent on the noise in  $A$ .

In a simple case where the white reference has the same noise as the projections:

$$\frac{A}{\sigma_A} = -\sqrt{N^{tot ref}} \ln(T) \sqrt{\frac{T}{1+T}} \quad (4.10)$$

The function in (4.10) varies with  $T$  as shown in figure 4.6. The optimum transmission for maximum signal to noise ratio is at  $T = 0.109$ , i.e. approximately 11% beam transmission.

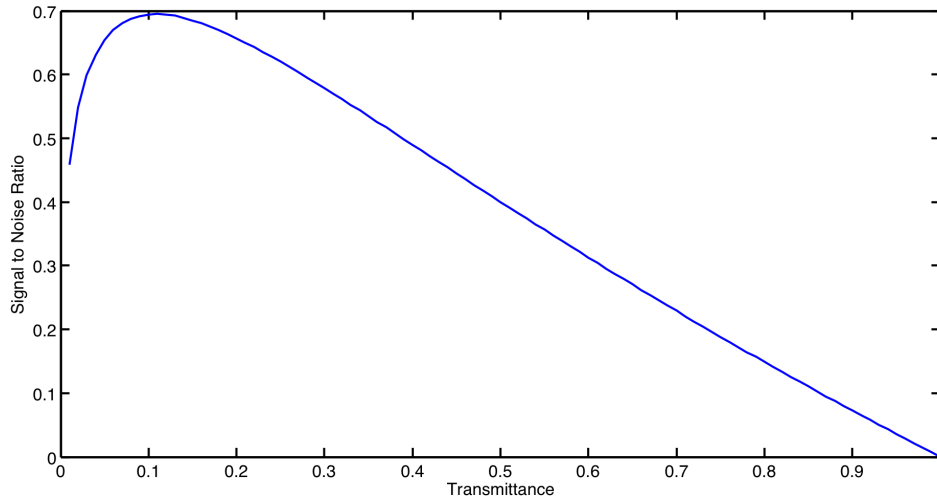


Figure 4.6: Theoretical variation of signal-to-noise ratio with beam transmission.

It can therefore be deduced that for an object with a high aspect ratio, the optimum SNR for the maximum and minimum material thicknesses would occur at drastically different beam energies. Combining two sets of radiographic projections, each optimised for a particular material thickness could potentially overcome the SNR problem.

### 4.3.2 Combining Multiple Projection Sets

The process of combining two projection sets into a single volume, often referred to as dual-energy imaging has been around for many years. The technique was originally

developed by Alvarez and Macovski (1976) to improve the contrast of biological structures in medical applications. Since then, most dual-energy developments have been in the medical field. Many medical CT systems now incorporate a dual source-dual detector arrangement so that both CT scans are performed within the same time frame, minimising patient dose.

The dual-energy technique relies on the decomposition of the linear attenuation coefficient at a specific energy,  $\mu(E)$  into a linear combination of basis functions (equation (4.11)). The following derivations are summaries of the dual-energy work performed by Alvarez and Macovski (1976); Gingold and Hasegawa (1992); Lehmann *et al.* (1981); Stonestrom *et al.* (1981). A further summary can be found in (Remeysen and Swennen, 2006)

$$\mu(E) = a_1 f_1(E) + a_2 f_2(E) + \dots + a_n f_n(E) \quad (4.11)$$

Where  $a_i f_i$  is the basis function for  $i = 1, 2, \dots, n$ . In the case of a dual-energy scan,  $i = 2$ , and the basis functions are the mass attenuation coefficients of the material under consideration at the two energies. Equation (4.11) therefore becomes:

$$\frac{\mu(E)}{\rho} = a_\alpha \frac{\mu_\alpha(E)}{\rho_\alpha} + a_\beta \frac{\mu_\beta(E)}{\rho_\beta} \quad (4.12)$$

where  $\rho$  is the density of the material,  $(\mu_\alpha/\rho_\alpha)$  and  $(\mu_\beta/\rho_\beta)$  are the mass attenuation coefficients at  $E_1$  and  $E_2$  respectively, and  $a_\alpha$  and  $a_\beta$  are the basis functions. The line integral of equation (4.12) is:

$$\int \mu(x, y, E) ds = A_\alpha \left( \frac{\mu_\alpha}{\rho_\alpha} \right) + A_\beta \left( \frac{\mu_\beta}{\rho_\beta} \right) \quad (4.13)$$

where  $A_j = \int \rho a_j(x, y) ds$ , with  $j$  referring to the basis functions  $\alpha$  and  $\beta$ .  $A_j$  therefore represents the length of material at each energy. In the case where the object is in the detector's field of view at all rotation angles, each pixel makes the same contribution in both scans, so the two scans can be combined to form a single CT data set. However, because the X-Ray source is polychromatic, beam hardening can give incorrect material lengths (more so at lower energies). To ensure each scan makes the same net contribution, the projection sets must be corrected for this beam hardening. Section 4.4 to 4.8 covers the procedure employed to deduce the beam hardening corrections required.

Previous applications of dual-energy CT have focused on optimising contrast between materials of different atomic no., however it is proposed that the same method can be used to compensate for the large variation in material thickness in high aspect ratio samples, using the same procedure.

Two cases for dual-energy scanning were tested in this work. Both were performed on a laminated composite plate measuring 89 x 55 x 2.8mm consisting of uni-directional carbon-epoxy plies. The plate had been impacted using a drop weight impact testing

machine at an energy of 12 J. Further information about the specimens and impact testing procedure can be found in Chapter 5 which covers the application of CT to imaging low velocity impact damage.

In the first case, two CT scans were performed at different energies. After correcting for beam hardening, the projection sets were combined into a single projection set, simply by summing and averaging the absorbances. This procedure is the same as that cited in equations (4.11) to (4.13). This method will be referred to as "**Case 1**" in the remainder of this work.

In the second case, the projections were again combined but this time a weighting factor was applied. The weighting factor gave a 90% weighting to the projection with the highest SNR. From section 4.3.1 we saw that the optimum SNR will depend on the fraction of transmitted X-rays, hence the low energy projections will be favoured when imaging the thin direction of a panel, and vice versa. In this second case, however, each pixel does not make the same contribution to the net absorbance at all projection angles. Therefore summing the projection sets does not give a correct result. To account for the weighting, one of the projection sets must be scaled to produce the correct thickness. This was achieved by experimentally deriving the linear attenuation coefficient of the material at each X-Ray energy on the Nikon 225kV CT system, which can then be used to scale the projections to the true thickness while maintaining the SNR. The specifics of the dual-energy CT experiment are provided in section 4.9. This method will be referred to as "**Case 2**" in the remainder of this work.

## 4.4 Manufacture of Step Wedges

In order to characterise the X-ray absorption properties in terms of attenuation and beam hardening characteristics, step-wedge panels were manufactured from both the MTM-45 UD and woven materials. The step wedge procedure is common practice in the X-ray field for characterising materials, and has been reported in several publications (Hammersberg and Mangard, 1998; Van de Castele *et al.*, 2004). The method involved manufacturing a component of the material under investigation which has steps of varying thickness which can be exposed to X-rays so that incremental path lengths can be imaged.

### 4.4.1 Panel Manufacture

Both materials studied in this work were supplied in pre-impregnated (pre-preg), uncured rolls 600mm wide. The materials are stored in a freezer to prevent curing. Rolls were stored at room temperature for 12 hours before removal from a sealed bag to prevent condensation build up. From these rolls, plies of 300mm x 300 mm were cut and laminated onto a flat steel tool surface which is coated with a polytetrafluoroethylene (PTFE) release film. For the panel with UD plies, each ply was laid down in an alternating orientation, symmetrical about the mid-plane of the laminate. Sixteen plies were used, resulting

in a lay-up of  $16:(0/90)_s$ . The plies of the woven material have both  $0^\circ$  and  $90^\circ$  fibre directions, so all plies are laid in the same orientation. Again, a total of sixteen plies were used.

To reduce the amount of porosity in the final plate, and aid laminate compaction, a de-bulking procedure was employed during lay-up. The laminate stack was covered with a perforated PTFE release film, nylon peel ply and nylon breather material. This stack was then covered with a de-bulking cover (a rubber sheet framed with aluminium and rubber base seals) and connected to a vacuum hose providing 0.08MPa vacuum. The laminate was de-bulked for ten minutes after the first ply is laid, and every 3 plies subsequently. Once all plies had been laid, the laminate stack was covered with the required vacuum bagging materials as shown in figure 4.7.

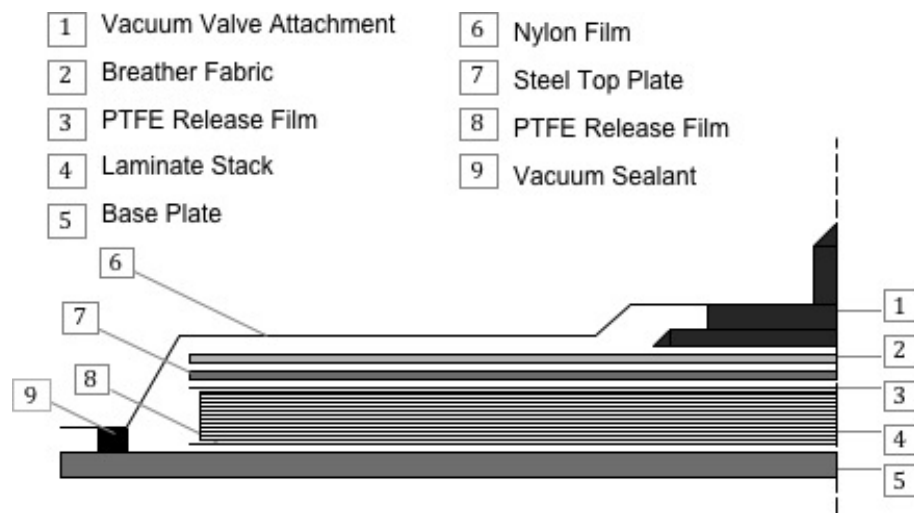
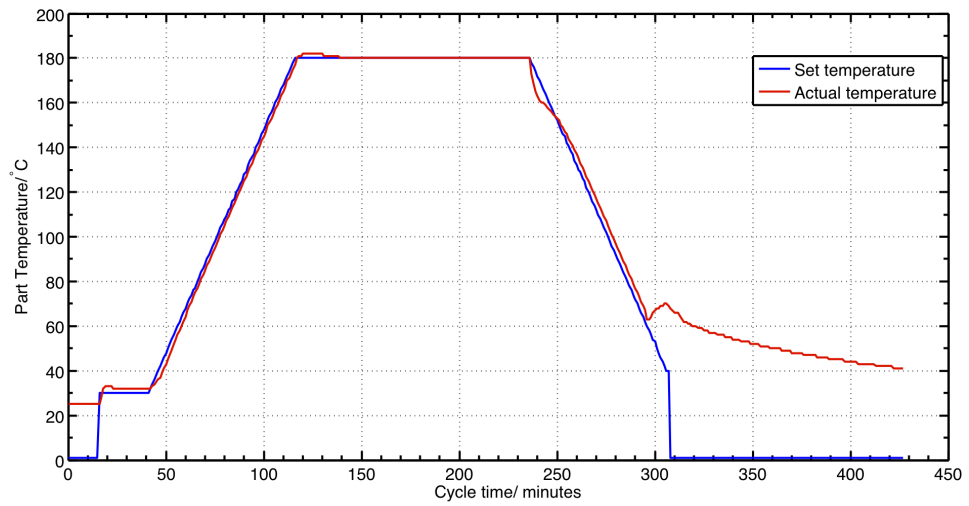
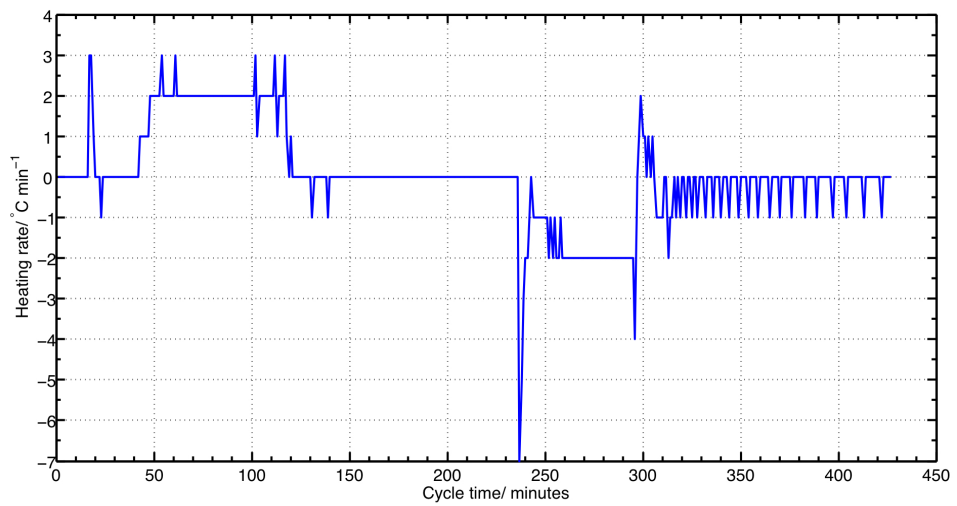


Figure 4.7: Vacuum bagging arrangement (Coenen, 2003).

The vacuum bagged panels were transferred into an autoclave for curing. This process applies heat and pressure to the laminate stack in order to consolidate the plies into a solid plate. Curing is the process of cross-linking the polymer network of the epoxy resin, in order to provide a solid medium through which stress can be transferred to the fibres. As both pre-preg materials used in this study comprise the same epoxy resin material, the step-wedge panels were cured together at a maximum temperature of  $180^{circ}$  and pressure of 0.7MPa (7 atmospheres). The heating rate was  $2^\circ\text{C}$  per minute. A thermocouple was taped to the vacuum bag inside the autoclave to monitor the part temperature during cure. The temperature-time relationship during cure, also known as the 'cure cycle' is shown in 4.8(a). The differential of the data in 4.8(b) gives the heating rate, which is shown not to exceed the manufacturer's specification of  $3^\circ\text{C}$  per minute at any point during the cure cycle. The cure cycle used was according to that specified by the material supplier.



(a) Cure cycle for consolidation of step-wedge plates. Set point (blue) and actual temperature (red)



(b) Heating rates throughout cure cycle shown in (a)

Figure 4.8: Cure cycle characteristics.

After removal of the solid laminates from the autoclave, both panels were sectioned using a diamond saw. The panels were sectioned in step-like increments ranging from 1mm to 256mm, each increment being double the thickness of the previous. Figure 4.9 is a photograph of the finished UD step-wedge.

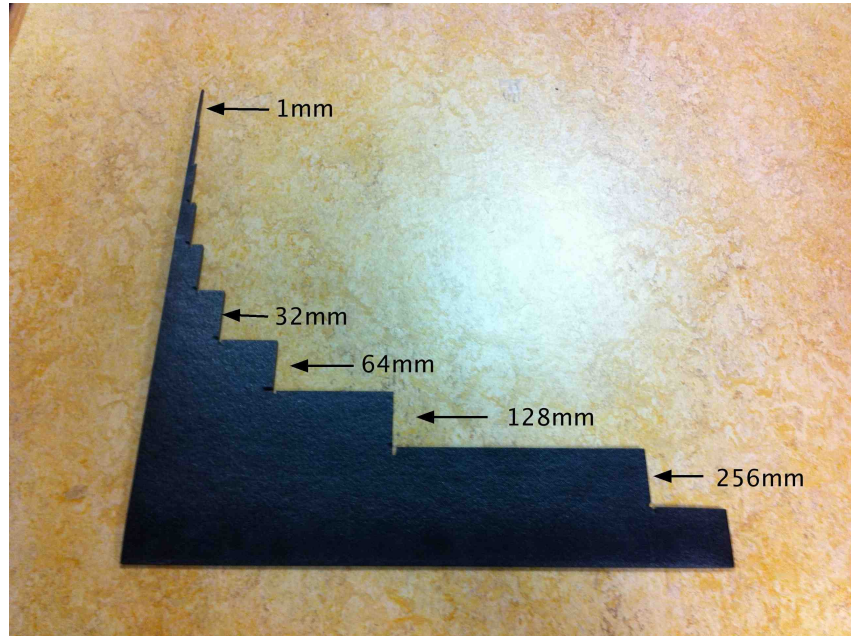


Figure 4.9: UD step-wedge.

## 4.5 Radiographic Imaging of Step Wedges

To quantify the response of the CFRP materials to X-rays, radiographs of each step-wedge were taken over a range of voltages with all four target materials (Cu, Mo, Ag, W). The step wedge was mounted on a sample holder fitted to the 5-axis manipulator gantry in the 225kV CT bay. The object was positioned with the long edge of the plate 5cm from the exit window of the X-ray source, so that only one step section was exposed during radiography. A schematic of the imaging set-up is shown in figure 4.10.

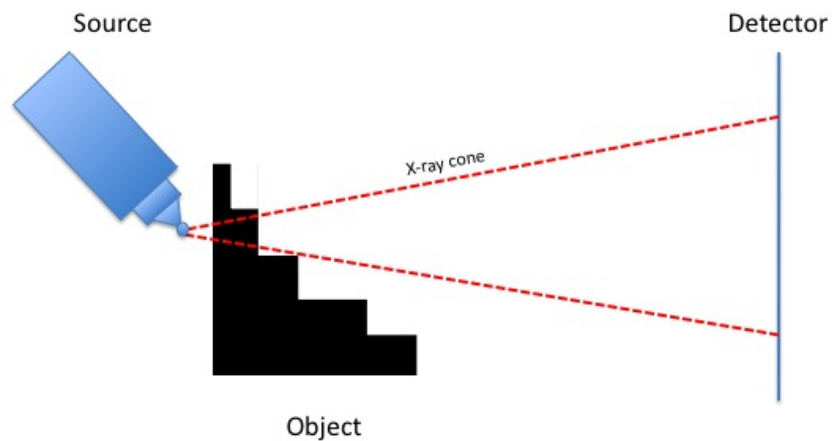


Figure 4.10: Schematic of step-wedge imaging experiment (not to scale).

Each step section was imaged from 20kV to 220kV in 10kV increments. It was found that to reduce noise to acceptable levels, the best approach was to image each step-section under the maximum possible exposure time of 4s, and average over 4 repeats per exposure. It was also found that all sections should be imaged at a given voltage, before increasing the voltage to the next value. This procedure was required due to image 'burn' which occurs under higher voltages. The detector was left to return to a stable condition for 10 minutes between voltage increments. Imaging conditions are shown in table 4.1.

A black reference image was collected before the detector had been exposed to any X-rays, using a 4s second exposure averaged over 4 frames with no detector gain. A white reference was also taken at each voltage increment under the conditions shown in table 4.1 but with no sample in the field of view.

Figure 4.11 gives examples of an 8mm section of the UD panel imaged under various voltages using the W target. The images are un-corrected, and so the outlines of the detector segments are visible, as well as the X-ray intensity variation over the detector area (bright in centre, reducing radially).

Table 4.1: Step-wedge imaging conditions.

Image Parameter	Value
Accelerating voltage	20kV-220kV
Filament current	250 $\mu$ A
Exposure time	4s
Frames averaged	4
Detector gain	off

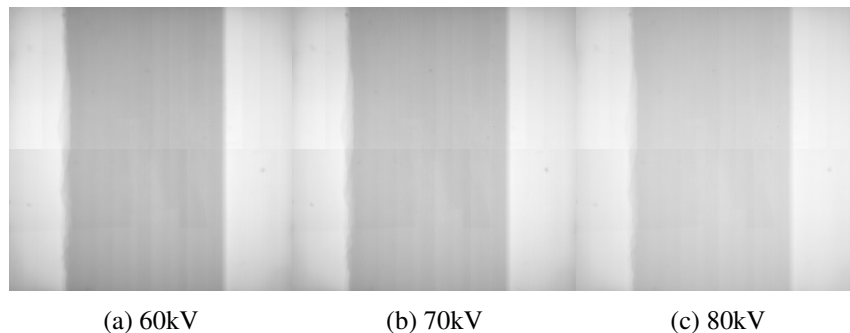


Figure 4.11: 8mm step-wedge section imaged under various voltages. These images are uncorrected, direct from the detector.

## 4.6 Image Analysis of Step Wedge Radiographs

Over 300 images were collected of each step-wedge sample, including black and white references. In order to deal with this amount of data, Matlab code was written to extract the necessary information from each radiograph.

The code performed the following operations on each projection:

1. Flat field correction
2. Calculation of transmittance
3. Calculation of absorbance
4. Calculation of linear attenuation coefficient
5. Calculation of signal-to-noise ratio in the absorbance image

The parts of the calculations which required values from the area within the object were performed on a crop from the central region of the projection. This technique was used to ensure measurements were taken through the actual thickness under consideration, as at increased thickness the rear surface of the step-wedge has a different magnification from the front. This results in a smaller area of the projection where the path length is at the value required. This principal is shown in figure 4.12.

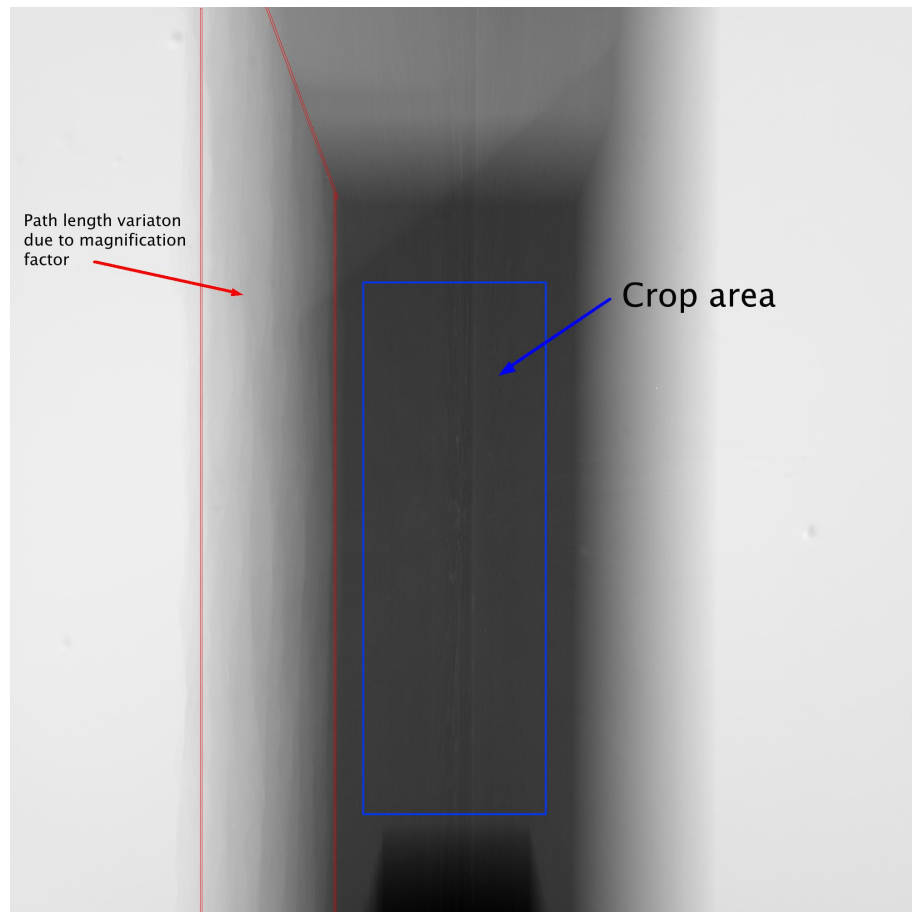


Figure 4.12: Radiograph of 64mm step section from UD step-wedge showing crop area for image analysis and magnification factor introducing variation of path length. Imaged using W source at 80kV and 200 $\mu$ A.

## 4.7 Step-Wedge Imaging Results and Discussion

Figures 4.13 to 4.16 show the transmittance curves for the Cu, Mo, Ag, and W targets respectively. The transmittance is the fraction of incident photons transmitted through the object, according to 4.14

$$T = \frac{I}{I_0} \quad (4.14)$$

Where

**T** is transmittance

**I** is the intensity of transmitted photons

**I<sub>0</sub>** is the intensity of incident photons

A transmittance value of 0 means that no photons penetrate the object, while a value of 1 means all photons pass through the object.

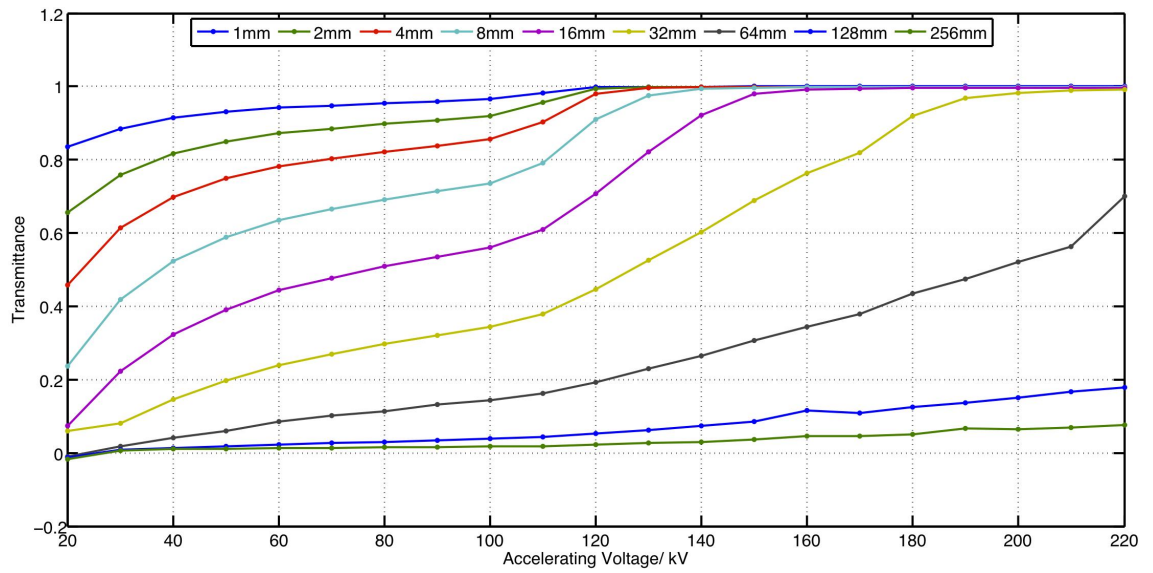


Figure 4.13: Transmittance vs. accelerating voltage for UD step-wedge using Cu target.

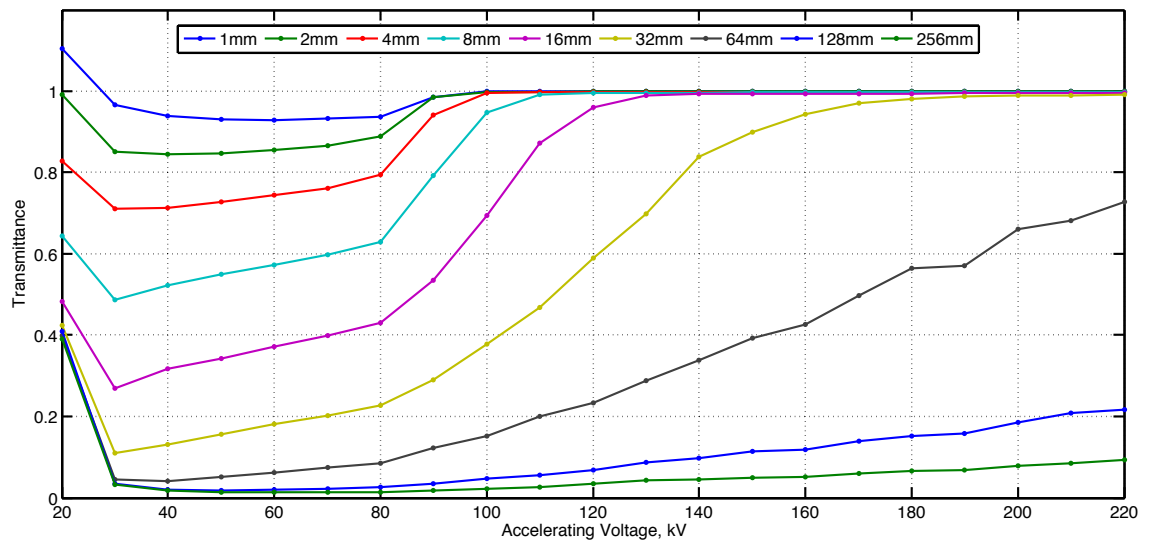


Figure 4.14: Transmittance vs. accelerating voltage for UD step-wedge using Mo target.

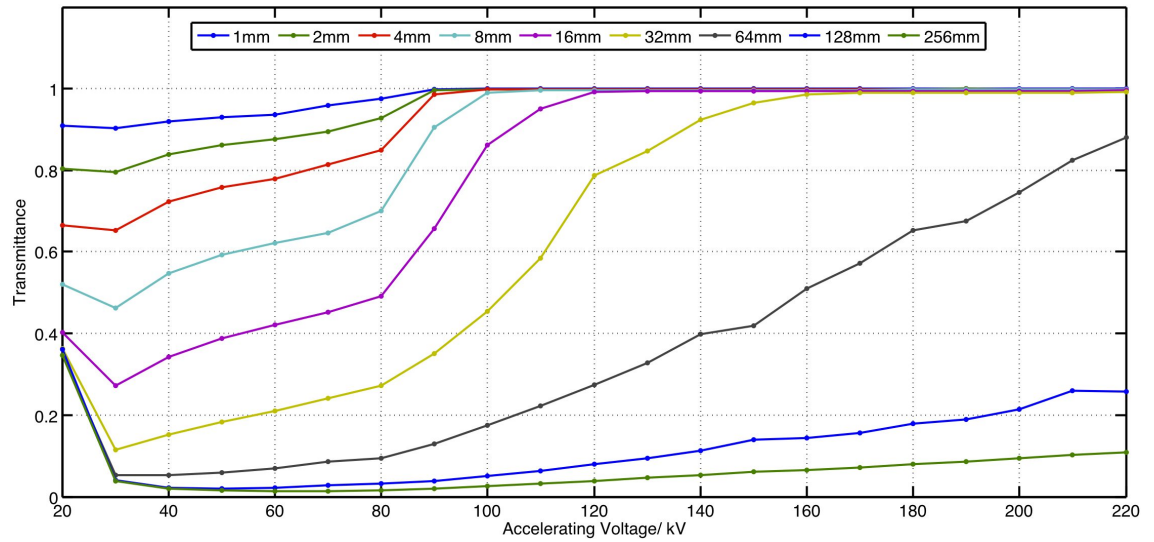


Figure 4.15: Transmittance vs. accelerating voltage for UD step-wedge using Ag target.

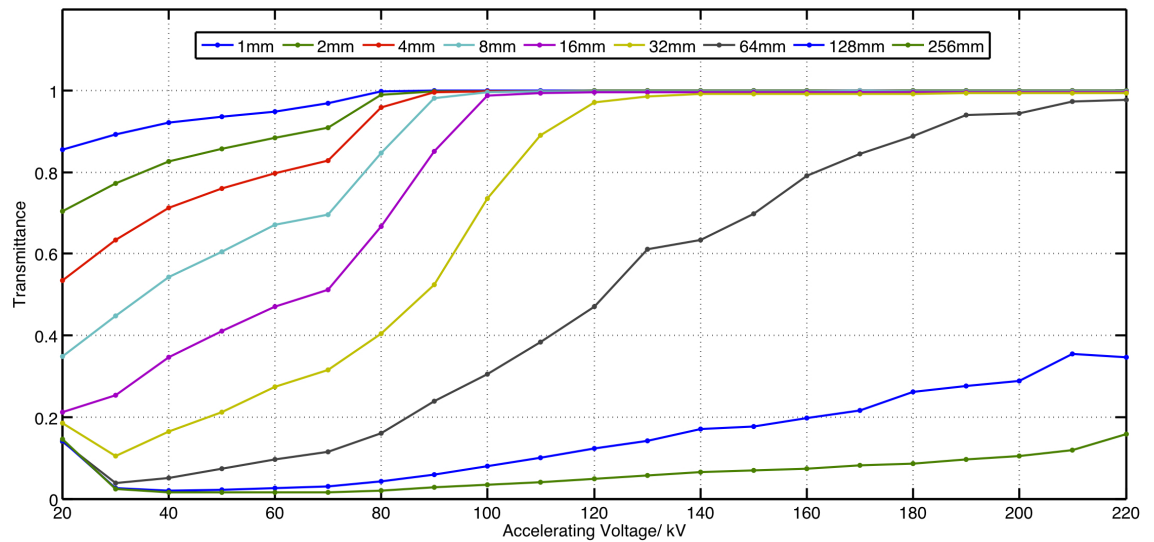


Figure 4.16: Transmittance vs. accelerating voltage for UD step-wedge using W target.

From the previous figures it can be seen that the transmittance data follow trends which would be expected from theory. In general, for a given thickness of material, the fraction of transmitted photons increases as the accelerating voltages increases. Likewise, the transmittance can be seen to generally decrease for a given accelerating voltage as material thickness increases. Many of the transmission lines appear to reach a transmittance value of 1, implying that all photons are penetrating the object. As the spectra at these energies still contain low energy photons however, it cannot be possible that all photons have been absorbed. The most likely explanation for this observation is that the detector has reached saturation under these conditions. When calculating the T values, the penetration is measured relative to the background counts ( $I_0$ ). Therefore when the penetration levels reach the detector saturation point, the transmittance will have a value of 1. In practice, however, this still limits the imaging capability at voltage-thickness combinations where  $T=1$  from the calculations, and the effective transmittance can indeed be said to be 1.

By plotting data sets from figures 4.13 to 4.16 together for the different target materials, the response of the material to the different X-ray spectra can be compared. Figures 4.17 to 4.19 compare the variation of the absorbance for the UD step-wedge over a range of voltages for the different target materials.

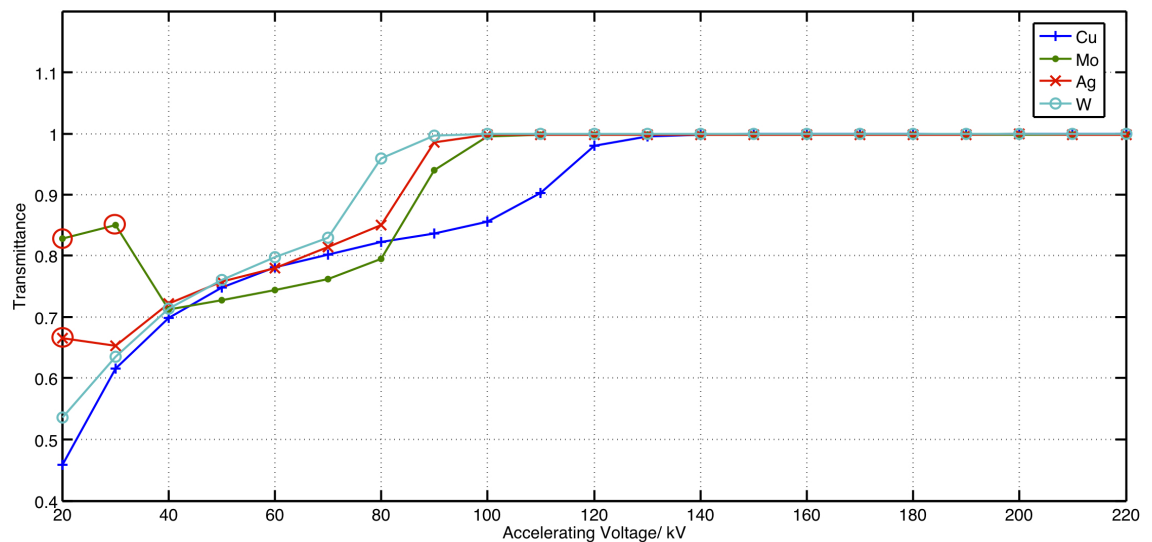


Figure 4.17: Variation of transmittance with accelerating voltage through 4mm of material for different target materials.

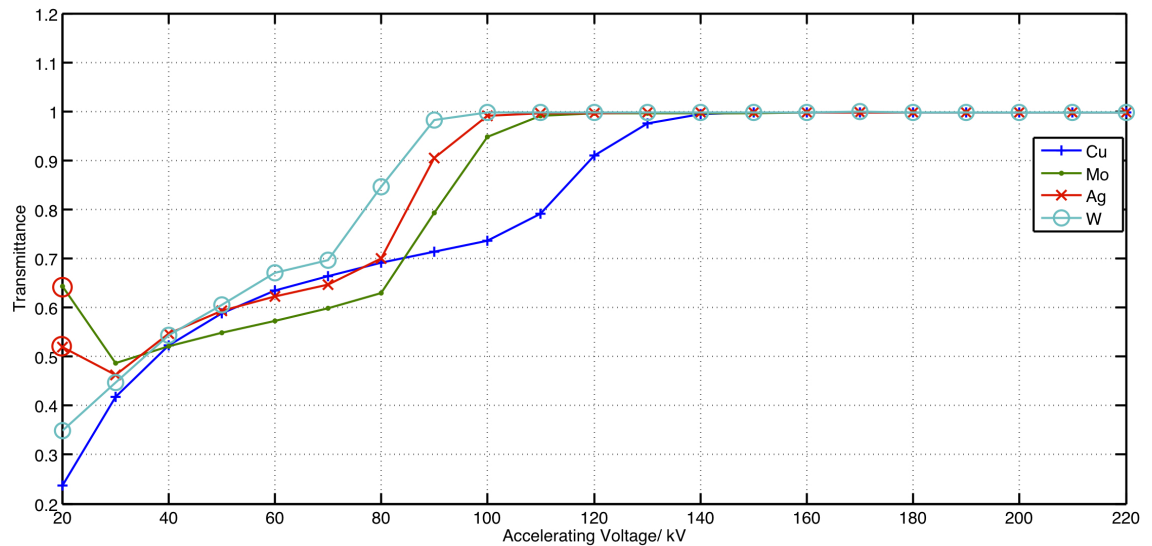


Figure 4.18: Variation of transmittance with accelerating voltage through 8mm of material for different target materials.

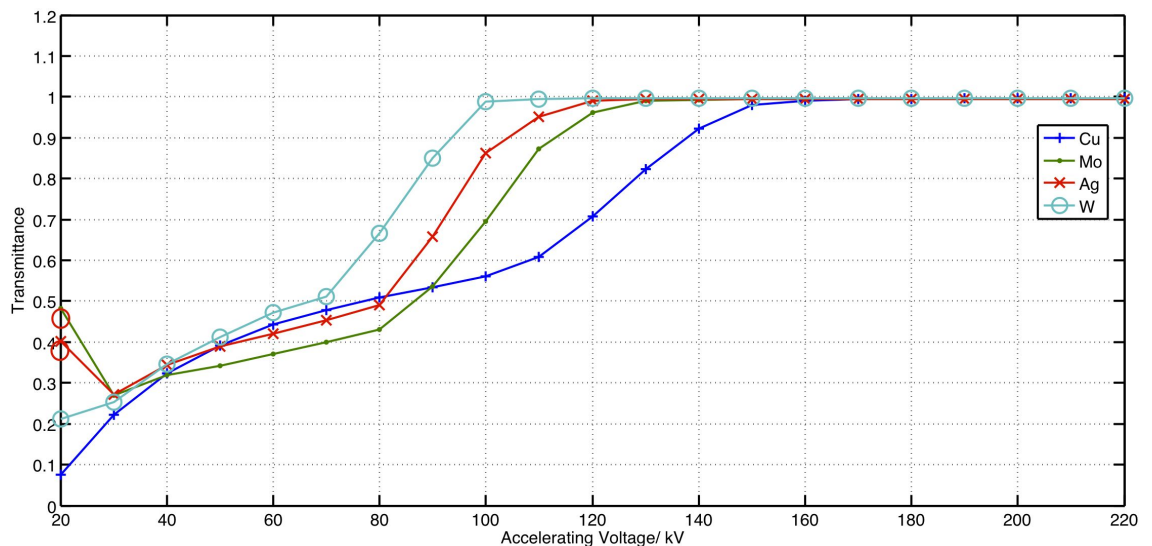


Figure 4.19: Variation of transmittance with accelerating voltage through 16mm of material for different target materials.

Up to accelerating voltages of approximately 70kV, the Cu, Ag, and W spectra show very similar transmission profiles, with the Mo target giving slightly lower transmittance. Above 80kV, however, the Cu target begins to show significantly lower transmittance compared to the other target material spectra. As seen in section A.5.2, at low energies the Cu and Mo spectrum have very similar characteristics. Although the Cu spectrum has fluorescence peaks at slightly lower energies than the Mo spectrum (8.0keV and 8.9keV compared to 17.4keV and 19.6keV), and therefore may be expected to show lower transmission, the Mo spectrum has a much higher flux at low accelerating voltages. This extra flux means that a higher proportion of the total flux are absorbed compared to the Cu spectra, resulting in lower T values. At higher voltages the Cu spectra were shown to

have a higher flux in the low energy fluorescence peaks compared with the Mo target, explaining why the transmission profiles are lower for the Cu spectra at higher voltages in figures 4.13 to 4.16.

Several anomalous transmittance values are seen in figures 4.13 to 4.16 at 20kV and 30kV accelerating voltages. These values are circled in red. These anomalous values appear to show increased transmittance values from what would be expected. It is proposed that these values occur due to the inefficiency of X-ray production at such low voltages. As a result of very low photon counts the image noise is very high and the white reference image has the same intensity as the black reference image resulting in no effect on the image when the sample is placed in the field of view. These values were not used in subsequent calculations of absorbance and linear attenuation coefficients for beam hardening corrections (section 4.8).

Further information can be obtained about the X-ray characteristics of the materials can be obtained by deriving the absorbance function,  $A$ , from the transmittance.  $A$  is given by:

$$A = -\ln \frac{I}{I_0} = -\ln(T) \quad (4.15)$$

The SNR of  $A$  is particularly important as reconstruction comprises the summation of absorbances. The values of  $A$  and associated SNR values were derived from the radiographic data using the Matlab code mentioned in 4.6.

Figure 4.20 shows an example of the variation of SNR with  $T$  for a 32mm section of the step-wedge imaged using the Cu target.

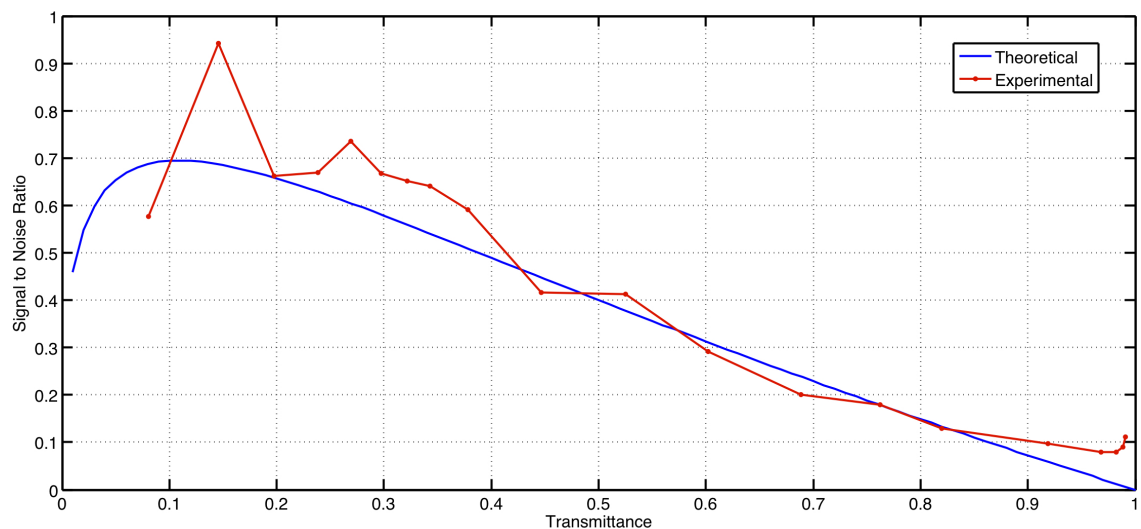


Figure 4.20: SNR vs.  $T$  for 32mm step-wedge section compared to theoretical prediction.

Figure 4.20 illustrates how the maximum SNR occurs at a transmittance of 14.5%, slightly above that predicted by theory (11%, see figure 4.6). By normalising the maximum value to 1, the figure shows that the measured values agree well with theory with

regards to the general fit of the data.

## 4.8 Beam Hardening Correction for CFRP Materials

A polychromatic X-ray source is used on the Nikon Metrology 225kV CT bay, resulting in beam hardening artefacts occurring during reconstruction. This concept was introduced in section 2.6.1. The average photon energy increases as the beam passes through the object, causing an underestimation of the linear attenuation coefficient towards the edges of the sample. This effect must be compensated for if a dual-energy CT scan is to be performed, so that the reconstruction algorithm can estimate the true thickness of material in each projection.

To achieve this, a beam hardening correction procedure using the data acquired from the step-wedge was used. This method uses a polynomial approximation to correct from a measured value of absorbance, to a correct value of absorbance, therefore allowing a correct approximation of thickness. Dainty and Shaw (Dainty *et al.*, 1976) demonstrated that a third-order polynomial can be successfully used to correct for beam-hardening of a polychromatic source. The procedure uses the roots of the polynomial to linearise the non-linear absorbance-thickness curve, an example of which is shown in figure 4.21 from experimental data (Cu target at 100 kV).

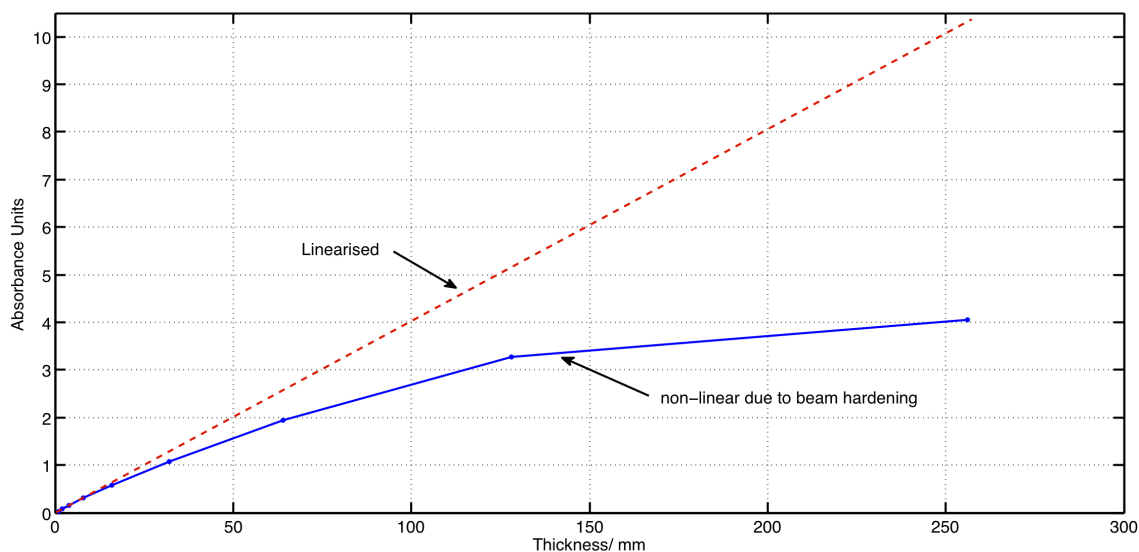
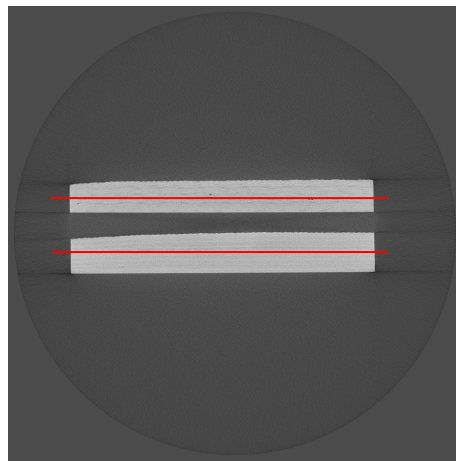


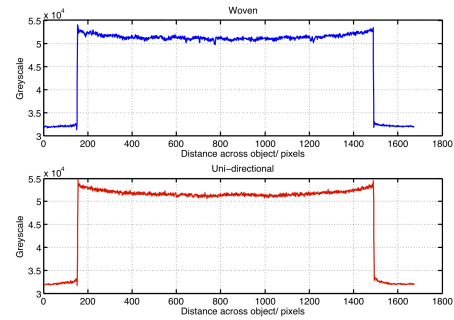
Figure 4.21: Beam hardening correction for Cu target at 100 kV.

In order to check the suitability of the beam hardening correction, three CT scans were performed on sections of the UD and woven step-wedges at 32, 64, and 128mm. The appropriate third-order polynomials were applied using Matlab to the projection sets, which were then reconstructed using CT Pro software. The following figures (4.22 to 4.24) illustrate CT slices from the un-corrected and corrected reconstructions for each thickness. Line profiles are plotted across the largest dimension of each sample to compare the effect

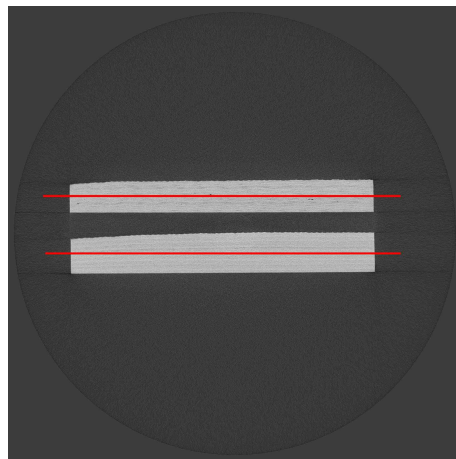
of the beam hardening correction.



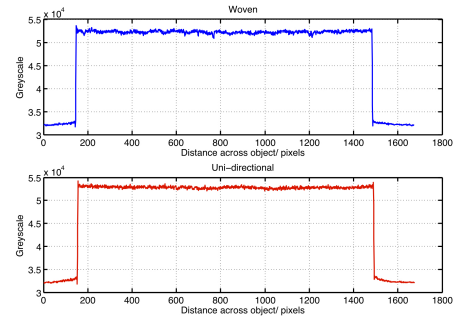
(a) Uncorrected woven (top) and UD (bottom) CT slice



(b) Line profiles across (a)

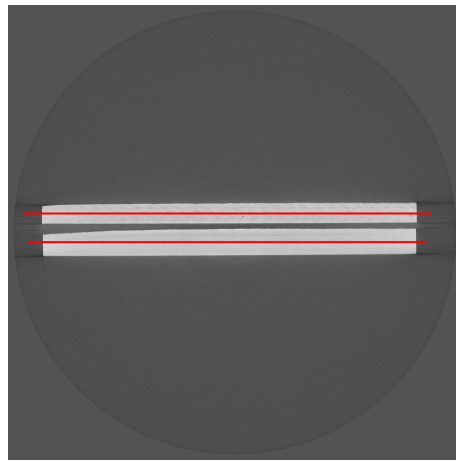


(c) Corrected woven (top) and UD (bottom) CT slice

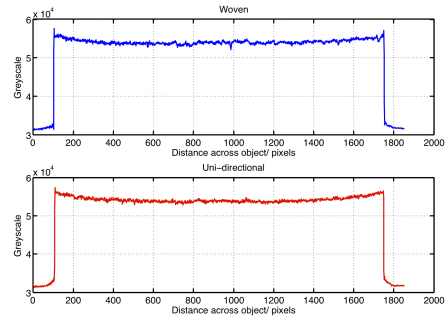


(d) Line profiles across (c)

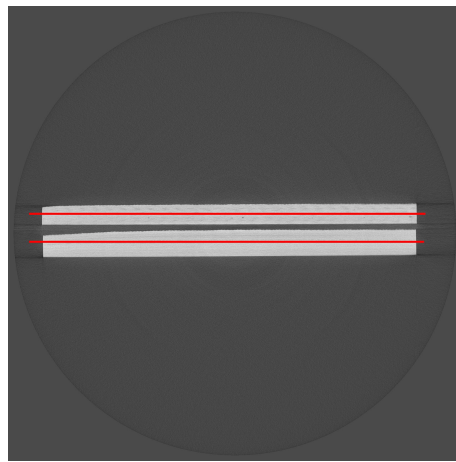
Figure 4.22: Illustration of beam hardening correction for 32mm step wedge sections. Imaged at 50kV.



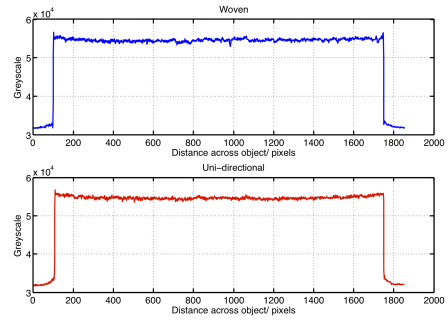
(a) Uncorrected woven (top) and UD (bottom) CT slice



(b) Line profiles across (a)



(c) Corrected woven (top) and UD (bottom) CT slice



(d) Line profiles across (c)

Figure 4.23: Illustration of beam hardening correction for 64mm step wedge sections. Imaged at 100kV.

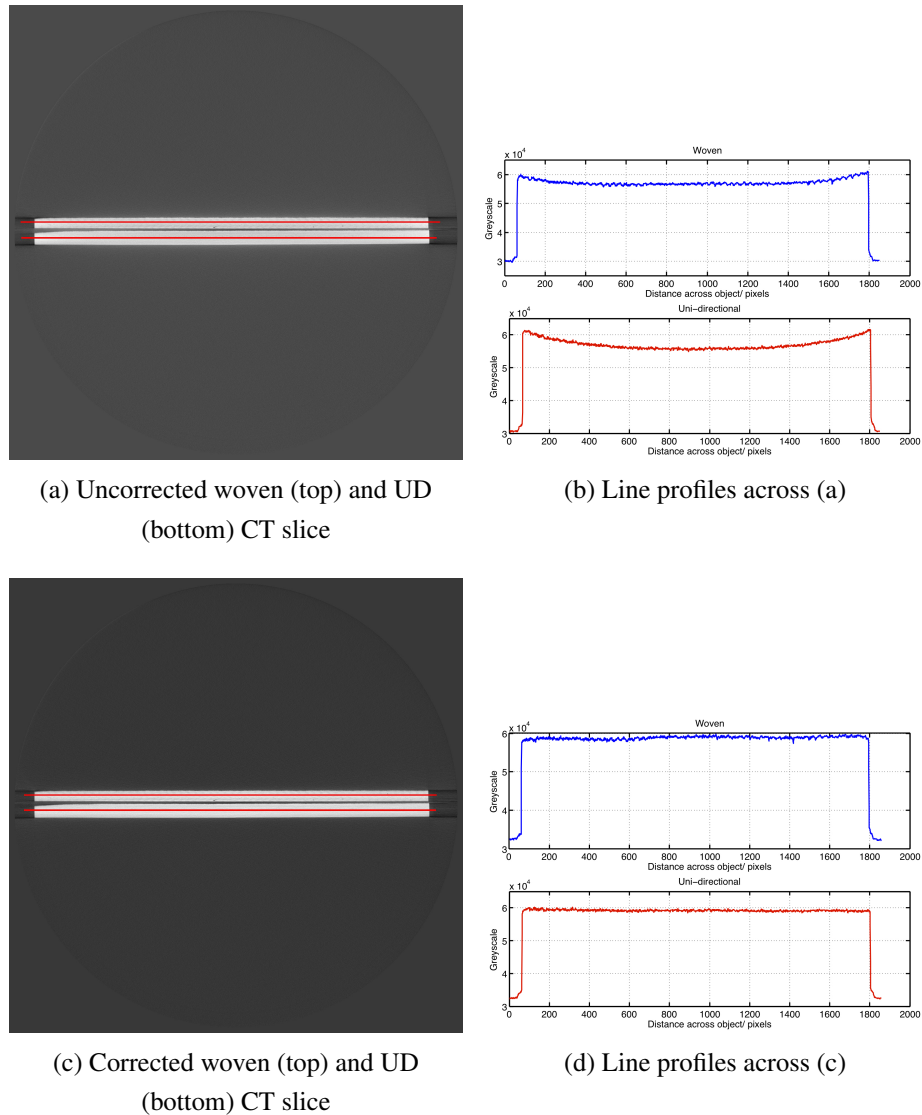


Figure 4.24: Illustration of beam hardening correction for 128mm step wedge sections. Imaged at 150kV.

In all three examples, the uncorrected images show reduced grey values in the centre of the objects due to beam hardening. As the above figures show, the beam hardening correction worked well for both materials across a range of thicknesses. By applying the appropriate correction polynomial this cupping effect was removed, restoring the central grey values to a correct value. In section 4.7 the data suggested that the absorption characteristics for both UD and woven materials were very similar. This observation is supported further by the beam hardening correction results, as by imaging the UD and woven sections together and applying the same correction, it can be seen that the correction works successfully for both materials.

## 4.9 Implementation of a Dual Energy Imaging Technique

This section describes how a dual-energy imaging procedure was implemented from observations made in the previous sections. This technique allows two CT scans performed at different energies to be combined, resulting in an optimised CT scan for high aspect ratio objects.

Section 4.8 showed the successful application of beam hardening correction parameters derived from the absorption measurements taking of CFRP step-wedge samples. In order to implement a dual-energy scan, these values are important as they allow two projection sets to be combined by correct deduction of the thickness of material from any radiograph. Effectively, two projections of a given material thickness taken at different accelerating voltages will give the same result by dividing the absorbance by the linear attenuation coefficient at each energy, if the attenuation is properly corrected for beam hardening:

$$t = \frac{A_{E_1}}{\mu_{E_1}} = \frac{A_{E_2}}{\mu_{E_2}} \quad (4.16)$$

where  $t$  is the material thickness,  $A_{E_1}$  and  $A_{E_2}$  are the absorbances at two different energies, and  $\mu_{E_1}$  and  $\mu_{E_2}$  are the linear attenuation coefficients at two different energies.  $A_{E_1}$  and  $A_{E_2}$  were determined experimentally, allowing  $\mu_{E_1}$  and  $\mu_{E_2}$  to be calculated according to (4.16)

By combining the absorbance images, and converting back into an artificial transmittance image (i.e. a radiographic projection) for all angular projections, two scans at different energies can be combined and reconstructed correctly.

### 4.9.1 Process Outline and Experimental

In order to produce a dual-energy CT scan, two individual scans are performed at accelerating voltages appropriate for the maximum and minimum material thicknesses for the object under investigation. The projection sets for each scan are then combined using a Matlab algorithm which was written by the author, this code can be found in Appendix B.

The code has a user interface which initially asks for the location of each projection set (referenced by the '.xtekct' file, which is produced by the data acquisition PC). The user then enters the coefficients of the appropriate beam hardening polynomials for each scan.

The code then loops through each angular projection for both scans, calculating an absorbance image and performing a beam hardening correction. As mentioned earlier, two cases of the dual-energy technique were applied. In *case 1*, the corresponding angular absorbance images were simply summed and averaged.

In *case 2* at each increment, the absorbance images were added with a weighting function applied in order that the projection with the highest signal-to-noise ratio is dominant.

A weighting of 90% was used. However, in this case, each voxel does not now make the same contribution to the final projection set (as mentioned in section 4.3.2). To compensate for this, the high energy projections were scaled by the linear attenuation coefficient to produce an absorbance which gave the same thickness as the low energy projection. This scaling therefore artificially reconstructs the true thickness of the object, as opposed to the absorbance value.

In both cases each dual-energy absorbance image is converted back into a new, dual-energy transmittance image (radiographic projection), and written to a new image file. This new projection set can be reconstructed using the commercial software CT Pro.

Figure 4.25 shows a graphical representation of the process of combining the CT projection sets using the case 2 approach.

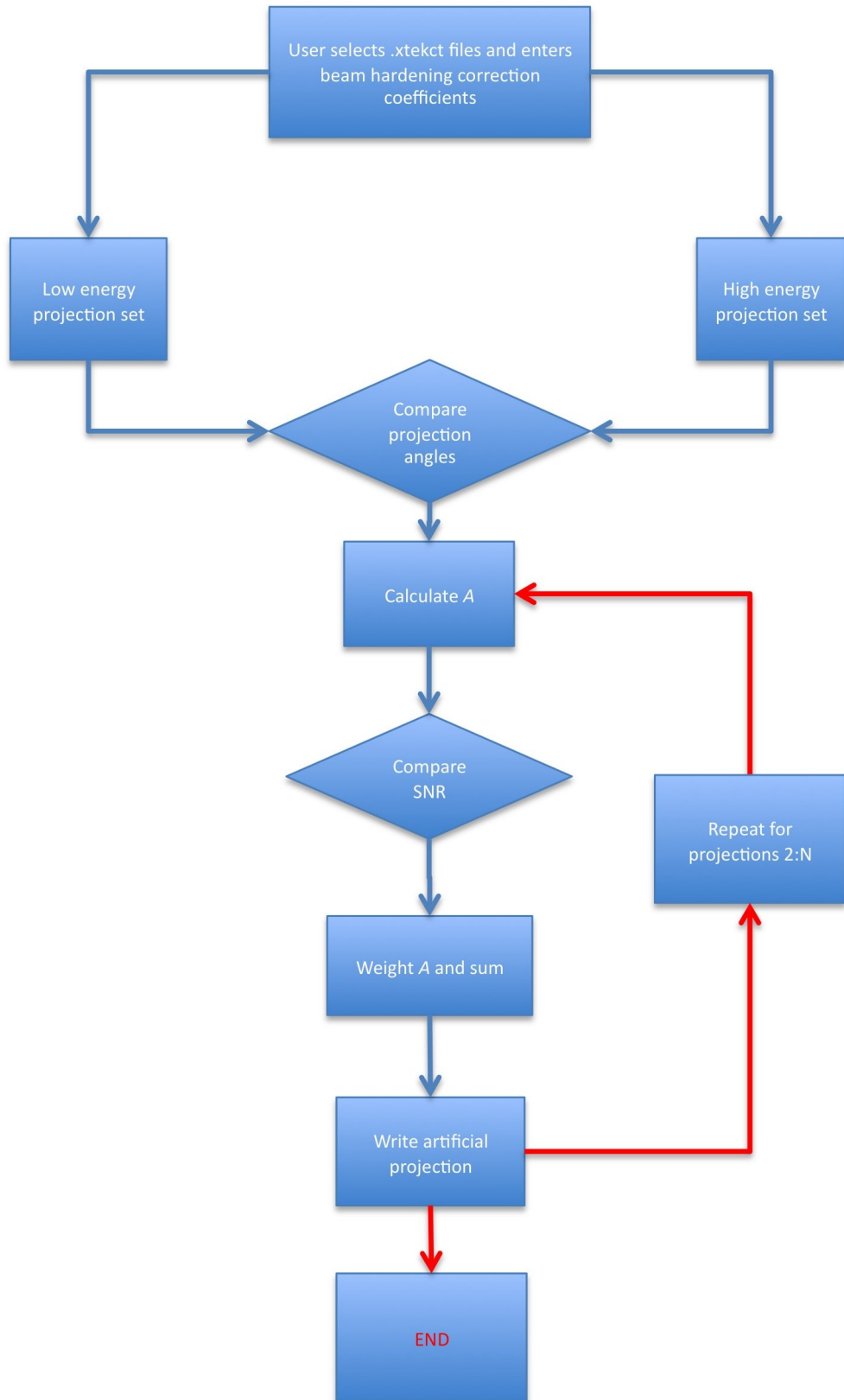


Figure 4.25: Process flow for combining two CT scans into a single, dual-energy projection set.

To test the effectiveness of the dual-energy approach, two objects were scanned under low- and high-energy conditions. Each object was also scanned a third time using 'compromised' beam conditions. The compromise conditions are obtained by ensuring a penetration level of at least 10,000 counts through the thickest object dimension without saturating the detector at any other projection angle (procedure according to Nikon Metrology User Manual).

The object imaged was an impact damaged sample of the same dimensions as the sample used for the damage tolerance study in Chapter 5.

The impact test sample was imaged at 40kV (LE), 110kV (HE), and 90kV (compromise). Scanning the impacted object allowed the algorithm to be tested on an object with internal features (i.e. cracks) and a high aspect ratio.

In order to simplify the procedure for this proof-of-concept stage, several assumptions about the object are made. These assumptions also reduce the amount of prior information which needed to be known about the sample, reducing the amount of experimental data which had to be acquired when acquiring the absorption data in 4.5. The assumptions are:

1. The material's response to X-Rays is isotropic and independent of ply orientation with respect to the beam path
2. The material is homogenous

No beam filtration was used in the dual-energy experiments performed in this work. This was to maximise absorption by maintaining low energy photons in the beam, but also to reduce the amount of beam hardening correction polynomials which had to be experimentally obtained.

## 4.9.2 Results and Discussion

Figure 4.26 shows the central reconstructed cross section of the impacted sample, under the three beam conditions studied (compromised scan, and the two dual-energy cases). Each image shows the regions from which image quality calculations were made (boxes 1 and 2) and the location of the line profile which is shown in figure 4.28. Boxes A, B, and C are shown at higher magnification in figure 4.27.

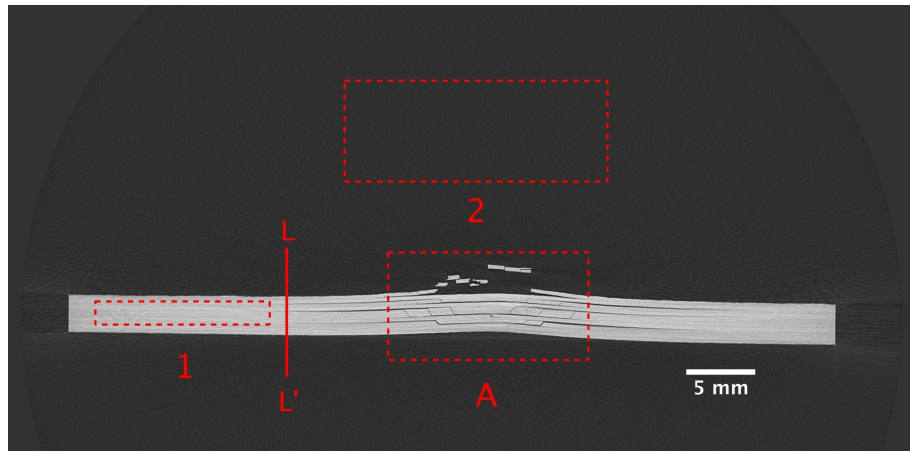
Apparent from the images is that both cases 1 and 2 give a geometrically correct reconstruction, i.e. they both reconstruct the thickness of the object correctly. As a result, the edges are sharp and the damage features are reconstructed correctly with no artefacts.

To compare the images, SNR and CNR were calculated from the areas outlined in figure 4.26. Five repeat scans were made under the same imaging conditions to obtain statistical significance.

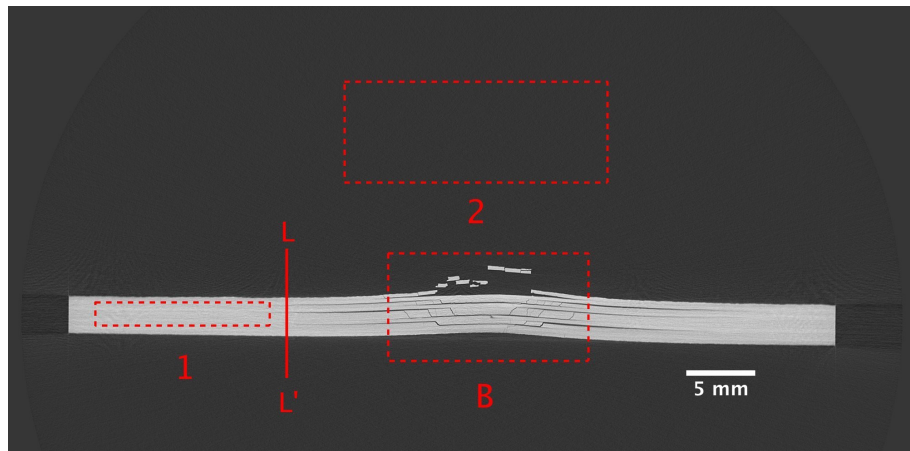
$$SNR = \frac{\bar{1}}{\sigma_1} \quad (4.17)$$

$$CNR = \frac{\bar{1} - \bar{2}}{\sigma_1} \quad (4.18)$$

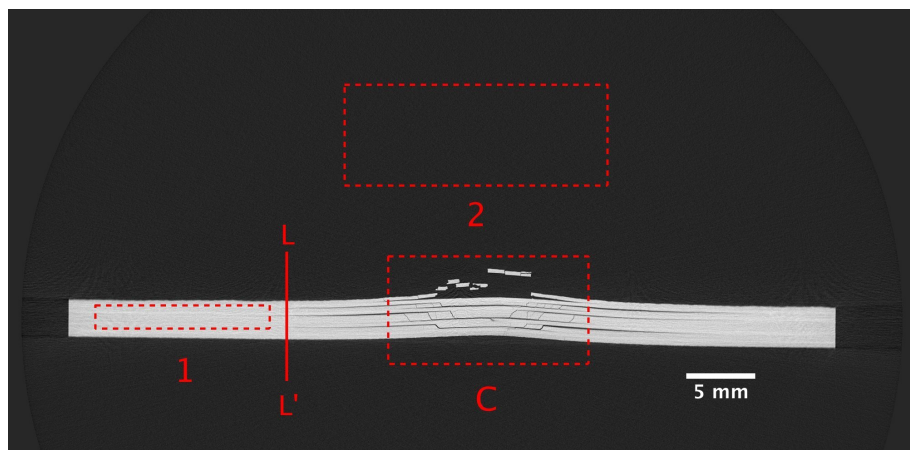
where  $\bar{1}$  is the mean pixel value in box 1,  $\bar{2}$  is the mean pixel value in box 2 and  $\sigma_1$  is the standard deviation of the pixel values in box 1.



(a) Compromise scan



(b) Dual energy case 1



(c) Dual energy case 2

Figure 4.26: Reconstructed cross sections for the compromised energy scan and the two dual-energy cases.

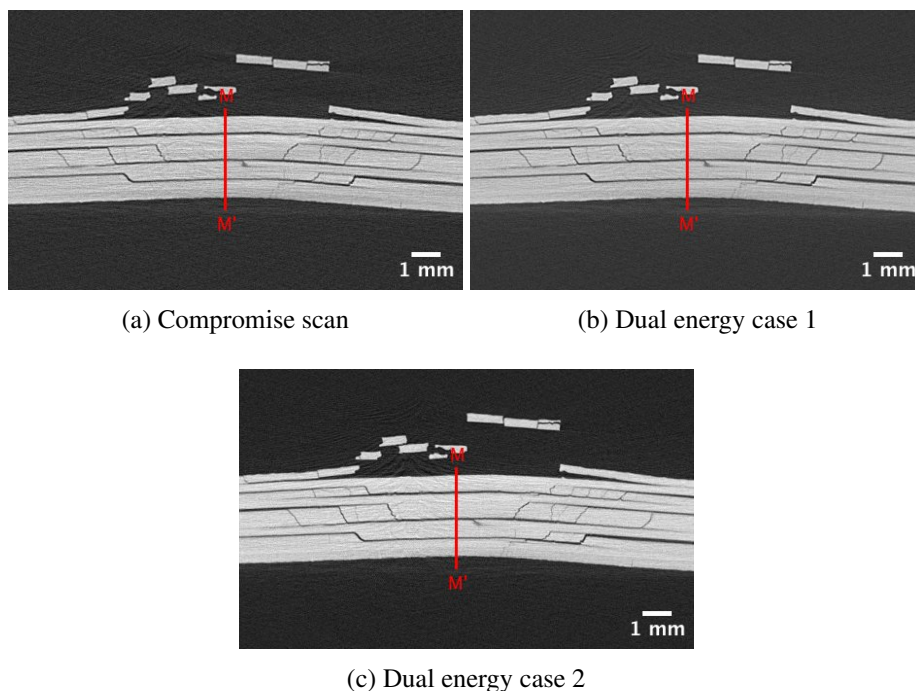


Figure 4.27: Zoomed views of selections A, B and C from 4.26

Table 4.2 gives the results of the image quality tests. It can be seen that both methods of dual-energy imaging have given an improvement in both SNR and CNR. Case 2, however, shows a much greater increase than case 1. Comparing case 1 with the compromised scan, a mean increase of around 20% and 30% in the SNR and CNR respectively are seen. It is likely that this image quality improvement arises from the fact that we are averaging over 2 projections when creating the dual-energy projection in case 1. As a result, background noise becomes smoothed giving an increase in SNR and CNR. In case 2, we are still averaging over 2 projections, but the SNR and CNR see a much larger increase; 66% and 109% respectively. This implies that both the noise and contrast have both been improved significantly in case 2. By weighting for the low thickness in many of the projections, the absorption is kept high giving good contrast, and likewise for the high thickness projections.

Table 4.2: Image quality results for the compromise and dual-energy cases.

Beam Condition	SNR	CNR
Compromise	9.42 ( $\pm 0.81$ )	3.87 ( $\pm 0.88$ )
DE case 1	11.48 ( $\pm 0.63$ )	5.56 ( $\pm 0.78$ )
DE case 2	15.70 ( $\pm 0.56$ )	8.09 ( $\pm 0.65$ )

The results given in table 4.2 are demonstrated by the line profiles across MM' from figure 4.27. Figure 4.28 shows that although case 1 gives slightly better image quality, the contrast between the object and background is not improved. As a result, the damage is

no more apparent within the object- the troughs in the line profile are virtually identical in the compromised and dual-energy case 1 scans. In case 2, however, the contrast between object and background is significantly improved. This results in the line profile troughs at the damage interfaces becoming much more pronounced.

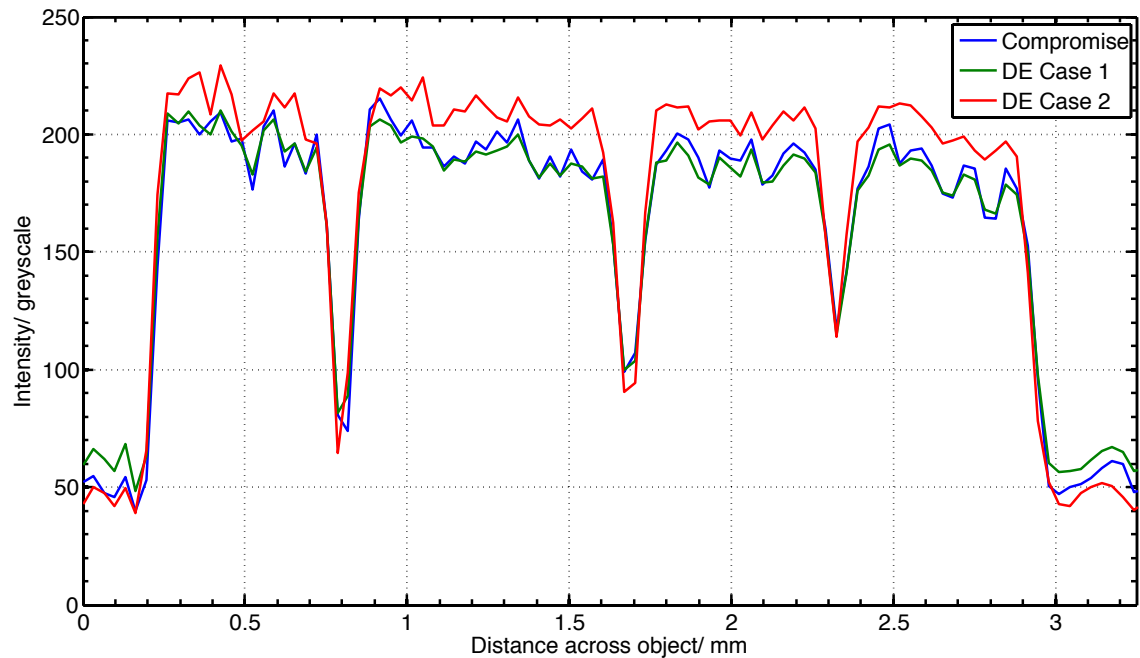


Figure 4.28: Line profiles across MM' from figure 4.27.

By applying an image threshold based on the background greyscale in each image (figure 4.29), it is apparent that the compromise scan produces a much noisier threshold, which includes pixels which are not damage. This noise is reduced in case 1, and even further in case 2.

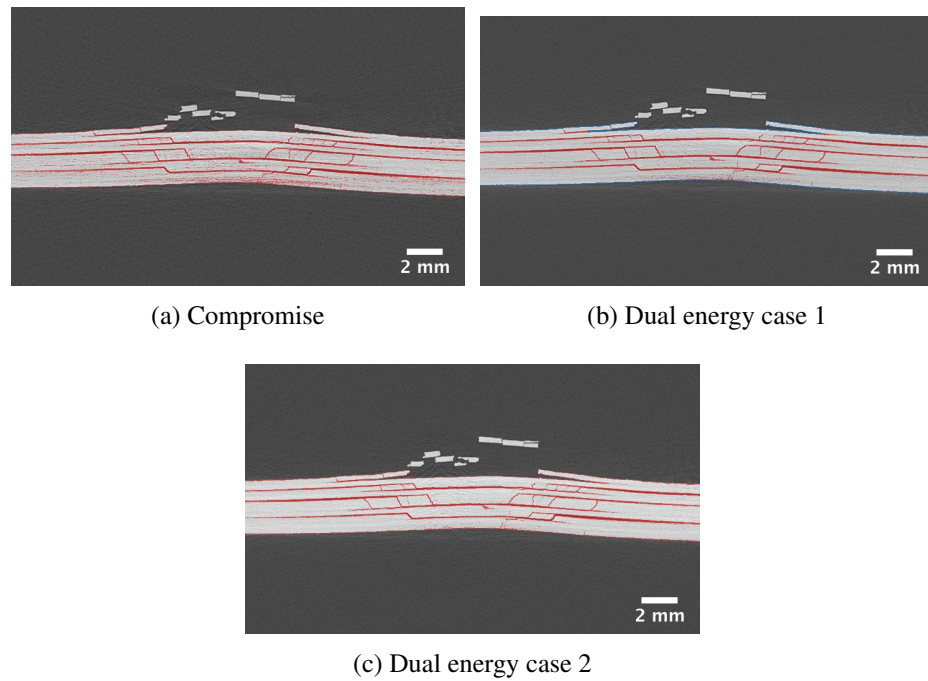


Figure 4.29: Resulting damage threshold when applying a threshold to the object equivalent to the background grey level in each case.

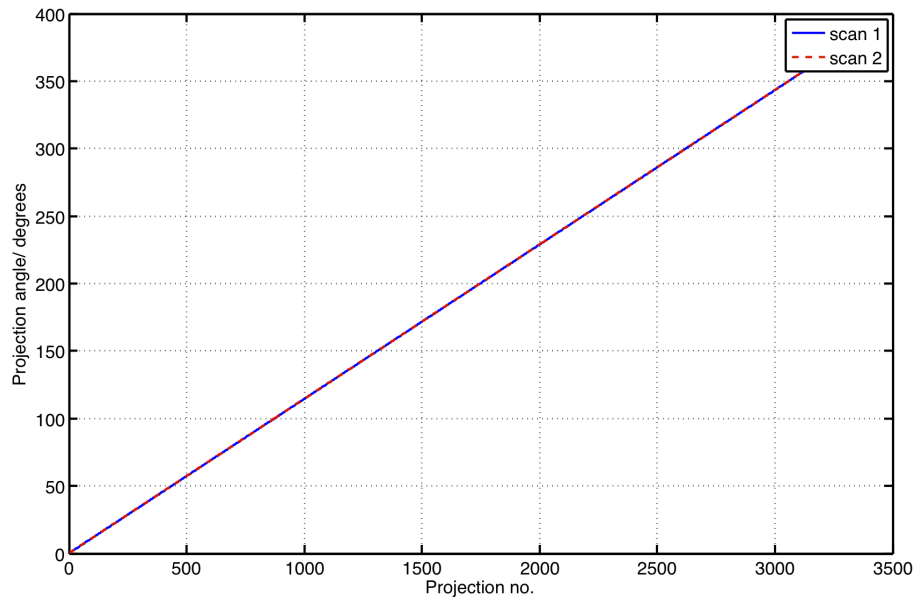
Although the noise in figure 4.29 is not particularly severe, applying noise reduction image filters could also remove some of the damage pixels. Although manual interaction is generally always necessary when segmenting such complex damage features (as will be seen in Chapter 5), any reduction in noise during the acquisition is extremely useful.

Consideration should also be given to whether the imaging experiments described represent a fair comparison between the compromised and dual energy cases. Specifically, this consideration arises because the dual energy cases are combining two projections per radiograph, compared to only one for the compromise case. For case 1, two radiographs were combined and averaged, while in case two the projections were combined on a weighted contribution. From the experimental data it was observed that case 2 gave the best improvement in image quality under the conditions investigated. This method used a weighting of 90% in favour of the image with the highest signal-to-noise ratio. Therefore only a small contribution from the second image was averaged into the dual energy data set. It could feasibly be proposed that the comparison is therefore valid, and that the dual energy approach would give a more efficient signal-to-noise ratio for high aspect ratio objects, as opposed to increasing scan times by using multiple averaged frames per projection, increased exposure time or higher numbers of projections. For completeness however, it would be of use to perform a full test matrix comparing all possible combinations against a dual energy case, although this would take a significant amount of time.

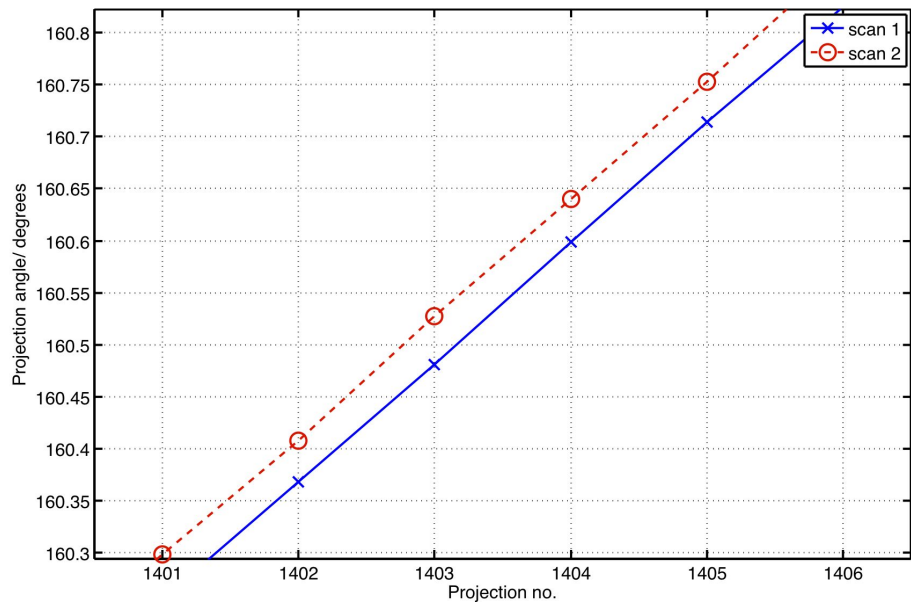
#### 4.9.2.1 Effect of Projection Misalignment

As the dual-energy procedure requires performing multiple scans, each projection set to be combined must have equivalent angular projections to prevent image blurring when summing the absorbance images. To ensure this agreement occurs, the rotation motor was calibrated to a very high number of projections by running a CT scan (with no sample) to 8000 projections. The Inspect-X acquisition software can then automatically correct the error in the rotation.

Plotting the rotation angle versus projection number for two consecutive scans using 3142 projections and 2s exposure time, shows that a slight angular error still exists between the two scans. Figure 4.30 illustrates the data for two consecutive scans. The maximum error was found to be  $0.06^\circ$ .



(a) Projection angles for two CT scans



(b) Zoomed in view of (a)

Figure 4.30: Angular data for two consecutive CT scans under the same imaging conditions.

For the sample sizes investigated in this section, however, this error seems to have no effect on the image quality. All features within the impact damaged object appear to be reconstructed as sharply in the dual-energy scan as for the conventional scans.

#### 4.9.2.2 Large Panels

Once it had been shown that the dual-energy method would work on the CFRP test coupons, it was hoped that the method could be applied to a panel with an extremely high aspect ratio. This would be a worst case scenario, where the degradation in SNR caused by the aspect ratio could cause problems in detection and/or image segmentation of any

defects. In order to test the dual-energy method, a defect panel supplied by the National Physical Laboratories (NPL) was imaged using a compromised energy setting, with a filtered high energy X-Ray spectrum and the dual-energy method. The panel was manufactured from uni-directional plies of carbon fibre reinforced epoxy in a quasi-isotropic lay-up. The panel contained polymer inserts as defects which varied in shape and size. Figure 4.31 is a photograph of the panel.

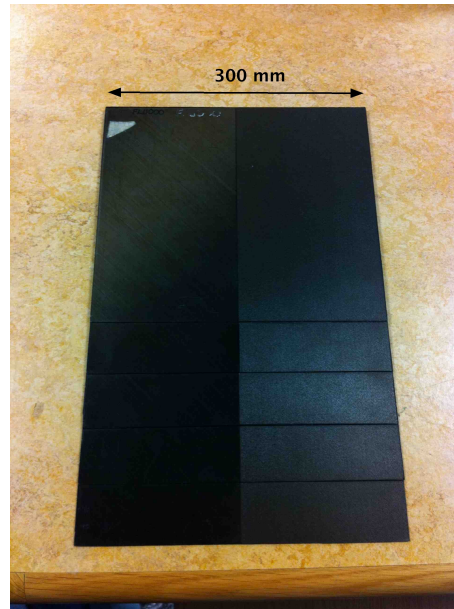


Figure 4.31: Photograph of NPL defect panel.

The panel was imaged using beam settings which were compromised for the high and low thickness directions, as well as under dual-energy conditions. Table 4.3 gives the settings used in each scan. No filtration was used in the dual-energy scans as the beam hardening corrections deduced from the absorption measurements (section 4.6) were based on an unfiltered beam.

Table 4.3: CT settings for dual-energy imaging of NPL panel.

Image Parameter	Compromise scan	Low energy scan	High energy scan
Accelerating voltage / kV	140	40	200
Target material	W	W	W
Current / $\mu\text{A}$	150	250	100
Filtration	2mm Cu	none	none
Exposure time/ s	2	2	2
No. frames per projection	1	1	1
No. projections	3142	3142	3142
Angular rotation/ degrees	360	360	360

Figure 4.32 shows reconstructed in-plane cross sections from the NPL panel. The defects were visible, but the SNR was very poor due to the use of a high energy, filtered

beam. Although it was possible to segment the defects to a certain degree, a lot of manual interaction and operator judgement was required. Due to time constraints, the defects in this panel have not been quantified in this work, but merely act as a demonstration tool.

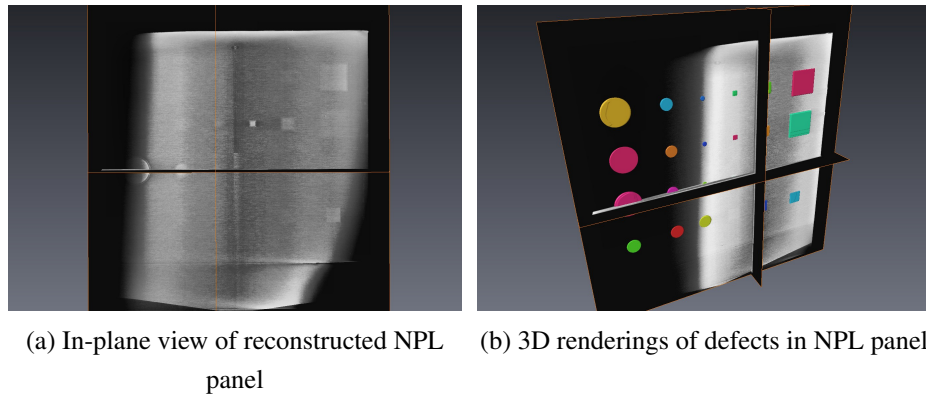
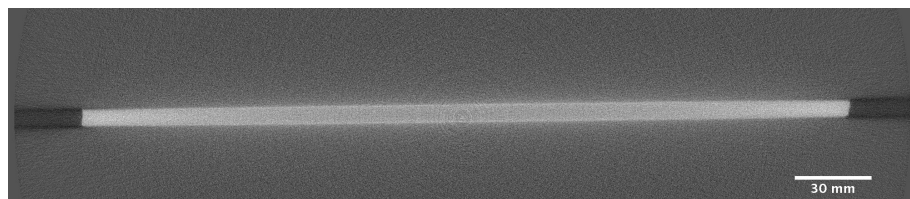
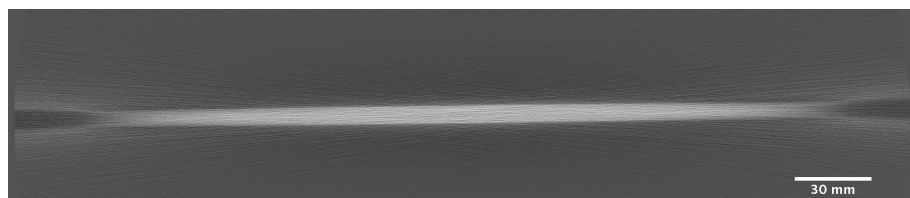


Figure 4.32: Reconstructed images of compromised scan of NPL panel.

Figures 4.33 (a) and (b) show reconstructed cross sections from the compromised and dual-energy scans of the NPL panel. It can be seen that the dual-energy scan has not accurately reconstructed the geometry of the object. Additionally, the SNR within the compromised scan has a distinctly poor SNR in the centre, where the signal appears to be barely higher than the background signal. The dual-energy scan has failed to reconstruct the object due to divergence of the beam hardening correction at such large material thicknesses found in the NPL panel. Figure 4.34 gives an example of this error. The polynomial which models the absorbance becomes badly fitting at high thicknesses and high accelerating voltages. As a result, applying beam hardening corrections to thick objects gives an incorrect reconstruction.

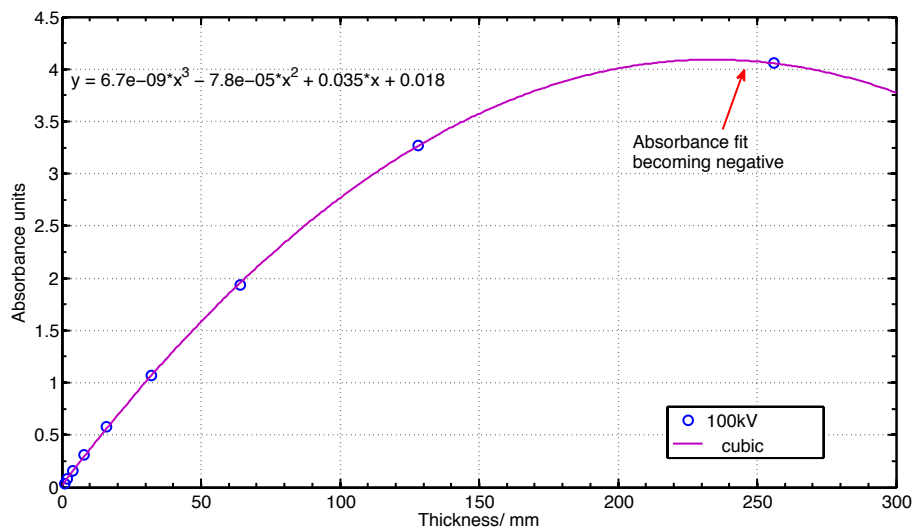


(a) Compromised scan

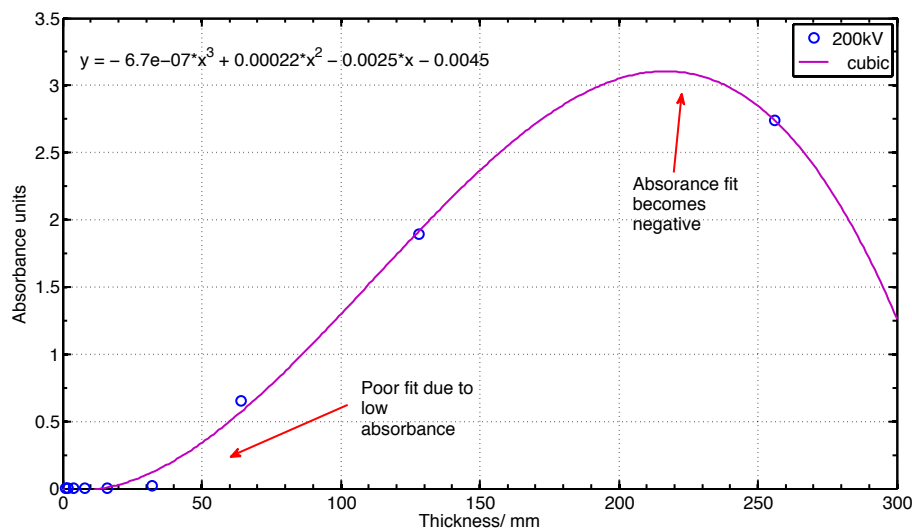


(b) Dual energy scan

Figure 4.33: Reconstructed cross sections of NPL panel.



(a) 100kV



(b) 200kV

Figure 4.34: Variation of absorbance with thickness in MTM-45 CFRP and associated third-order polynomial fits for beam hardening correction with the tungsten target material.

Figure 4.34(a) shows good polynomial fit with the data until 128mm. Approaching 256mm, however, the fit starts to give a reduced absorbance value. Physically this is impossible, and must mean the polynomial fit breaks down at these high thicknesses. Forecasting forward to 300mm gives a significantly incorrect absorbance value. Figure 4.34(b) results in errors at both ends of the thickness scale at 200kV. At low thickness, the almost total transmittance of the X-Ray beam results in almost zero absorbance, meaning the polynomial becomes badly fitting in the range where the beam is being significantly attenuated. This low thickness error then propagates to an even worse fit at higher thicknesses than was seen in (a), even though the voltage is higher and hence beam hardening should occur to a lesser extent.

## 4.10 Chapter Summary and Conclusions

The work presented in this chapter has demonstrated the first application of a dual-energy CT imaging to high aspect ratio CFRP plates on a laboratory X-Ray CT system.

By imaging a step-wedge made of the material of interest, an effective beam hardening correction procedure based on absorption measurements was demonstrated. A third-order polynomial beam hardening correction procedure worked well for the materials under investigation. The beam-hardening investigations also revealed that better radiographic image contrast can be obtained by proper target selection during CT scanning. For example, at higher energies the Cu target was shown to produce a spectrum which was attenuated to a much greater extent than the other target materials.

Two cases of dual-energy imaging were proposed, both of which improved the SNR and CNR in the sample geometry of interest (an impact test coupon). Case 1 provided an increase of 20% and 30% in the SNR and CNR respectively. Case 2 provided an increase of 66% and 109% in the SNR and CNR respectively. However, the first case (a simple summation) did not improve absolute contrast between the object and background. The second case did improve the image contrast significantly due to the optimised projection weighting, which was dependant on the material thickness and SNR in a particular projection.

Although the technique worked well for small coupons where the maximum X-Ray path length was less than 100 mm, the difficulty in deducing appropriate beam hardening correction values at larger thicknesses prevented the dual-energy imaging of very large (300 mm width) objects. In the case of the NPL panel, a better image was achieved by filtering a moderately high energy beam and using a high filament current to generate high X-Ray flux.

The method shows potential for imaging large CFRP objects, provided a better beam hardening approximation can be developed. This could be achieved experimentally by imaging a step-wedge with larger thickness (perhaps up to 500 mm), to allow better polynomial correction curves to be calculated. Including filtered beam measurements in this experiment would also expand the range of energies and thicknesses the procedure could be applied to. A modelling approach to the beam hardening, using the energy sensitive spectra measurements (Appendix B) could also be used to improve the results.

## CHARACTERISATION OF LOW VELOCITY IMPACT DAMAGE TOLERANCE OF CARBON FIBRE REINFORCED PLASTIC

### **5.1 Introduction**

This chapter presents a study on the impact damage tolerance in two commonly used aerospace CFRP materials, and the use of X-Ray CT to characterise and quantify that damage. The literature shows no examples of systematic quantification of impact damage in CFRP using laboratory CT systems.

Damage was induced using the drop-weight impact method, a common procedure for assessing the impact damage tolerance of fibre reinforced composite materials. Post-impact behaviour was quantified by the miniaturised Hogg and Prichard compression after impact (CAI) test (Prichard and Hogg, 1990). Industry standard non-destructive investigation using ultrasonic C-scan was used to quantify the nature of the damage in terms of location and size. These results were then compared to damage information obtained from CT imaging.

Mechanical testing in the form of the interlaminar shear test was used to relate material properties to the damage tolerance of each material, as well as to account for differences in performance between the two materials.

A method for quantifying damage in CT data sets is presented, which shows good correlation with C-scan data. The types of damage identified using CT, and the measurements made also agree well with published literature on the subject.

The aims of this chapter were therefore:

- To characterise and damage in CFRP materials subject to low velocity impact damage
- To develop a CT data processing methodology to allow quantification of impact damage
- To compare CT damage results to ultrasonic C-scan

## 5.2 Materials

Two materials commonly used to manufacture primary structures in aerospace applications were studied. These were pre-impregnated MTM-45 uni-directional (UD) , and pre-impregnated MTM-45 plain woven materials, supplied by Advanced Composites Group (Derbyshire, UK). Both materials use carbon fibres as the reinforcement. The matrix is a toughened epoxy resin. The materials were chosen as they act as a baseline for the use of CFRP in aerospace structures. Compared to more recent material developments such as 3D woven, or stitched material, the microstructures are relatively simple and potentially more simple to characterise using CT. Table 5.1 gives some material data.

Table 5.1: Selected material properties for MTM-45 from material supplier's data sheet.

Property	Uni-directional	Woven
Fibre type	IM7	AS4 plain weave
Areal weight/ gsm	280	193
Cured ply thickness/ mm	0.28	0.21
0°Tensile strength/ MPa	1500	904
0°Tensile modulus/ Gpa	120	64
90°Tensile strength/ Mpa	15	858
90°Tensile modulus/ Gpa	6	61

## 5.3 Panel Manufacture

All test coupons used in this study were manufactured according to British Standard BS 1268 (British Standards, 2001)(British Standards, 2005). Panel lay-up was carried out as described in section 4.4. Plies of each pre-preg material were cut using an automated ply cutter to reduce fibre misalignment.

To produce enough impact test coupons for statistically significant results, two 300 x 300 mm panels for each material were manufactured. Each panel consisted of 10 plies. For the UD material, ply angles of 0°and 90°were used, giving a complete lay-up of  $[(0/90)_2/0]_s$ . The woven panels also consisted of 10 plies, but as this material was plain woven each ply contains both 0°and 90°fibre orientations, hence each ply was laid up in the same orientation to give a  $[0/90]_{10}$  laminate.

The laminate stack was de-bulked for 5 minutes after the first ply was laid down, and after every 3 subsequent plies. In total, therefore, 4 de-bulks were carried out giving a total de-bulking time of 20 minutes. This procedure reduces the amount of entrapped air in the laminate stack, which would lead to severe porosity and poor consolidation of the laminate if not removed.

All four panels were cured at the same time, within the same vacuum bag, to ensure manufacturing conditions were equivalent for all test pieces. The same cure cycle as mentioned in section 4.4 was used, i.e. 2 hours at 180°C and 7atm. The resulting mean laminate thicknesses were 2.73 mm ( $\pm 0.12$  mm) and 2.22 mm ( $\pm 0.02$  mm) for the UD and woven materials respectively.

Once the laminates were cured, impact test coupons measuring 89 mm x 55 mm were sectioned from the cured panels using a diamond saw. Although there is no official standard for the miniaturised impact samples used in this work, the samples were cut so that edge parallelism was within the tolerance of British Standard 18352 (0.02 mm) in order to prevent sample buckling during the compression after impact test.

## **5.4 Drop Weight Impact Testing**

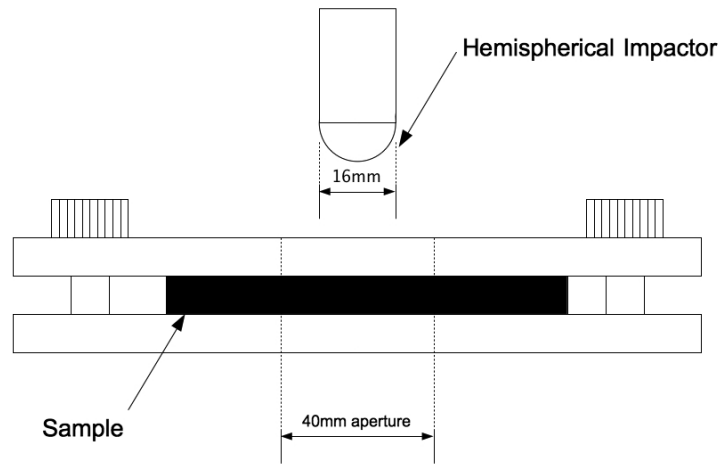
In order to induce damage in the sample materials a drop weight impact testing machine was used to deliver a low velocity impact. In these tests, the maximum velocity of the impactor was approximately 2m/s for an impact energy of 12 J, where the impactor weighs 4.3 kg. Samples were tested over a range of energies up to 12 J to simulate the type of impact energies thin laminates experience during service, such as tool drops.

### **5.4.1 Drop Weight Impact Experimental Procedure**

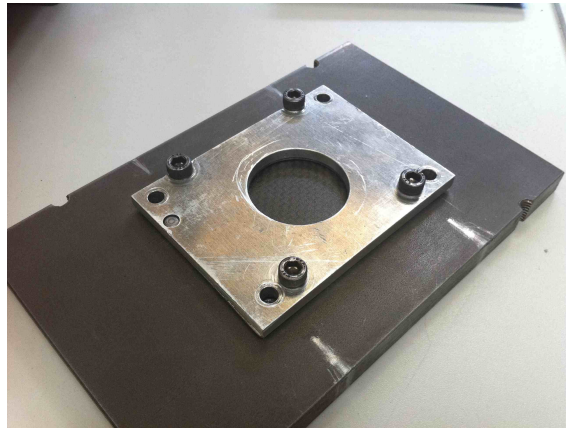
Impact testing was performed using the Instron CEAST 9350 drop weight impact testing machine. This equipment consists of a tower which holds a variable mass impactor. The impactor may have different shaped 'tups' fitted which form the contact point between mass and sample. In this work, an impactor mass of 5 kg and a hemispherical tup of 20 mm diameter were used. The sample is clamped at the bottom of the tower by a rigid holding device which consists of steel plates, clamps, and a 40 mm circular aperture. Figure 5.1 is a photograph of the impact tower, and figure 5.2 illustrates the dimensions of the sample holder.



Figure 5.1: Instron CEAST 9350 drop weight impact testing machine.



(a)



(b)

Figure 5.2: (a) Schematic showing impact test conditions, adapted from (Prichard and Hogg, 1990). (b) Photograph of sample holder containing a woven plate.

The impact testing machine is fitted with several instruments which allow test data to be acquired, such as light sensors and force transducers. These allow impactor velocity, force and test time durations to be acquired. The equipment is also fitted with an anti-rebound device to prevent repeated impacts of the sample. Although strain gauges were not attached to the samples, it is assumed that the forces measured in the impactor are representative of the forces experienced by the sample due to the very high stiffness of the impacting object and test rig.

Impacts were performed at 3, 6, 9 and 12 J for both the UD and woven samples. Five samples were impacted at each energy.

## 5.4.2 Results and Discussion

Figure 5.3 shows typical force-time relationships at an impact energy of 12 J for the UD and woven materials. The UD material displays characteristic behaviour of an initial load drop between 2-3kN due to the onset of delamination, followed by a steady increase to maximum load. In contrast, the woven material does not display a first failure in the same manner as the UD material, but rather shows a load drop close to the peak load. In the case of the 12 J impact it was observed that this load drop probably occurred due to significant fibre tow damage causing back face breakout.

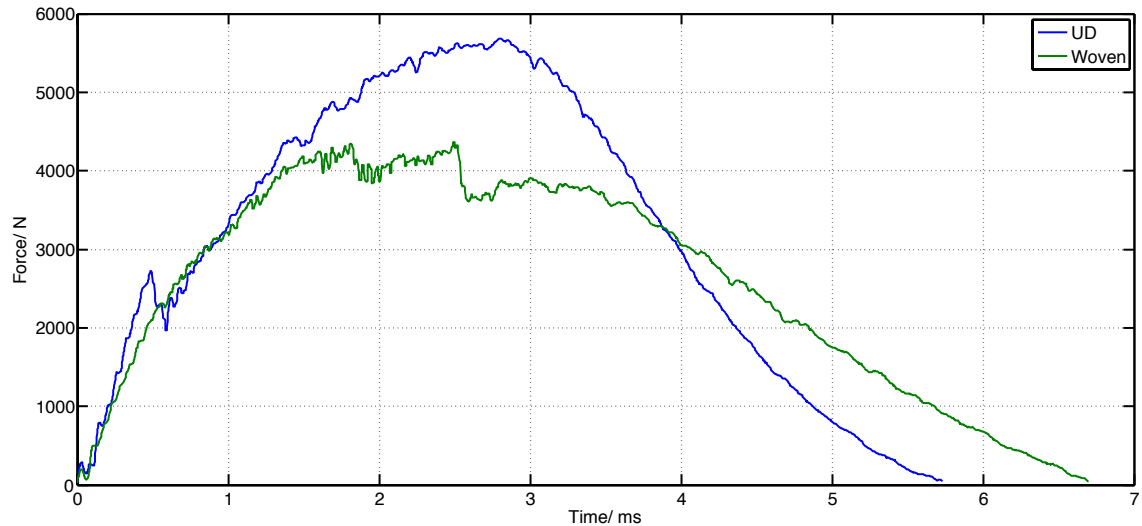


Figure 5.3: Typical force-time relationships at an impact energy of 12 J for the UD and woven materials

Typical force-displacement curves for a 12 J impact are shown in figure 5.4. The curves show a hysteresis loop whereby only some of the displacement is regained as a result of energy absorption by damage mechanisms. By integrating the force-displacement relationship to obtain the area within the hysteresis curve, the energy absorbed during the impact can be quantified, as shown in figure 5.5.

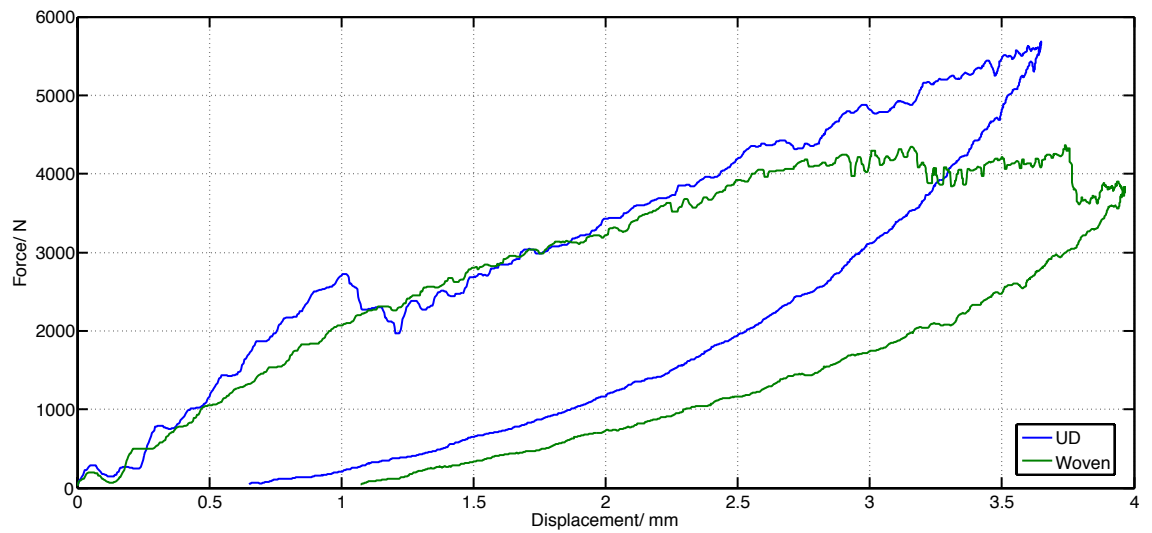


Figure 5.4: Typical force-displacements curves for a 12 J impact

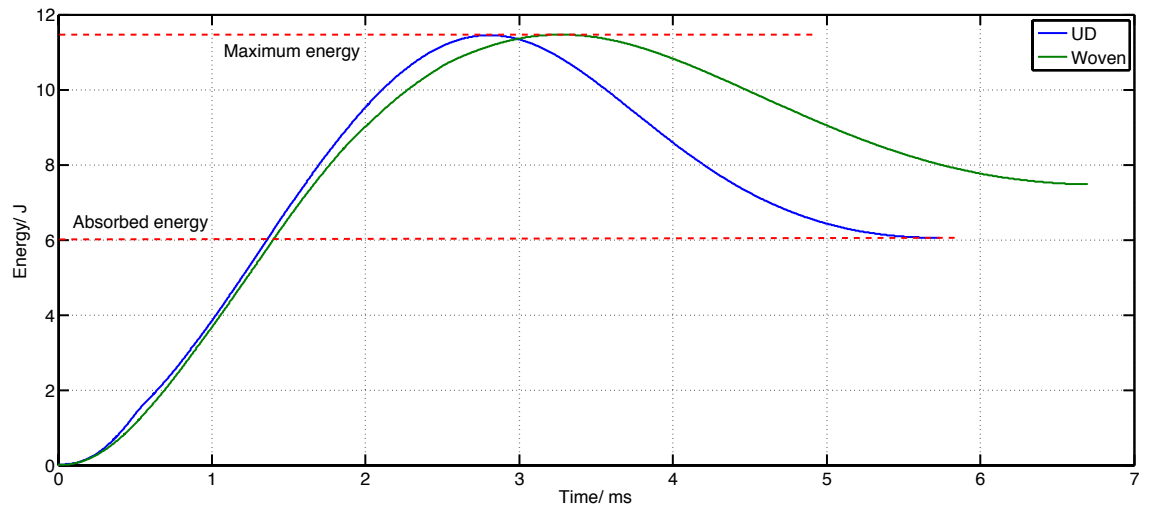


Figure 5.5: Typical energy-time curves for a 12 J impact

Figures 5.6 and 5.7 show typical force-time relationships for the UD and woven materials respectively under impact energies ranging from 3-12 J.

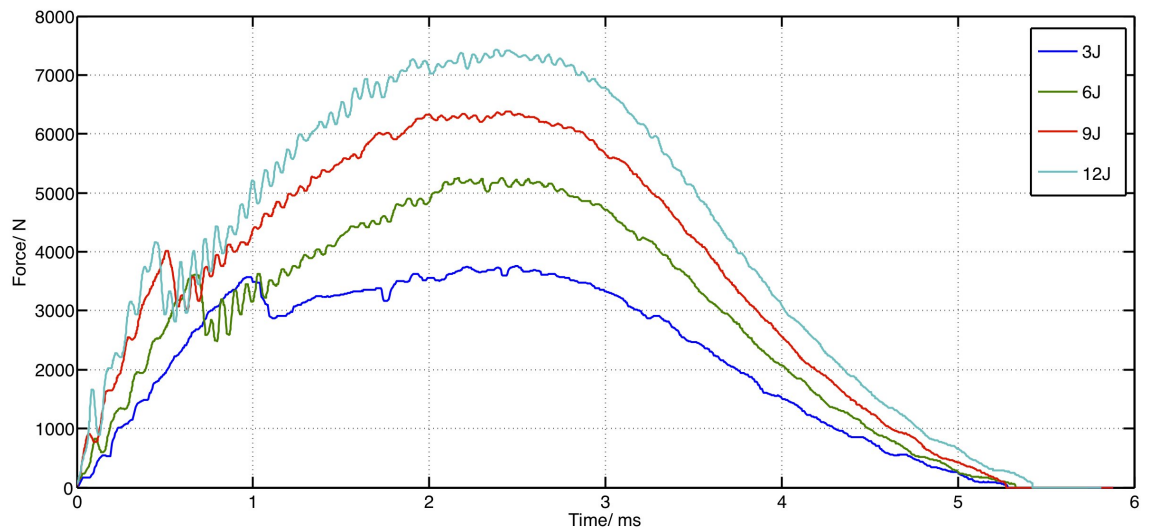


Figure 5.6: Typical force-time curves under various impact energies for the UD material

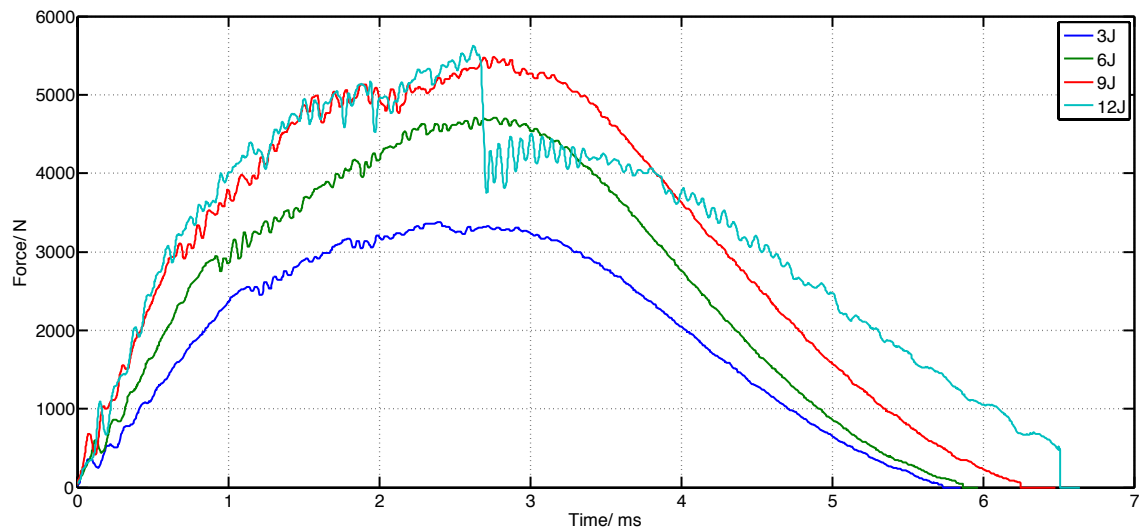


Figure 5.7: Typical force-time curves under various impact energies for the woven material.

In general the UD materials show significant load drops at around 50% of the maximum load experienced. This load drop is the initial onset of damage, known as first failure. In the case of the UD material this is likely to be the onset of delamination between plies (Adams and Miller, 1975; Bradshaw *et al.*, 1973; Cantwell and Morton, 1991). The slope of the force-time curve is then seen to decrease before reaching the peak load, at which point the load gradually returns to zero. It can be seen that for the UD materials, the onset of first failure is largely independent of impact energy. This observation has been reported many times in the literature and is a typical characteristic of this type of material (Cantwell and Morton, 1991; Hitchen and Kemp, 1995; Liu, 1988; Richardson and Wisheart, 1996). Performing an unpaired T-test on the load at first failure for the UD materials (5 repeats at each impact energy), showed no statistically significant difference

(95% confidence), resulting in a mean load at first failure of  $3.35 \pm 0.36$  kN. Table 5.2 gives the p-values for the different test combinations.

Table 5.2: p-values for first failure loads in UD materials under various impact energies

T-test comparison	p-value
3J vs. 6J	0.31
3J vs. 9J	0.09
3J vs. 12J	0.14
6J vs. 9J	0.28
6J vs. 12J	0.43
9J vs. 12J	0.08

Conversely, the woven samples do not display a significant first failure or load drop. Instead, a progressive mode of failure is observed with a fairly constant slope up to 50-75% of the maximum load. After this point, the slope of the curve is seen to reduce while displaying many small load drops but no significant failure event. At 12 J a large load reduction is observed, which was due to significant back face damage after a high degree of fibre failures had occurred. This load drop was seen to occur in all 5 samples tested at 12 J immediately after the peak load was reached.

Figure 5.8 compares the mean peak impact force experienced by both materials under various impact energies. Both data series reveal an almost linear relationship between peak force and impact energy, although the curve seems to level out at 12J for the woven sample. This levelling most likely occurs due significant fibre failures occurring somewhere between 9 and 12J, which is implied by the significant load fall off in the force-time curve at 12 J.

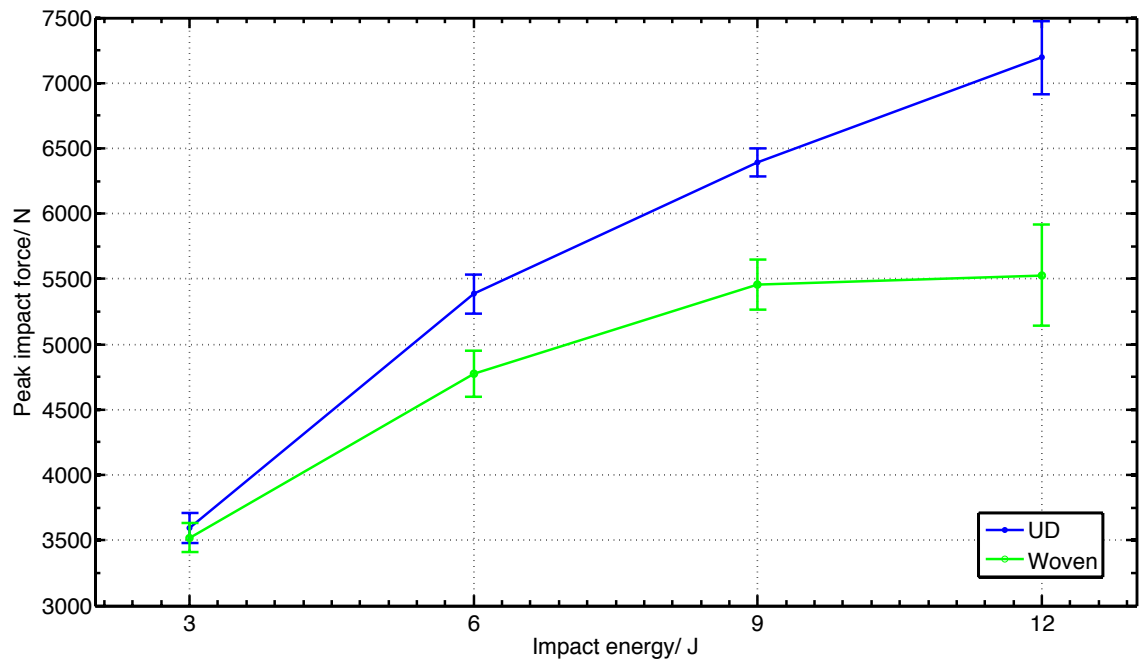


Figure 5.8: Peak impact force for UD and woven materials under various impact energies.

Calculation of the total absorbed energy revealed statistical differences between the materials at all impact energy levels. Figure 5.9 shows the absorbed energies under the various impact energies, followed by the statistical analysis values in table 5.3. The data shows a linear trend relating the impact energy to absorbed energy between 3 and 9 J, but the values at 12 J make a deviation from this pattern. The absorbed energy at 12 J is higher than would be predicted by the linear relationship seen at lower energies. The force-time relationships at this energy revealed significant failure events in both the UD and woven materials at 12 J impact, probably due to increased fibre failures, and would explain the accelerated increase in absorbed energy. This observation is discussed further in the imaging section (5.7)

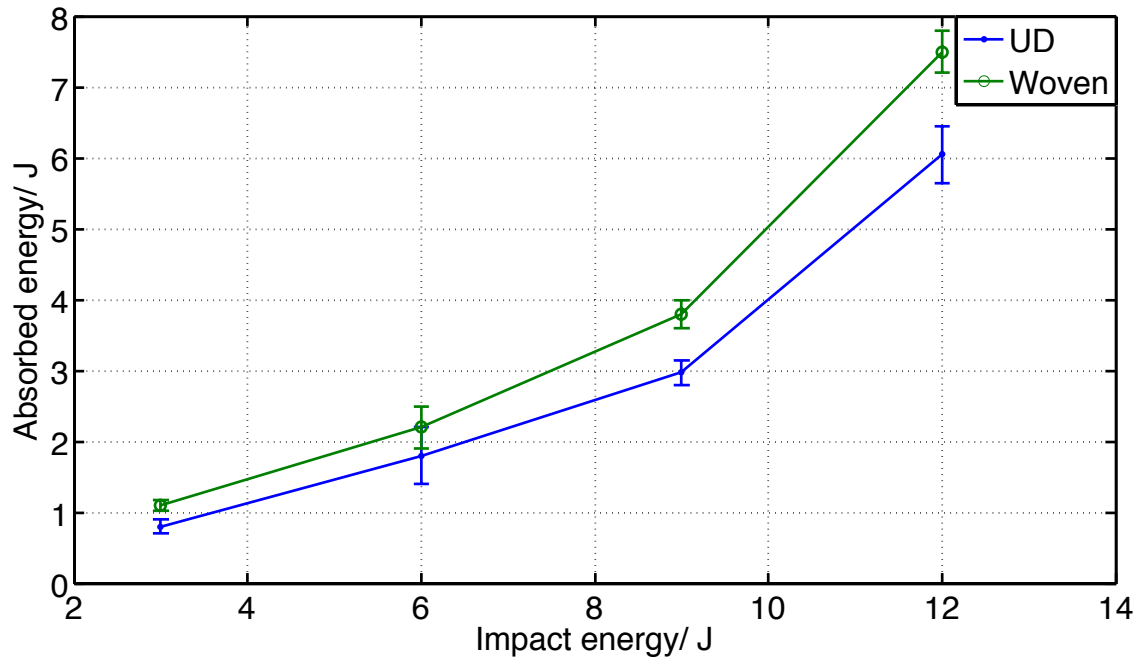


Figure 5.9: Comparison of absorbed energy at various impact energies for UD and woven materials.

Table 5.3: p-values for absorbed energies in UD and woven materials

T-test comparison	p-value
3J	0.045
6J	0.49
9J	0.044
12J	0.03

Examining the force-deformation curves revealed that the woven samples experienced a larger deflection (under the impactor) across all impact energies. Figure 5.10 shows the displacements for both materials against impact energy. The relationships for both materials are seen to be linear. This observation is expected, as the woven material has a lower ply stiffness, and will therefore deflect further for a given load.

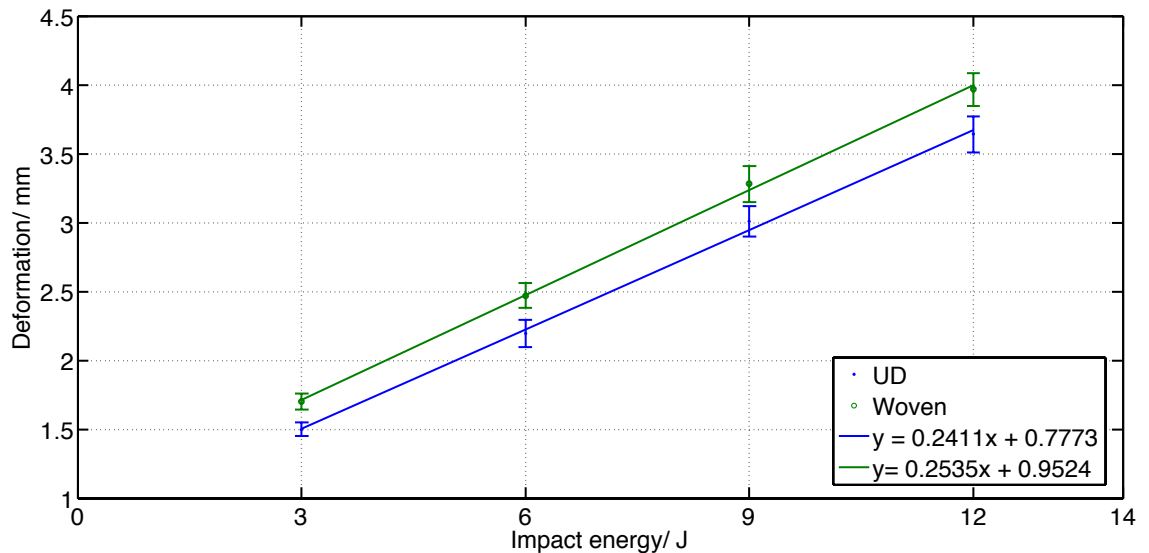


Figure 5.10: Vertical deformation under the impactor for UD and woven materials under various impact energies.

#### 5.4.2.1 Summary

The work in this section has illustrated the low velocity impact behaviour of a toughened epoxy reinforced with two different fibre architectures using an instrumented drop weight impact testing machine. Observations were made on the relationships between the force, displacements, and energy absorption of the different materials with respect to impact energy and elapsed time. The tests revealed a 'threshold' energy in the UD materials where delamination onset occurs, which was approximately 3.35kJ. Conversely, the woven materials did not display any significant first failure event. The results implied progressive damage was occurring during the impact event. It was also observed that the woven materials showed a higher degree of deformation during the impact event across all impact energies, due to the lower stiffness of this material. The woven material also showed a higher degree of energy absorption at all impact energies compared to the UD material. These observations are discussed further in relation to the X-ray tomography observations in section 5.7.

## 5.5 Compression After Impact Testing

Compression after impact testing (CAI) is often used as a method of comparing the damage tolerance of different materials with respect to impact damage. This section describes the experimental procedure followed to assess the CAI strength of the samples which were impacted in section 5.4 using a miniaturised testing rig. This test methodology was developed in the 1990's by Hogg and Pritchard (Guild *et al.*, 1993; Pritchard and Hogg, 1990) at Queen Mary University, London.



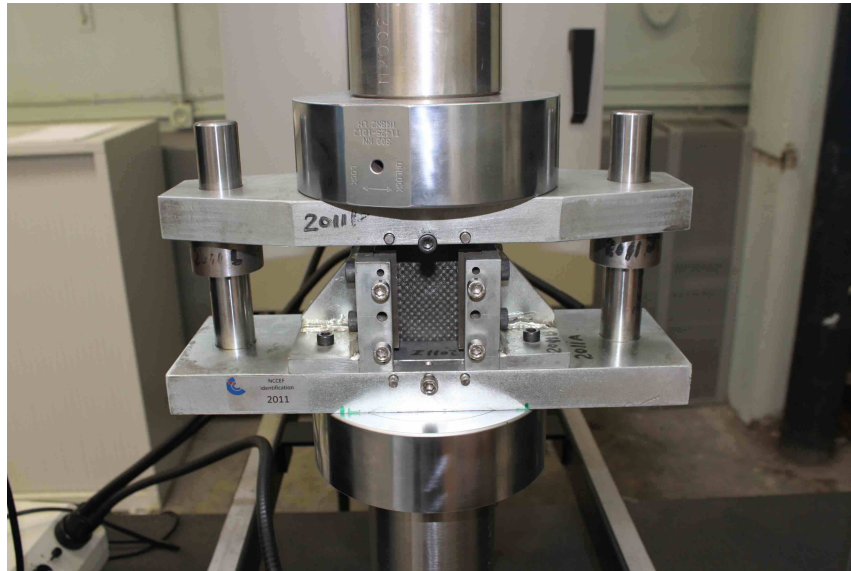


Figure 5.12: CAI rig with a sample mounted in the 600 kN hydraulic test machine

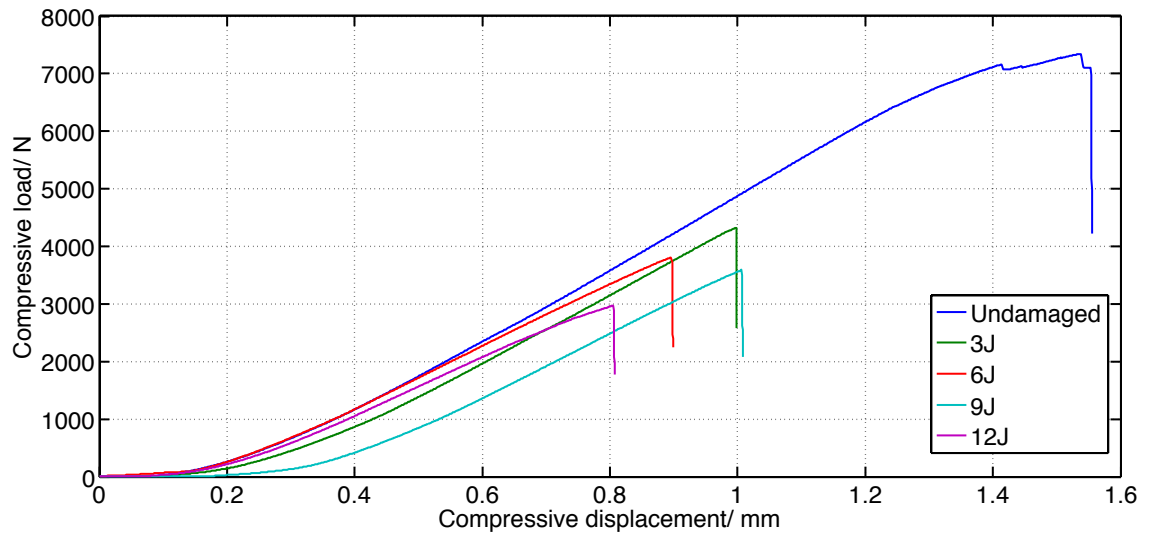
The loading platens are brought into contact with the CAI rig, until a small load (approximately 5-10N) is registered. The load scale is then balanced to zero, and testing can commence. Samples were loaded to failure, under displacement control at a rate of 1mm/minute.

Five undamaged test coupons of both candidate materials were first tested to establish a baseline strength, along with associated standard deviations. Each of the five samples tested at respective impact energy levels were subsequently loaded to failure in the CAI rig. Load and displacement values were recorded to allow calculation of peak failure load, compression modulus, compression strength, and approximate strain to failure.

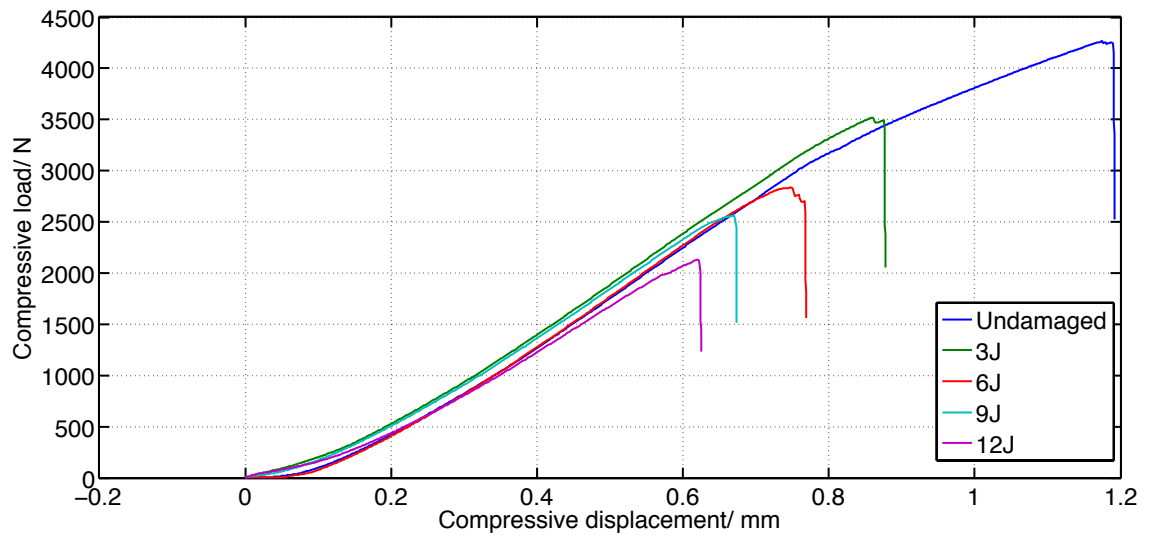
Prior to testing, one sample from each impact energy set, and one sample from the undamaged set (for both UD and woven materials) had linear strain gauges attached to the front and back face. These strain gauges were used to assess the extent of any bending occurring during the tests, which may in turn imply buckling of the laminate.

## 5.5.2 Results and Discussion

Figures 5.13 (a) and (b) show typical load-displacement curves for the UD and woven materials in undamaged and damaged states. Immediately apparent is the significant reduction in the maximum loads achieved by both materials after impact damage has been induced. Both materials display brittle failure behaviour, displaying constant stiffness until ultimate load. Furthermore, it can be seen that the force-extension behaviour of each material appears independent of the impact energy the sample has experienced. It would appear, therefore, that the amount of damage sustained has no effect on the compression stiffness of either UD or woven materials, but severely effects strength. Although these curves give an indication that impact events have an effect of the CAI performance of both materials, obviously the strength values must be derived to give a real comparison.



(a) Uni-directional



(b) Woven

Figure 5.13: Typical load-displacement curves for UD and woven CAI samples after various impact energies

Figure 5.14 shows the relationship between CAI strength and impact energy for the UD and woven materials. For both materials a reduction in CAI strength is seen at all impact energy levels.

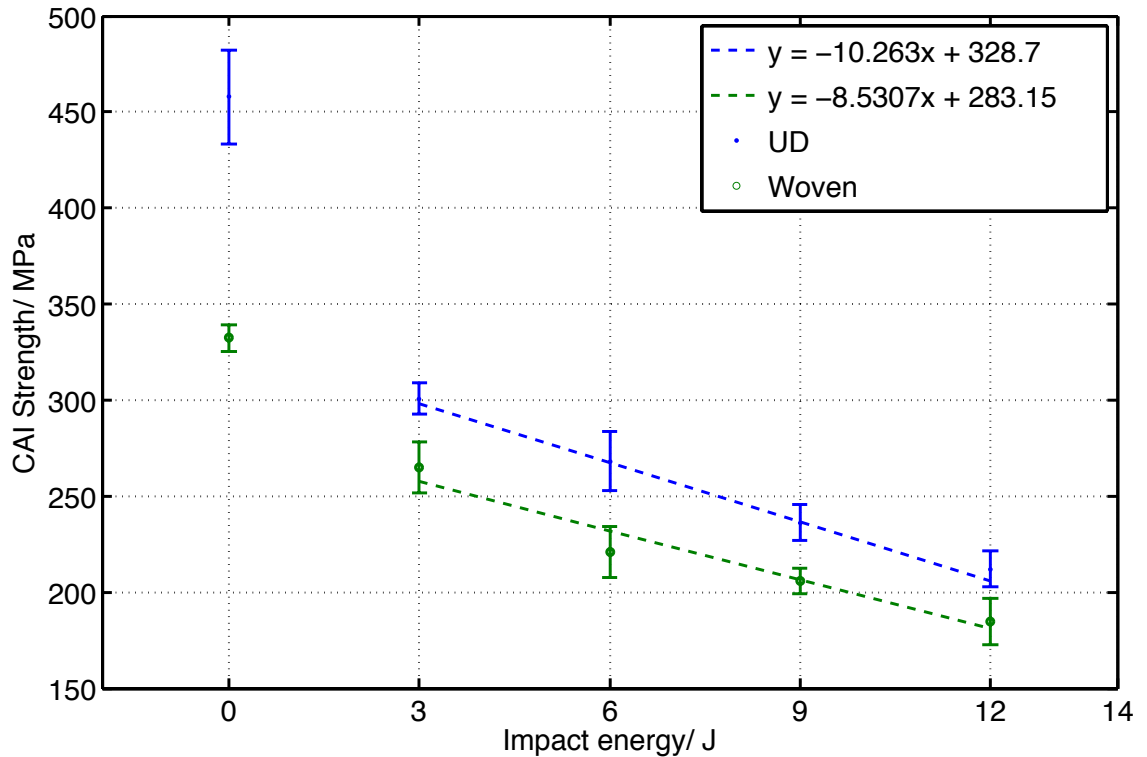


Figure 5.14: Compression after impact strength vs. impact energy for UD and woven materials.

The above figure shows that the UD material loses a mean 35% of its undamaged strength after only a 3 J impact, whereas the woven material loses only 20%. This observation can be explained by the mechanical data obtained in section 5.4.2, where the UD material was seen to display the onset of damage even at 3J, whereas the woven material displayed more progressive damage evolution. These results will be discussed further in section 5.7 when the data is compared with measurements of the damage using X-ray tomography and C-scan.

Taking into account the CAI strength values once impact damage has occurred, both materials display a linear relationship between residual strength and impact energy. Despite the fact that the scatter in the data is quite high, T-tests showed differences in the CAI values at 95% confidence levels. Therefore it is statistically reasonable to draw the conclusion that the relationship is linear, and differences in CAI are observed, as the p-values in tables 5.4 and 5.5 show.

Table 5.4: p-values for CAI strength in UD samples under various impact energies

T-test comparison	p-value
3J vs. 6J	0.0226
3J vs. 9J	0.0006
3J vs. 12J	0.0001
6J vs. 9J	0.0039
6J vs. 12J	0.0001
9J vs. 12J	0.0036

Table 5.5: p-values for CAI strength in woven samples under various impact energies

T-test comparison	p-value
3J vs. 6J	0.0007
3J vs. 9J	0.0001
3J vs. 12J	0.0001
6J vs. 9J	0.049
6J vs. 12J	0.0019
9J vs. 12J	0.0094

Figure 5.15 gives a final overview of the relationship between CAI strength and impact by considering the absorbed energy. The relationship follows trends seen in the previous figures, whereby CAI strength is reduced with increased energy absorption.

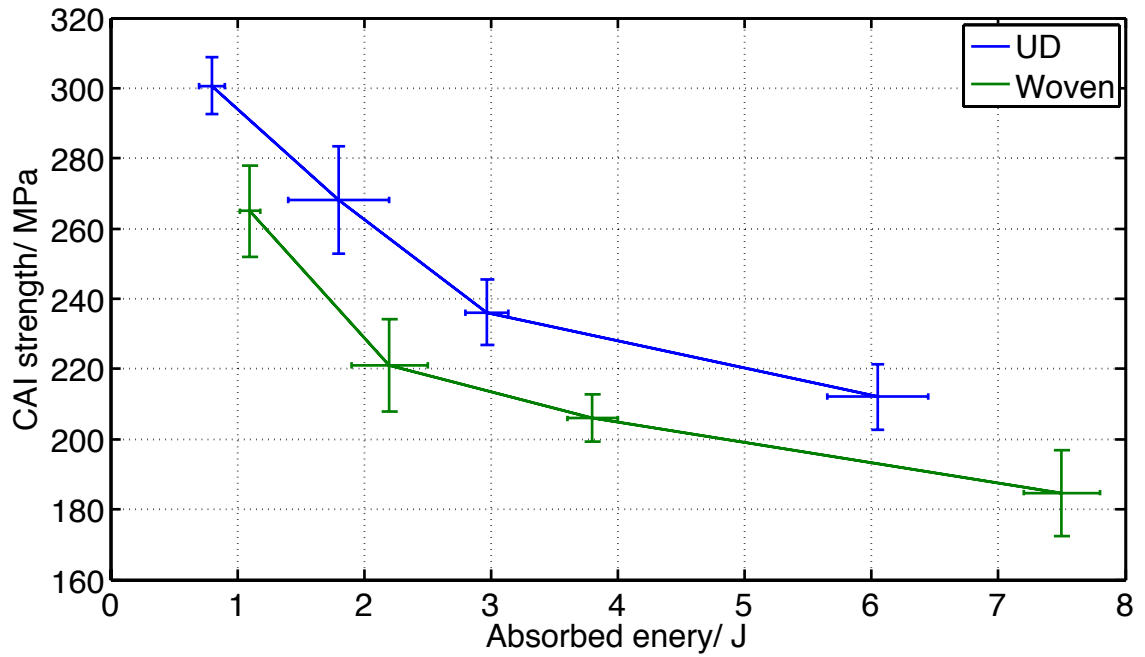


Figure 5.15: CAI strength vs. absorbed energy for UD and woven materials.

### 5.5.3 CAI Testing Summary

This section has shown that low velocity impact in the range 3-12 J can cause appreciable reduction in compression after impact strength for both UD and woven materials. Additionally, the the introduction of impact damage has virtually no effect on the compression stiffness of either UD or woven materials. The UD material displayed a higher reduction in CAI strength loss after 3 J compared to the woven material (35% vs 20%), although the ultimate strength values for the UD material remained consistently higher across all energies. Statistical analysis showed a linear relationship between impact energy and CAI strength for both UD and woven materials, and p-values provided statistical evidence of consistently reducing CAI strength with increasing impact energy. The mechanisms of failure and types of damage relating to the values observed in this section will be discussed in section 5.7.

## 5.6 Interlaminar Shear Testing

The interlaminar shear strength (ILSS) of a laminated composite material has been shown to be an indicator of the degree of damage tolerance of a material. Therefore, to provide supporting evidence for the observations of damage tolerance due to drop weight impact testing, the ILSS of both candidate materials were measured. This experiment follows the procedure described in British Standard BS EN 2563(Standards, 1997).

The test involves measuring the apparent interlaminar shear strength of a laminated composite by performing a flexural test. Effectively the test measures the resistance to

delamination under shear loads which act parallel to the lamina, which implies the quality of the fibre to resin interface. The specimen has a rectangular cross section, which is placed on two supports and loaded in the centre by a hemispherical loading nose.

### 5.6.1 Specimen Preparation

Samples were cut from the panels described in section 5.3 using a diamond saw. Figure 5.16 illustrates the test geometry (left) and sample geometry (right). Symbols and values are explained in table 5.6. Five samples from each material were tested.

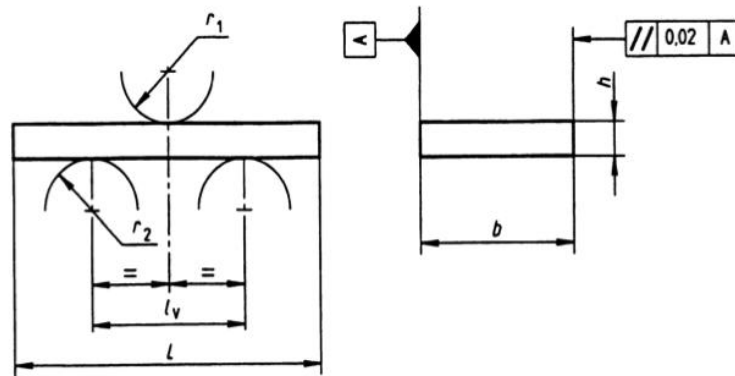


Figure 5.16: Test and sample geometries for the interlaminar shear strength test Standards (1997)

Table 5.6: Interlaminar shear test symbols

Symbol	Value
$r_1$	Support radius, $3 \pm 0.1 \text{ mm}$
$r_2$	Support radius, $3 \pm 0.1 \text{ mm}$
$b$	Sample width, $10 \pm 0.2 \text{ mm}$
$L$	Sample length, $20 \pm 0.25 \text{ mm}$
$l_v$	Distance between supports

For testing, the distance between supports,  $l_v$ , is adjusted to meet the condition shown in equation 5.1:

$$l_v = (5.\bar{h}) \pm 0.1 \text{ mm} \quad (5.1)$$

The dimensions  $h$  and  $b$  of each sample were measured three times at the centre of each sample using a micrometer with 6 mm flat faces accurate to 0.01 mm. The standard specifies that the samples should have a thickness scatter of :

$$\frac{h_{max} - h_{min}}{\bar{h}} \leq 0.05 \quad (5.2)$$

Table 5.7 shows the measured values of thickness, with associated scatter values. It can be seen that both sample sets lie within the scatter tolerance.

Table 5.7: Interlaminar Shear Measured Sample Dimensions

Material	$h_{min}$ / mm	$h_{max}$ / mm	$\bar{h}$ / mm	$\sigma$ / mm
UD	2.79	2.93	2.85	0.049
Woven	2.2	2.26	2.228	0.026

### 5.6.2 Interlaminar Shear Test Experimental Procedure

Samples were mechanically tested using an Instron 50 kN hydraulic test machine, using a loading rig defined in the British Standard Standards (1997). Figure 5.17 shows the test equipment with a sample mounted in the loading rig.



Figure 5.17: Interlaminar shear strength test rig with a sample in place

The sample is mounted within the loading rig, and positioned so that the centre of the specimen is within 0.02 mm of the centre of the loading nose with respect to the supports. The sample is then loaded under displacement control, ensuring that the loading rate is at a constant  $1 \pm 0.1$  mm/min.

The load is recorded as a function of loading nose displacement at a frequency of 10Hz. The load at failure,  $P_R$  is observed as the first reduction in load on the load-displacement curve, as illustrated in figure 5.18

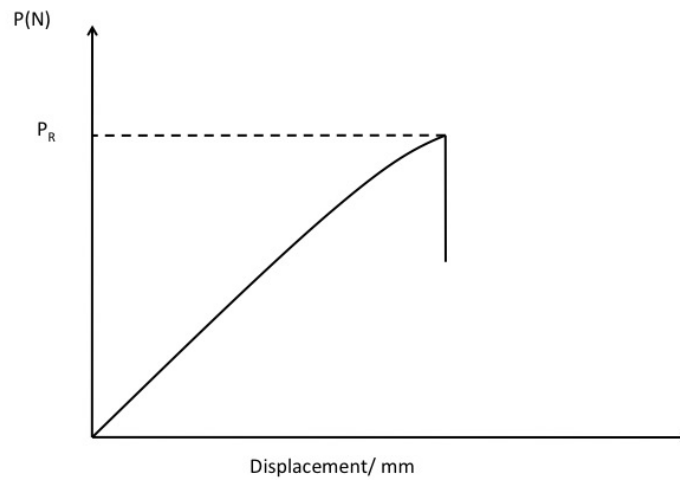


Figure 5.18: Schematic load-displacement curve for an interlaminar shear strength sample, showing load at first failure,  $P_R$

The apparent interlaminar shear strength is then calculated by equation 5.3.

$$\tau = \frac{3P_R}{4bh} \quad (5.3)$$

Where:

- $\tau$  is the apparent interlaminar shear strength (MPa)
- $P_R$  is the maximum load at first failure (N)
- $b$  is the width of the specimen (mm)
- $h$  is the thickness of the specimen (mm)

### 5.6.3 Results and Discussion

Figure 5.19 shows typical load-displacement curves for the UD and woven materials. Both materials displayed the expected mechanical behaviour of linear force-displacement with a pronounced first failure in all samples.. This failure type was therefore concluded as a valid ILSS test.

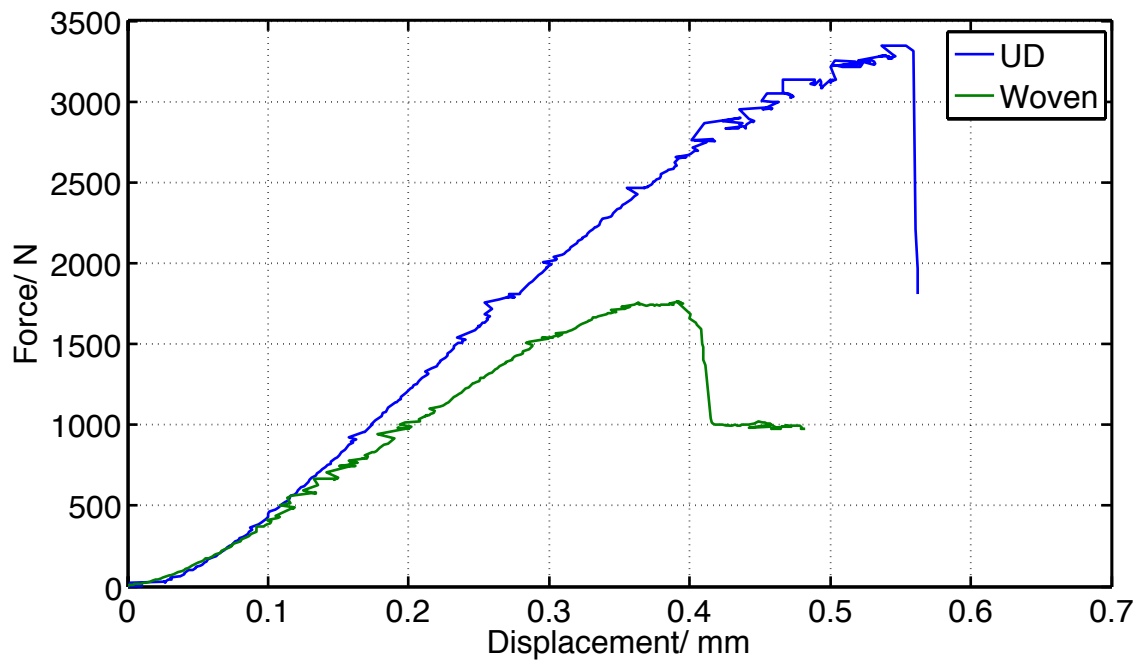


Figure 5.19: Typical Force-displacement profiles for UD and woven materials during the ILSS test.

Equation (5.3) was then used to calculate the apparent ILSS values, which are given table 5.8. Statistical comparison using an unpaired T-test showed the values were different to over 99% confidence.

Table 5.8: ILSS values for UD and woven materials

Material	Interlaminar shear strength/ MPa
UD	87.28( $\pm$ 5.8)
Woven	60.05( $\pm$ 0.54)
p-value <0.0001	

As expected, the UD material shows a much higher ILSS than the woven. The higher fibre volume fraction obtained with UD materials, the increased stiffness and strength of the fibres in the UD material, and the increased interfacial bonding area between the UD fibres and matrix all contribute to this increased ILSS. The consequences of this high ILSS are discussed in section 5.7 with respect to the impact damage characteristics.

## 5.7 Imaging Impact Damage in CFRP coupons

This section details several experiments performed on imaging low velocity impact damage in CFRP materials. The main focus of this section is the 3D X-ray tomographic imaging and characterisation of the damage which was induced using the drop weight impact testing equipment (section 5.4). Imaging experiments were also performed using transmission C-Scan to map the damage in 2D.

### 5.7.1 Dual Energy X-ray CT of impacted CFRP coupons

Many authors have used 2D imaging techniques such as C-Scan and optical microscopy to examine impact damage in CFRP materials. Although C-scan is non-destructive and allows fast acquisition times, its spatial resolution is generally limited to  $\sim 1\text{mm}$  and features become overlaid. This means, for example, that delaminations in individual plies cannot be quantified separately. Optical microscopy, as well as de-ply techniques are destructive and therefore prevent any further investigations on a given sample.

The purpose of this section was to show that laboratory based X-ray tomography is a useful and accurate tool for the qualitative and quantitative characterisation of impact damage in CFRP. Although several authors have used CT to image damage in CFRP materials, much of the work has been qualitative. The majority of published quantitative work has been performed in synchrotrons.

In this section, the impacted CFRP coupons described in section 5.4 were imaged using the dual-energy CT technique which was covered in chapter 4. As discussed in the literature review and Chapter 5, imaging composite plates is a trade-off between several parameters including resolution, sample size, image contrast and signal-to-noise ratio.

#### 5.7.1.1 CT Imaging Methodology

As discussed in the literature review and Chapter 5, imaging composite plates is a trade-off between several parameters including resolution, sample size, image contrast and signal-to-noise ratio. This initial imaging study aimed to image the full dimensions of each impacted sample, in order that the full dimensional extent of the damage be mapped. To achieve this, the impact samples were imaged in 8 batches. Each batch contained 5 samples impacted at a single impact energy, table 5.9 gives the batch numbers and sample conditions. The imaging geometry resulted in a voxel size of  $48\mu\text{m}$ . The dual-energy imaging technique was used to improve the SNR and produce a better quality CT data set which could be segmented more easily to allow for quantification of damage regions.

Table 5.9: Sample batches for CT imaging

Batch no.	Sample No.	Material	Impact energy
1	A1-A5	UD	3J
2	A6-A10	UD	6J
3	A11-A15	UD	9J
4	A16-A20	UD	12J
5	B1-B5	Woven	3J
6	B6-B10	Woven	6J
7	B11-B15	Woven	9J
8	B16-B20	Woven	12J

Figure 5.20 shows a schematic of the imaging set up. The samples were held in a vice-like sample holder, with the laminate plane perpendicular to the plane of the detector. Each batch of samples was scanned twice for the purpose of the dual energy imaging. The first scan was performed at 40kV, the second at 100kV. Table 5.10 shows the imaging parameters used for each scan.

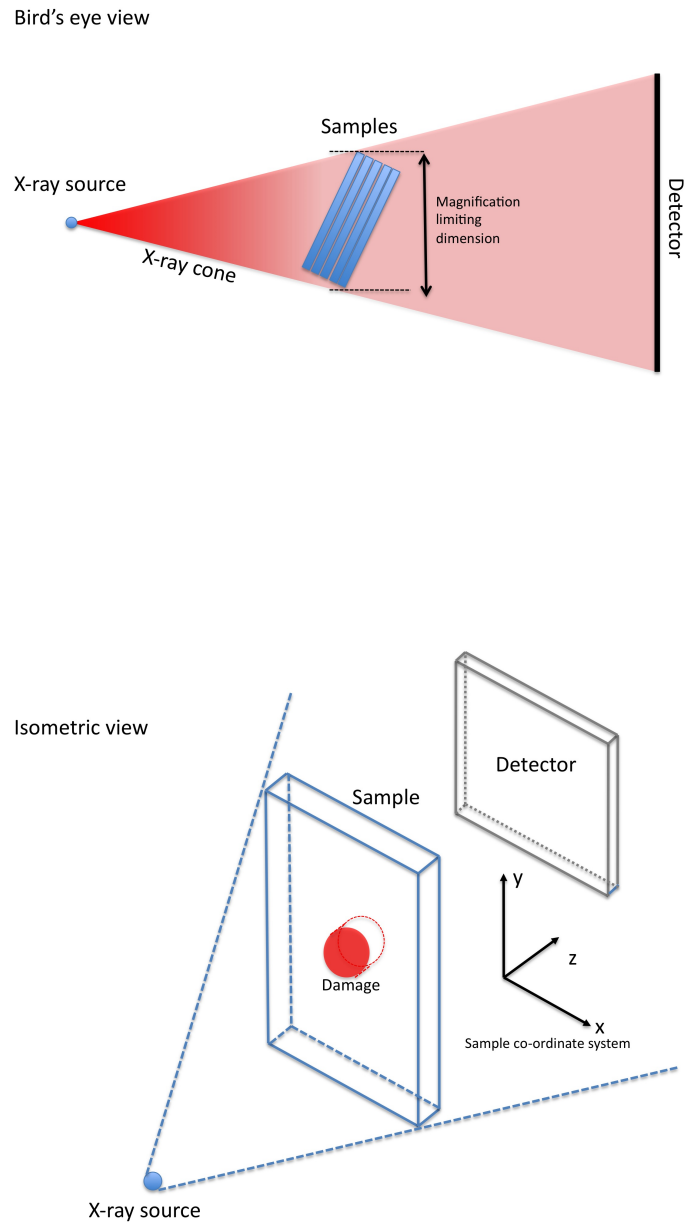


Figure 5.20: Schematic of scan setup for CT imaging of impacted samples (not to scale).

Table 5.10: Imaging parameters for dual energy scanning of impacted samples.

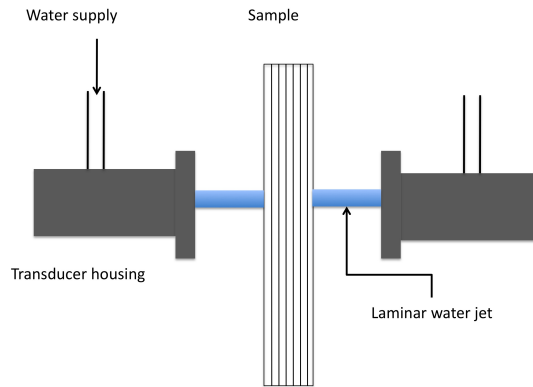
<b>Imaging Parameter</b>	<b>Low energy scan</b>	<b>High energy scan</b>
Target material	Copper	Copper
Accelerating voltage	40kV	100kV
Filament current	250 $\mu$ A	150 $\mu$ A
Frame exposure time	2s	2s
No. of projections	3142	3142
Digital gain	2	2
Voxel size	48 $\mu$ m	48 $\mu$ m

The two data sets (low and high energy) for each scan were then combined and reconstructed using the method outlined in section 4. As the data sets are reconstructed in 32-bit floating point format, the reconstructed volumes were converted to 8 bit format. This has the advantage of reducing the data set file size by a factor of 4, and improves image contrast in the reconstructed cross sections.

### 5.7.2 Ultrasonic C-Scan of impacted CFRP coupons

Ultrasonic C-scan is an industry standard method for assessing whether CFRP components contain defects such as impact damage. In order to have a baseline comparison for the amount of damage detected using the CT system, all impacted test coupons were tested using a transmission-type ultrasonic C-scan system. This imaging method gives a 2D in-plane map of a component, by measuring the attenuation of an ultrasonic wave. A detailed explanation of the principle was given in Chapter 2.

The system used in this study was a Midas NDT Systems transmission scanner, capable of scanning objects up to 2 m x 4m in size. Figure 5.21 shows a schematic of the inspection system along with a photograph of the hardware.



(a) Schematic



(b) Photograph

Figure 5.21: Midas NDT Ultrasonic Transmission C-scan equipment

To ensure reliable measurements, a laminar water jet is used to carry the ultrasonic wave between the transducers and sample surface.

Samples were stacked side by side in an appropriate sample holder and scanned with a 10MHz transducer at a rate of 100 mm/ minute, giving a spatial resolution of approximately 1mm.

The raw C-scan data was processed using image processing software ImageJ to map the 2D damage area in each sample.

## 5.8 Imaging Results and Discussion

This section presents the imaging results obtained using CT and ultrasonic C-Scan to image impact damage in the UD and woven samples. Initially a qualitative discussion is presented on the types of damage apparent in both materials using X-ray CT, before

quantitative measurements are discussed and compared with C-scan images.

## 5.8.1 Qualitative X-ray CT Results

### 5.8.1.1 Unidirectional Samples

For the UD samples it was found that the typical forms of damage reported in the literature were resolvable when scanning with a resolution of  $50\mu\text{m}$ , i.e. when the entire sample was within the field of view of the X-ray cone.

Figure 5.22 shows a reconstructed cross section of a 12 J impacted coupon directly under the impact zone. Delaminations between plies extending in the plate axis away from the impact zone are clearly visible, along with inter-ply matrix shear cracks connecting the delaminations.

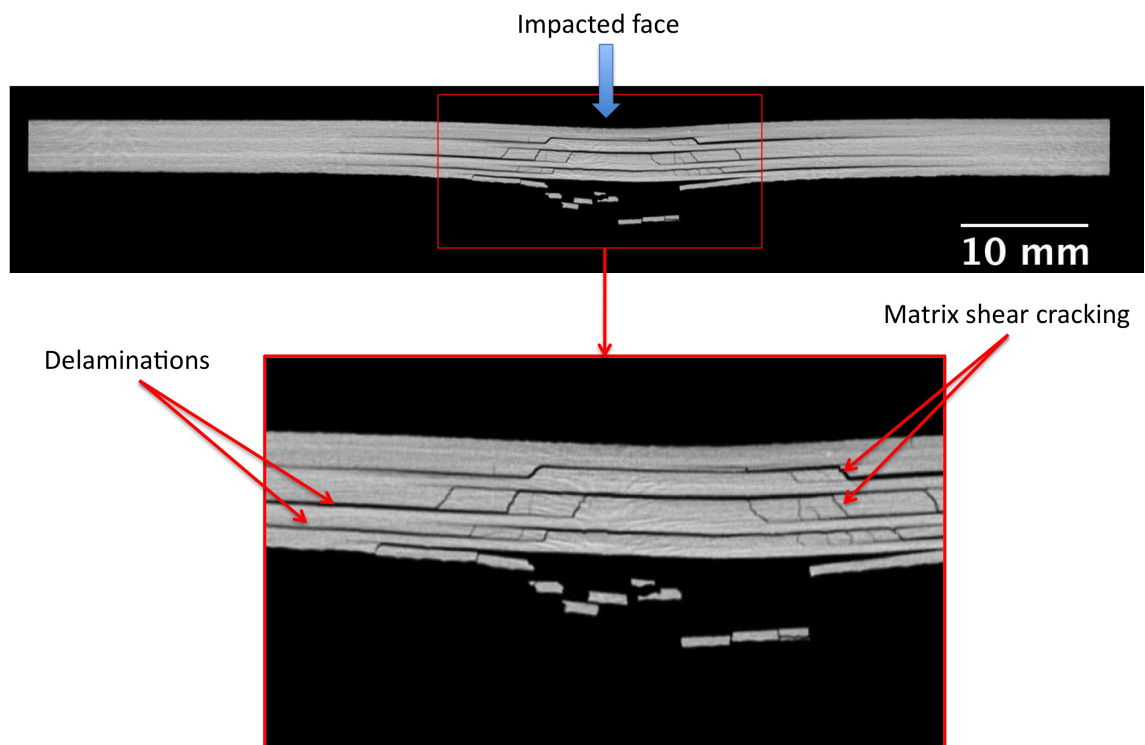


Figure 5.22: Typical reconstructed cross section of damage in a UD plate subjected to 12 J impact

The delaminations were seen to grow in area and move radially outwards from the impact location as they propagated downwards into the sample from the impact area, creating a characteristic pyramid shaped damage pattern. Figure 5.23 highlights the visible damage when viewed in the plane of the plate (i.e. in the laminate stacking plane).

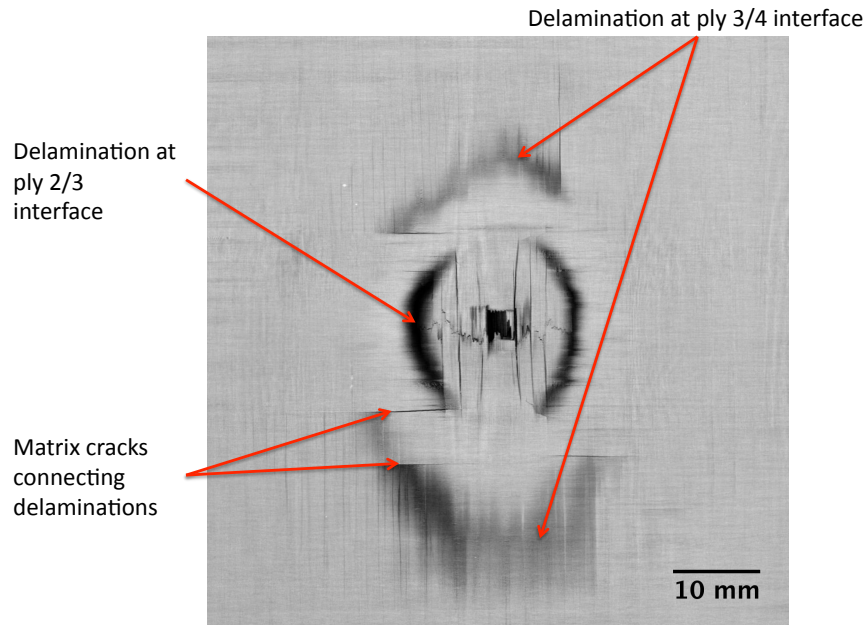


Figure 5.23: Typical in-plane damage in a UD plate. Due to out-of-plane curvature, damage in multiple plies is observed in a single reconstructed cross section.

As illustrated above in figure 5.23, multiple delaminations may be apparent in any one slice. This is due to out of plane curvature at higher impact loads, which results in several plies being visible in the in-plane reconstructed cross section. The principle is illustrated in figure 5.24

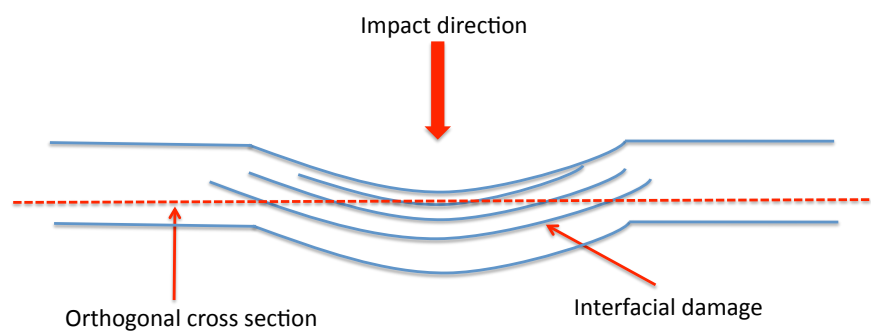


Figure 5.24: Exaggerated schematic of how out-of-plane deformation causes damage at multiple ply interfaces to appear in a single CT cross section.

Figure 5.25 shows 3D renderings of typical damage volumes due to the various impact energies. The delamination area was observed to increase with higher impact energy, and produces a characteristic diamond shaped pattern. The delaminations were seen to

preferentially extend in the ply directions, i.e in the X and Y directions relative to the sample co-ordinate system.

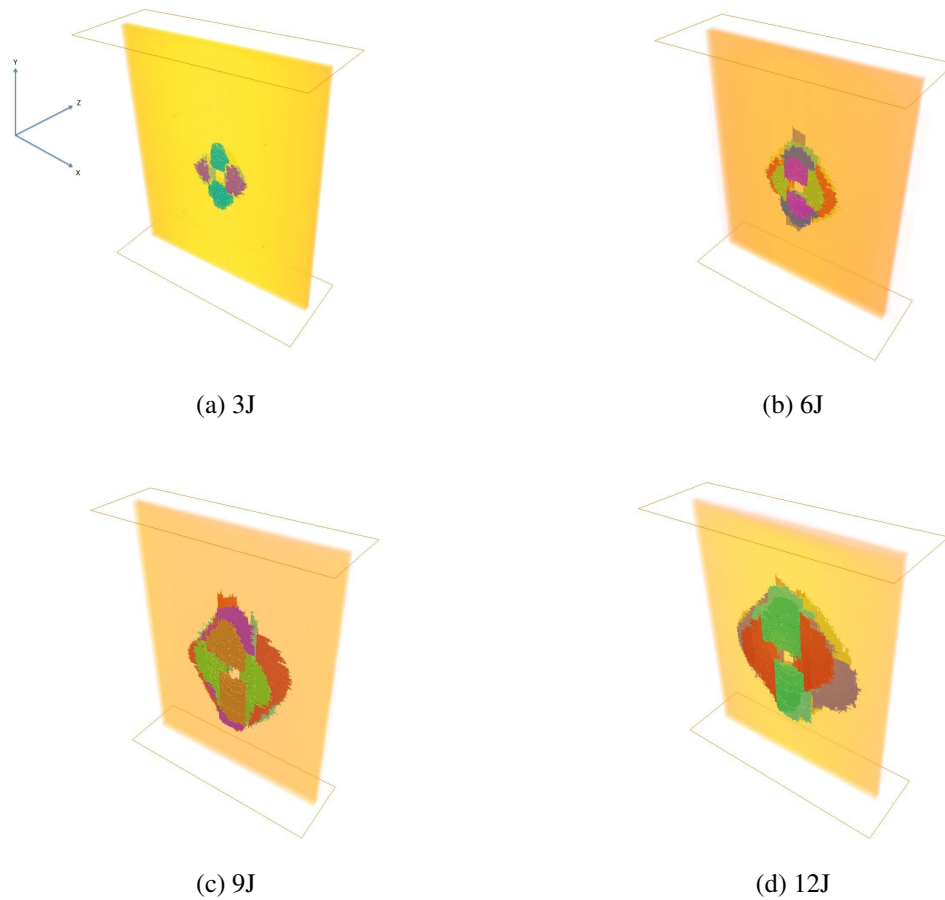


Figure 5.25: 3D renderings of UD impact samples showing relative damage areas

### 5.8.1.2 Woven Samples

Figure 5.26 shows a typical CT cross section of damage in a woven sample which was subjected to a 12 J impact. The figure that compared to the UD material, the damage is less well defined, showing a very high degree of damage confined generally to the location directly under the impactor and propagating down through all the plies. Similar to the UD material however, the woven plies displayed increased damage towards the back face of the sample. Although delamination was observed to exist in the woven materials, it did not appear to propagate to the same extent as the UD materials. The delaminations were also observed to have a more tortuous path, due to the fibre undulations causing deviation of the cracks. A large density of matrix was observed along with what appear to be several tow failures. However, due to the resolution achieved by capturing the full plate in the CT scan it is very difficult to successfully separate and quantify each damage mechanism. As a result it was deemed necessary to perform region of interest (ROI) investigations to further characterise the damage (see chapter 6)

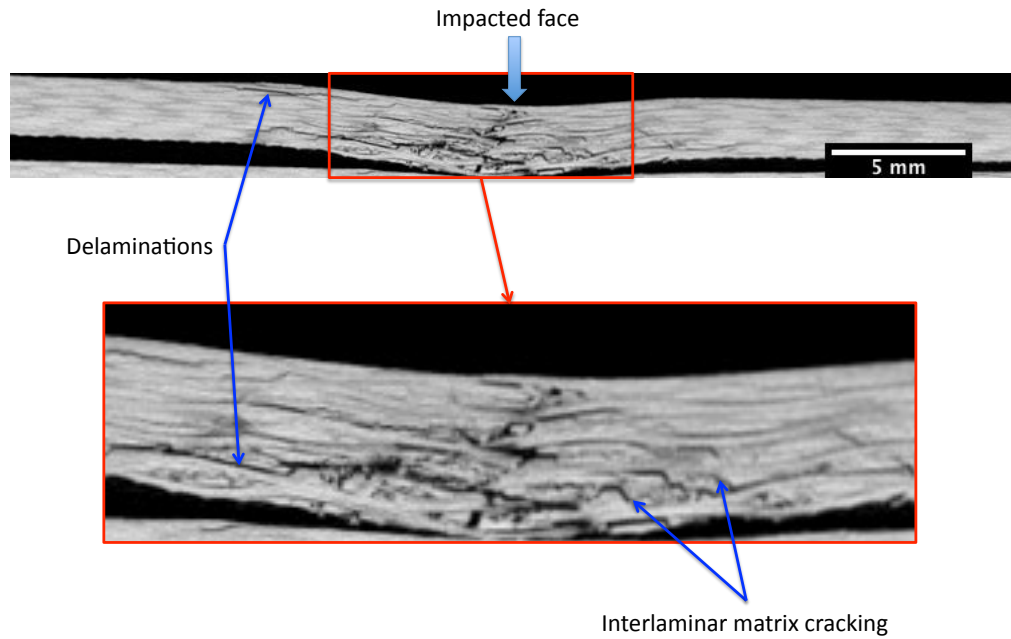


Figure 5.26: Typical reconstructed cross section of damage in a woven plate subjected to 12 J impact.

Figure 5.27 shows how the damage appears in a CT cross section in the plane of the sample. Individual fibre tows are resolved, with resin pockets visible at the tow interlacement points. It is also apparent that due to the reduced extent of the damage, and low contrast difference between the object and background it is quite difficult to identify damage compared to that seen in the UD materials.

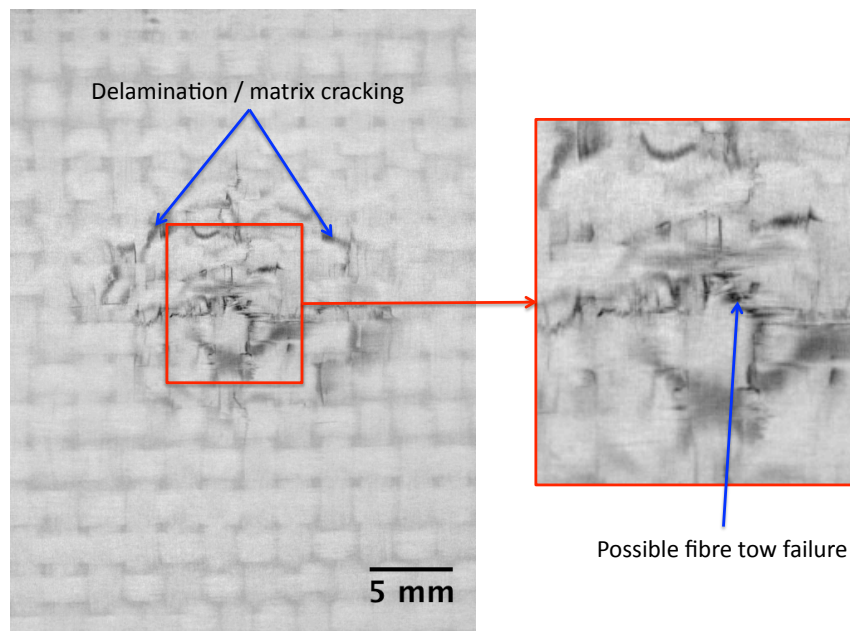


Figure 5.27: Typical in-plane damage in a woven plate.

Figure 5.28 shows 3D renderings of typical damage volumes due to the various impact energies. As with the UD material, the damage was seen to extend preferentially in the ply direction, but with a less well-defined shape. As will be seen in the next section which discusses the quantification of the damage, for the woven materials the induced damage was seen to propagate evenly through the thickness of the sample rather than spread outwards as was observed in the UD materials.

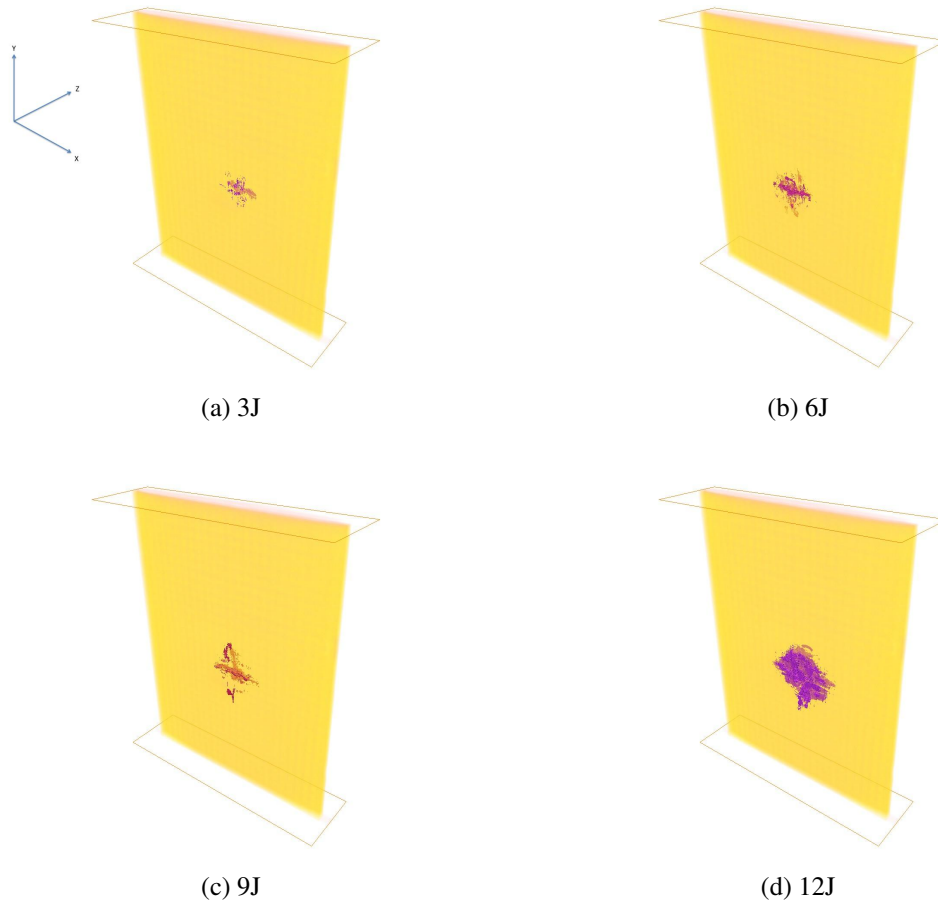


Figure 5.28: 3D renderings of woven impact samples showing relative damage areas

## 5.8.2 Quantitative X-Ray CT Measurements

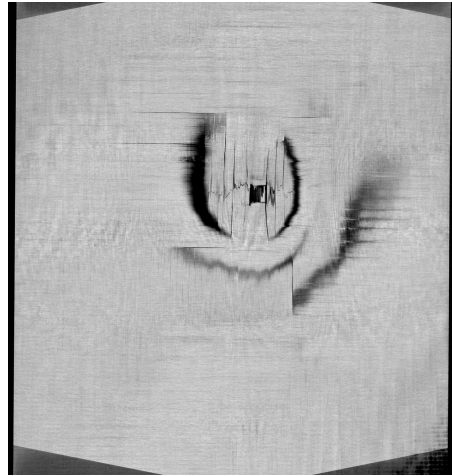
In order to demonstrate the engineering usefulness of CT as a tool for quantifying damage in CFRP materials, image thresholding was applied to acquire numerical information about the damage state in the UD and woven materials. This allowed characterisation of damage in terms of areas, volumes, and through-thickness distributions.

### 5.8.2.1 Image Processing

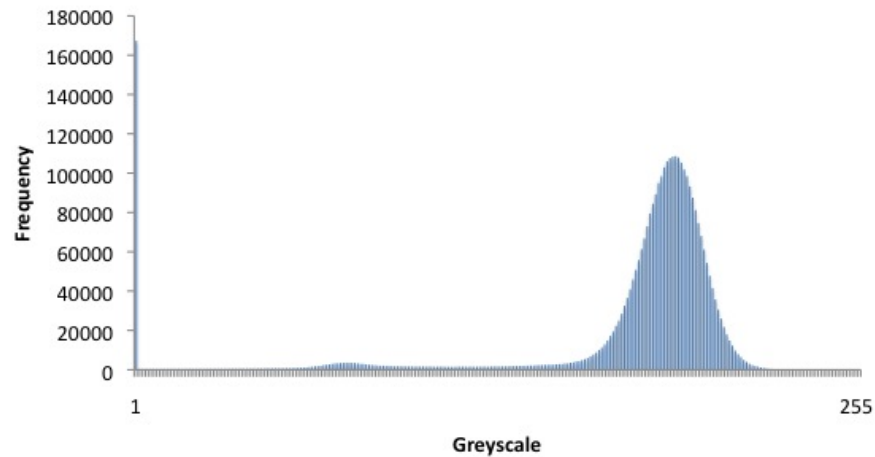
Data visualisation software Avizo® was used to view the reconstructed CT data sets of the impacted samples, as well as perform image segmentation to quantify damage. Image thresholding is based on the separation of image features based on pixel intensities. CT imaging produces greyscale images (i.e. a pixel value may vary on a scale from black to white), and therefore the images are thresholded on their grey value, often referred to as 'greyscale'.

To threshold the damage in the impacted specimens '*histogram thresholding*' was used as a simple approach to determining which pixels belonged to a damage zone. Histogram-based segmentation methods analyse the peaks and troughs present in an im-

age histogram, and are therefore dependent on pixel intensities. Figure 5.29 shows an example CT slice from an impacted sample, and its associated histogram.



(a) Reconstructed CT slice of a 12J impacted CFRP plate



(b) Image histogram of (a) Object pixels are associated with the broad peak to the right.

Figure 5.29: CT slice and associated histograms of an impacted sample.

The peaks in an image histogram represent the various homogenous phases in a material. Thresholds can be set between the peaks to segregate the image. Peaks in a histogram may also be referred to as ‘*modes*’ (Russ, 2007). From figure 5.29 a reasonable amount of peak broadening is apparent in the histogram mode representing the CFRP sample. Generally this broadening is due to image noise. Additionally, the bulk material is made up of two materials with very similar densities (fibres and resin), which are not separately resolvable. A contribution to broadening of the peak can be expected due to overlapping of the fibre and resin signal contributions.

To reduce some of the influence of noise in the reconstructions, a noise reduction filter, known as a ‘*median*’ filter was applied to the data sets. This filter is a simple edge-preserving smoothing filter and works by sorting pixels covered by an  $N \times N$  mask

according to their grey value. The centre pixel is then replaced by the median of these pixels, i.e., the middle entry of the sorted list (Avizo 7 Users Guide, 2011). In this case, a  $3 \times 3$  filter was used.

Figure 5.30 shows the effect on the histogram of applying the median filter to the image in figure 5.29(a).

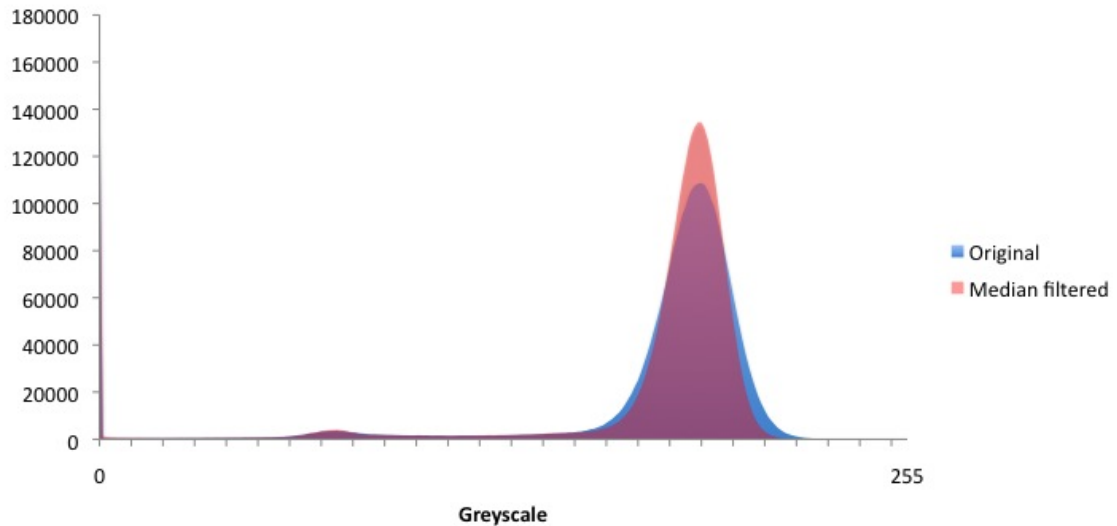


Figure 5.30: Effect of applying a  $3 \times 3$  median filter to the image in figure 5.29.

It was found that to successfully threshold the damage in the impacted specimens a high degree of manual interaction in association with histogram thresholding was required. The difficulty in thresholding arises because of the complicated and interacting nature of the damage. Delaminations and cracks effectively have a similar greyscale to the background (i.e. air), and so using a global threshold value easily separates the entire damage volume from the object. However, this is not a representative indication of the damage state as we would like to know the proportions and locations of each type of damage. Because the different types of damage have similar grey values, automatic greyscale thresholding is ineffective in separating the damage. In order to overcome this issue, the ‘*brush-within-range*’ tool in Avizo was used to locally threshold the damage areas in each impact sample. Segmentation was performed on every 5 CT slices, and an automatic interpolation applied to threshold the damage areas between the manually segmented slices. The greyscale range was set to include pixels with greyscale intensities ranging from the mean damage area value to 50% of the mean bulk material intensity. This approach is typical for edge detection thresholds, where the intensity varies over an edge such as the boundary between material and a crack. Visual criticism was used to confirm whether the correct pixels had been selected. Ideally a more robust algorithm for detection and separation of the damage features would be implemented, but time constraints prevented this approach. However, considering the correlation between the quantified CT damage results and those obtained using C-Scan, it can be proposed that a reasonable level of

accuracy was achieved using the current method.

Figure 5.31 shows how a combination of local histogram thresholding and manual segmentation allows the different forms of damage to be separated in a UD impacted sample.

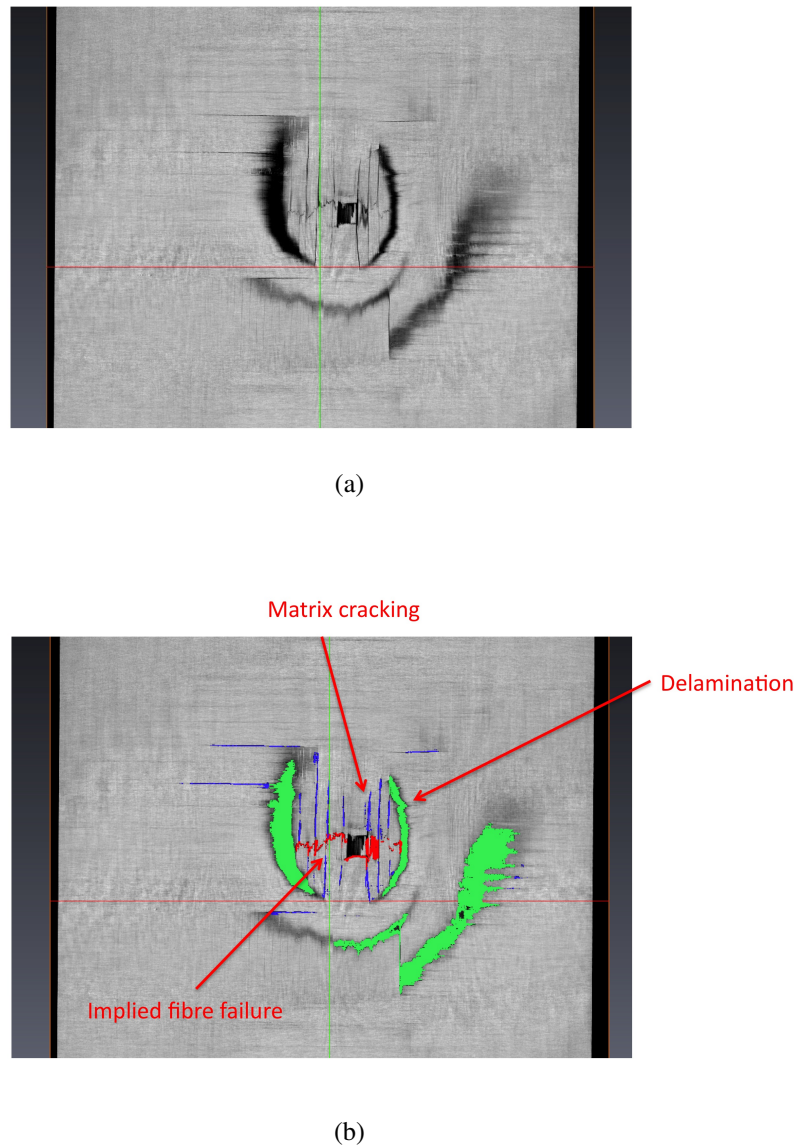


Figure 5.31: Example of damage thresholding in a UD plate which was subjected to 12 J impact. Sample is viewed in XY plane.

Due to the resolutions achieved in this experiment it was decided more appropriate to concentrate on the global damage present in the samples. In the case of the UD material, this meant restricting the damage segmentation to looking at only delaminations in the first instance. For the woven material, the difficulty in identifying the different damage features to acceptable accuracy also mean that the total damage area was measured in this

case. The next chapter which focusses on ROI imaging goes on to discuss the micro-mechanical damage features in more detail (i.e. matrix cracking and fibre/ tow failures).

### 5.8.2.2 Quantifying Damage in UD samples

By thresholding the delaminations for each sample at incremental impact energies, it was possible to define the area of delamination at each damage interface. In the first case, image masks were generated describing the encompassed area of each delamination within a given CT slice. Figure 5.32 shows an example of the image masks created for the first damage interface in a UD sample impacted at 3 J. The individual areas are summed to provide a greyscale image of the total damage area of the delamination, of which the area can be calculated knowing the pixel size and total number of pixels with a value greater than the background.

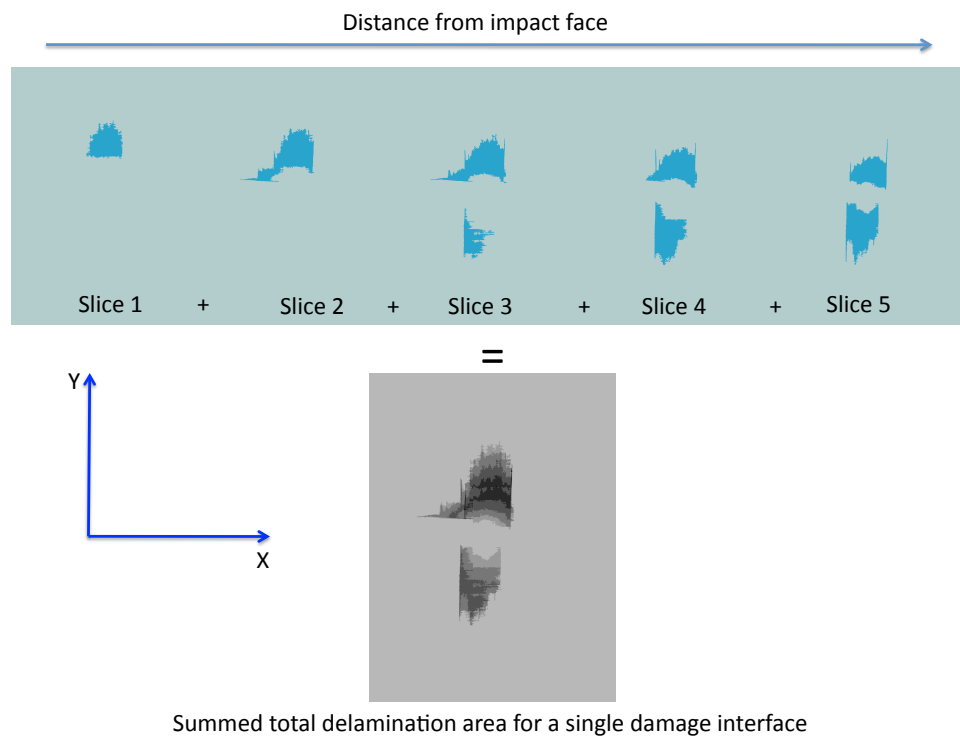


Figure 5.32: Summation of image masks encompassing delaminations with individual CT slices for a UD sample impacted at 3 J.

By repeating the above procedure, the delamination area for all damage interfaces can be projected onto a single image, and directly compared with C-scan data. Figure 5.33 shows summed masks for various impact energies compared to C-scan images. Side by side comparisons are for the same sample in each case.

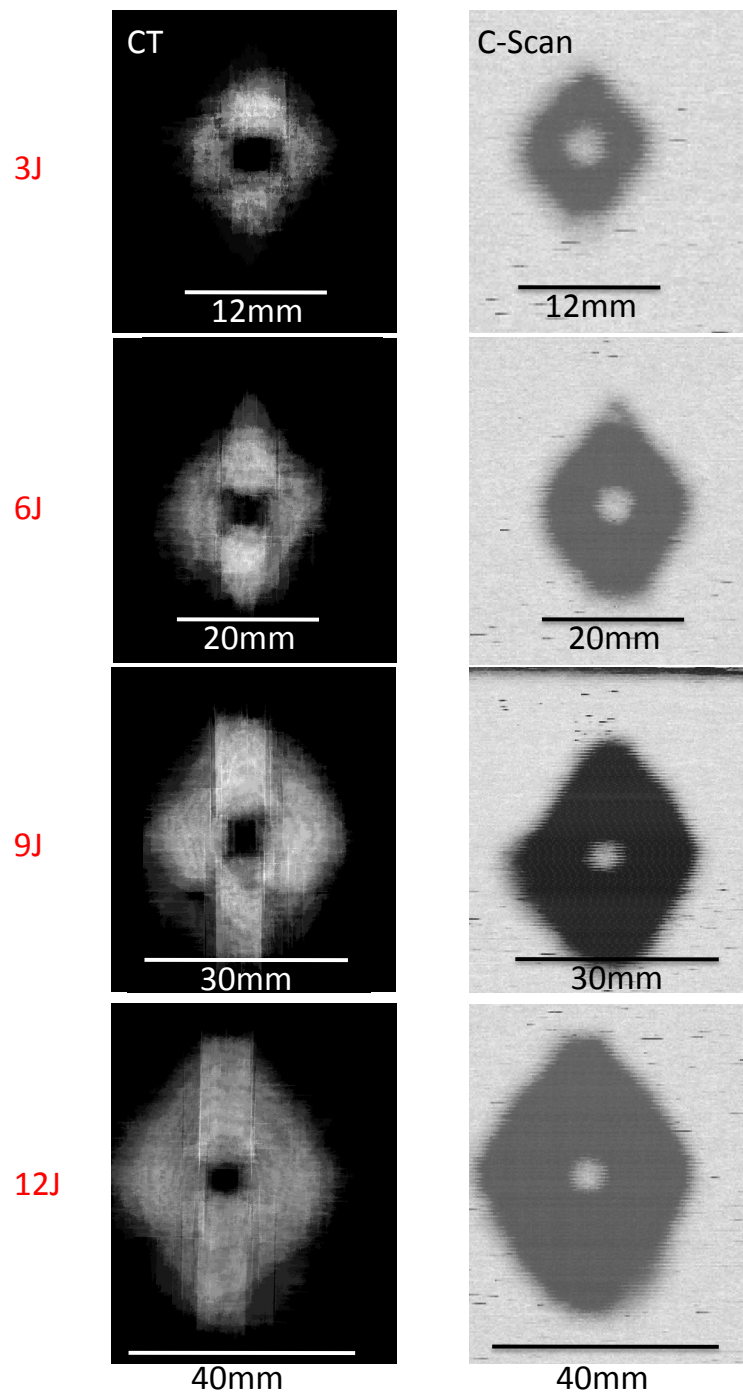


Figure 5.33: In-plane delamination area under increasing impact energies for UD material. CT images (left column) are through-thickness summations of total in-plane damage, compared against transmission C-scan data (right column).

Figure 5.33 shows that CT imaging provides very similar damage patterns and areas to transmission C-scan when summing the in-plane damage through the object thickness.

A characteristic diamond shaped pattern is formed, with an undamaged region in the centre corresponding to the impact location. This observation is characteristic of UD materials and has been reported in many publications. Although no delamination occurs in this region, it is not to say no damage occurs at all. In fact, plastic deformation was seen to occur under all impact energies at the impact face, causing indentation under the impactor and outward displacement at the back face. While this local plastic deformation does not appear to produce delamination, it is likely that damage perhaps in the form of fibre displacement, fibre failure, and matrix micro-cracking may have occurred directly under the impactor. However it was not possible to observe any of these mechanisms at a resolution of 50  $\mu\text{m}$ , which is logical as the carbon fibres in this material have a diameter of less than 5  $\mu\text{m}$ .

Figure 5.34 shows the in-plane damage areas measured using CT and transmission C-scan. The figures shows that a linear relationship exists between the damage area and impact energy. Each data point is a mean (plus standard deviation error bars) for 5 samples tested at each energy. The values for both methods agree well, and statistical analysis showed that due to the scatter, no significant statistical difference was observed between the two methods of measurement. Comparing the data sets for each impact energy found p-values of greater than  $p = 0.05$  in all cases.

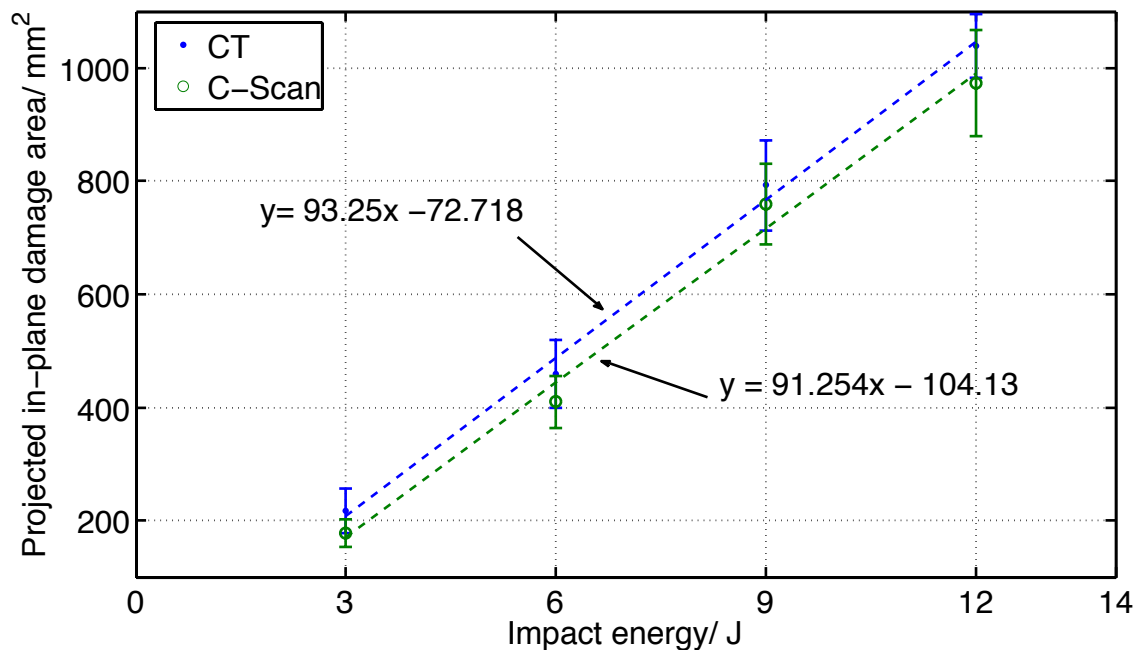


Figure 5.34: In-plane damage area for UD samples measured with CT and C-scan.

The results presented in figure 5.34 are consistent with papers such as Ambu *et al.* (2006); Choudhry (2009); Dear and Brown (2003); Tan *et al.* (2011a,b); Yan *et al.* (2010); Yang and Cantwell (2010), who all documented a linear relationship between impact and energy and damage area.

By plotting the evolution of damage area through the thickness of the plate, an idea

of how the damage propagates through the material can be obtained. Figures 5.35 to 5.38 show the measured damage area as a function of depth for each set of impacted samples. The figures show mean values (of 5 samples), bounded by the standard deviation. These values are taken from in-plane measurements direct from the CT reconstruction and are therefore not considering the out-of plane deformation which was discussed in figure 5.24.

In the 3 J case, seven damage interfaces are clearly defined by peaks in the damage area. These peaks are spaced at regular intervals, and correspond closely with the ply thickness. It can be seen that no damage was measured at the mid-ply boundary, a typical observation under impact conditions where the two plies about the mid-plane have the same orientation. This lay-up results in no stiffness mismatch at the symmetry, preventing delaminations from propagating into this layer.

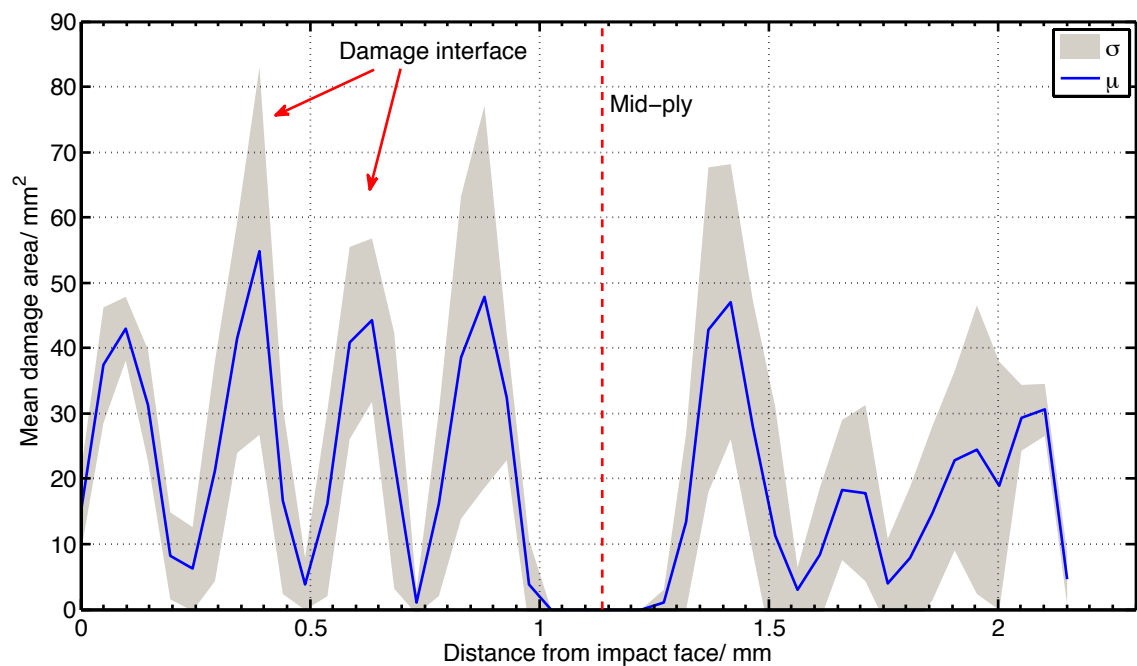


Figure 5.35: Mean damage area as a function of depth for the 3 J impact

With increasing impact energy, the following figures reveal that the damage area for each interface generally increases. Plotting the damage area with respect to depth, however, results in the damage peaks merging towards higher energies. This observation is again consistent with the increasing out of plane deformation, where damage from several interfaces appears in the same CT slice. This observation points out the importance of the interpretation of CT data when analysing objects with planar damage, but where the object is globally deformed. Damage at the symmetry plane, however, is seen to be virtually zero at all impact energies, as the central trough is maintained in all figures.

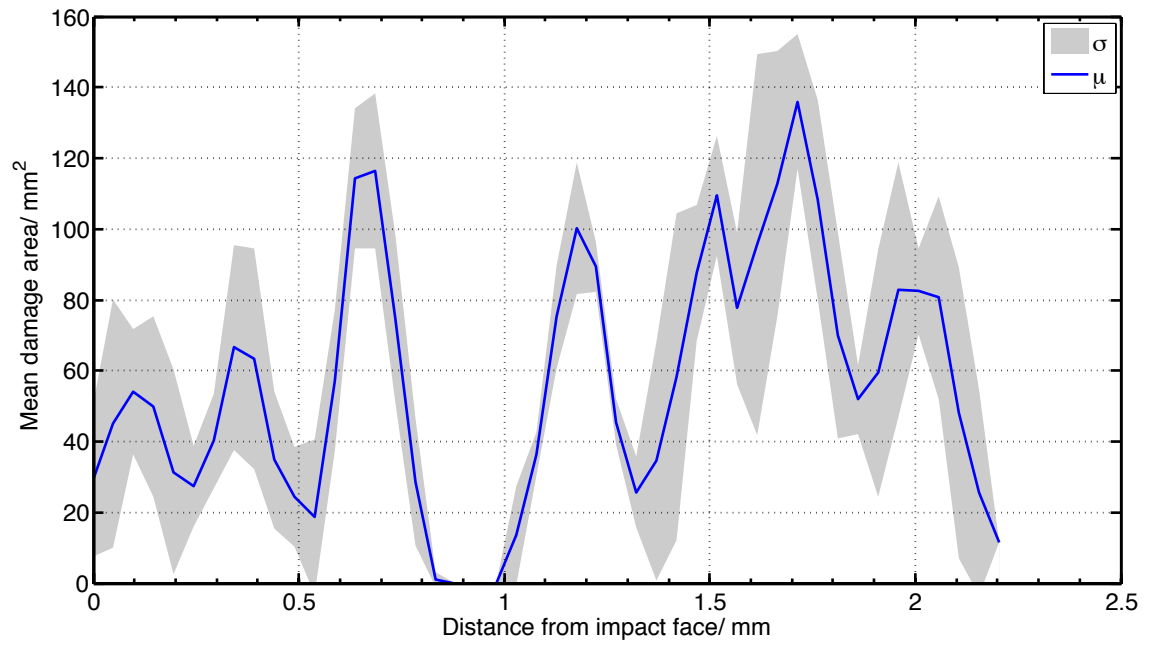


Figure 5.36: Mean damage area as a function of depth for the 6 J impact

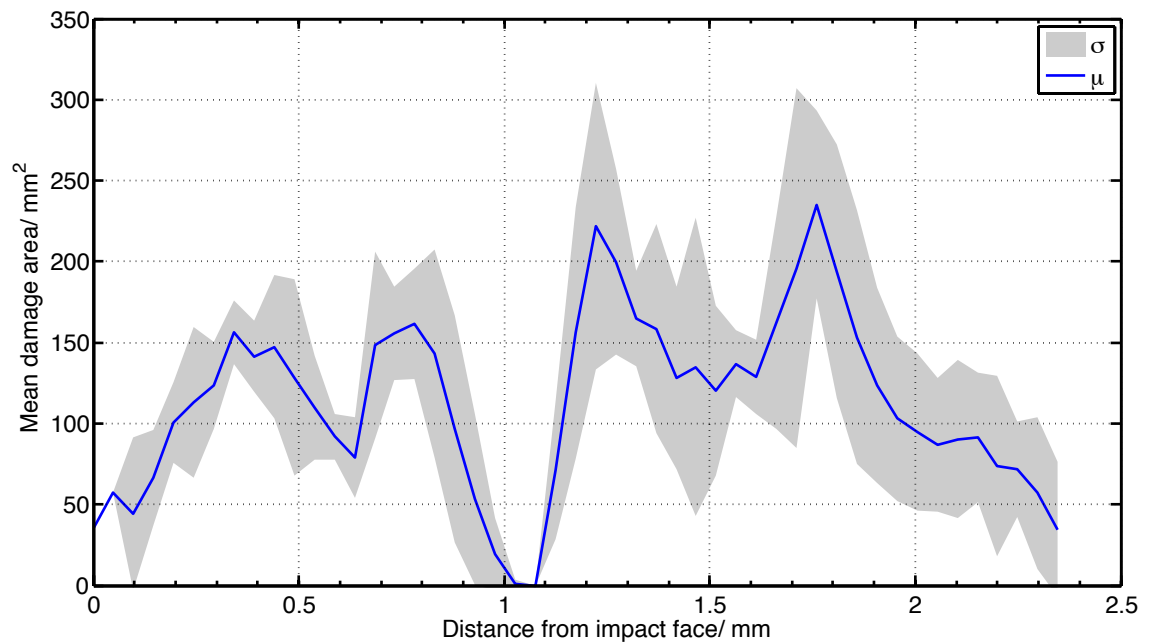


Figure 5.37: Mean damage area as a function of depth for the 9 J impact

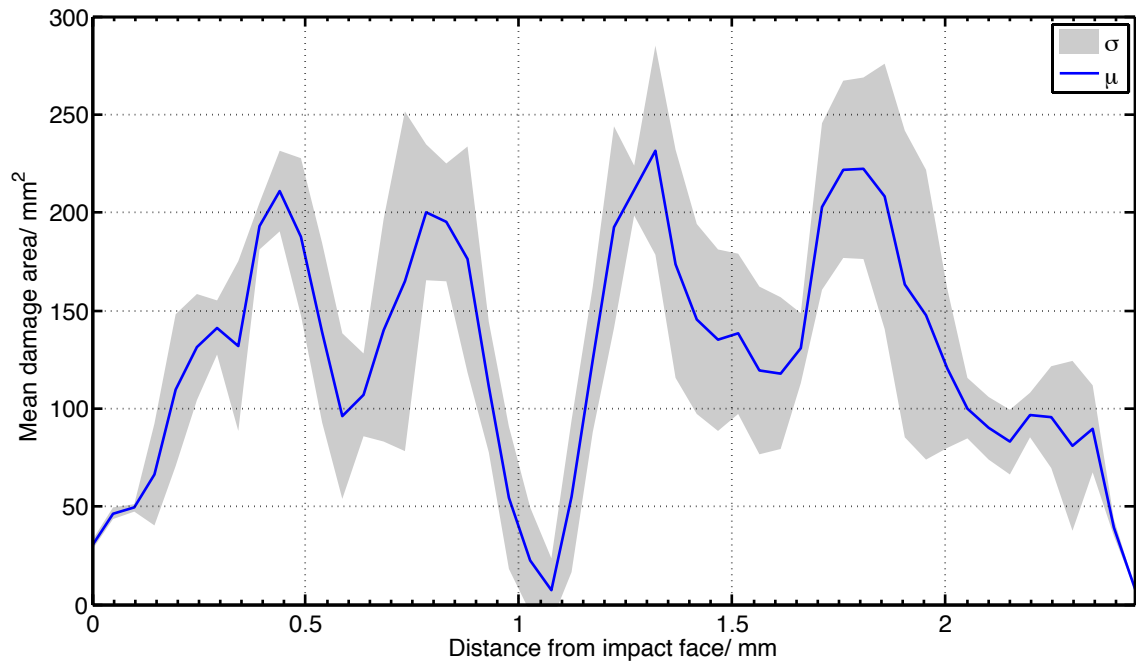


Figure 5.38: Mean damage area as a function of depth for the 12 J impact

Although the above figures give a general appreciation of the damage distribution in the samples, a more robust approach was taken to further quantitatively describe the damage. By measuring the in-plane areas of the individual damage interfaces by using the mask summation procedure described in figures 5.32 and 5.33 it was possible to accurately assess how the area of damage interfaces vary through the thickness of a particular sample, and under different impact energies. Figure 5.39 shows this distribution of interfacial damage for the various impact energies.

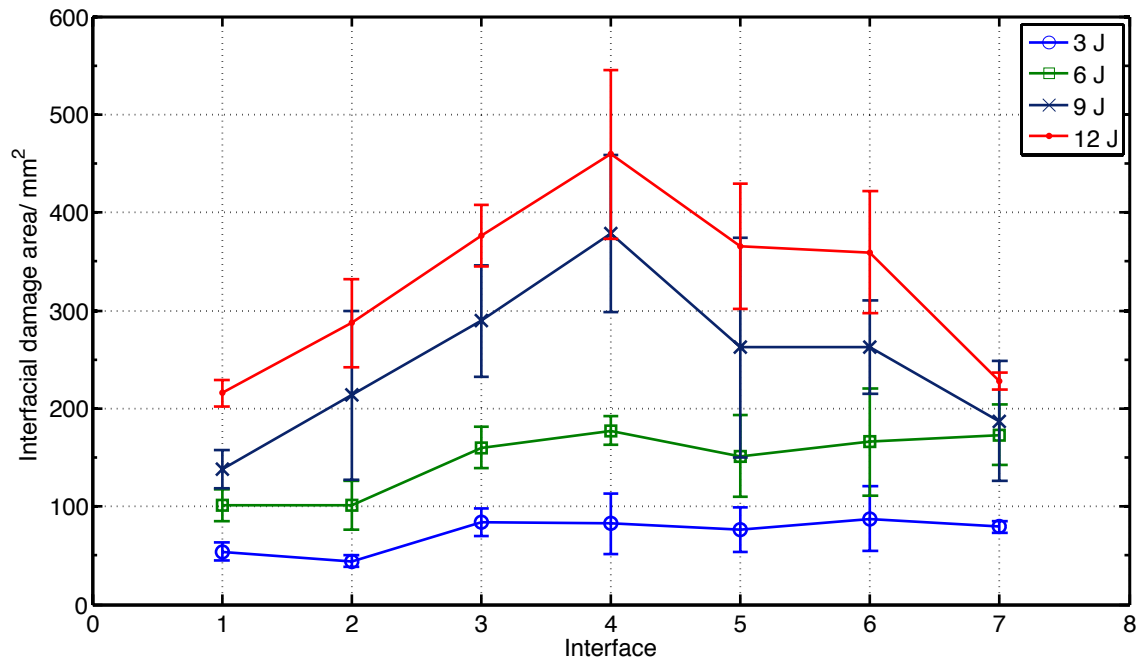


Figure 5.39: Interfacial damage area for individual ply interfaces under various impact energies for the UD material.

Considering the damage evolution in the 3 and 6 J samples from the data in figure 5.39, there is a fairly constant degree of damage at each interface. Performing un-paired T-tests (tables 5.11 and 5.12) showed in both cases that damage areas were only statistically different in the first two plies compared to the other interfaces. Damage area was observed to be lower in these first two plies by approximately 50% compared to the other interfaces. This reduced damage is probably due to compressive constraint directly under the impactor, causing ply compression and possible fibre damage as opposed to propagating delaminations in-plane. The damage then spreads out to form delaminations of equal area at the remaining interfaces. Examining the damage areas in the 9 and 12J samples, also reveals a similar trend. It would appear that a damage peak forms in the central plies in both cases, which would suggest a transition to a bending type failure due to the increased displacement during impact. Due to the high scatter in the results however, T-tests showed it was not possible to make this conclusion (tables 5.13 and 5.14). Again, the statistical tests showed no significant difference between the damage areas in the bulk of the sample, although the front and back face damage areas were seen to be significantly from the central interfaces. To make further conclusions it is proposed more repeat impact tests would have to be made. It is clear however, that damage at all interfaces is increasing at higher impact energies.

Table 5.11: P-values for interfacial damage areas after 3 J impact.

<b>Interface</b>	1	2	3	4	5	6	7
1	x	0.081	0.036	0.079	0.077	0.060	< 0.001
2	x	x	< 0.001	0.025	0.016	0.020	< 0.001
3	x	x	x	0.928	0.530	0.825	0.512
4	x	x	x	x	0.717	0.804	0.870
5	x	x	x	x	x	0.542	0.776
6	x	x	x	x	x	x	0.593
7	x	x	x	x	x	x	x

Table 5.12: P-values for interfacial damage areas after 6 J impact.

<b>Interface</b>	1	2	3	4	5	6	7
1	x	0.977	0.001	<0.001	0.036	0.432	0.018
2	x	x	0.004	<0.001	0.048	0.043	0.004
3	x	x	x	0.168	0.690	0.832	0.461
4	x	x	x	x	0.228	0.674	0.807
5	x	x	x	x	x	0.652	0.375
6	x	x	x	x	x	x	0.804
7	x	x	x	x	x	x	x

Table 5.13: P-values for interfacial damage areas after 6 J impact.

<b>Interface</b>	1	2	3	4	5	6	7
1	x	0.977	0.001	<0.001	0.036	0.432	0.018
2	x	x	0.004	<0.001	0.048	0.043	0.004
3	x	x	x	0.168	0.690	0.832	0.461
4	x	x	x	x	0.228	0.674	0.807
5	x	x	x	x	x	0.652	0.375
6	x	x	x	x	x	x	0.804
7	x	x	x	x	x	x	x

Table 5.14: P-values for interfacial damage areas after 12 J impact.

<b>Interface</b>	1	2	3	4	5	6	7
1	x	0.009	<0.001	<0.001	0.001	0.001	0.132
2	x	x	0.613	0.348	0.659	0.684	0.020
3	x	x	x	0.077	0.743	0.602	<0.001
4	x	x	x	x	0.086	0.068	<0.001
5	x	x	x	x	x	0.883	0.001
6	x	x	x	x	x	x	0.002
7	x	x	x	x	x	x	x

By considering the extent to which damage spreads horizontally and vertically from the impact zone, further insights into the failure processes can be gained. In all cases for the UD material it was found that the distance from the centre of the sample to the edge of any given damage interface increased with depth through the laminate, despite the fact that the individual damage areas did not significantly alter. Interestingly, the delaminations were observed to grow in preferential directions. Damage interfaces were seen to grow in preferential directions, alternately. For example, the first interface always grew in the 0° ply direction, followed by delaminations preferentially moving outwards in the 90° direction in every other interface. Figure 5.40 shows examples for a 12 J impacted sample.

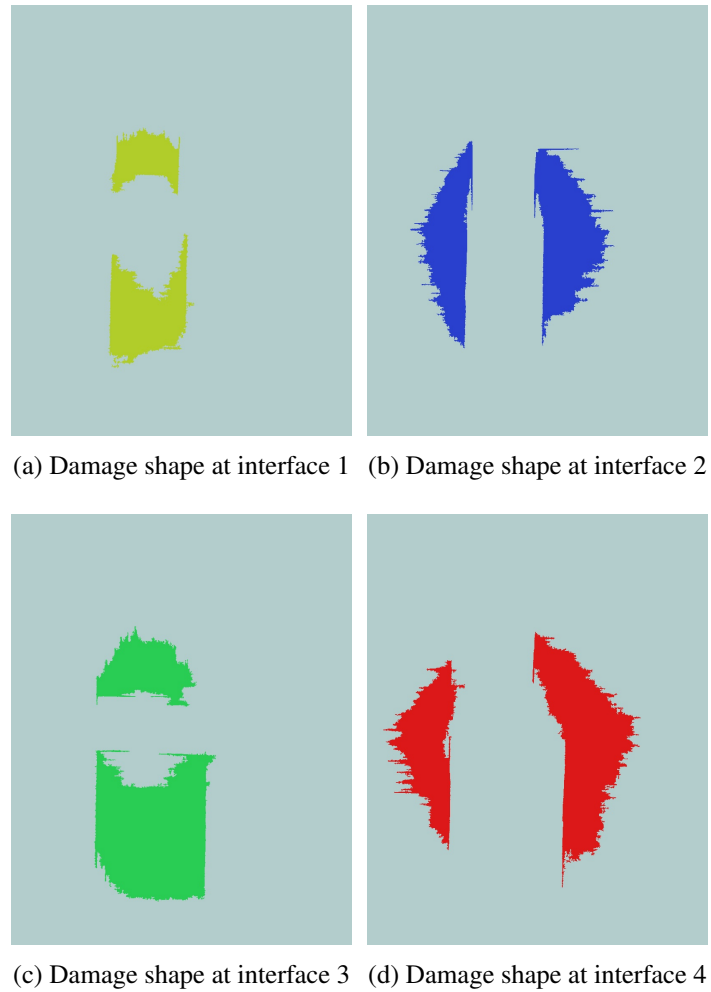


Figure 5.40: Typical damage shapes at ply interfaces in a UD sample impacted at 12 J.

This alternating damage shape has been reported as an artefact of the shear stress distribution through the sample (Bednarczyk *et al.*, 2007; Joshi and Sun, 1985; Richardson and Wisheart, 1996). The direction of delamination orientation, and subsequent direction of movement through the thickness of the laminate is dependent on the orientation of the ply above the delamination. An interface below a  $0^\circ$  ply will therefore move in that orientation. Figure 5.41 illustrates a recent solution proposed by NASA for how the dominant shear stress direction changes through the thickness of a quasi-isotropic laminate.

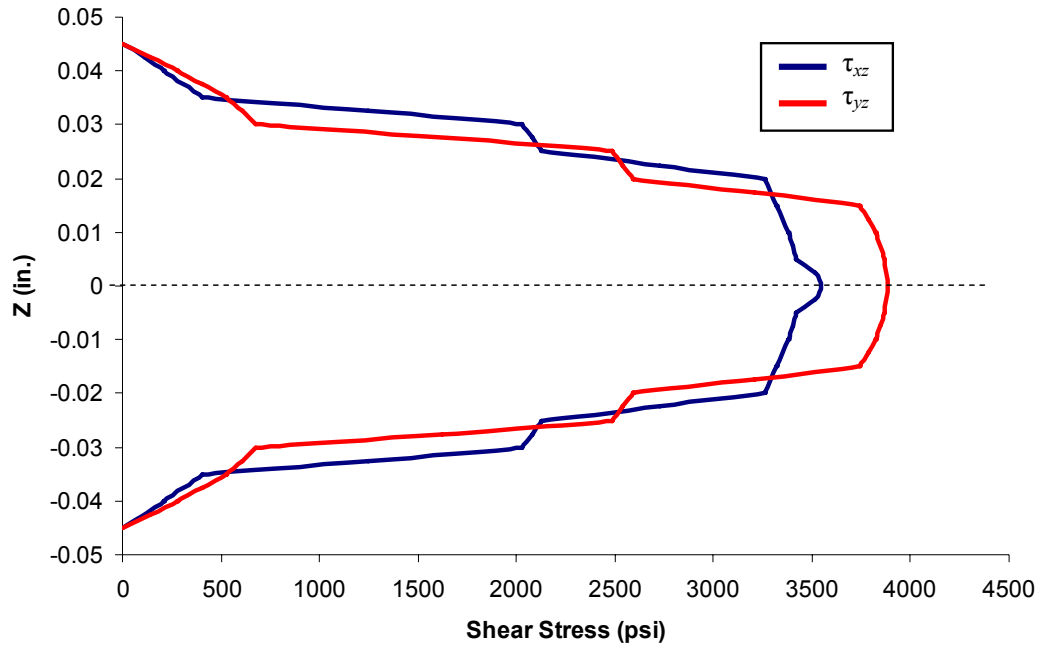


Figure 5.41: Distribution of shear stress in a quasi-isotropic laminate (Bednarczyk *et al.*, 2007)

Although the solution presented in figure 5.41 is not for the same lay-up configuration study used here, it provides an explanation of the mechanism which may be the cause of the alternating delaminations. Application of a laminate theory numerical analysis would be needed to provide the full evidence for this observation.

By comparing the maximum extents of the delaminations, further characterisation of the damage evolution can be obtained and related to impact and CAI results. Figure 5.42 shows the how the maximum horizontal and vertical damage extents vary with impact energy.

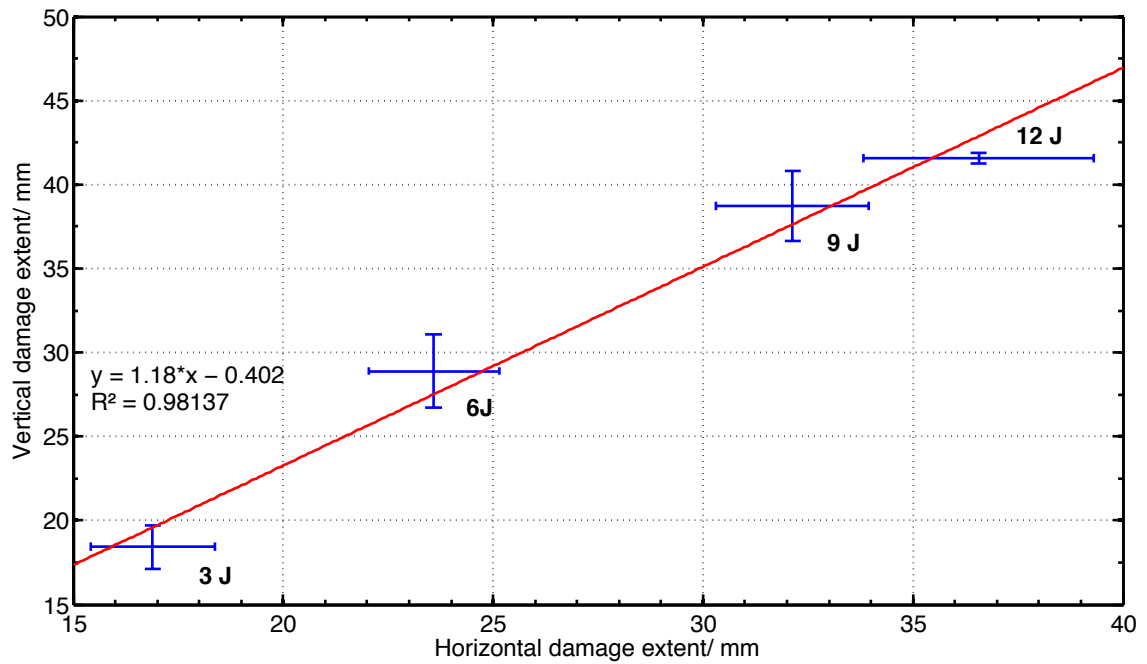


Figure 5.42: Horizontal and vertical damage extent in UD samples under various impact energies.

Figure 5.42 shows a linear relationship between vertical and horizontal damage extent with increasing impact energy. The trend is biased slightly towards the vertical damage extent, but in the case of 12 J, the damage was constrained by the edge of the aperture holding the sample. This observation would suggest that the damage is a function of both horizontal and vertical damage extent, in addition to the plastic damage induced under the impactor. By increasing the vertical damage extent, the support of the central  $0^\circ$ plies is reduced, increasing the likelihood of buckling during CAI testing. Additionally, the increasing horizontal extent of damage reduces the cross sectional area available for stress transfer to the fibres, effectively reducing the load bearing area for sustaining compression load- also leading to a reduction in CAI strength. Many papers have been published in the literature regarding the direct cause of CAI failure, and many different damage parameters have been suggested as the most important for correlating damage and CAI results. For example, Prichard and Hogg (Prichard and Hogg, 1990) proposed damage width due to delamination was the main damage criterion effecting failure, due to the residual area to support compressive load. Projected delamination area (de Freitas and Reis, 1998) and delamination area coupled with impact induced fibre damage (Soutis, 1997; Soutis and Curtis, 1996) have also shown to be suitable criteria. The results shown here seem to reinforce the observations found in the literature. Although it is beyond the scope of this work to improve understanding of the fundamental damage mechanisms, it has been shown that CT can be used to quantify damage in a way which complements more detailed studies of failure from a mechanics/ analysis perspective using other techniques (such as optical microscopy and C-scan).

### 5.8.2.3 Quantifying Damage in Woven Samples

Initial quantification on the woven samples was performed in the same manner as for the UD samples, using the mask summing procedure previously described in figure 5.32. Figure 5.43 compares the damage area masks for CT vs. the areas obtained from the transmission C-scan. Although both measurement techniques reveal a characteristic damage area, in this instance the CT appears to reveal less damage area than the C-scan. The CT images do, however, reveal an intensity variation which highlights a higher degree of damage in the centre. This intensity variation is not apparent in the C-scan images due to the inability of transmission C-scan to differentiate overlaid damage. Interestingly this comparison between CT and C-scan is in contrast to the measurement for the UD materials where measurements were statistically identical over the full range of samples measured. By plotting the measured damage area in the woven samples and comparing the CT and C-scan measurements, there is a significant disparity between the measured area (figure 5.44).

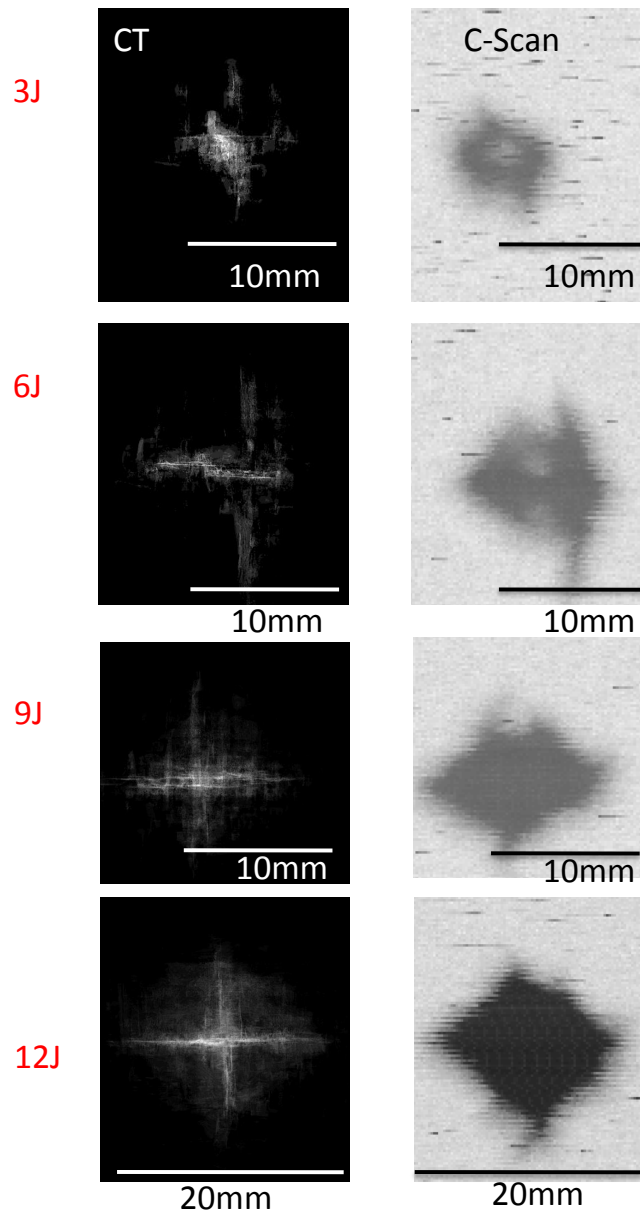


Figure 5.43: In-plane damage area under increasing impact energies for woven material. CT images (left column) are through-thickness summations of total in-plane damage, compared against transmission C-scan data (right column).

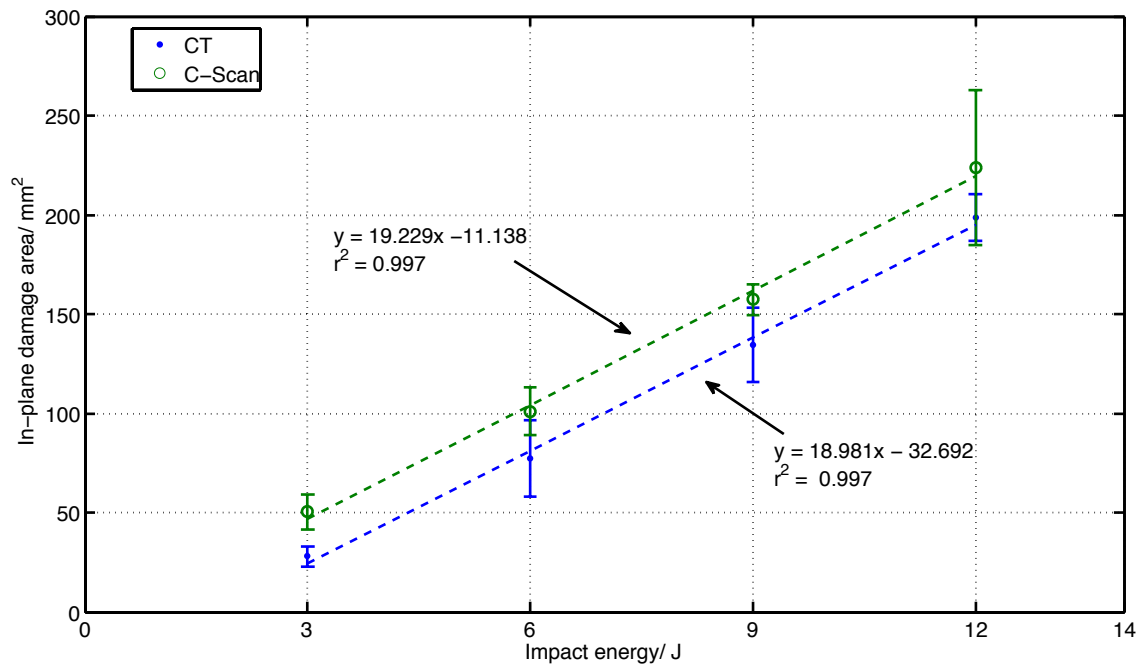


Figure 5.44: Variation of in-plane damage area with impact energy for woven material.

Two possible explanations exist for the differences in measured areas observed in figures 5.43 and 5.44. The first is due to the partial volume effect; the resolution achieved in imaging the entire sample, coupled with the scale of individual damage features means that these features only occupy several pixels through the thickness of the object. This results in a reduced grey value for the damage compared with larger damage features (i.e. those seen in the UD samples), causing fewer pixels to be selected for a given threshold. The second, and possibly additional, reason could be due to the user's discretion when thresholding. As the damage appears very similar in greyscale to resin pockets found in the woven material, it was very difficult to assess which features were actually damage at this resolution. Examining the graphical relationship in figure 5.44, however, would suggest this is unlikely as the gradients of the CT and C-scan trend lines are virtually identical. It would be very difficult to achieve such a close trend if manual error were the sole cause of thresholding differences.

Despite any errors which may be arising in the thresholding, the results still convey the fact that the relationship between impact energy and damage area is linear (as was seen in the UD materials). By examining the evolution of damage through the thickness, we can see that damage in the woven materials initiates at the front and back surfaces at low energies, before propagating into the central regions at higher energies (figures 5.45 to 5.48). Making statistical comparisons, however, was difficult with the woven material due to the high frequency of small delaminations and cracking regions. This meant that specific damage interfaces between plies were not observed.

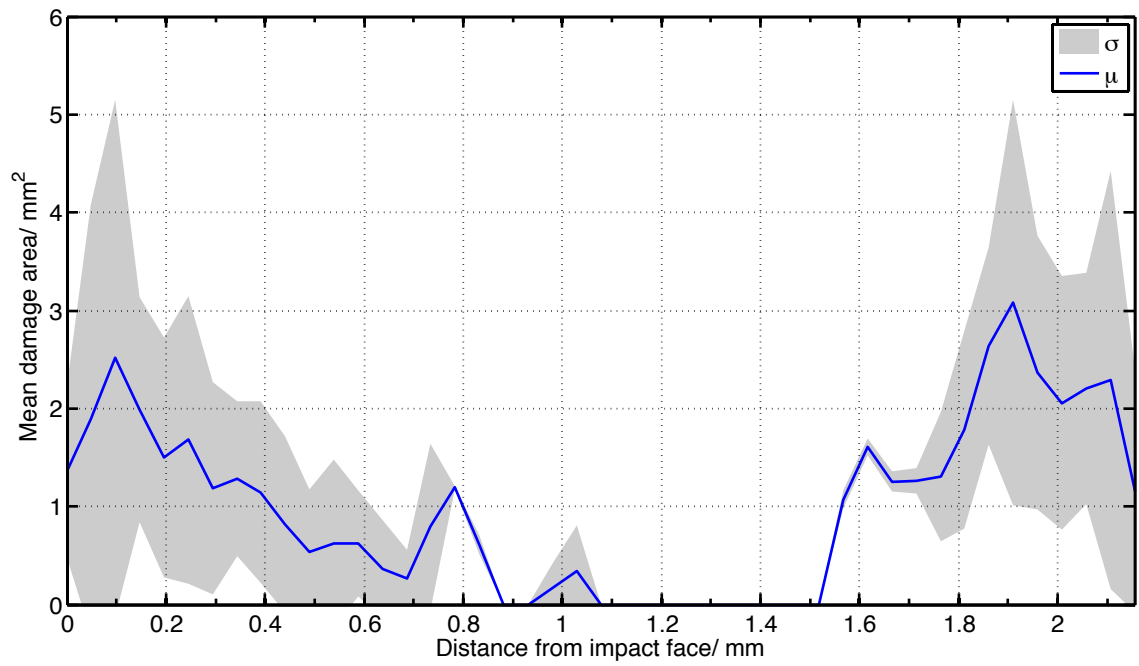


Figure 5.45: Mean damage area as a function of depth for the 3 J impact

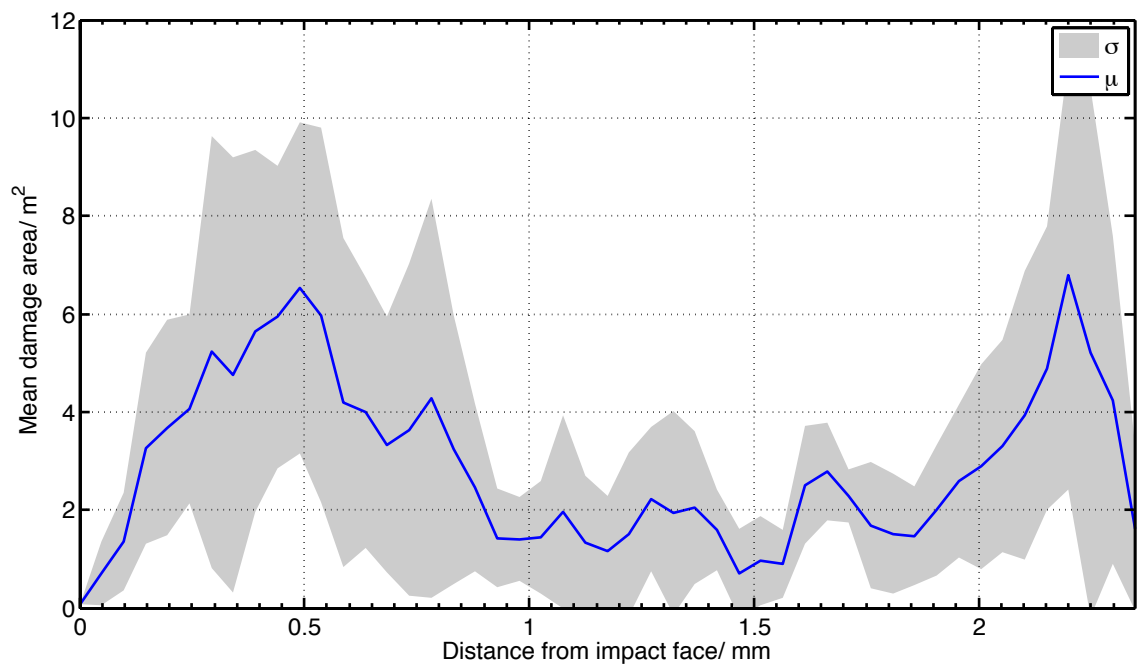


Figure 5.46: Mean damage area as a function of depth for the 6 J impact

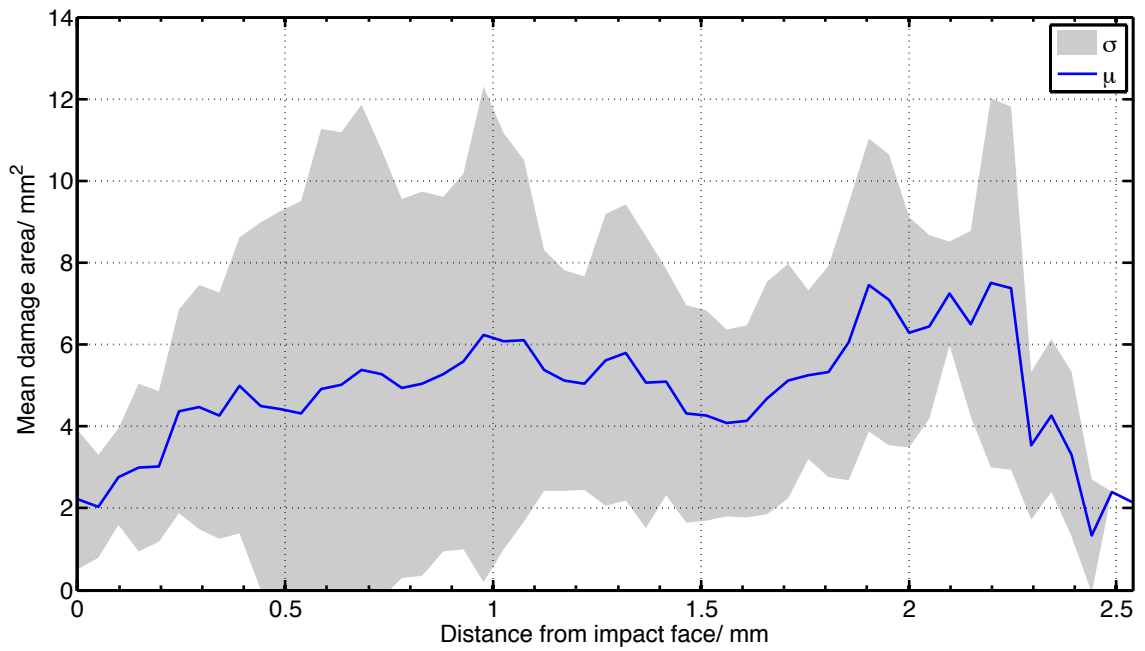


Figure 5.47: Mean damage area as a function of depth for the 9 J impact

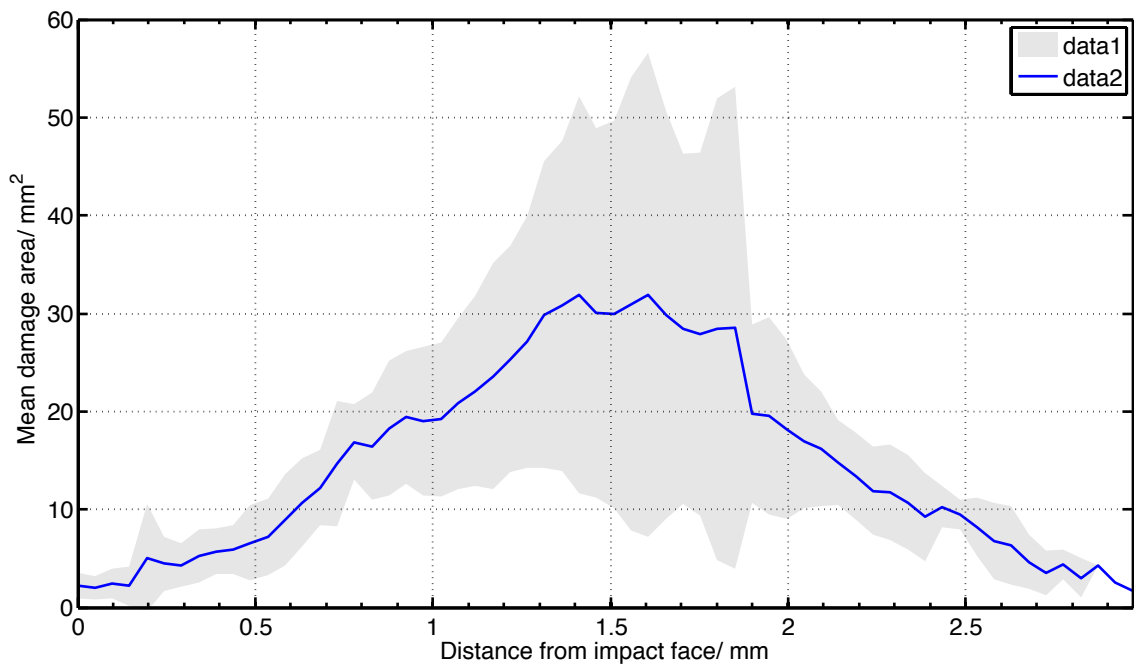


Figure 5.48: Mean damage area as a function of depth for the 12 J impact

Interestingly, the extent of damage (i.e. the horizontal and vertical distances over which damage was spread) did not appear to change through the thickness of any given plate. In contrast to the UD material, where interfacial damage moved away from the impact site through the plate thickness, it appears the damage is constrained to the region under the impactor for the woven materials.

As figure 5.49 shows, a linear relationship exists between the vertical and horizontal damage extents, but even at 12 J, the damage extent only just exceeds the diameter of the

impactor (20 mm). This feature is a common property of woven materials, whereby the fibre tow waviness increases crack path tortuosity and prevents delamination and crack growth outwards (manifested as an increased fracture toughness), but allows propagation of damage down into the plate. By preventing outwards crack growth, the reduction in compression strength (as a fraction of the undamaged strength) is less severe in the woven materials. This characteristic was shown experimentally to be the case in section 5.5.

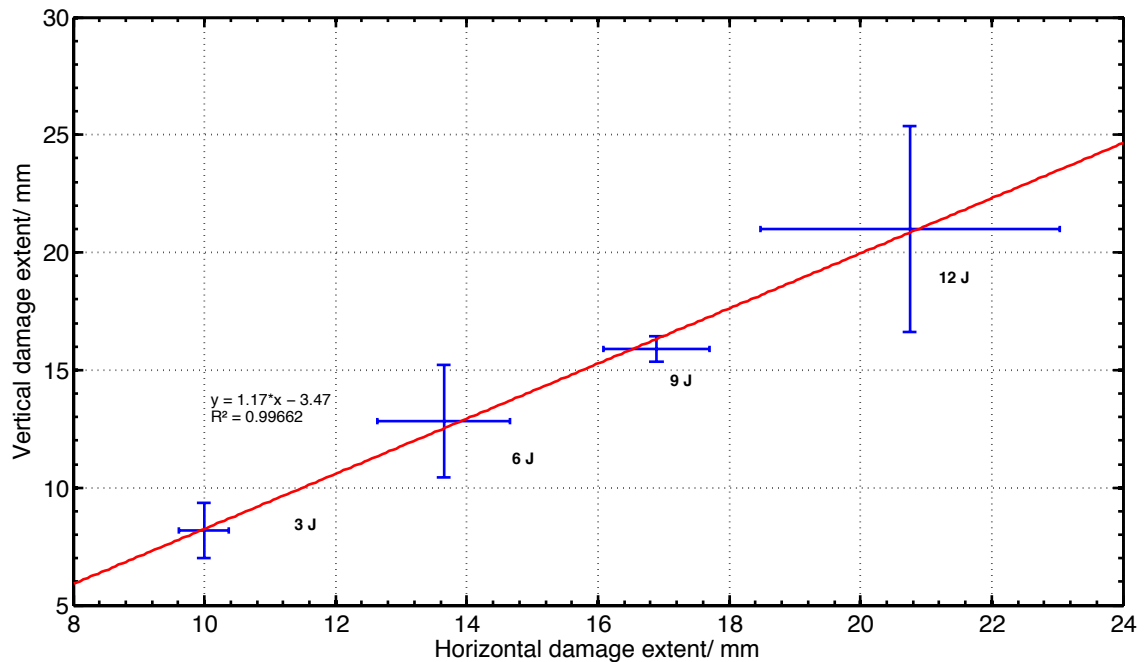


Figure 5.49: Horizontal and vertical damage extent in the woven material under various impact energies.

With reference to the interlaminar shear strength tests which were reported in section 5.6, the CT imaging results show that the high ILSS of the UD material prevents significant damage propagating directly down from under the impact point. Instead, the damage clearly moves away from the impact zone through delamination. Conversely, the reduced ILSS of the woven composite means that failure of the matrix can occur more easily in the through-thickness direction. In-plane damage progression however, is halted by the waviness of the fibre tows which increase the in-plane fracture toughness. These observations are demonstrated further in the section regarding region of interest imaging, Chapter 6.

## 5.9 Chapter Summary and Conclusions

The work presented in this section has shown that CT can be used as an effective tool in the non-destructive evaluation of impact damage in miniaturised CAI plates, in both UD and woven materials. The imaging technique allowed the identification of the types of damage in both materials. For the UD materials, matrix cracking, delaminations and

implied fibre failures were identified as damage mechanisms. Similar damage was observed for the woven materials, although significant fibre tow failures were seen to occur at higher impact energies. The resolution achieved in imaging the woven materials however prevented a level of analysis comparable with that performed on the UD materials being achieved.

An image segmentation and masking methodology allowed the quantification of damage in both materials, which allowed measurements to be compared to transmission C-scan data. It was found that measurements made on the UD materials agreed well between CT and C-scan, but a significant difference was observed when comparing data for the woven materials. The relatively low resolution and partial volume effects were deemed to be the case for this disparity in measuring the woven samples, and it was proposed that a region of interest CT experiment should be performed to better identify the damage mechanisms in woven materials.

The quantification methodology allowed CT data to be related to observations on impact damage and CAI failure made in the literature by other methods. The results obtained in this study agreed well with that found in the literature, and by characterising damage in 3D, observations made in the literature have been strengthened by supporting evidence.

Regarding the damage results observed here compared to those in the literature, the impact damage response of UD and woven CFRP materials has been well documented. Early work on experimental characterisation of impact damage by authors such as Bradshaw *et al.* (1973); Cantwell and Morton (1990); Chamis *et al.* (1972); Dorey *et al.* (1985); Joshi and Sun (1985); Morton and Godwin (1989); Rogers (1971) highlighted the characteristic damage mechanisms and shapes of delamination patterns. The results shown here are consistent with this early work. Work presented in this thesis has further confirmed results by authors such as Ambu *et al.* (2006); Choudhry (2009); Dear and Brown (2003); Tan *et al.* (2011a,b); Yan *et al.* (2010); Yang and Cantwell (2010), concerning issues such as the relationship between damage area and impact energy, compression after impact relationships, and the types of damage present in the materials. As these characteristic damage mechanisms and patterns are so well documented, more recent papers have not substantially added to the fundamental understanding of impact damage processes. However, these more recent papers have generally used experimental damage observations to provide evidence in support of advances in damage models, materials improvements such as resin toughening, or validation of NDT processes (as in this work).

## REGION OF INTEREST IMAGING OF IMPACT DAMAGE IN CFRP

### 6.1 Introduction

This chapter covers the application and assessment of two different data completion methods for performing region of interest (ROI) imaging on impact damage in CFRP materials. The work in Chapter 5 demonstrated the ability to characterise damage by imaging the full object, but was not able to provide sufficient resolution for high quality imaging of matrix cracking in either candidate materials. Imaging was particularly difficult in the woven material due to the high number of very small cracking features, and low contrast between resin pockets and damage. Impact samples of both materials were therefore imaged under region of interest conditions to assess damage at a higher resolution. To assess the effectiveness of ROI data completion methods, two algorithms were applied to ROI scans of an impacted CFRP coupon. ‘Level’ extension and ‘cosine’ extension methods were used, and are described in detail in section 6.3.2. The effect of the number of projections taken under ROI conditions was also explored and compared with the data completion methods.

Samples of UD and woven materials impacted at 3, 6, 9 and 12 J were then imaged under region of interest conditions to assess the damage at a high resolution.

The aims of this work were therefore to:

- Modify existing ROI algorithms, allowing them to function on the micro-CT systems at the HMXIF
- Assess the practical application of two ROI algorithms for imaging damage in CFRP laminates
- Apply ROI imaging to characterise damage at a high resolution

## 6.2 Background

Under ideal circumstances, CT imaging of objects using cone beam geometry should be performed with the entire object within the FOV of the detector. If this is not the case, truncation and missing data artefacts can arise. The type of artefacts which can arise were discussed in Chapter 3, along with the various methods which have been implemented to overcome these. Figure 6.1 is an illustration from Amos (2010), which gives a simplified overview of how missing data occurs due to ROI scanning.

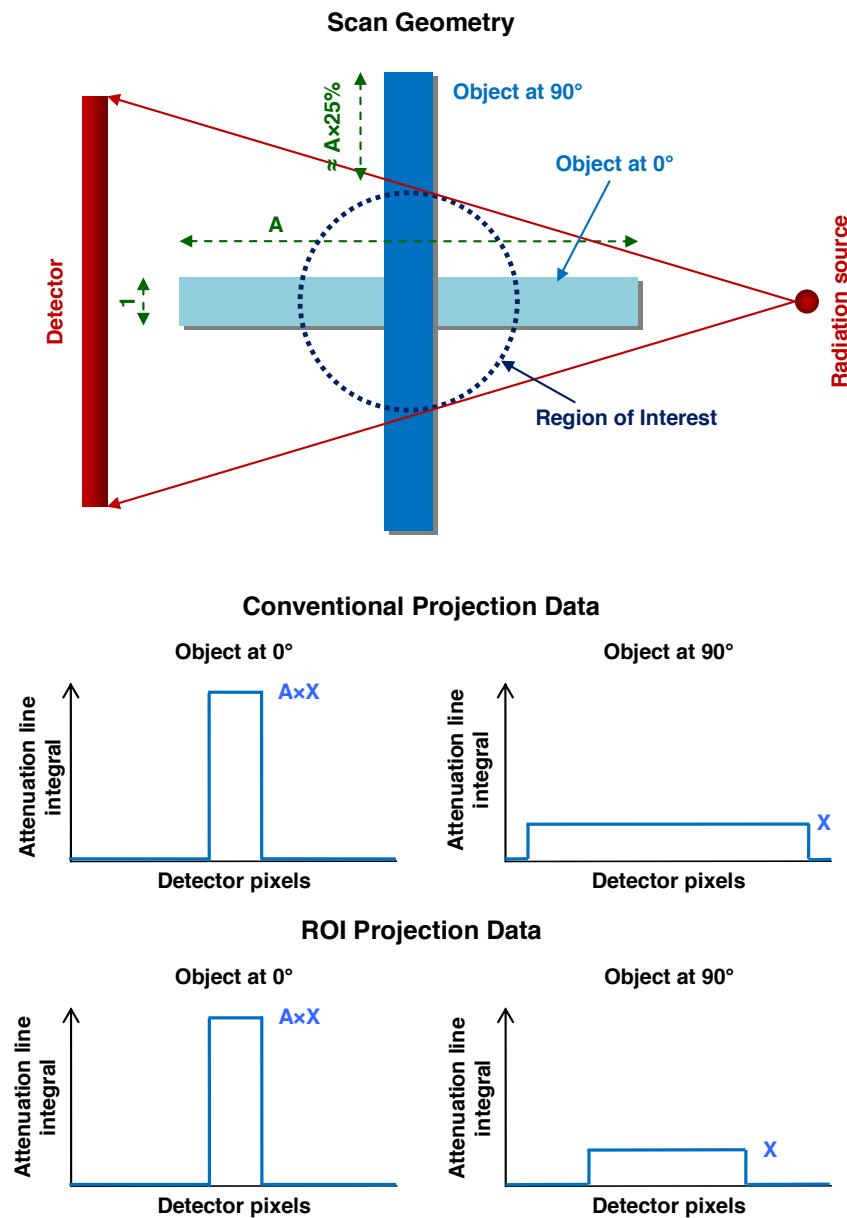


Figure 6.1: Simplified explanation of missing data problem.

Figure 6.1 illustrates that by filling the FOV with only 50% of the maximum object dimension, projections taken at  $90^\circ$  contain 50% of the attenuation information compared to projections at  $0^\circ$ . This mismatch in attenuation data is the cause of truncation and missing data artefacts.

In many circumstances it may be necessary to image a CFRP sample under high magnification conditions, but undesirable to physically section the object to fit within the FOV. The work presented here, considering impact damage, is a perfect example of the need for ROI imaging. Cutting the sample is undesirable for two reasons. Firstly that sectioning may propagate or change existing damage. Secondly, further mechanical testing may be required on the samples which are being imaged, as was done in this work by CAI testing.

To assess the effectiveness of ROI data completion methods, two algorithms were applied to ROI scans of an impacted CFRP coupon. 'Level' extension and 'cosine' extension methods were used, and are described in detail in section 6.3.2. Samples of UD and woven materials impacted at 3, 6, 9 and 12 J were then imaged under region of interest conditions to assess the damage at a high resolution.

To the authors knowledge, no ROI imaging concerning impact damage in CFRP on laboratory micro-CT systems has been published.

## **6.3 Assessment of ROI data completion methods**

To assess the effectiveness of ROI data completion methods, two algorithms were applied to ROI scans of an impacted CFRP coupon. A level extension and cosine extension methods were used, and are described in detail in section 6.3.2 This coupon was of the same dimensions as those imaged in Chapter 5, and was impacted using the drop weight impact tower at an energy of 12 J.

### **6.3.1 Imaging Experimental Method**

A coupon of UD CFRP consisting of 10 plies and measuring 89 x 55 mm (as used in Chapter 5) was CT imaged under ROI conditions by setting a magnification whereby the magnification results in the object exceeding the detector FOV. This experimental set up is shown in figure 6.2. The imaging conditions for the CT scan are provided in table 6.1. A second scan was also performed with the sample physically cut to the size of the original ROI, so that the width of the object fell within the detector FOV. Imaging conditions were otherwise exactly the same as for the ROI scan.

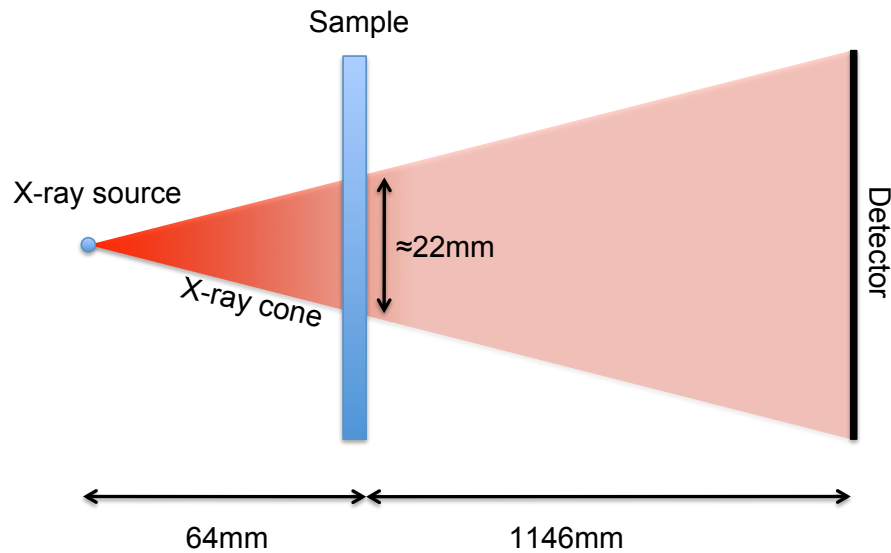


Figure 6.2: ROI imaging setup

Table 6.1: Image conditions for ROI imaging of impact test coupon

Image Variable	Condition
Target Material	Molybdenum
Accelerating voltage	80 kV
Filament current	250 mA
Frame exposure time	1 s
Number of projections	3142
Rotation angle	360°
Magnification	18 X
Effective pixel size	11 $\mu\text{m}$
Approximate field of view	22 mm

### 6.3.2 Data Completion Methods

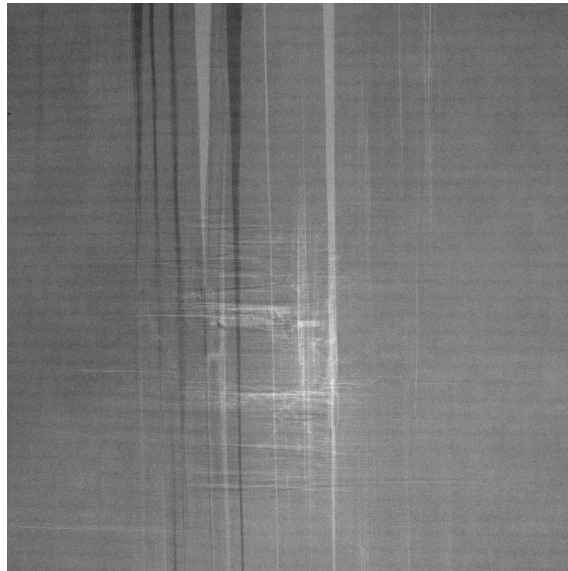
Two data completion methods were applied to the ROI data set. The first was a level extension method, proposed by Kyrieleis *et al.* (2010). This method extends the radiographic projections at each side of the projection by a set amount. The pixel values for each edge's extension are the same as the edge pixel value at the corresponding side of the object. The second method uses a sinogram extension, whereby the edge values are tailed off to the background intensity using a half sine wave function. The equation of the sine wave was specified by Amos (2011) as shown in equation (6.1).

$$y = \frac{(y_1 + y_2)}{2} + \frac{(y_1 - y_2)}{2} \cos \left( (x - x_1) \frac{\pi}{d} \right) \quad (6.1)$$

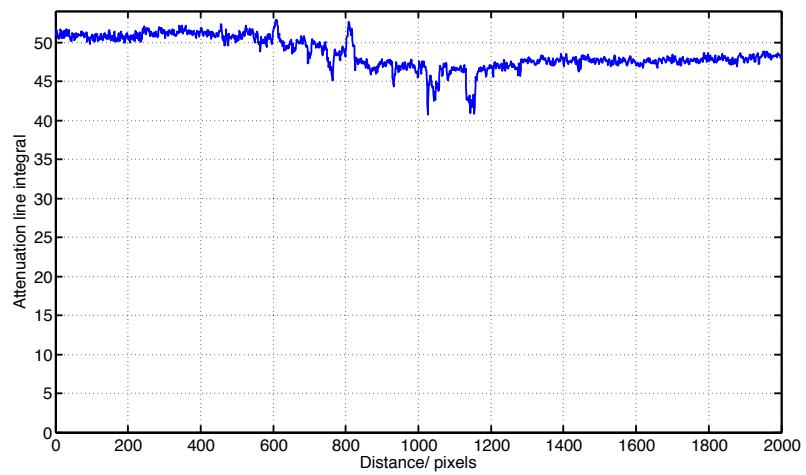
Where  $y_1$  is the start pixel value,  $y_2$  is the end pixel value,  $x$  is the pixel number,  $x_1$  is the first pixel number and  $d$  is the length of the tail (Amos, 2011).

In both extension cases Matlab code was used to apply the corrections to the original projection sets. The Matlab code was provided by Matt Amos (a previous EngD student), but was modified to account for the larger detector on the Nikon Metrology Custom Bay, and to interface with the current version of the reconstruction software CT Pro. For each completion method three sets of projections were generated, using 100, 500 and 1000 pixel extensions at each edge of the projection. This resulted in projections measuring 2200, 3000, and 4000 pixels across respectively.

Figures 6.3 to 6.6 show an example projection from four of the data sets, along with a corresponding attenuation line integral profile across the projection. The attenuation line integral is shown rather than a simple line profile across the object, as it is this parameter which is reconstructed. The attenuation line integral is simply the negative logarithm of the original projection. Starting with the original ROI data set (6.3, figures 6.4 and 6.5 then show examples of data completion with 500 pixel extensions. The data sets with 100 and 1000 pixel extensions have similar characteristics, the pixel extension length just varies. Figure 6.5 details that using the cosine extension method achieves a close match with the ‘ideal’ projection, where the entire object fits within the detector FOV (see figure 6.6).

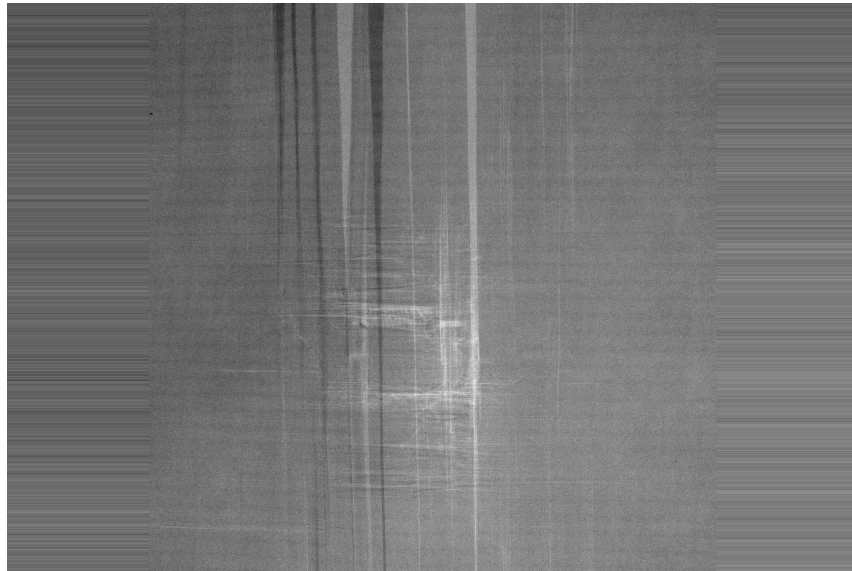


(a) ROI projection of impact damage area

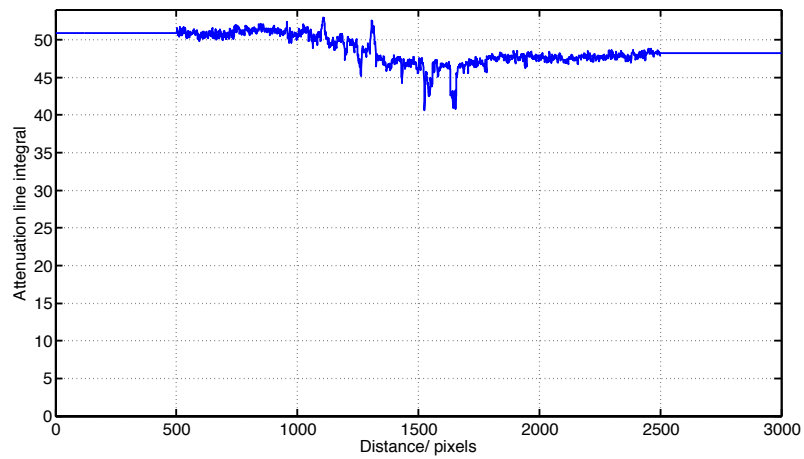


(b) Attenuation line integral across central pixel row in (a)

Figure 6.3: Projection and line profiles with no data completion.

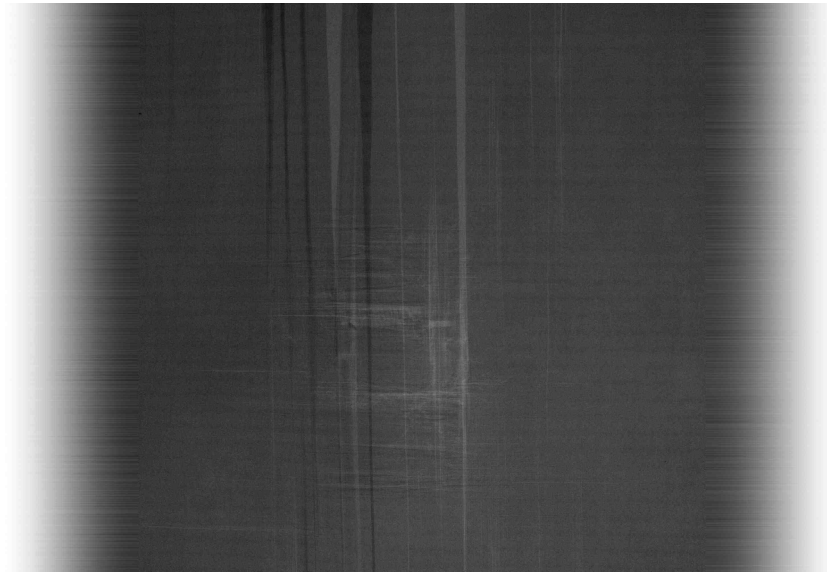


(a) ROI projection of impact damage area with a 500 pixel level extension at each edge

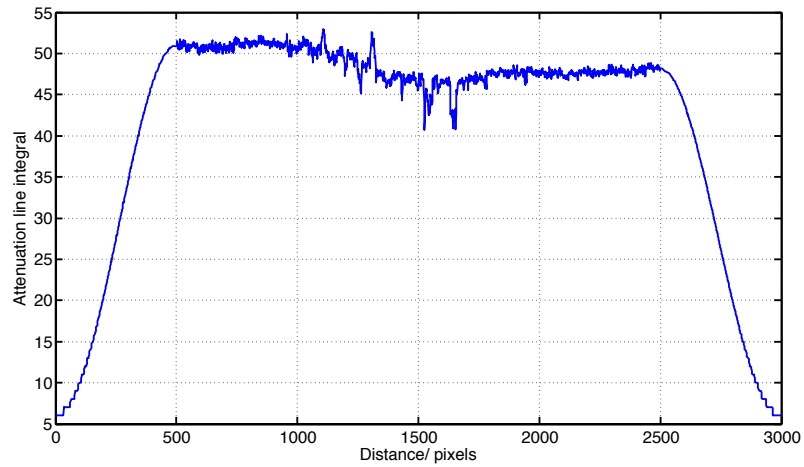


(b) Attenuation line integral across central pixel row in (a)

Figure 6.4: Projection and line profiles with level extension data completion.

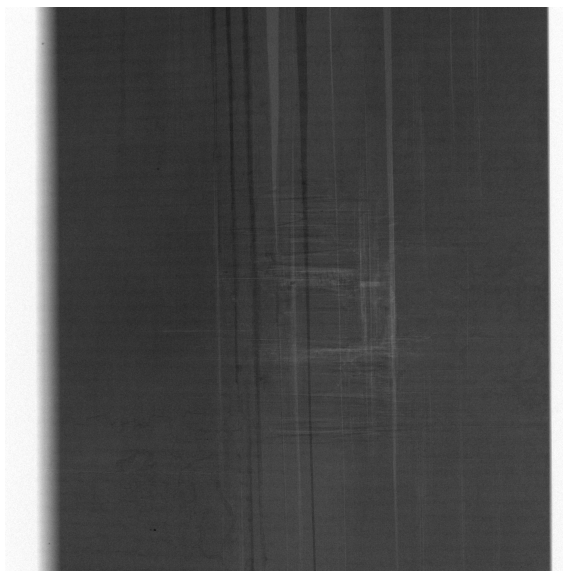


(a) ROI projection of impact damage area with a 500 pixel cosine extension at each edge

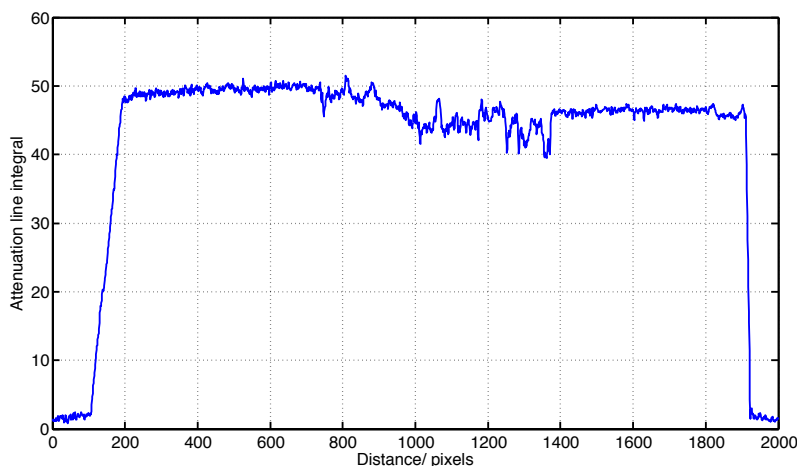


(b) Attenuation line integral across central pixel row in (a)

Figure 6.5: Projection and line profiles with cosine extension data completion.



(a) ROI projection of impact damage with sample physically sectioned



(b) Attenuation line integral across central pixel row in (a)

Figure 6.6: Projection and line profiles with object sectioned to fit within ROI field of view.

### 6.3.3 Results and Discussion

This section presents image analysis results from the ROI imaging experiments. Initially, a comparison between ROI imaging and physically sectioning the sample is made. An analysis of the data completion methods then follows.

#### 6.3.3.1 ROI vs. Sectioning

The central slice from each data set was reconstructed using the commercial reconstruction software CT Pro, using all 3142 projections. These central slices were output in 32-bit floating point number form to preserve the original greyscale values, allowing a direct comparison to be made between different data sets.

Comparing the original ROI scan with no data padding against the scan performed on the physically sectioned sample highlights several features. Firstly, the noise in the ROI scan is significantly higher than in the sectioned scan. Secondly, a general loss in signal intensity within the object is seen in the ROI scan, apparent as reduced object brightness. A bright ring around the edge of the reconstruction in the ROI is also apparent. This ringing artefact is characteristic of ROI scans and is caused by the data truncation introducing high frequency artefacts at the edge of the projections. These artefacts are amplified by a ramp filter in the reconstruction algorithm. The combination of increased noise and reduced object intensity results in reduced signal-to-noise (SNR) and contrast-to-noise (CNR) ratios in the ROI scan. Figure 6.7 shows the reconstructed cross sections of the ROI and sectioned data sets. Table 6.2 then gives respective image quality parameters.

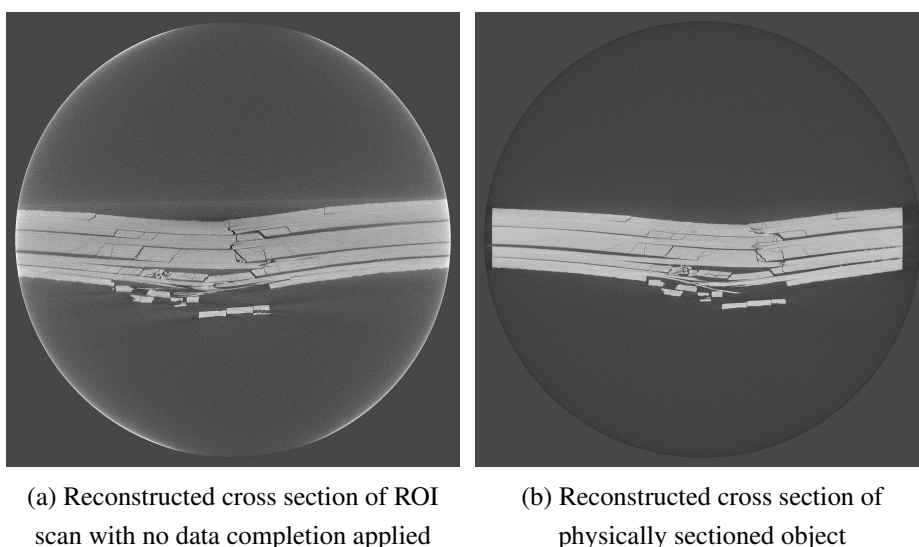
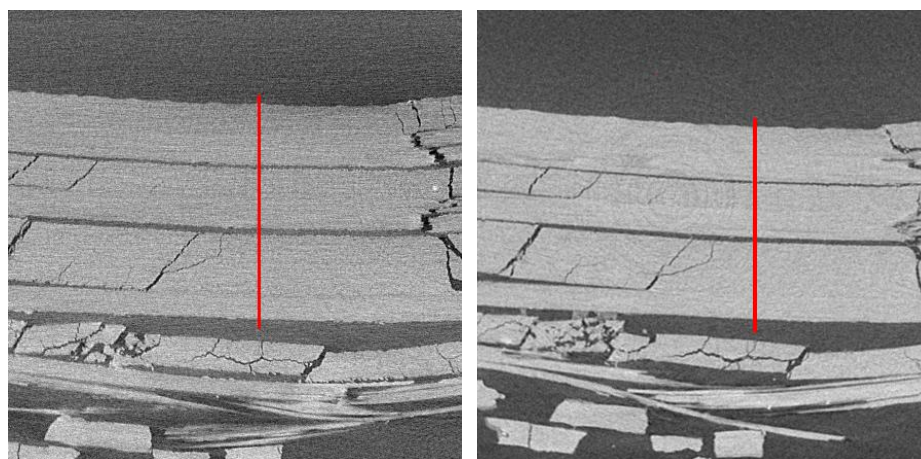


Figure 6.7: Comparison of ROI and sectioned cross-sections of impacted CFRP sample.

Table 6.2: Image quality indicators for sectioned and ROI scans.

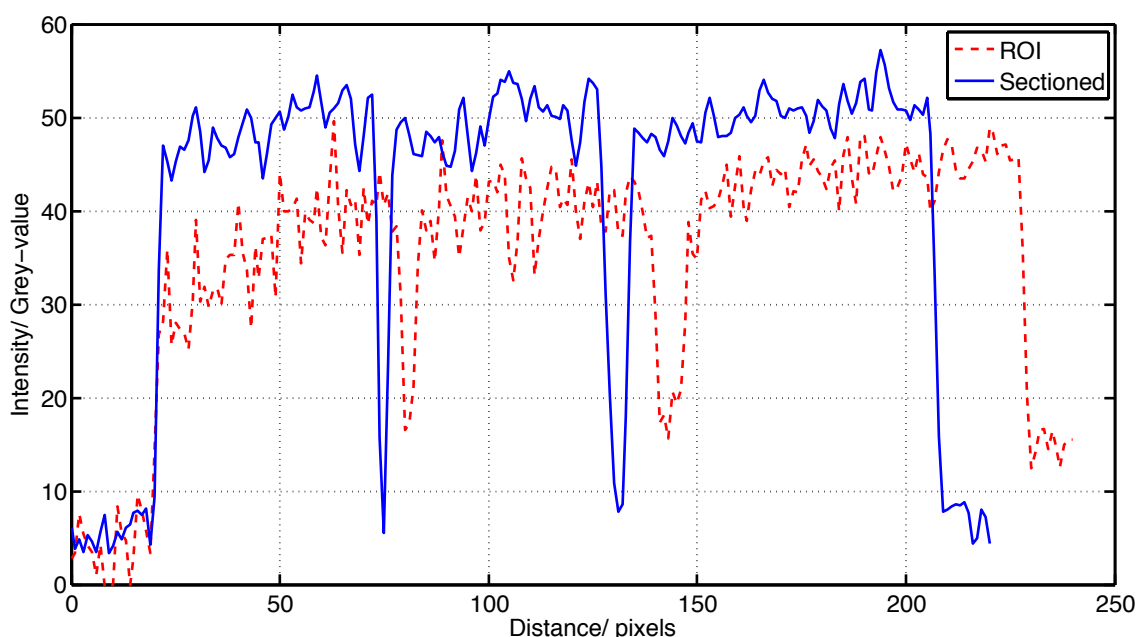
Image Quality Indicator	Scan Type	
	Sectioned	ROI
Mean background brightness/ greyscale	-1.01	2.50
Mean object brightness/ greyscale	50.67	43.49
Mean object standard deviation (noise)	3.92	7.15
Object signal-to-noise ratio	12.94	6.08
Object contrast-to-noise ratio	13.19	5.73

As a result of the degradation in image quality, object features (in this case cracks and delaminations) become more difficult to identify from the background. Drawing a line profile across corresponding features in the ROI and sectioned scans illustrates how feature contrast is reduced (figure 6.8).



(a) Cropped view of ROI scan with no data completion applied

(b) Cropped view of sectioned scan



(c) Line profiles across (a) and (b)

Figure 6.8: Cropped views of ROI and sectioned scans demonstrating loss in feature contrast. Note that line profiles are slightly offset due to sample not being scanned in exactly same position once it had been sectioned.

From figure 6.8 it can be seen that contrast between the object and damage is reduced. Interestingly however, the edge contrast at the damage points is not significantly altered. The gradient of the greyscale line at the damage interfaces is very similar in both scans (10 grey values / pixel in the ROI scan, and 11 grey values / pixel in the sectioned scan). Performing a ROI scan, therefore, has not significantly degraded the ability to identify the damage features present in the centre of the reconstructed slice. The introduction of ringing artefacts and reduced CNR, however, do cause difficulties during image segmentation as figure 6.9 shows. By applying a global ISO 50 threshold to segment the object from the background, the influence of the ringing artefacts and increased noise is apparent.

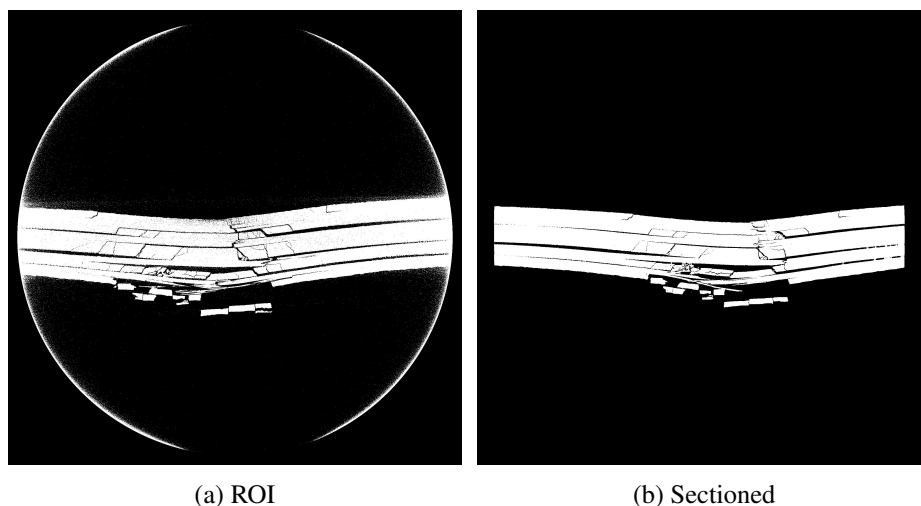
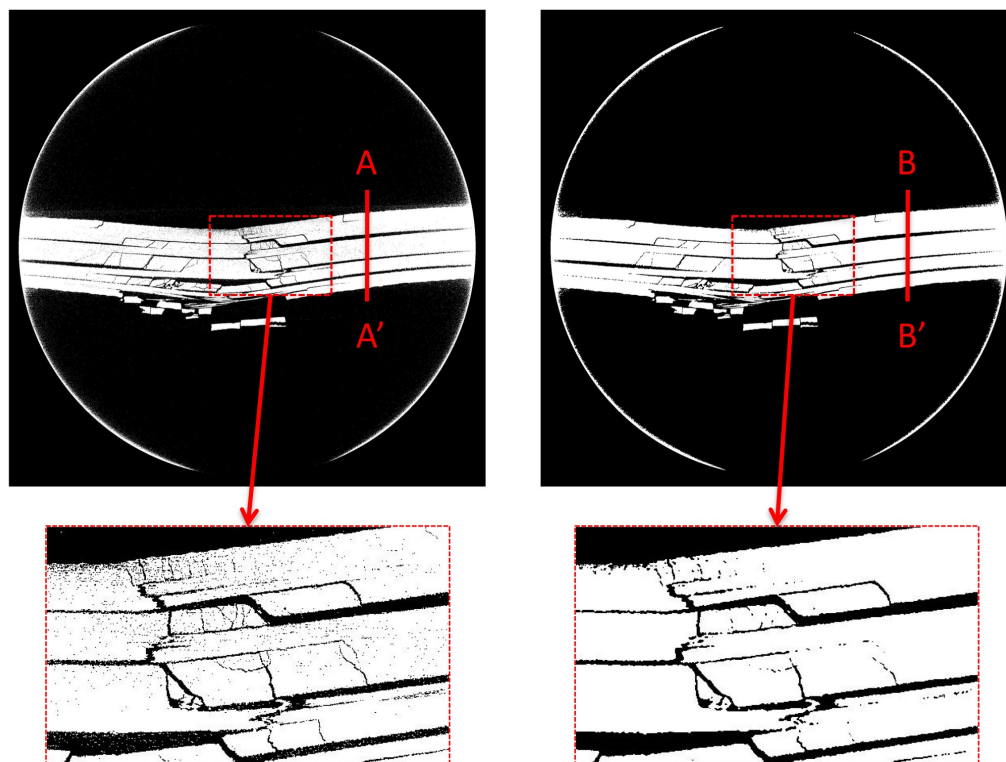
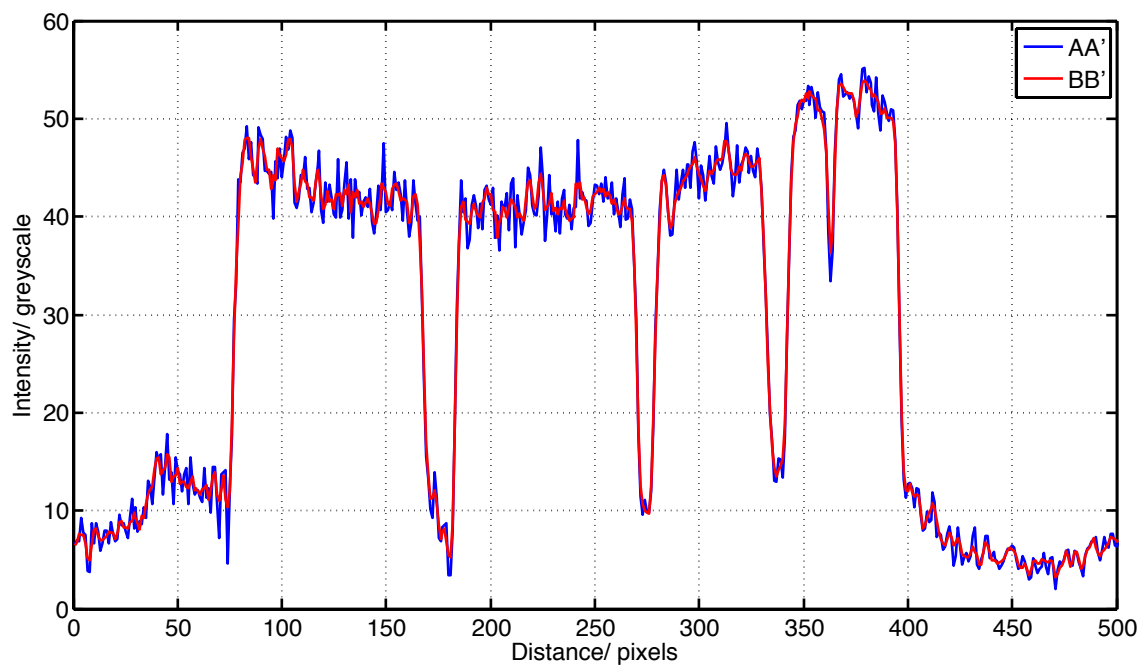


Figure 6.9: ISO 50 thresholds of ROI and sectioned CT scans

Figure 6.9 shows that performing thresholding of the object in the ROI scan tends to include pixels around the circumference of the reconstructed CT slice as these pixels have similar intensity values to the object. The increased noise also results in random dark pixels included within the object, and random light pixels to appear within the cracking / delamination regions. In practise this noise has significant effects on the time taken to process CT data as a high degree of manual interaction during thresholding is required to ensure correct selection of appropriate features. Although processing filters such as noise reduction can be applied, inevitably these involve some type of trade-off. For example, applying noise reduction filters can help to remove random noise away from the edges of the reconstruction, but decreases edge contrast at damage features or remove small features completely. Figure 6.10 compares the original ROI against a noise-reduced version which uses a 3 x 3 pixel noise reduction filter. Small cracks in the region of 1-2 pixel dimensions are eliminated and object-crack contrast is slightly reduced. Edge contrast at major features, in this case delaminations, is not significantly affected, as shown in the line profiles across AA' and BB' (figure 6.10(b)).



(a) Original ROI data (left) vs. 3 x 3 pixel noise reduction (right) both thresholded to ISO 50.



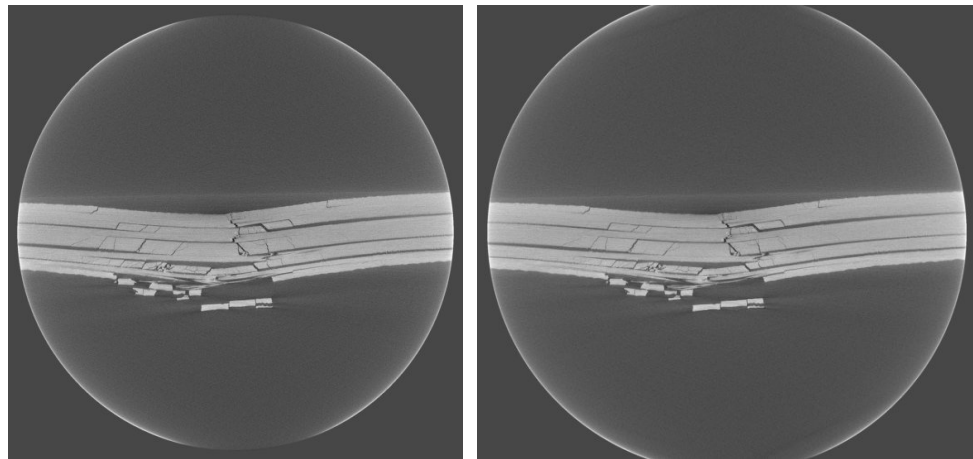
(b) Intensity line profiles across AA' and BB' from (a).

Figure 6.10: ISO 50 image segmentation of original ROI data versus a 3 x 3 pixel noise reduction.

### 6.3.3.2 Data Completion Results

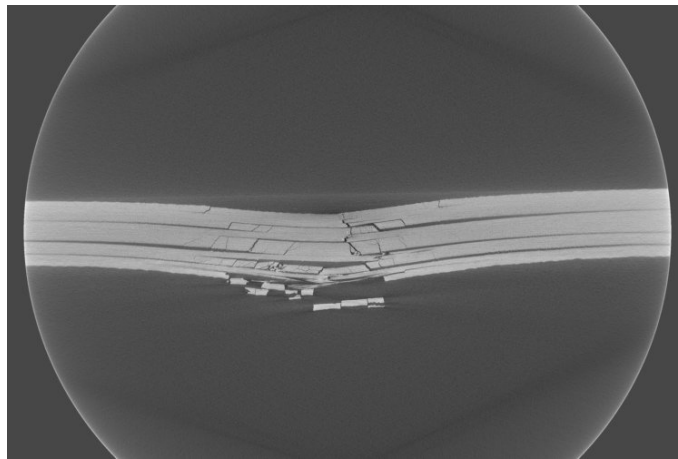
Figures 6.11 (a)-(d) are reconstructed cross sections of the impacted sample with various level extensions applied. The data sets range from 0 to 1000 pixel extensions at each edge, compared to the original truncated data with no extension applied. Increasing the length of the level extension has the effect of moving the characteristic ROI ringing artefact further away from the centre of the reconstruction. The intensity of the ringing artefacts, however, does not reduce. In contrast, figure 6.12 illustrates that the cosine extension moves the ringing artefact further away from the centre of the reconstruction, but also reduces its intensity to the background intensity when using 1000 pixel extension. The cosine extension does however, blur the ringing artefact over a larger area before removing its effect completely. The reconstructed cross sections in 6.11 (a)-(d) are displayed to their relative sizes. By increasing the data extension, the reconstructed area becomes larger but pixel size is maintained, in this case 11  $\mu\text{m}$ .

This reconstruction area increase has practical implications because it means the data file size also increases with increased data extensions. For example, a normal reconstructed CT slice from a 2000 x 2000 pixel detector is 16MB, whereas a cross section extended by 1000 pixels results in a 32 MB cross section. Obviously this can place significant computational strain on the reconstruction process. In practise, only the section within the ROI would be reconstructed to reduce memory consumption, but the radiographic projections forming the reconstruction would still double in data size. A typical scan with 3142 projections could therefore consume up to 50,272 MB (at 8 MB/projection).

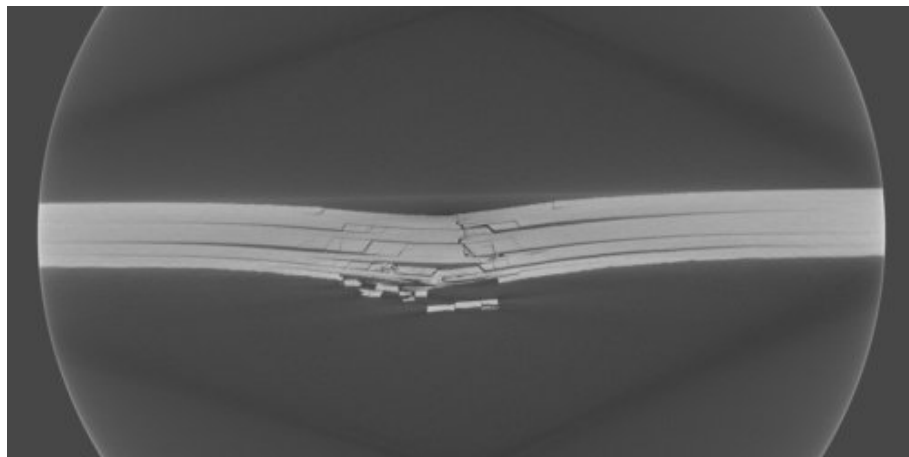


(a) Original ROI data with no data extension

(b) Level extension with 100 pixels at each edge

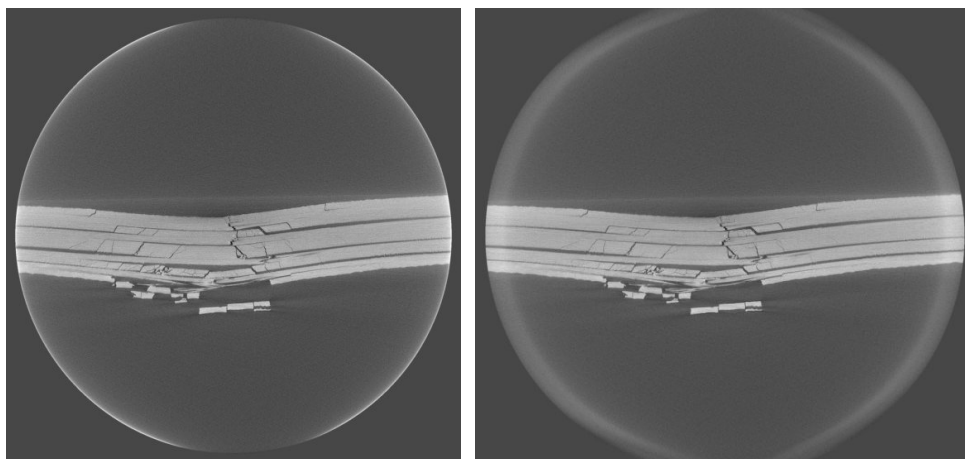


(c) Level extension with 500 pixels at each edge



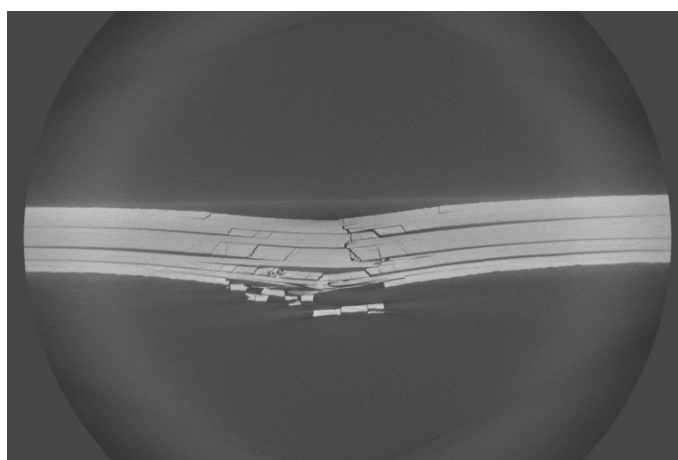
(d) Level extension with 1000 pixels at each edge

Figure 6.11: ROI reconstructions using level extension method

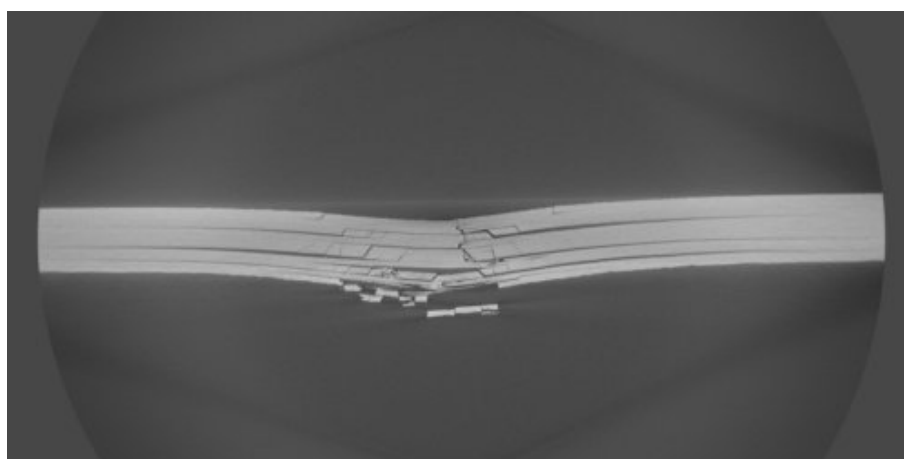


(a) Original ROI truncated data with no data extension

(b) Cosine extension with 100 pixels at each edge



(c) Cosine extension with 500 pixels at each edge

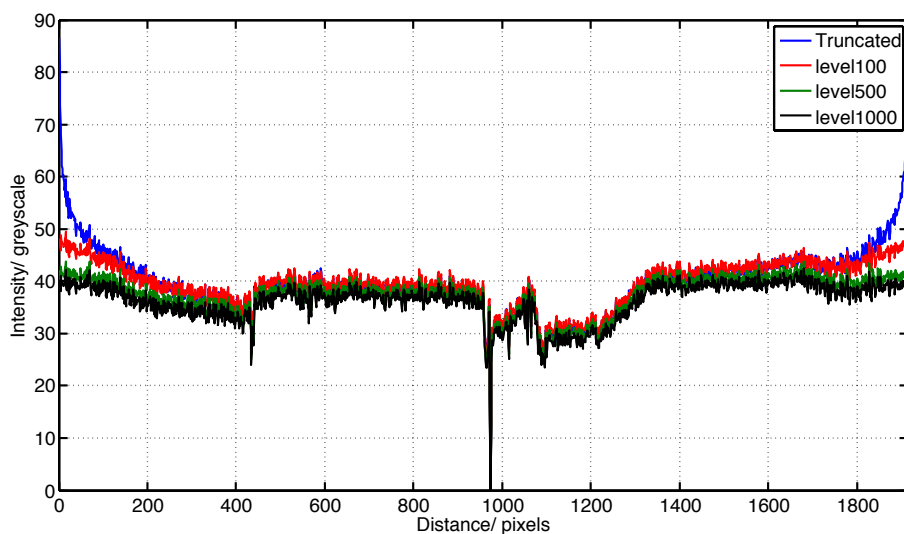


(d) Cosine extension with 1000 pixels at each edge

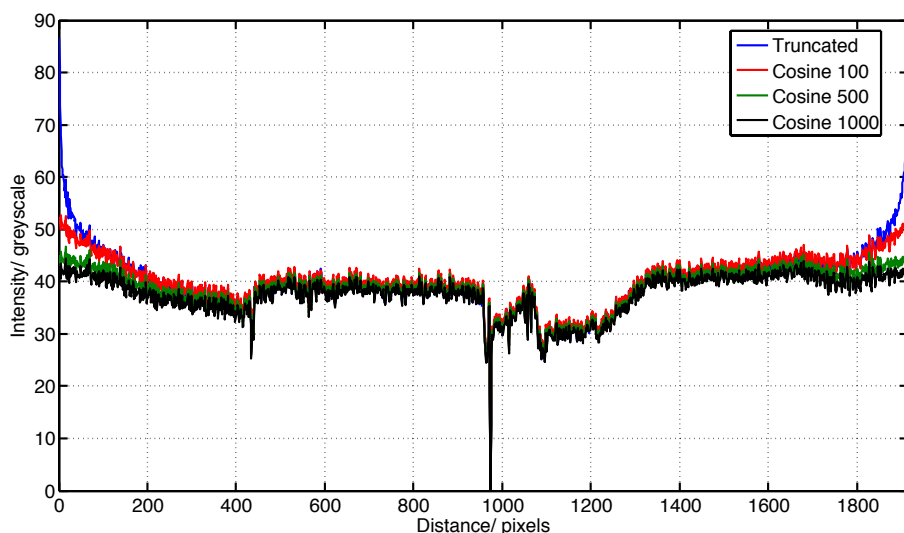
Figure 6.12: ROI reconstructions using cosine extension method

From figures 6.11 (a)-(d), the ringing artefacts were seen to move away from the initial ROI using the level extension, and be completely removed with the cosine extension of 1000 pixels. By plotting a line intensity profile across a pixel distance equivalent to the

original ROI, comparisons between the two extensions can be made. Figure 6.13 shows the brightness variation across the object using the two extension methods, compared to the original truncated ROI.



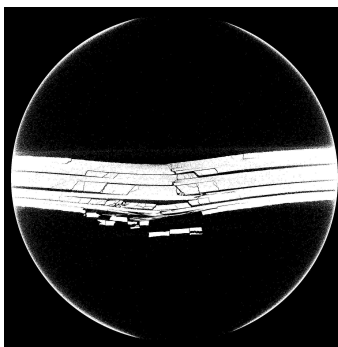
(a) Line profiles across 6.11(a)-(d).



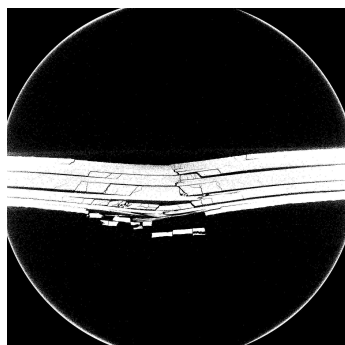
(b) Line profiles across 6.12(a)-(d).

Figure 6.13: Line profiles across the centre of the object using level and cosine extension methods.

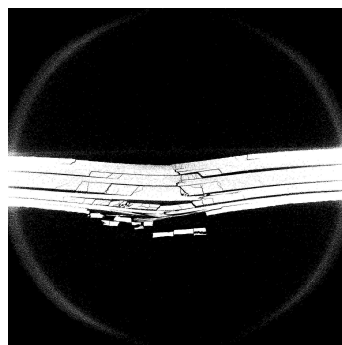
From figure 6.13, within the ROI both methods of data extensions perform similarly. The increased brightness at the edge of the object is suppressed well in both methods. The edge brightness is suppressed to reasonable levels by using a 500 pixel extension in both cases, with little improvement at 1000 pixel extension. The effect on image segmentation, again using an ISO 50 threshold, is displayed in figure 6.14.



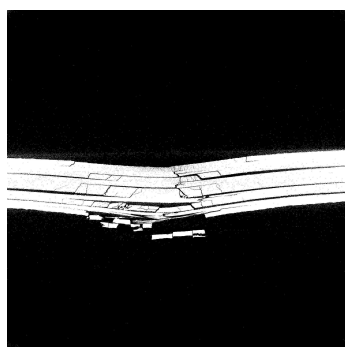
(a) Original truncated ROI



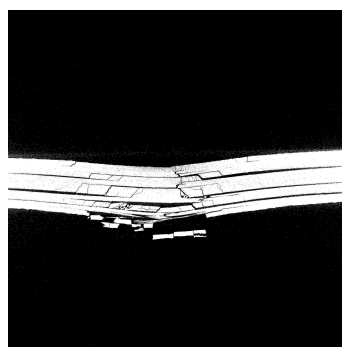
(b) 100 pixel level extension



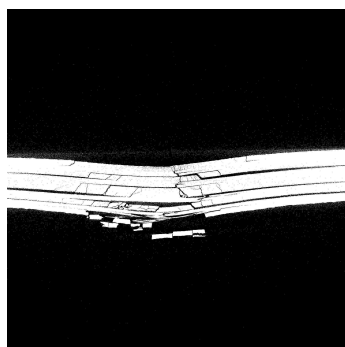
(c) 100 pixel cosine extension



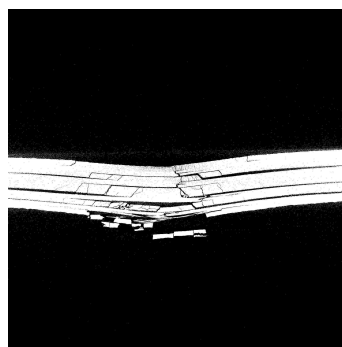
(d) 500 pixel level extension



(e) 500 pixel cosine extension



(f) 1000 pixel level extension



(g) 1000 pixel cosine extension

Figure 6.14: ISO 50 thresholds of original truncated ROI data and extension methods using various tail lengths.

Under all three extension conditions, the level and cosine methods give similar segmented results. As table 6.3 shows, both give virtually identical results in terms of image

quality indicators, showing neither degradation nor improvement over the original truncated data. Although minor differences are seen (1 or 2%), it is difficult to say whether this is a statistically significant difference without performing several repeat scans and data extensions. Such a small difference, if it were statistically significant, would be unlikely to have any effect on segmentation results.

Table 6.3: Image quality indicators within the object for level and cosine data completion methods

Extension length/ pixels	SNR		CNR	
	Level	Cosine	Level	Cosine
100	6.07	6.12	5.51	5.53
500	5.88	6.01	5.53	5.54
1000	5.92	5.75	5.54	5.56

In summary, it is apparent that using data completion techniques has improved the imaging results in terms of artefact suppression. Edge ringing artefacts were successfully suppressed, giving practical improvement for segmentation of impact damage towards the edges of the ROI. The damage in this case was, however, mainly confined to the centre of the object where ringing artefacts did not have much influence in the truncated ROI scan, meaning the identification of damage features was not significantly affected. The sharpness of damage features were not significantly affected by the presence of ringing artefacts in the truncated data, but their contrast against the background was reduced. From a global thresholding perspective, this ringing effect did have an effect on the number of pixels selected as part of the object when using ISO 50 thresholding. Under the conditions studied here, an extension of 500 pixels managed to overcome the ringing artefacts to the point where they no longer affected thresholding results. Image noise still remains a problem with ROI, however, as this is not improved by using data completion methods. The next section looks at how the number of projections has a significant influence on the image quality. Although both data extension methods were seen to produce similar results in terms of image quality and ringing artefact suppression, the cosine method offers a significant advantage in that it allows automatic centre of rotation calculation. Because the edge of the object is tailed to the background intensity level, artificial edges are produced at the extent of the object. The automatic centre of rotation routine in CT Pro is based on edge sharpness, and cannot function in cases where there is low absolute contrast between the object and background, and edges are outside the field of view. Obviously ROI of CFRP meets both of these criteria, hence using the cosine method overcomes the edge detection problem.

## 6.4 Effect of Number of Projections on Image quality in ROI Scans

In addition to implementing the level extension method on synchrotron CT data, (Kyrieleis *et al.*, 2010), demonstrated the suitability of using extra projections in ROI imaging when compared to full FOV imaging. Section 6.3.3 shows that for the high aspect ratio objects used in this study, data completion methods were effective at removing ringing artefacts but had no influence on other image quality indicators such as contrast-to-noise ratio. A study on the effect of the number of projections used in the reconstruction was performed to assess the applicability of using extra projections when ROI imaging on a cone beam system.

### 6.4.1 Experimental Method

A 55 x 89 mm CFRP coupon which had been impacted at 12 J was imaged using the CT imaging procedure described in 6.3. Six CT scans were performed, using 197, 393, 786, 1571, 3142 and 6284 projections. Table 6.4 gives the imaging conditions used in the experiment.

Table 6.4: Image conditions for ROI imaging of impact test coupon using varying projection numbers

Image Variable	Condition
Target Material	Molybdenum
Accelerating voltage	80 kV
Filament current	250 mA
Frame exposure time	1 s
Rotation angle	360°
Magnification	31 X
Effective pixel size	6.3 $\mu\text{m}$
Approximate field of view	12.6 mm

Once the data sets had been acquired, the central slice from each CT scan was reconstructed using CT pro. No data completion methods were applied to the projections.

### 6.4.2 Results and Discussion

Figures 6.15(a)-(f) show the central reconstructed slice from the ROI scans, starting with 6284 projections and ending with 197 projections. Immediately apparent is the increasing noise as the number of projections is reduced, along with a gradual degradation of the features that are clearly visible. The very small matrix cracks which do not fully

cross a ply are particularly reduced in clarity. The major delaminations (running left to right), however, remain visible even with 197 projections. The contrast of these delaminations is reduced, but moreover they appear increasingly blurred.

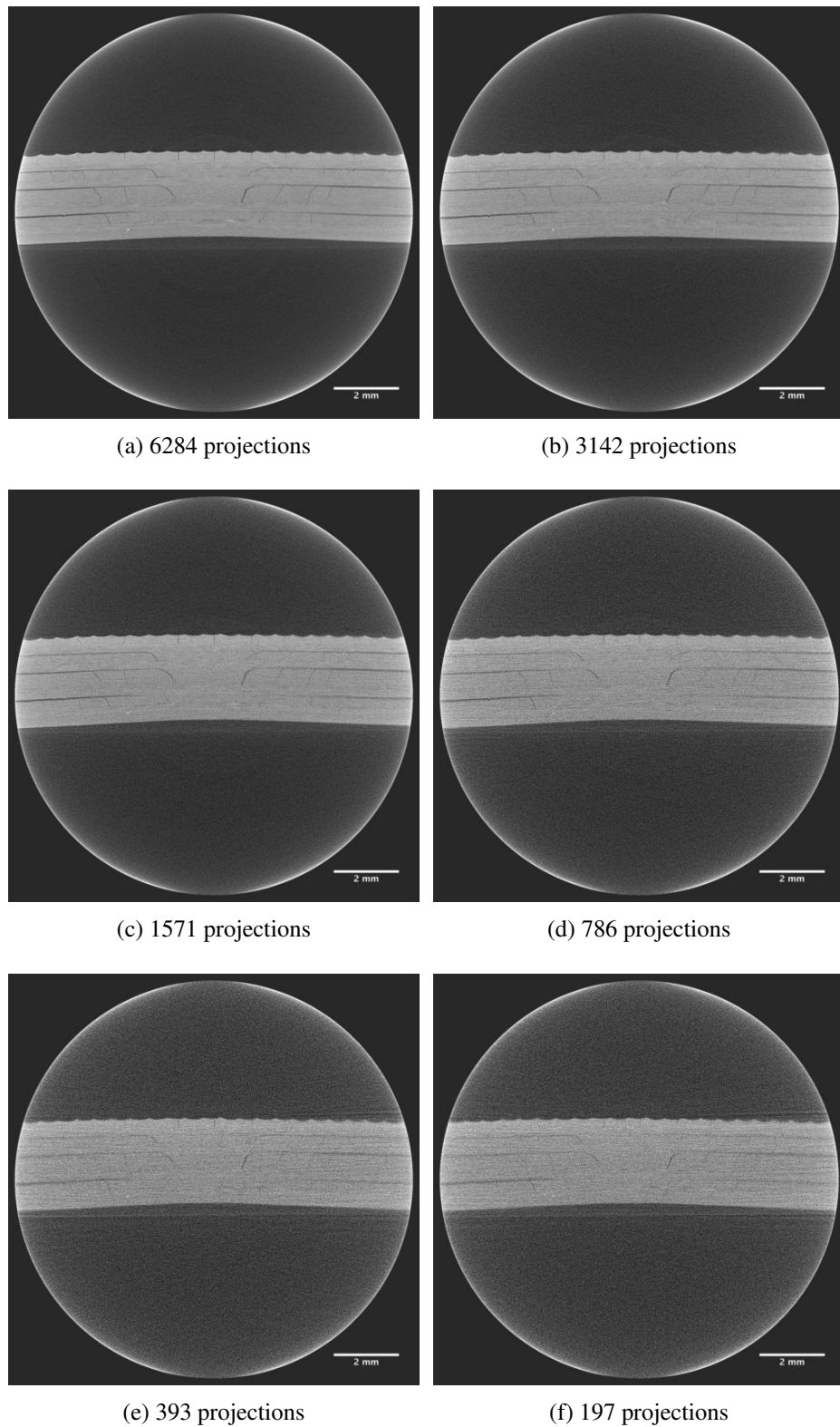


Figure 6.15: ROI reconstructions with varying numbers of projections

To quantify the effect of the number of projections, several image quality measurements and intensity line profiles were taken from each cross section. Figure 6.16 shows the locations where these measurements were taken from.

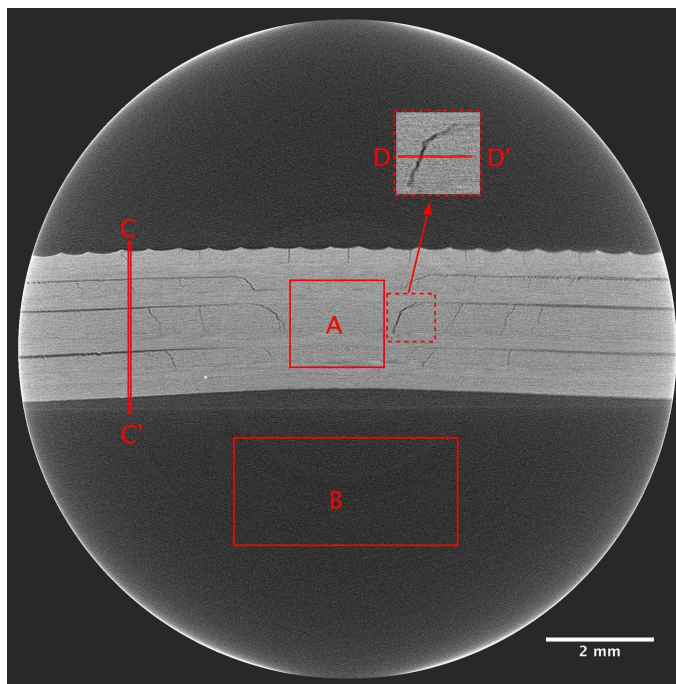


Figure 6.16: Location of measurements for image quality indicators and line profiles.

To calculate signal- and contrast- to-noise ratios, pixel values were averaged over two areas from each cross section. Region A allows calculation of the SNR in the object by comparing the mean pixel value (signal) to the standard deviation (noise). Subtracting the signal value in B from that in A and dividing by the noise in A results in the CNR. Line profiles across CC' and DD' allowed examination of the contrast of delamination and shear crack damage respectively. Figure 6.17 shows the variation of SNR and CNR with number of projections. In contrast to the image quality behaviour observed in full field-of-view samples, neither SNR or CNR appear to have reached a plateau by 6284 projections. Although the rate of increase in image quality is reducing between 3142 and 6284 projections, results suggest significant quality improvements could be achieved with more projections. This observation is in agreement with the results presented by (Kyrieleis *et al.*, 2010), in that the optimal number of projections for ROI reconstruction is greater than for full FOV reconstruction. It is unlikely that local microstructural features play a significant role in the SNR values obtained in the bulk material, as the material contains a high volume fraction of uni-directional fibres, the resolution is below the scale of these fibres, and the resin is of virtually identical attenuation coefficient as the fibres. Furthermore, porosity appears to be very low and no pores were counted in the SNR measurements for the bulk material.

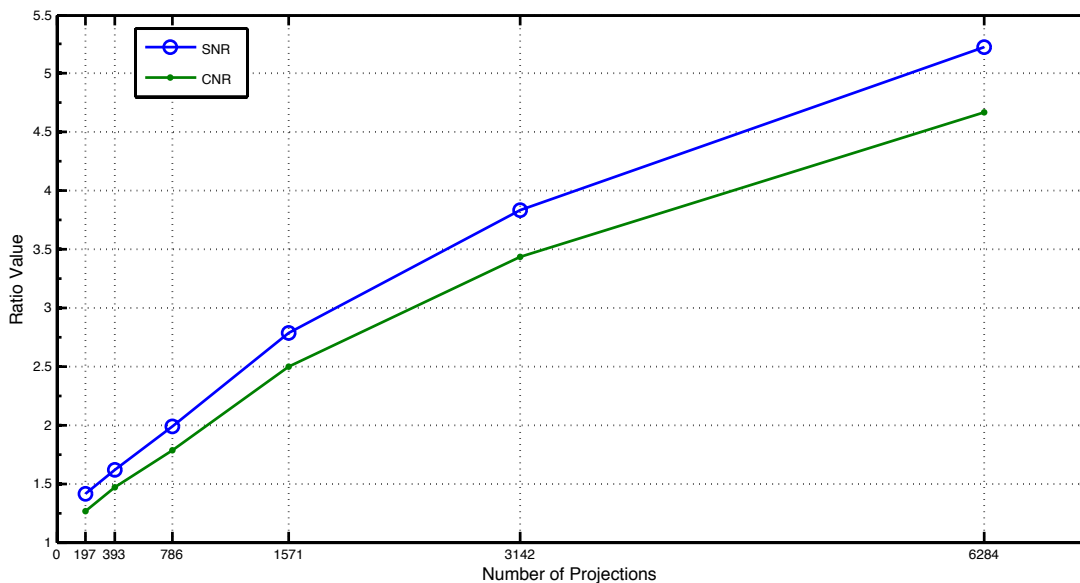


Figure 6.17: Variation of SNR and CNR with no. of projections for ROI scan of impacted sample.

Although the image quality was significantly improved by using 6284 projections, the practical application is somewhat limited. Figure 6.18 reveals that the delaminations covered by the line profile CC' in figure 6.16 are still significantly separated from the background with only 1571 projections. The widest delamination is in fact still apparent in the line profiles even at 786 projections. Likewise, figure 6.19 contrast of the shear crack measured by line profile DD' from figure 6.16 is still apparent at 786 projections. It could perhaps be implied that some remnants of the features are visible using just 197 projections, but noise peaks of equal amplitude have also been introduced, making this a difficult conclusion to make.

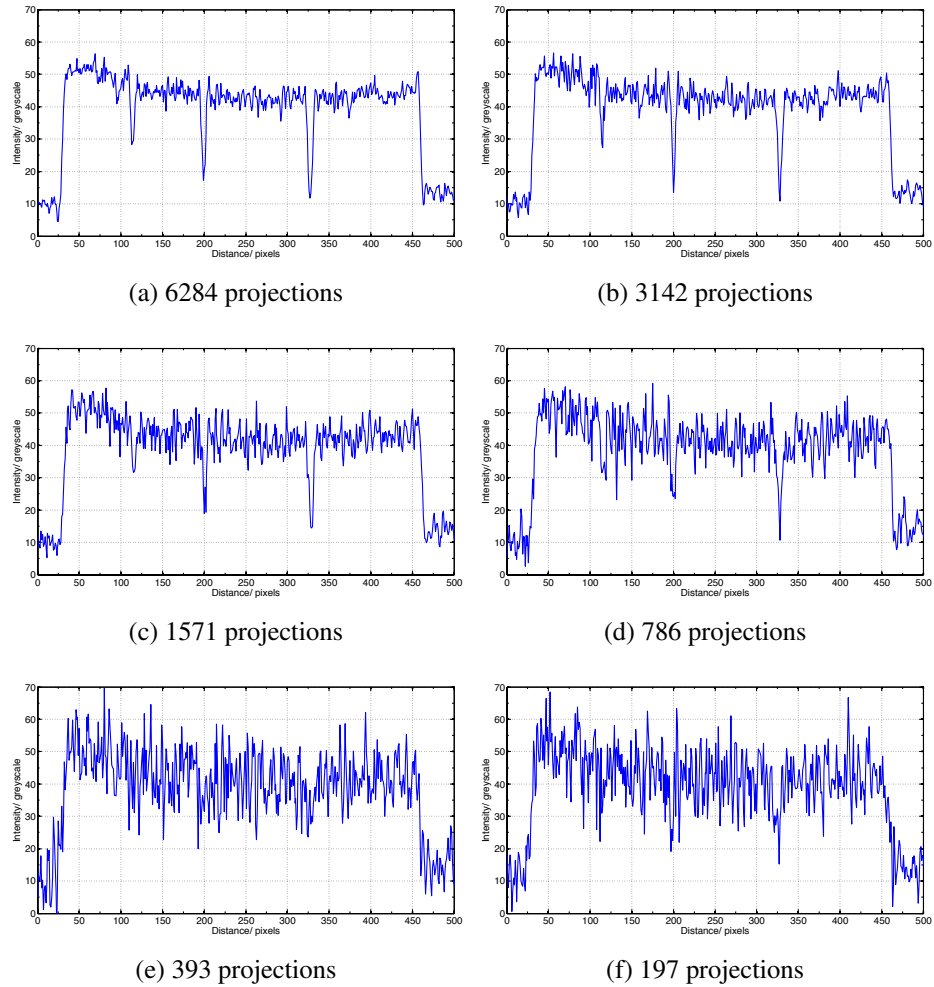


Figure 6.18: Line profile across CC' in figure 6.16, showing delamination contrast with decreasing numbers of projections used in ROI imaging of impact damage.

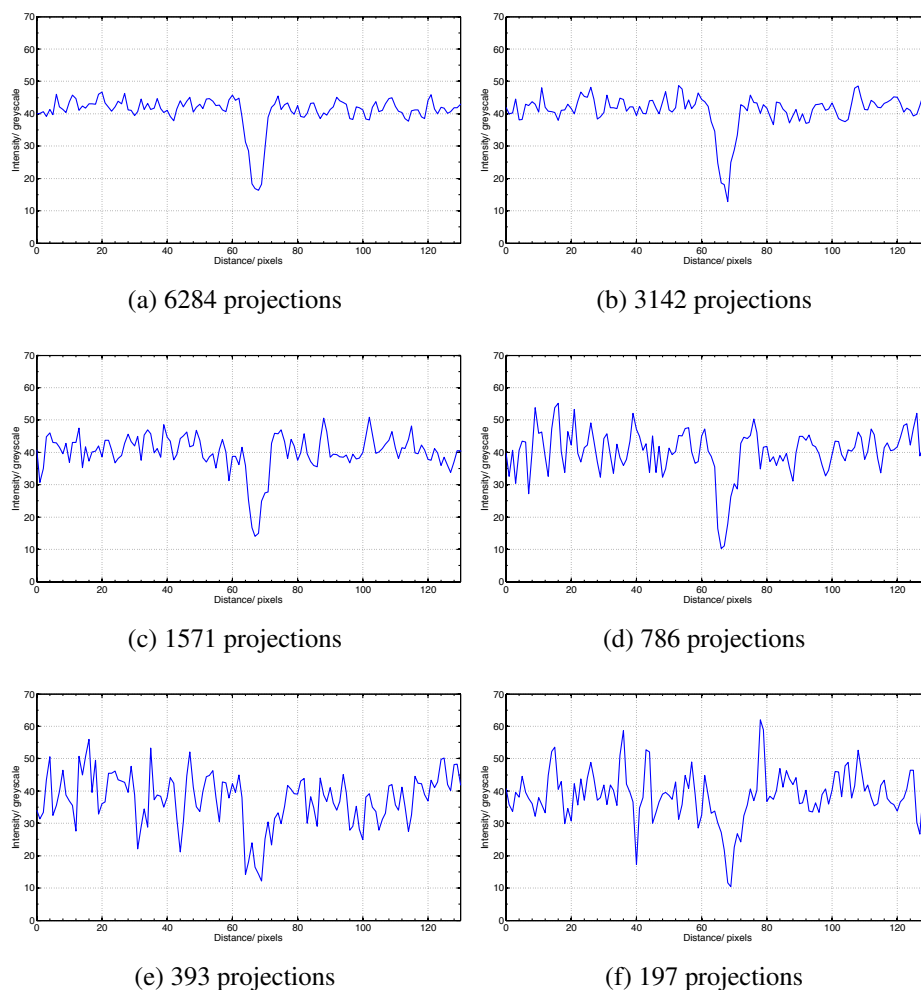


Figure 6.19: Line profile across CC' in figure 6.16, showing shear crack contrast with decreasing numbers of projections used in ROI imaging of impact damage.

Performing an automatic region growing thresholding based on the grey values in the centre of the damage features gives an indication of the effect of CNR on the quantification of damage. Figure 6.20 shows the damage area obtained in each projection case. It can be seen that the reducing CNR ratio with decreasing projections has a significant effect on the damage features which are segmented, as well as the area. Initially the damage area increases as the threshold grows into noisy areas surrounding the damage, but then reduces as contrast between the damage and object reduces. Eventually the noise becomes almost indistinguishable from the damage and the automated thresholding struggles to pick up the damage. Even the small matrix cracks which are visible by eye become lost in the noise by 1571 projections. Although manual segmentation could improve results, the complexity of the damage and the amount of time required to do so prevented further segmentation studies, but should be considered for further work.

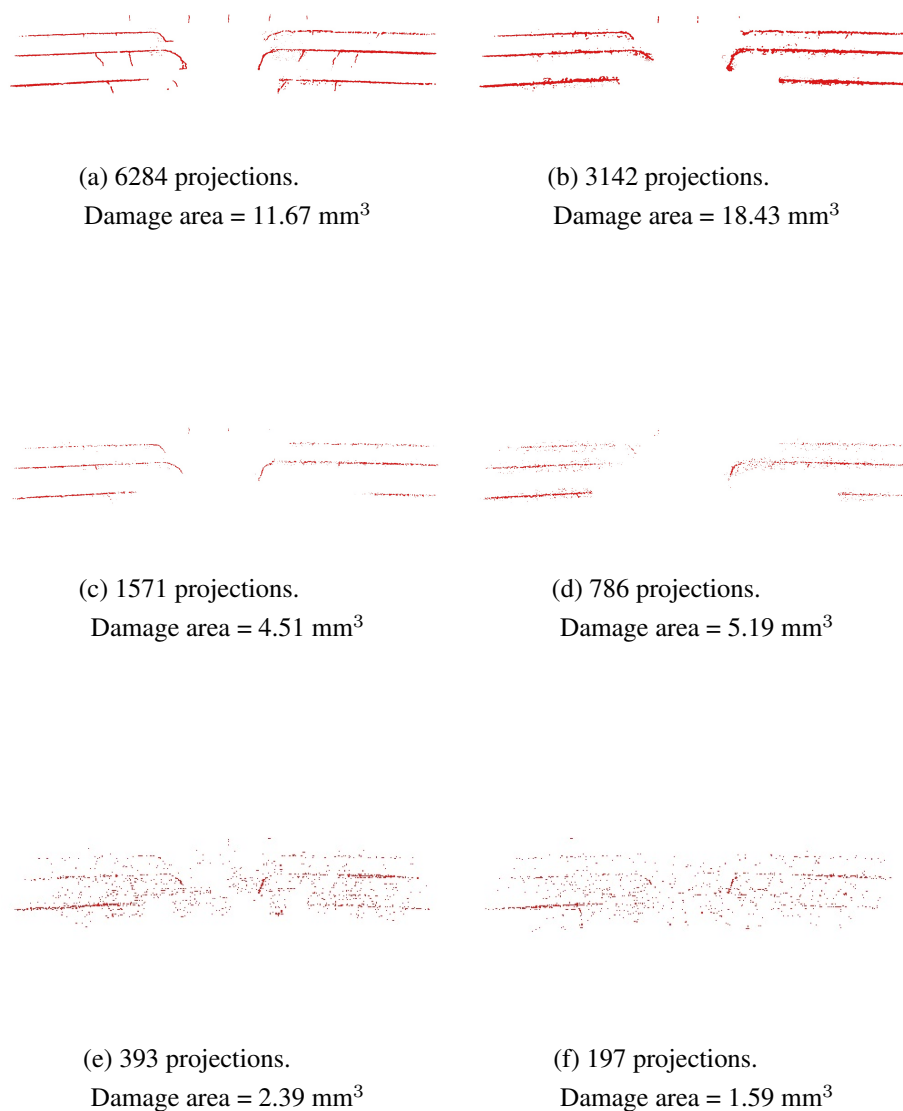


Figure 6.20: Segmented damage areas as a function of projections used in the reconstruction.

In summary, the number of projections taken when performing ROI CT scans has a significant effect on the image quality. It was found that a significant increase in image quality can be obtained by using 6284 projections, with the results suggesting further increases could be obtained by using even more projections. This observation was in contrast to performing full field-of-view tomography where the image quality becomes limited towards 3142 projections (see Appendix A). The degradation in image quality by using fewer projections suggests that at least 3142 should be taken to gain an accurate picture of impact damage at the higher resolutions shown in this section. The blurring of features and increased noise below this number resulted in the loss of some damage features and a significant reduction in the damage area measured using automated thresh-

olding. This result could likely be improved through the use of manual segmentation methods, but the sheer amount of time this takes would make the process uneconomical.

## 6.5 ROI Imaging of Impact Damage

In Chapter 6, CT imaging was used to characterise the global extent of damage in UD and woven CFRP materials. Although this procedure was successful in characterising and quantifying the extent of in-plane damage, it was difficult to assess the micro-mechanisms of damage due to insufficient resolution and low contrast. In order to characterise further the types of damage found in the UD and woven materials, the samples investigated in Chapter 5 were imaged under ROI conditions before the CAI testing was performed. Due to time constraints only one sample from each impact energy was imaged.

### 6.5.1 Experimental Method

Samples were imaged using the same CT setup described in figure 6.2, with a slightly increased magnification. Two frames of 1 s exposure were also averaged to reduce noise, giving a total acquisition time of 2 s per projection. Two CT scans were performed; one for the UD material and one for the woven material. In each scan four samples (3, 6, 9, 12 J) were stacked together and imaged at the same time, providing a reconstructed volume encompassing approximately 18mm<sup>3</sup>. Table 6.5 gives the imaging conditions used in the scans.

Table 6.5: Image conditions for ROI imaging UD and woven impacted coupons

<b>Image Variable</b>	<b>Condition</b>
Target Material	Molybdenum
Accelerating voltage	80 kV
Filament current	250 mA
Frame exposure time	1 s
Frames per projection	2
Number of projections	3142
Rotation angle	360°
Magnification	22.5 X
Effective pixel size	8.9 μm
Approximate field of view	18 mm

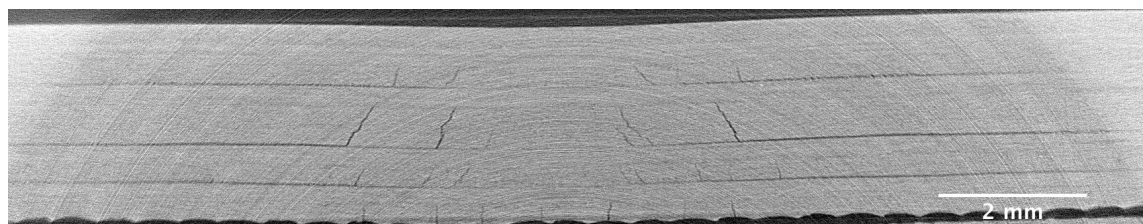
After acquisition of the two CT data sets, a cosine data extension of 500 pixels was added to both data sets to reduce ringing artefacts and assist with centre of rotation calculation.

## 6.5.2 Results and Discussion

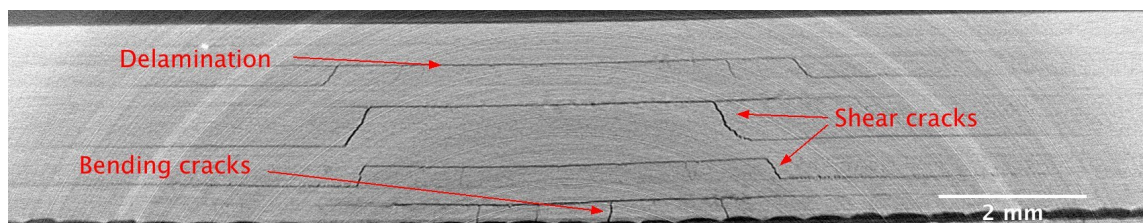
This section presents the imaging results of the ROI investigations. All references to co-ordinate systems and planes are the same as that outline in figure 5.20, Chapter 6. Due to the resolution achieved in these experiments, the field of view is contained entirely within the extent of the damage zones in both UD and woven materials. Due to the complex nature of damage observed on the micro-scale, particularly for the woven composites, the discussion of damage under ROI conditions is generally qualitative.

### 6.5.2.1 Uni-Directional Material

Figures 6.21 to 6.24 are reconstructed cross-sections of UD impacted samples ranging from 3-12 J. Each figure shows the XZ plane directly under the impactor contact point, (a), and 5mm from the contact point, (b). In terms of the damage mechanisms which are visible, the ROI scans provide limited extra information about the UD samples. The delaminations and inter-laminar shear cracks which were visible in the full-FOV scans (Chapter 6) are the dominant damage features. In all cases it can be seen that the region directly under the impactor and in the centre of the cross section is relatively free from delaminations or shear cracks (see (a) in each of figures 6.21 to 6.24). Moving away from the impact contact point results in delaminations moving into the central regions, connected by matrix shear cracks. As the impact energy is increased, the density of these matrix shear cracks in any given cross section also increases. However, attempting to quantify this effect did not yield any numerical trends due to the relatively small area of these defects compared to the delaminations which extend across the entire field of view in all cases due to the high magnification. The high scatter of damage volume, typical to composite materials, also makes deducing damage statistics impossible with only one sample at each energy.

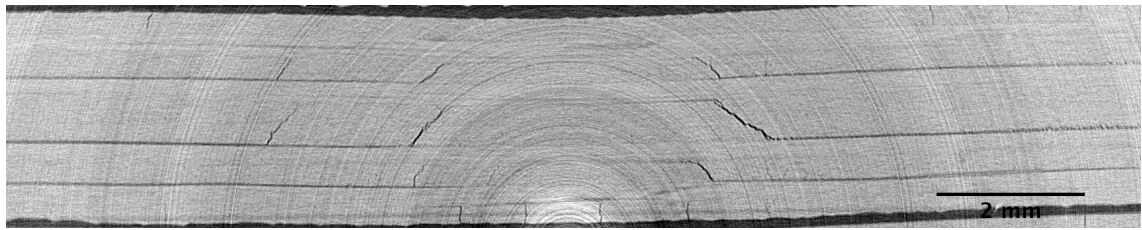


(a) Directly under impactor tip

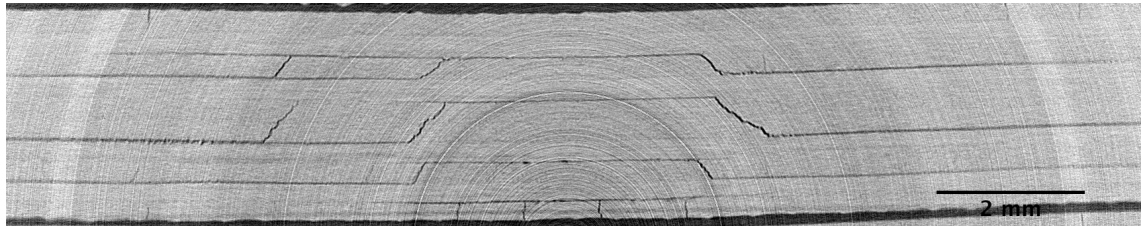


(b) 5mm from impactor tip

Figure 6.21: Reconstructed cross sections in XZ plane of UD material. 3 J impact.

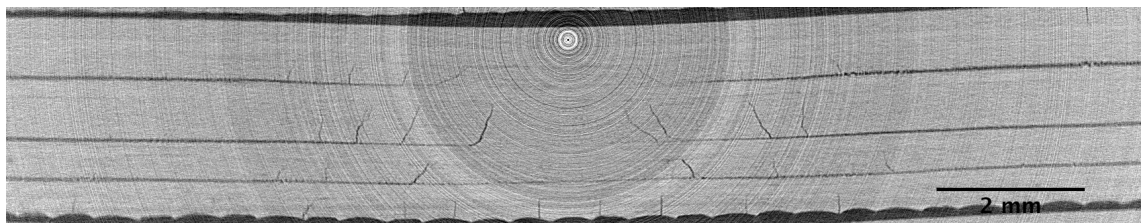


(a) Directly under impactor tip



(b) 5mm from impactor tip

Figure 6.22: Reconstructed cross sections in XZ plane of UD material. 6 J impact.

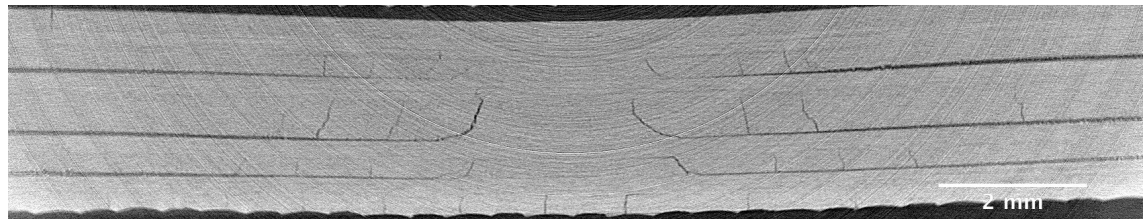


(a) Directly under impactor tip

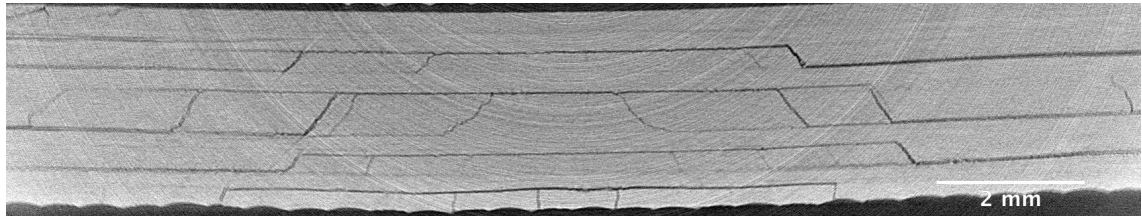


(b) 5mm from impactor tip

Figure 6.23: Reconstructed cross sections in XZ plane of UD material. 9 J impact.



(a) Directly under impactor tip



(b) 5mm from impactor tip

Figure 6.24: Reconstructed cross sections in XZ plane of UD material. 12 J impact.

Also visible from the high resolution ROI scans are bending cracks on the back face of the sample. These bending cracks were not visible in the full FOV scans, and are approximately 1-2 pixels wide. Propagating in a direction perpendicular to the back face, these bending cracks appear to initiate directly under the impact zone, as opposed to the shear cracks which do not appear directly under the impact tip. These bending cracks then extend along the  $0^\circ$  direction and form a delamination at the ply interface adjacent to the back face of the plate. Following these cracks through all the CT slices, it was found that the remaining shear cracks and delaminations linked to these bending cracks in all energy cases. It can therefore be supposed that these cracks actually initiate the other types of damage caused by the impact event. In addition to resolving the back face bending cracks, the ROI imaging has already revealed that many more shear cracks exist between the delamination interfaces than initially found in the full FOV imaging. Many of these interlaminar shear cracks, however, are extremely fine and do not penetrate all the way through a given ply to join with the subsequent delamination.

Unfortunately the resolution achieved in the ROI scans was still not able to directly resolve any fibre damage. Due to the impact energies and bending displacements experienced (especially at 12 J) that significant numbers of fibres will have fractured or at least de-bonded from the matrix. Further work investigating damage on a fibre and interface level would certainly reveal more damage mechanisms, and should be considered as an important area to further the work presented here.

### 6.5.2.2 Woven Material

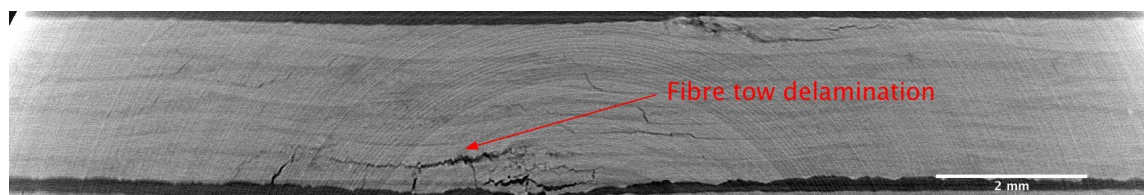
The results in Chapter 5 demonstrated that at low energies (3 and 6 J), the damage in the woven materials was most significant at the front and back faces. Increasing impact energy caused propagation of damage down through the sample, but it did not significantly spread out. In those imaging experiments however, it was very difficult to ascertain the

precise mechanisms of damage. Low contrast between the object and background, in addition to low resolution combined with partial volume effects were the cause of this difficulty. In contrast to the ROI results from the UD material, ROI imaging of the woven material provided significant improvement in the visibility of damage mechanisms.

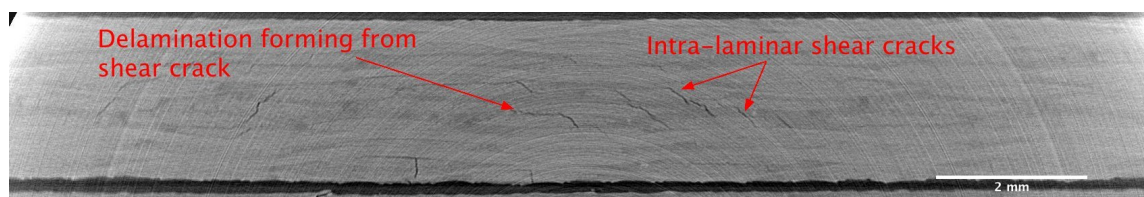
Figures 6.25 to 6.28 show reconstructed cross sections for each impact energy. Similar to the results shown for the UD material, cross sections at the impactor contact point and 5mm from the contact point are shown.

In the 3 J sample, the main damage mechanisms observed were shear cracking and delamination. The delaminations, as for the UD material, were found to propagate from the end of a shear crack. In this case, however, the delaminations did not propagate over a wide area compared to those found in the UD material. The delaminations were found to be numerous but prevented from spreading by the tortuous path created by the undulating fibre tows. Some tow splitting was apparent at the impact site and corresponding region on the back face.

At 6 J, the numerous small delaminations grow in size and begin to coalesce. Matrix cracking was found to begin penetrating through the resin infiltrated fibre tows, forming intra-tow damage. This damage mechanism was not observable in the imaging experiments performed in Chapter 6.

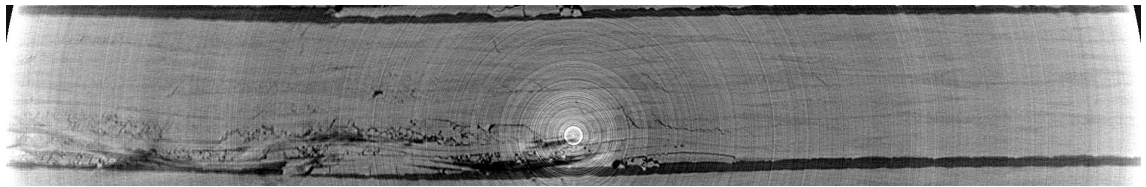


(a) Directly under impactor tip

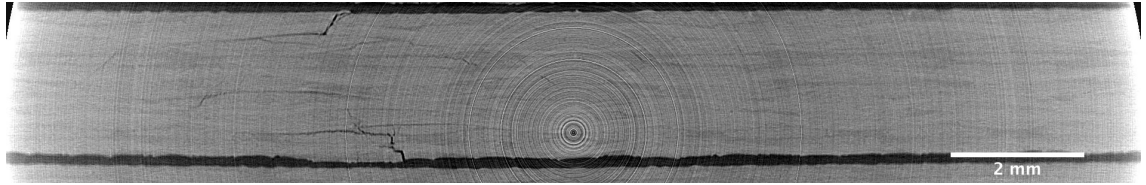


(b) 5mm from impactor tip

Figure 6.25: Reconstructed cross sections in XZ plane of UD material. 3 J impact.

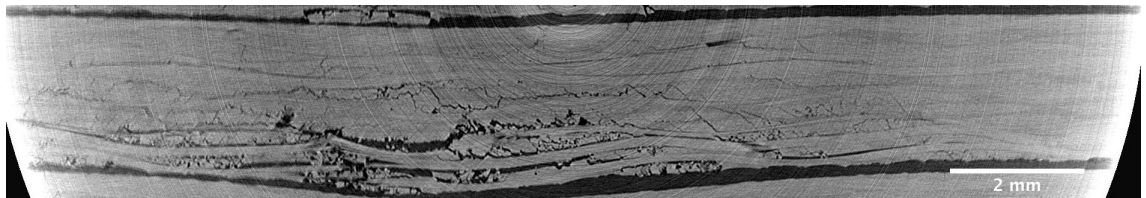


(a) Directly under impactor tip

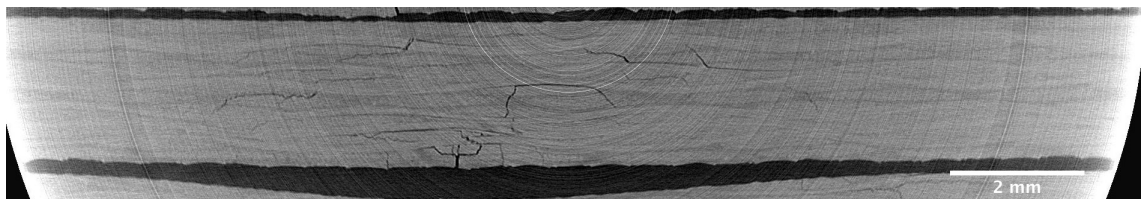


(b) 5mm from impactor tip

Figure 6.26: Reconstructed cross sections in XZ plane of UD material. 6 J impact.

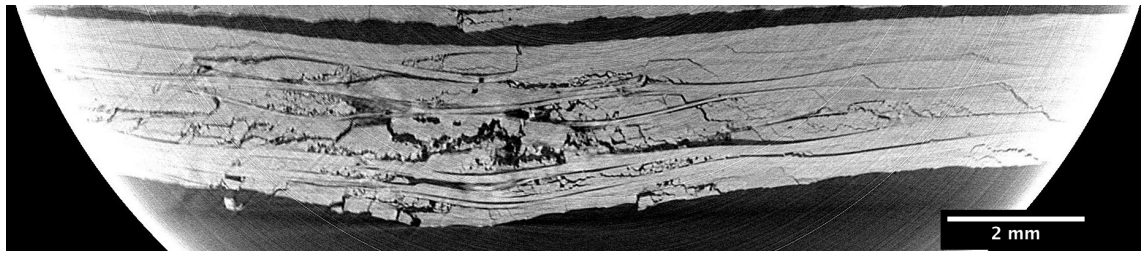


(a) Directly under impactor tip

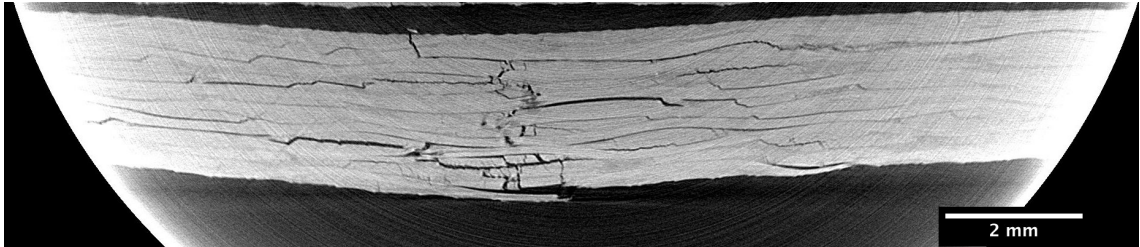


(b) 5mm from impactor tip

Figure 6.27: Reconstructed cross sections in XZ plane of UD material. 9 J impact.



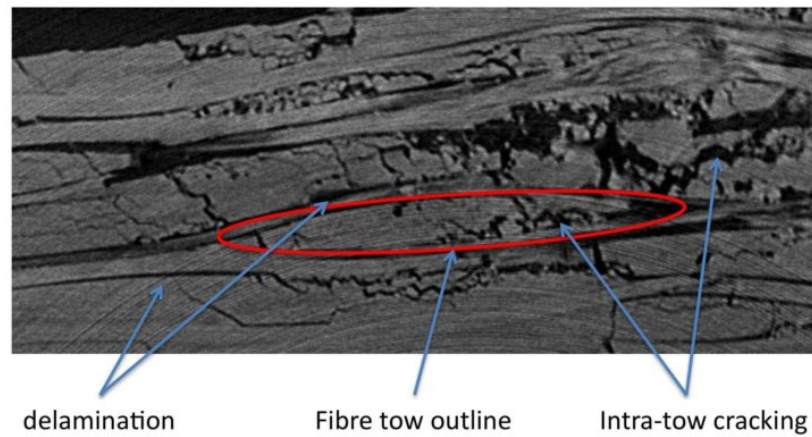
(a) Directly under impactor tip



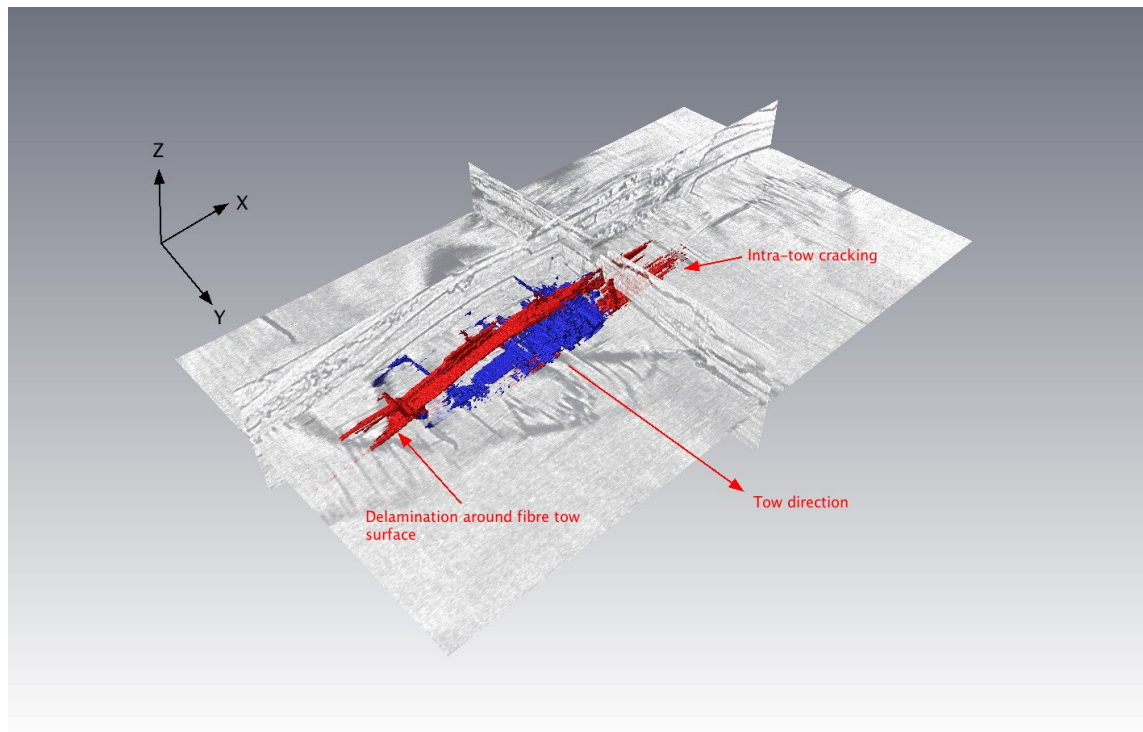
(b) 5mm from impactor tip

Figure 6.28: Reconstructed cross sections in XZ plane of UD material. 12 J impact.

Figures 6.27 to 6.28 show a general increase in the damage mechanisms observed at 3 and 6 J. Extensive delamination and out of plane displacement causes fibre tows to separate and displace significantly from each other. The intra-tow damage mechanism becomes a significant fraction of the damage observed, and complete tow fracture is evident at 12 J. Clearly the damage mechanisms evident in the woven materials are much more complex in terms of their interaction with microstructural feature and their propagation through the material when compared with the UD materials. Figure 6.29 is a 3D rendering showing the interaction of a delamination with intra-tow cracking. The delamination has propagated around the surface of the fibre tow, then finds a path into the fibre tow and propagates along the tow direction. This type of damage was found in both the warp and weft fibre tows (i.e. the  $0^\circ$  and  $90^\circ$  tows).



(a) Magnified view of tow damage in woven CFRP sample subject to 12 J impact.



(b) 3D rendering of (a)

Figure 6.29: Propagation of a delamination into a fibre tow in plain woven CFRP.

In all cases, the most severe damage is constrained to the area directly under the impactor contact point. This observation is in contrast to the propagation of damage in the UD materials, where damage was seen to propagate from the back face and move conically around the impact location. Manual segmentation based on the damage greyscale reveals the rapid decline of the damage moving away from the impactor contact point. Figure 6.30 shows the damage area in  $mm^2$  in the  $XZ$  plane as a function of distance from the impactor.

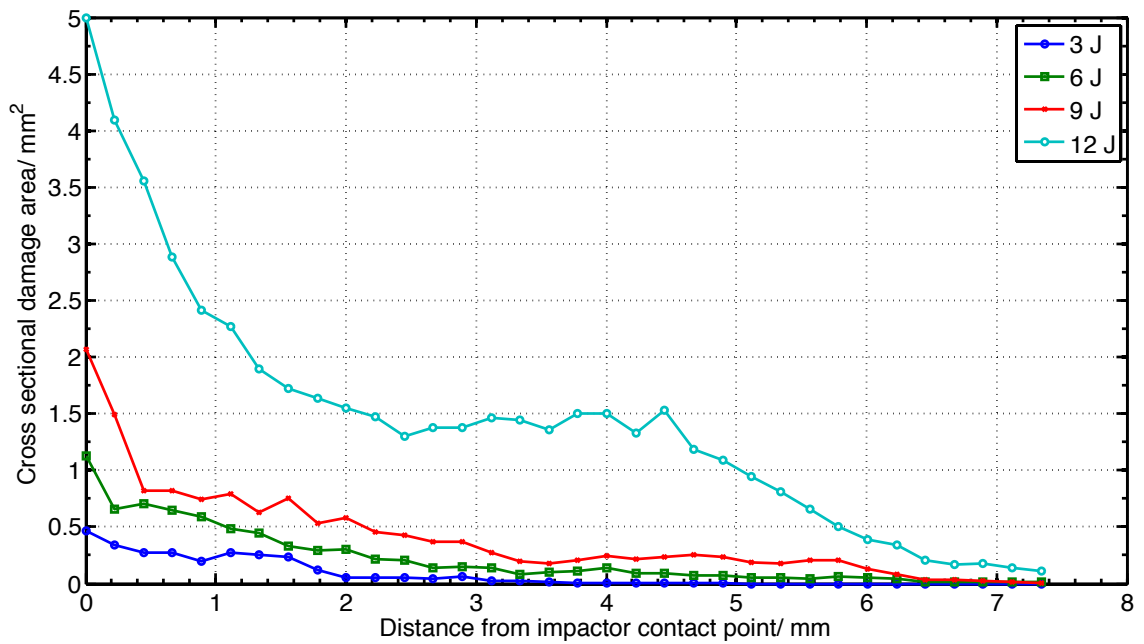


Figure 6.30: Variation of cross sectional damage area with distance from impactor contact point in plain woven CFRP.

Although figure 6.30 cannot be said to be statistically significant, it does suggest a trend at all impact energies. The large increase in damage between 9 J and 12 J can be attributed to significant tow damage which was observed at 12 J. This behaviour was also evident in the force-time curves in Chapter 6 (section 5.4), which displayed significant load drops after the peak load under 12 J impact.

## 6.6 Chapter Summary and Conclusions

The work in this section has shown the application of ROI data completion methods can significantly improve the overall image quality on the current generation of cone-beam CT systems with large detectors. Although not strictly necessary for the identification of damage mechanisms, by reducing the ringing artefacts caused by data truncation, the segmentation of impact damage in CFRP materials was shown to be more accurate. In terms of suppressing ringing artefacts, both the cosine and extension methods gave very similar results. The cosine method however, has the advantage that it allows automatic centre of rotation calculations to be performed when reconstructing data sets. Practical implementation of data completion methods for full volume reconstruction (i.e 2000 pixel<sup>3</sup> data sets) will depend heavily on the end use, due to increased data storage, memory and processing requirements. Data completion methods could prove useful in other applications. For example, in the case of image based modelling finite element models are generated from CT data sets. In these models, material properties are often based on CT grey values and so local intensity variations due to artefacts need to be suppressed.

The ROI studies here showed that the high aspect ratio of CFRP samples is actually a benefit under ROI conditions, as many of the projections are not truncated. This situation was highlighted when scanning 4 samples together (section 6.5; the use of a 500 pixel cosine extension was not able to suppress the ringing artefacts to the extent observed when scanning a single object. Further work should be performed to assess the relationship between aspect ratio, absolute thickness and the amount of data truncated outside the field of view in order to select the optimum ROI conditions for imaging CFRP. It was also noted from the data presented that noise becomes a significant issue when imaging CFRP under ROI conditions, mainly due to the relatively low absorbance of the materials. In future it is suggested that this is compensated for by using a much higher X-ray flux.

ROI imaging allowed further damage mechanisms in both UD and woven materials to be identified. In the case of UD materials, back face bending cracks were resolved and deemed to be the initiation point for the remaining damage. Very small ( $<18\mu\text{m}$ ) intralaminar cracks which did not propagate through to subsequent delaminations were also identified. Due to the dominance of delamination damage in terms of cross section area, little quantitative information was gained from ROI imaging in the UD case. Although it was clear by eye that intra- and interlaminar matrix cracking volume increased as both a function of distance from the impact zone and impact energy, segmentation methods need to be improved to allow quantitative data to be extracted under these conditions. Time permitting, a thorough manual segmentation approach could be used to map only the cracking, but this would take an extremely long time considering the number of CT slices and matrix cracks in a single impacted sample.

ROI imaging of the woven samples proved to be more useful. The improved resolution allowed the many individual damage mechanisms to be identified. The density and spatial extent of these mechanisms prevented their identification in the full field of view imaging performed in Chapter 5. The damage mechanisms identified in the woven material consisted of shear cracks and small delaminations under low energy impact, progressing to coalescence of delaminations, increased shear cracking, fibre tow failure and intra-tow cracking at higher energies. These complex damage mechanisms account for the increased impact energy absorption of the woven material compared to the UD. The microstructural features of the woven material, such as tow waviness and higher resin volume fraction result in higher fracture toughness values preventing the spread of damage. This type of behaviour has been reported in many publications, and the tomographic studies performed here have reinforced that understanding. Although damage in the woven materials was seen to be contained under the impactor, as a result of the lower interlaminar shear strength (Chapter 5), damage did propagate easily between layers. This observation demonstrates a structure-property trade off typical of composite materials. The woven structure has increased energy absorption and prevented damage spread, but the tow waviness and reduced volume fraction cause lower initial stiffness and strength values.

## IMAGING DAMAGE USING GRATING INTERFEROMETRY X-RAY TOMOGRAPHY

### 7.1 Introduction

The work in this chapter focuses on the use of a grating interferometry based X-ray tomography system to image impact damage in uni-directional CFRP plates. The experimental work was performed at the *Centre Suisse d'Electronique et de Microtechnique* (CSEM) in Zurich, Switzerland. The system used in this study is novel technology developed by PhD students and staff at CSEM, and is derived from similar imaging set-ups used on synchrotrons such as the Swiss Light Source (SLS). Due to the physical set-up of the system, it is able to provide three modes of imaging simultaneously; typical *absorption*, *differential phase contrast*, and *dark field* imaging. As such, the work presented in this chapter is known to be the first application of interferometer based tomography on a laboratory based X-ray source to examine impact damage in CFRP.

The aims of this chapter are to:

- Demonstrate the use of grating interferometer CT to image impact damage in CFRP
- Evaluate the types of damage visible using the different imaging modes possible with interferometer CT
- Show the technique can be used to obtain quantitative damage information
- Compare the technique to standard micro-CT and ultrasonic C-scan

These aims were met by performing radiography and tomography on a physically sectioned quasi-isotropic CFRP laminate. Further experiments were then performed using only radiographs (projections) on 3 test coupons which had been impacted at 5, 10 and 15 J. These coupons had the same dimensions as the miniaturised CAI plates used in the previous chapters (55 x 89 mm, 10 plies).

## 7.2 Background

Due to the weak attenuation of X-Rays by low atomic number materials, such as carbon reinforced polymer composites, it is often difficult to obtain significant image contrast in thin samples. This principle was discussed and illustrated in the previous chapters in this thesis. An image method known as phase sensitive X-Ray imaging has been shown to be effective at providing additional information about weakly absorbing materials. This method is based on differences in the refractive index of X-rays at, for example, interfaces between materials of similar density.

The phase sensitive method, however, requires high spatially and/ or temporally coherent X-ray sources (Kottler *et al.*, 2007). As a result, the technique has generally been limited to application on high brilliance sources such as those on synchrotrons. The technique has not been compatible, therefore, with standard laboratory or industrial applications where high powered, polychromatic and incoherent X-Ray sources are used. These industrial sources have such characteristics in order to produce a high enough X-Ray flux to keep imaging times reasonable.

A novel imaging method based on the use of interferometer gratings (specifically, a Talbot-Lau interferometer) has recently been developed at CSEM, which aims to overcome some of the problems associated with applying phase contrast imaging with a non-coherent X-Ray source.

The system consists of a polychromatic X-Ray source, three separate silicon gratings ( $G_0$ ,  $G_1$  and  $G_2$ ) and an area detector. The first grating, placed close to the source, splits the original photon beam into an array of spatially coherent individual sources (Kottler *et al.*, 2007). The sample is placed between  $G_0$  and  $G_1$  during imaging. The object causes slight refraction of the X-Ray beam (scattering), through an angle  $\alpha$ . The imaging procedure is then based on locally detecting these angular deviations Pfeiffer *et al.* (2006). The angular deviation is directly proportional to the local gradient of the objects phase shift, hence the term 'differential phase contrast'. The angular deviation is related to the phase shift by:

$$\alpha = \frac{\lambda}{2\pi} \frac{\partial \Phi(x, y)}{\partial x} \quad (7.1)$$

Where  $x$  and  $y$  are the cartesian coordinates perpendicular to the optical axis,  $\Phi(x, y)$  is the phase shift of the wavefront, and  $\lambda$  is the wavelength of the radiation.

Figure 7.1 shows schematics of the basic principles behind how the system operates. Figure 7.2 then illustrates the angular deviation relative to the gratings, highlighting how stepping of the gratings can image specific scattering angles.

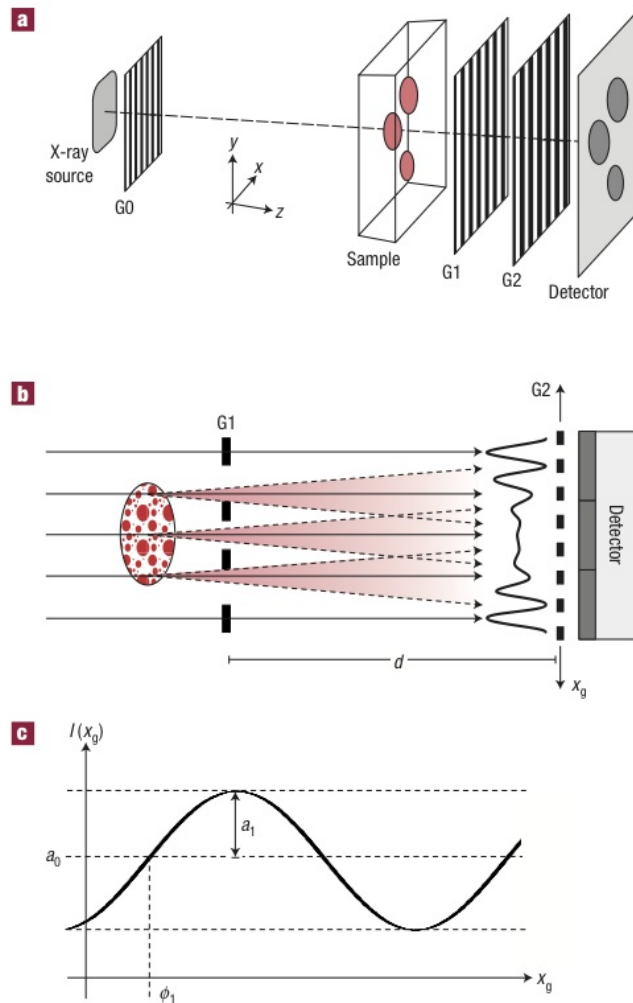


Figure 7.1: Set-up of grating interferometer CT. (a) Set-up with a source grating  $G_0$ , a phase grating  $G_1$  and an analyser absorption grating  $G_2$ . (b) Through the Talbot effect a linear periodic fringe pattern is created behind  $G_1$  in the plane of  $G_2$ . (c) Intensity modulation detected in a detector pixel when one of the gratings is scanned along  $X_g$ . A loss in the amplitude of the oscillation due to the scattering of X-rays in the specimen (degradation of the coherent wavefront) can be used to extract images with dark-field contrast. (Image and caption reproduced from Pfeiffer *et al.* (2008)).

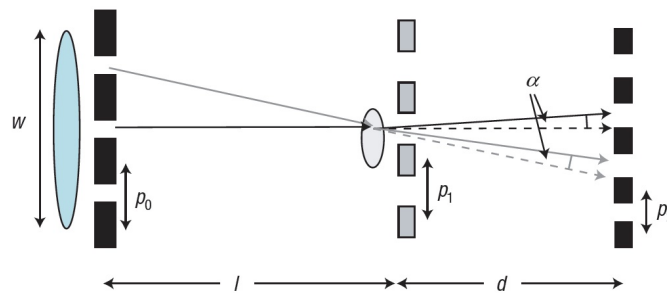


Figure 7.2: Illustration of angular deviation in differential phase imaging (Pfeiffer *et al.*, 2006)

In the experimental setup shown in figure 7.1, grating  $G_1$  causes the photons passing through the sample to form a linear periodic fringe pattern in the plane of  $G_2$ . By translating  $G_2$ , local variations in signal intensity allow the different imaging signals to be obtained; conventional absorption, phase contrast and scatter (dark-field). These signals can be obtained using a conventional imaging detector. The dark field image is one of the major novelties of this system. Absorption, differential phase, and dark field projections can be reconstructed from the signals, then reconstructed into tomographic volumes using a standard filtered back-projection algorithm.

For weakly absorbing objects, the local phase gradient  $\partial\Phi(x, y)/\partial x$  is directly measured by detection of the local signal intensity. The recorded pixel intensity,  $\mathbf{I}_k$ , forms a sinusoidal curve as a function of the phase step,  $\mathbf{k}$  given by (Revol *et al.*, 2010):

$$I_k \approx a_0 \left[ 1 + v \cdot \sin \left( 2\pi \frac{kn_{per}}{N_{ps}} + \varphi \right) \right] \quad (7.2)$$

Where  $N_{ps}$  is the number of phase steps. The phase stepping process therefore allows inference of the mean,  $\mathbf{a}_0$ , visibility,  $\mathbf{v}$ , and phase,  $\varphi$  signals. These three image types are calculated by comparing the sample measurement (object in the field of view) against a reference measurement (no object in field of view) (Revol *et al.*, 2010).

The classical transmission image is given by the decrease in beam intensity due to absorption in the object, while the dark field image is given by the decrease in visibility in the phase stepping curve due to scattering. The differential phase image is formed due to the angular deviation of the beam induced by a gradient in the phase shift of the beam after propagation through the object Pfeiffer *et al.* (2006).

By acquiring a sequence of phase stepped images at rotational increments, a filtered back projection algorithm can be used to reconstruction a 3D tomographic data set. Each contrast mode (transmission, differential phase, and scattering) can be reconstructed separately to build a 3D distribution of the absorption coefficient  $\mu(x, y, z)$ , index of refraction  $n(x, y, z) = 1 - \delta(x, y, z)$  and the linear diffusion coefficient  $\epsilon(x, y, z)$  respectively (Revol *et al.*, 2010). While the transmission and scattering images can be effectively reconstructed using a conventional filtered back-projection algorithm, a modified FBP algorithm is employed to obtain the DPC reconstruction. This is due to the extra information contained within the phase shifted images. For an object described by  $g(x, y, z)$ , as shown in figure 7.3, the projections through the object at an angle  $\omega$  to the x-axis are given by the Radon transform Radon (1917):

$$G(y', \omega) = \int_{-\infty}^{\infty} g(x', y') dx' \quad (7.3)$$

When considering the DPC imaging mode, the experimental set up not only gives the ordinary line projection of the object function (as in absorption mode), but also the line projection of the partial derivative of the object function (Pfeiffer *et al.*, 2007):

$$D(y', \omega) = \int_{-\infty}^{\infty} \frac{\delta g(x', y')}{\delta y'} dx' \quad (7.4)$$

Therefore, conventional FBP reconstruction of the DPC line projection will not give a correct reconstruction of the original object function. The filter function in conventional FBP has been adapted by the group at CSEM to give a correct reconstruction. This function is shown in figure 7.3b.

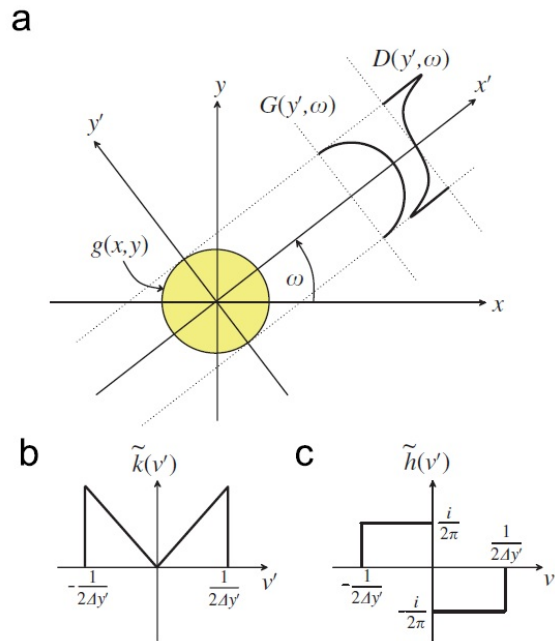


Figure 7.3: Tomographic reconstruction (a) Projection geometry. (b) Backprojection filter function for absorption line integrals. (c) Backprojection filter function for gradient (DPC) projection integrals (Pfeiffer *et al.*, 2007).

More detailed explanations of how the system works can be found in (Kottler *et al.*, 2007; Pfeiffer *et al.*, 2008; Revol *et al.*, 2010, 2011b; Revol *et al.*, 2011). Figure 7.4 shows example projections of a polymer felt-tip pen using the various imaging modes.

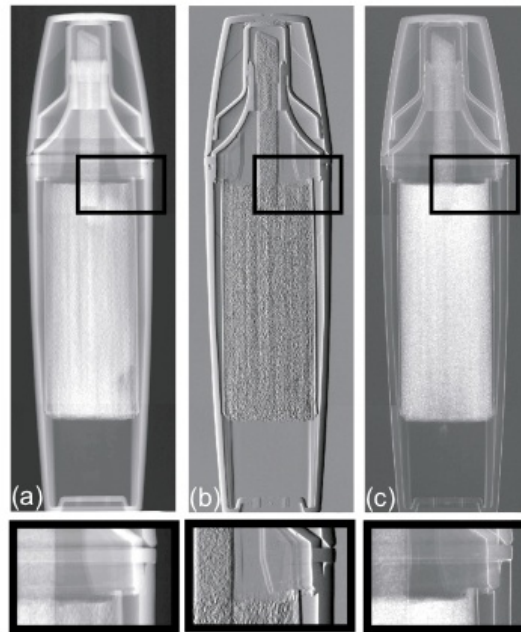


Figure 7.4: Example images of a felt-tip pen. (a) Transmission (b) Differential phase contrast (c) dark field. From Revol *et al.* (2011b).

### 7.3 Experimental Method

A 25mm wide coupon (labelled Z1) was cut from a CFRP plate of lay-up  $[0/+45/90/-45/0]_s$  (10 plies). This sample was taken from a plate used in another project in the North West Composites Centre (University of Manchester), and so the lay-up was not chosen for a particular reason other than it contained lamina of several fibre orientations. The plate had previously been subjected to a low-velocity impact of 20 J, using the drop weight impact method outlined in Chapter 5.

The plate was placed into a vice-like sample holder within the cabinet of the tomography equipment, which rotates the sample through an angle of  $360^\circ$  as in conventional CT. The experimental set-up is shown in figure 7.5, which shows the relative positions of sample, gratings, and detector. Photographs of the sample are shown in figure 7.6. Figure 7.7 then describes the co-ordinate system used in this experiment.

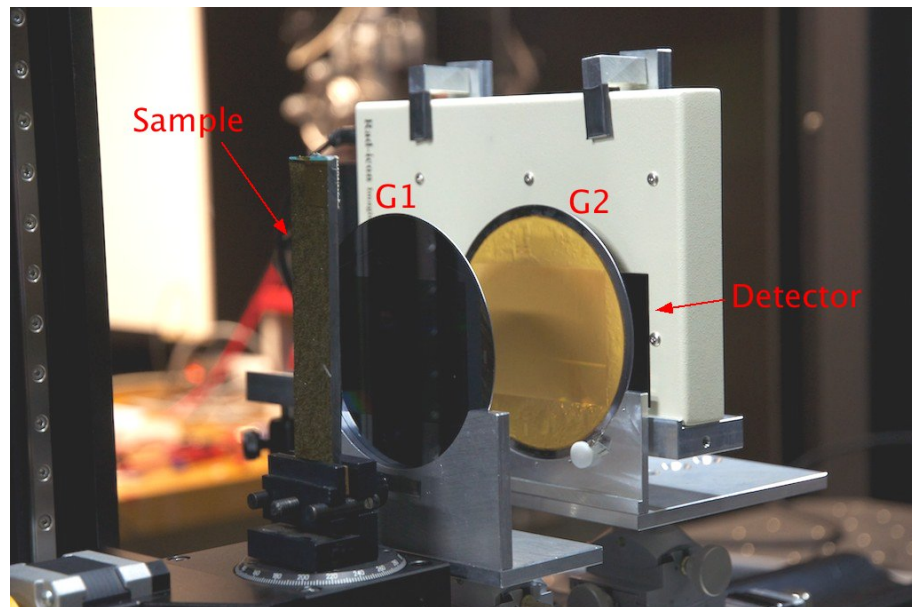
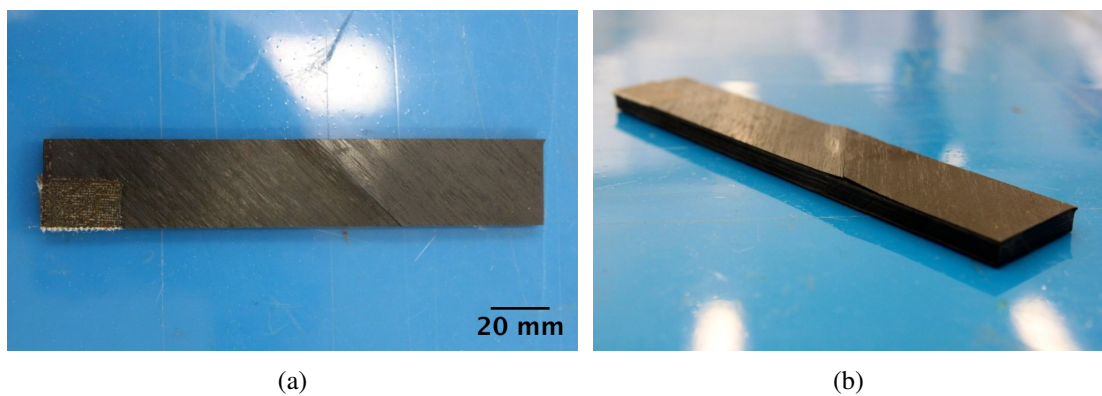


Figure 7.5: Experimental set-up of grating interferometer tomography equipment at CSEM.



(a)

(b)

Figure 7.6: Photographs of sample Z1.

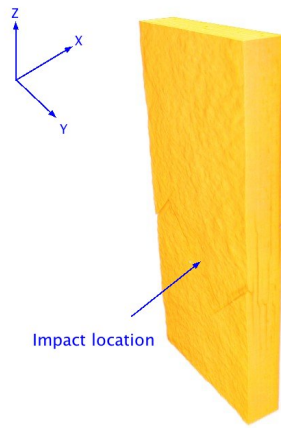


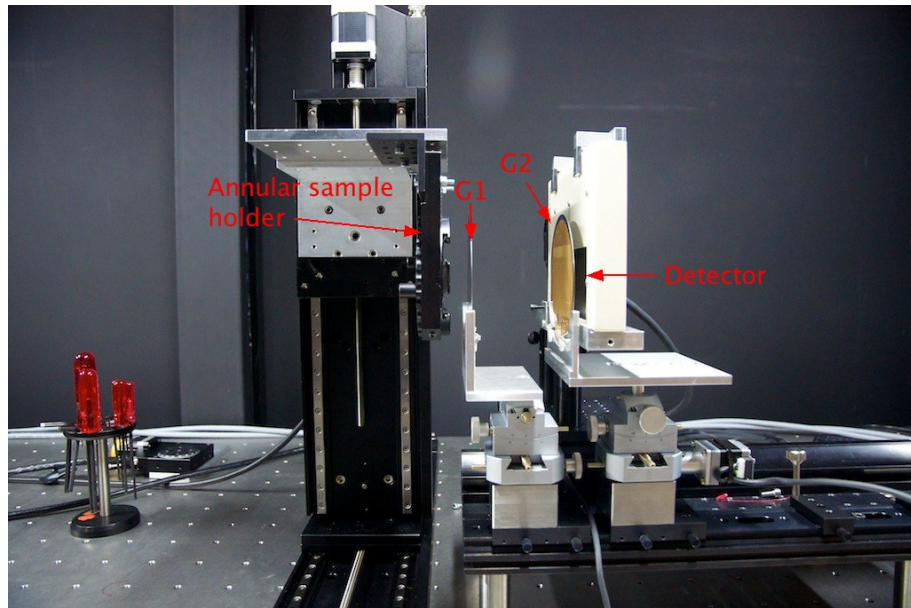
Figure 7.7: Sample co-ordinate system used to describe geometry in the grating experiment.

Table 7.1 gives the imaging parameters used in the tomographic imaging of sample Z1. Due to the number of stepping positions for grating G2, the total scan time was approximately 12 hours.

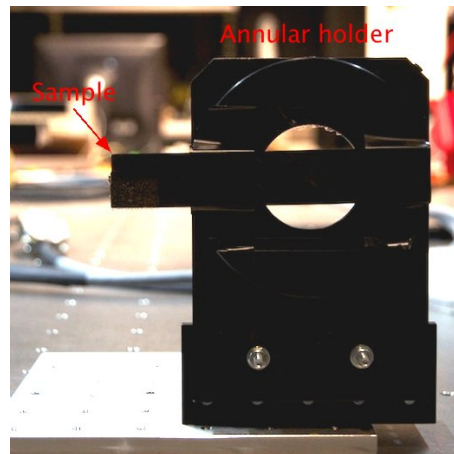
Table 7.1: Imaging parameters for grating interferometer tomography of sample Z1.

<b>Imaging Parameter</b>	<b>Value</b>
Target material	Tungsten
Accelerating voltage	35kV
Filament current	250 $\mu$
X-Ray spot size	1 mm
Frame exposure time	60 s
No. of projections	720
No. of G2 step positions	6
Voxel size	47 $\mu$ m
Source-sample distance	500 mm
Sample-G1 distance	30 mm
G1-G2 distance	60 mm

After the tomographic data had been collected, the sample was remounted in an annular rotating sample holder and projections were taken of the specimen at various rotation angles around the optical axis ( $X$  axis). Projections were taken at increments of  $15^\circ$  between  $0^\circ$  and  $90^\circ$ . These projections were taken to assess the effect of specimen orientation with respect to the optical axis on the absorption, differential phase, and dark field (scattered) projections. Figure 7.8 shows the experimental set-up of this projection-only experiment.



(a) Experimental overview.



(b) Close up of annular specimen holder.

Figure 7.8: Experimental set-up for variation of sample orientation with respect to optical axis.

Additionally, the impacted coupon was also scanned at the HMXIF using the Nikon Custom Bay CT scanner for comparison with the CSEM equipment. The reconstructed data was resampled to match the voxel size of the CSEM system ( $47\mu\text{m}$ ).

Table 7.2: Imaging parameters for tomography of sample Z1 at HMXIF.

<b>Imaging Parameter</b>	<b>Value</b>
Target material	Tungsten
Accelerating voltage	60kV
Filament current	250 $\mu$
Frame exposure time	2 s
No. of projections	3142
Magnification	14X
Voxel size	14 $\mu$ m (47 $\mu$ m resampled)

## 7.4 Results and Discussion

### 7.4.1 Projections

Figure 7.9 shows projections which were acquired as part of the tomographic data acquisition on sample Z1. Projections are shown for angular rotations of  $0^\circ$ ,  $30^\circ$  and  $90^\circ$  around the Y-axis, where the impacted face of the coupon is parallel to the plane of the detector at  $0^\circ$ . Each row of figures shows the absorption, differential phase, and scattered signal for each projection angle respectively.

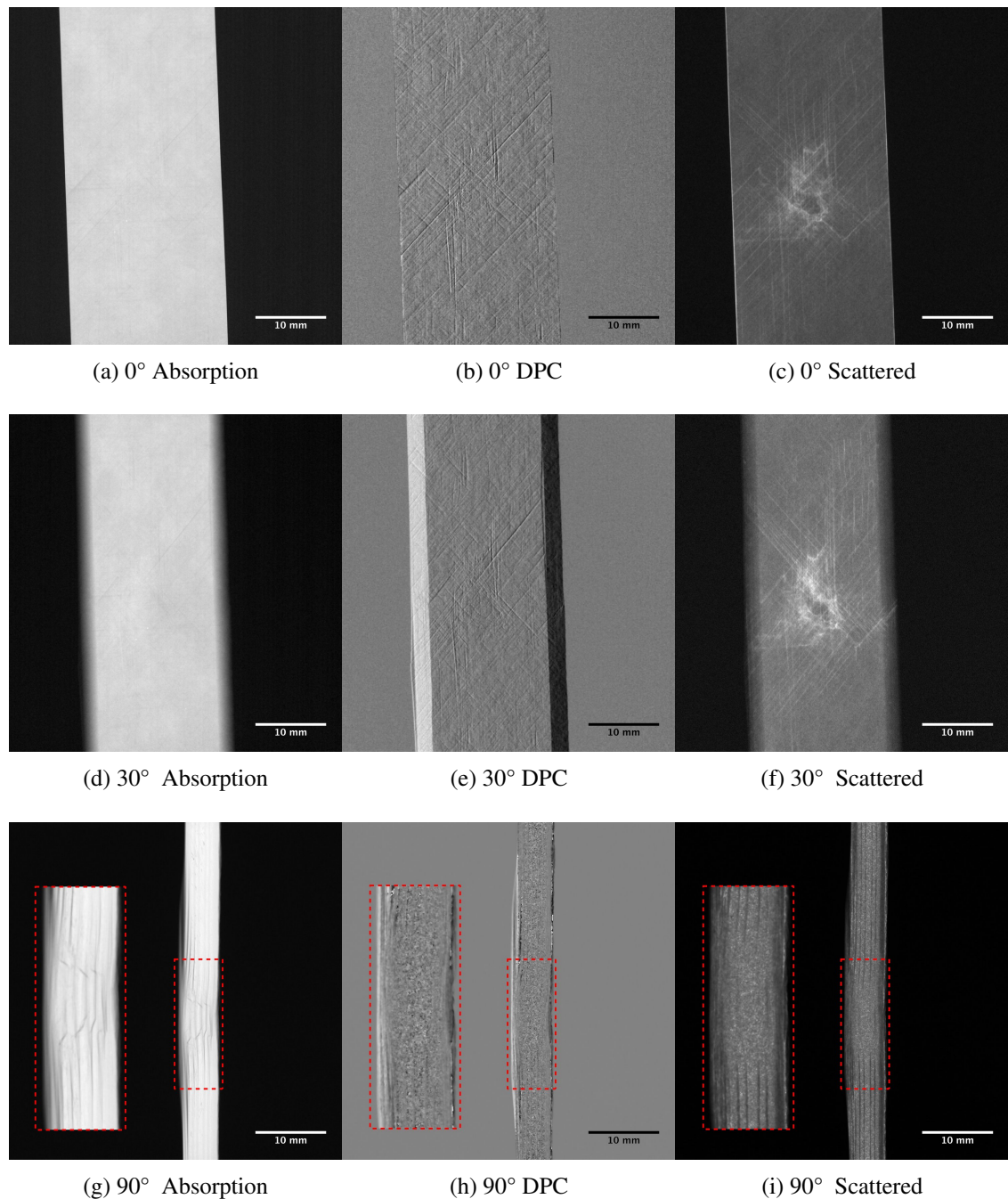


Figure 7.9: Absorption, differential phase contrast (DPC), and scattered projections of sample Z1. Rotation angle specified is around the Y tomographic axis.

Figure 7.9 shows the the standard absorption imaging gives little information about any damage present at  $0^\circ$  or  $30^\circ$  . By  $90^\circ$  however, the impact induced delaminations and shear cracks are visible. This observation is typical of conventional radiography, as the damage accounts for a significant proportion of the X-Ray path length at this orientation, and therefore produces a strong signal. The DPC projections show very little information within the object at all rotation angles, although a fine needle-like pattern is seen in the  $0^\circ$  and  $30^\circ$  projections, corresponding to the fibre orientations. Strong artefacts are also at  $30^\circ$  at the left and right edges of the object in the DPC image, due to the strong phase contrast between the object and air. At  $90^\circ$  , virtually none of the internal damage is visible compared with the absorption image. Interestingly the scattered projections show significant bright areas around the impact location in both  $0^\circ$  and  $30^\circ$  projections. A network of the needle-like bright lines is also seen in these projections, again corresponding to the fibre orientations in the sample. At  $90^\circ$  , however, similar to the DPC projections very little damage information is present in the scattered image. Although the delaminations are clearly visible, none of the shear cracks which were apparent in the absorption image are present. These observations suggest that the scattering signal is particularly sensitive to some mechanism of damage through the use of a single projection, in contrast to conventional absorption imaging. Performing an ultrasonic C-scan on the sample revealed the the projected delamination area as shown in figure 7.10. This C-scan was acquired in the same manner as discussed in Chapter 5.7.2.

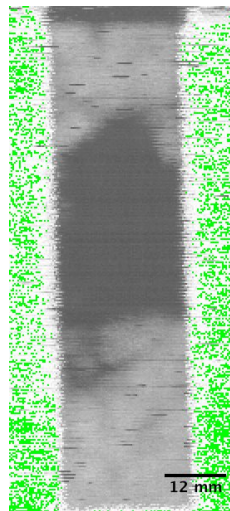


Figure 7.10: Ultrasonic C-scan of sample Z1, showing delamination area. Spatial resolution approximately 1 mm.

Comparing figure 7.10 with the scattered images in figure 7.9, it is apparent that the scattered imaging is not particularly sensitive to the delamination damage in a single projection. This is not to say however, that the delamination would not be characterised when performing a full CT scan. However, it does appear that the scattered imaging must be very sensitive to smaller damage features such as matrix micro-cracking. This would be expected due to the small angle scattering of X-Rays which occurs at micron- and

sub-micron scale interfaces (Pfeiffer *et al.*, 2008).

Because the occurrence of ultra-small angle scattering is directly related to variations of electron density in the sample, features which are smaller than the detector pixel size can be observed. Micron and sub-micron features such as matrix micro-cracking and porosity can therefore be detected using this imaging method, despite the experimental voxel size being only 47  $\mu\text{m}$ . Published applications of this phenomenon have included the analysis of porosity in aluminium welds (Revol *et al.*, 2011a), and detection of explosive materials (Pfeiffer *et al.*, 2008).

The physical origin of this small angle scattering is due to phase shifts in the X-Ray beam caused by small material inhomogeneities. Propagation of the X-Ray beam through the material results in variations of the wavefront,  $\phi_f$  which are small compared to the pixel size (Revol *et al.*, 2011a). Broadening of the beam occurs due to these variations, equivalent to a loss of coherence in the X-Ray beam. The interference fringes then appear blurred at the detector, causing a decrease in the visibility function,  $v$ . Theoretical expressions for the scattering function were developed by Yashiro *et al.* (2010). Assuming the variation in the phase signal over a single pixel follows a Gaussian distribution, the scattered signal can be expressed as:

$$V(m, n) = \exp(-\sigma^2(m, n)(1 - \gamma(-N_{p1}; m, n))) \quad (7.5)$$

Where  $\sigma$  is the width and  $\gamma$  is the normalised autocorrelation function in the  $x$ -direction of the Gaussian distribution,  $\phi_f$ . Detailed information can be found in Yashiro *et al.* (2010).

The experimental observations discussed in this section are explored further in section 7.4.2 when compared with the reconstructed tomography data.

Figure 7.11 shows the results of rotating the sample around the optical axis. Only three of the angular positions are shown here from the seven that were taken.

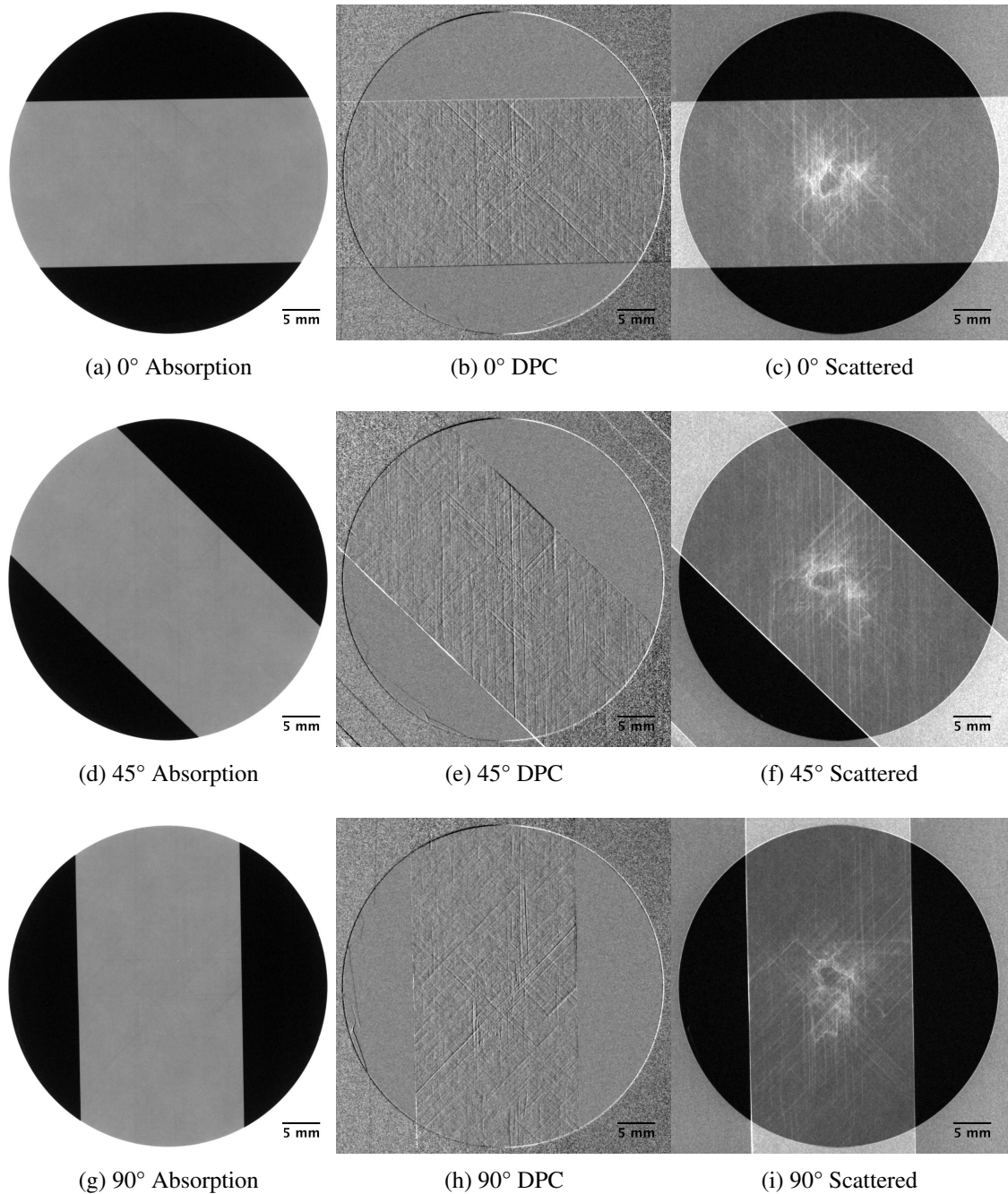


Figure 7.11: Absorption, DPC and scattered projections of sample Z1. Rotation angle specified is around optical ( $X$ ) axis.

The projections in figure 7.11 reveal that the absorption imaging mode is not sensitive to the relative angle between damage features and the optical axis. Similarly, the DPC images show little change in overall intensity or contrast at the damage features. In contrast to the absorption and DPC projections, the scattered projections do show a change in intensity of the damage features as the sample is rotated. The central bright area, corresponding to damage in the immediate vicinity of the impact zone shows a gradual loss in intensity as the rotation angle is increased from  $0^\circ$  to  $90^\circ$ . Also apparent from the scattered projections is that the cracks which are aligned in the vertical direction appear

brighter. This suggests that cracking in the different plies gives a stronger signal depending on the relative angle to the optical axis.

Figure 7.12 gives intensity line profiles across a region near the centre of the impact location. The precise location is shown in the inset projection. To ensure the line profiles were taken across the same features in all projections, each projection was rotated around the optical axis to match it with the  $90^\circ$  projection. Image software ImageJ was then used to plot line profiles across matching regions in each projection.

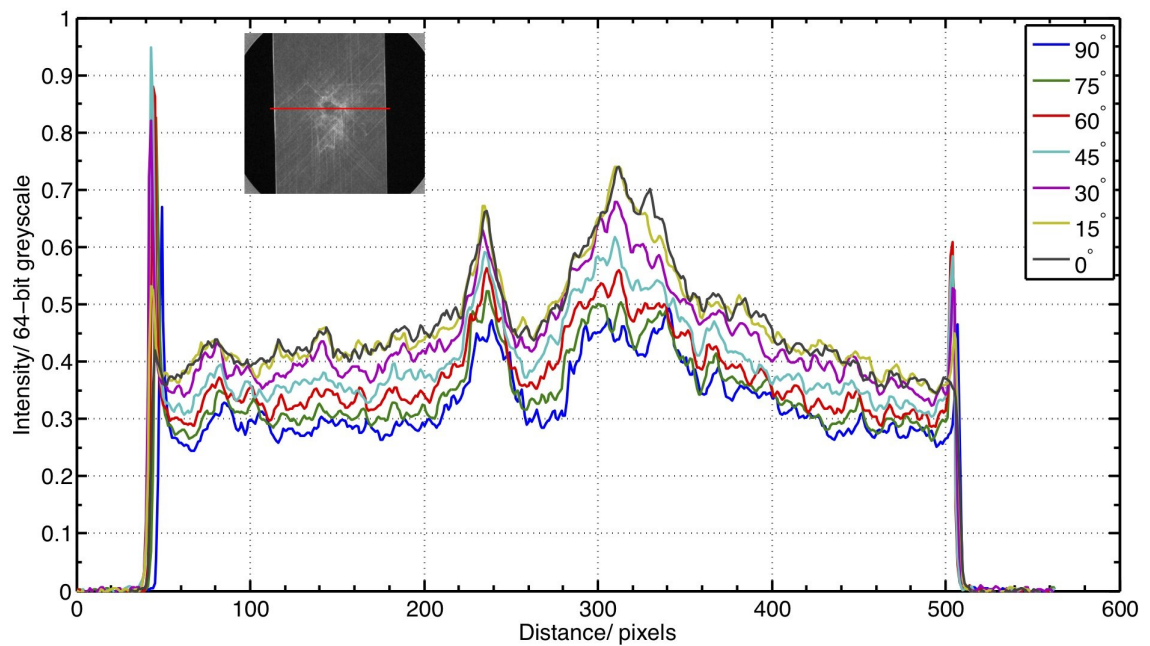


Figure 7.12: Intensity line profiles across damage area (inset) of sample Z1 under various optical axis rotation angles.

Figure 7.12 clearly shows the general increase in signal intensity of the damage surrounding the impact zone as the rotation axis decreases from  $90^\circ$  to  $0^\circ$ . An increase in the intensity of the edge artefacts is also observed.

## 7.4.2 Tomography

Figure 7.13 shows reconstructions of sample Z1 in the  $XY$  plane, at a position directly underneath the impact location. The images are rotated to fit next to each other for comparison, with the impact face being on the left of each image. Figures 7.13 (a)-(c) are from the CSEM interferometer system, while (d) is a section from a down-sampled CT scan performed on the Nikon Metrology Custom Bay at the HMXIF for comparison.

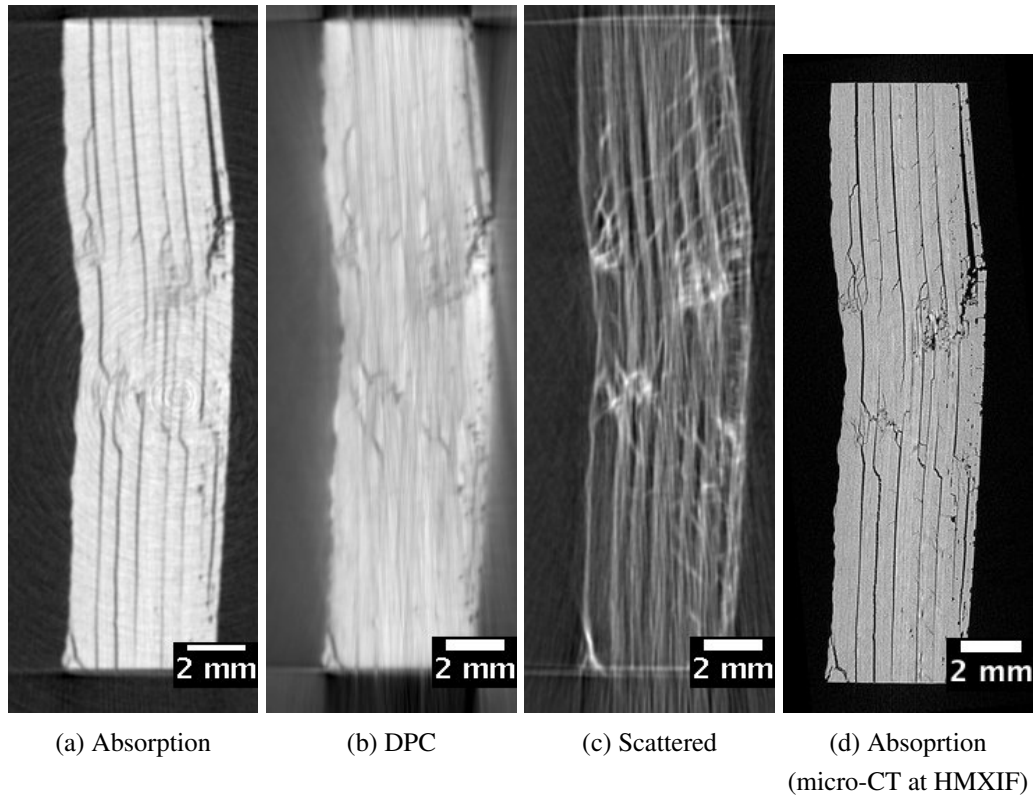


Figure 7.13: Reconstructed slices of sample Z1 in  $XY$  plane. Impacted face on left.

Figure 7.13 (a) shows that the reconstructed absorbance image resembles a typical cross sectional CT image obtained from an absorption based CT system. Comparing this with the image obtained from the HMXIF system (7.13 (d)), similar damage mechanisms are observable. Although the resolution in the CSEM absorption image is lower, delaminations and shear cracks are still clearly visible. Smaller matrix cracks which are apparent in the HMXIF scan are lost, due to the intrinsic voxel size of the CSEM detector. The cross section from the DPC image, however, shows significant differences to the absorption cross section. The delaminations positioned away from the impact zone are not visible, and significant glow artefacts surround the object. Many of the shear cracks however, are still visible. The scattered image, 7.13(c) shows significant sensitivity to the matrix shear cracks which are visible in the absorption and DPC images, but also reveals many bright features which are not present in either the absorption or DPC images. This is particularly true for the area immediately adjacent to the impact zone. The scattered image shows a strong signal which corresponds to a dense network of matrix micro-cracking in 7.13(d), which is not particularly apparent in 7.13(a) or (b).

Figure 7.14 shows reconstructions of sample Z1 in the  $XZ$  plane, the long axis of the sample extends vertically in these images. In this orientation, the absorption image (7.14 (a)) again shows the delamination and shear cracks associated with the impact damage, comparable with that seen in 7.13 (d). The DPC image in this orientation, 7.14 (b), now shows little direct evidence of the shear cracking or delaminations apart from the

significant cracking at the front and back faces. The bulk of the cross section shows a generally degraded intensity where the shear cracks exist, but no individual features are apparent. Conversely, the scattered cross section, 7.14 (c) shows strong signals detailing the conical shape of the matrix cracking moving from the front to the back face of the sample. The scattering image, furthermore, also shows some contrast at the ply interfaces away from the impact zone.

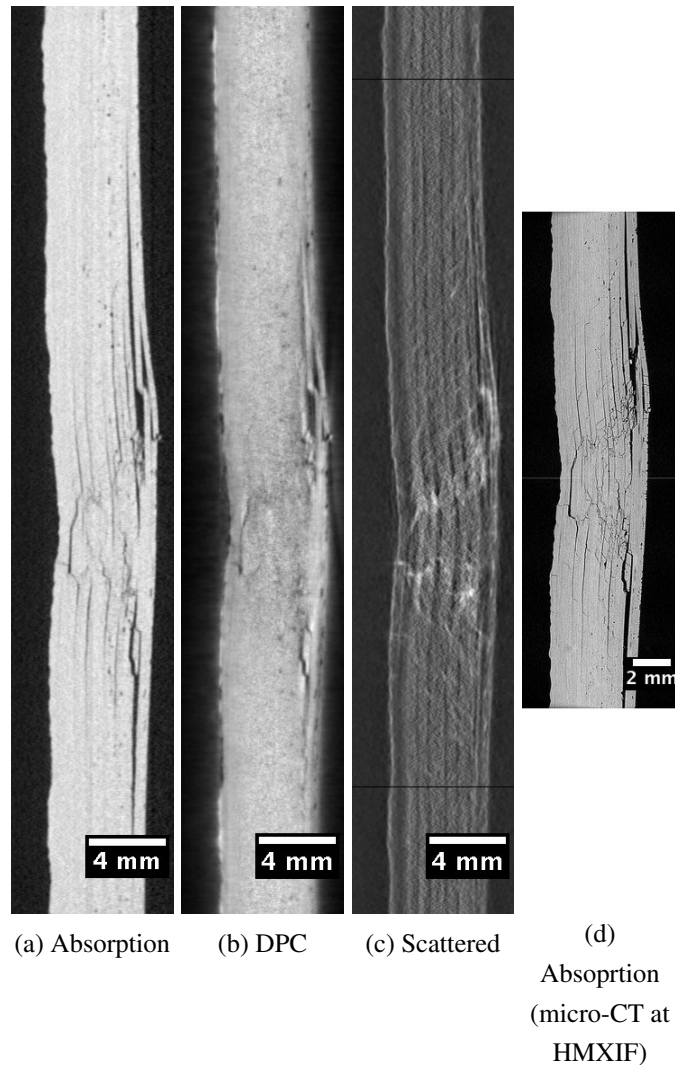
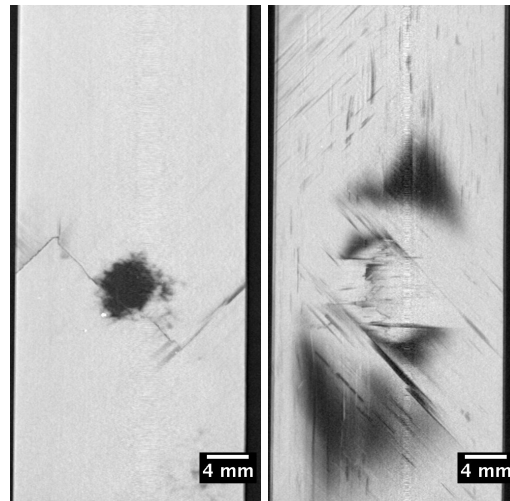


Figure 7.14: Reconstructed slices of sample Z1 in  $XZ$  plane. Impacted face on left.

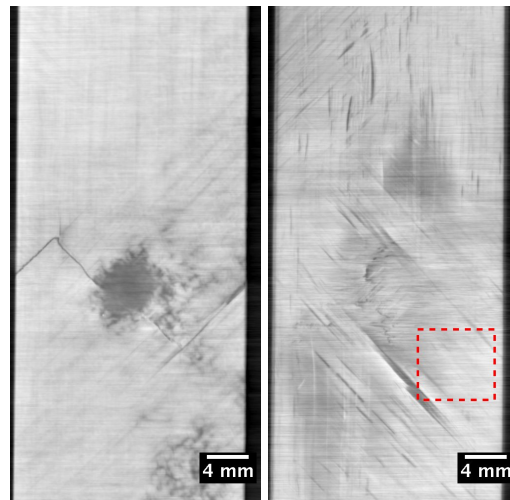
Figures 7.15 (a)-(c) show the in-plane ( $YZ$ ) cross sections. The absorption image, 7.15 (a), shows the delamination and matrix cracking with significant contrast. Delaminations in all three ply directions can be seen extending from the impact zone. Interestingly, figures 7.15 (b) and (c) show reduced signs of artefacts in both the DPC and scattered images, compared to the cross sections in the other planes. In the  $YZ$  plane, the DPC image shows characteristics of both the absorption and scattered image, albeit with reduced contrast between the object and damage. The scattered image shows high intensity at the cracking features, but the delamination area does not have a particularly strong contrast.

On closer examination, however, both the DPC and scattered images contain horizontal artefacts, which can be seen in figure 7.16. These images are magnified views of 7.15 (d) and (f) respectively.



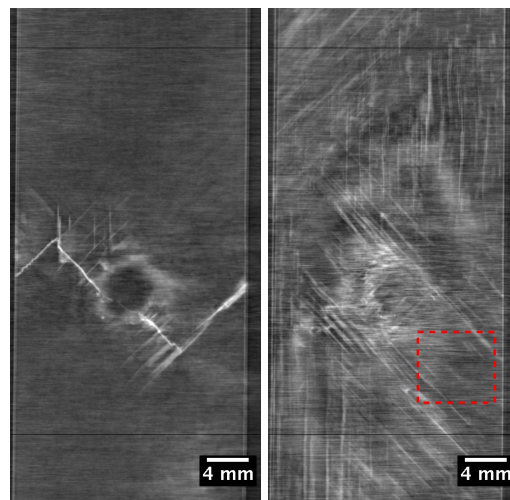
(a) Absorption 0.5mm  
below impact face

(b) Absorption in  
laminata centre



(c) DPC 0.5mm below  
impact face

(d) DPC in laminata  
centre



(e) Scattered 0.5mm  
below impact face

(f) Scattered in  
laminata centre

Figure 7.15: Reconstructed slices of sample Z1 in  $YZ$  plane. Impacted face on left.

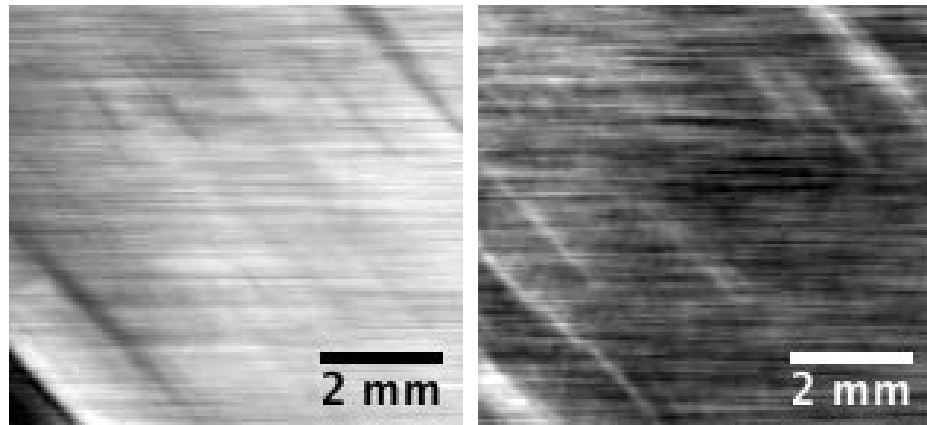


Figure 7.16: Local artefacts in DPC and DF  $YZ$  plane images, magnified from figure 7.15

As a result of the artefacts associated with the DPC and scattered reconstructions, it was very difficult to perform accurate data segmentation to quantify the visible damage in each reconstruction. Despite the relatively good SNR obtained in the scans, the artefacts made a significant contribution to the signal also, giving noisy threshold results with little relation to the main damage volume. Figures 7.17 show examples of 3D renders for each of the imaging modes using the CSEM equipment. It is apparent that the delamination is dominant in the absorption image, and cracking in the DPC and scattered data. However, due to the high amount of data smoothing which had to be applied to the DPC and scattered data, the renderings do not display the full extent of the damage.

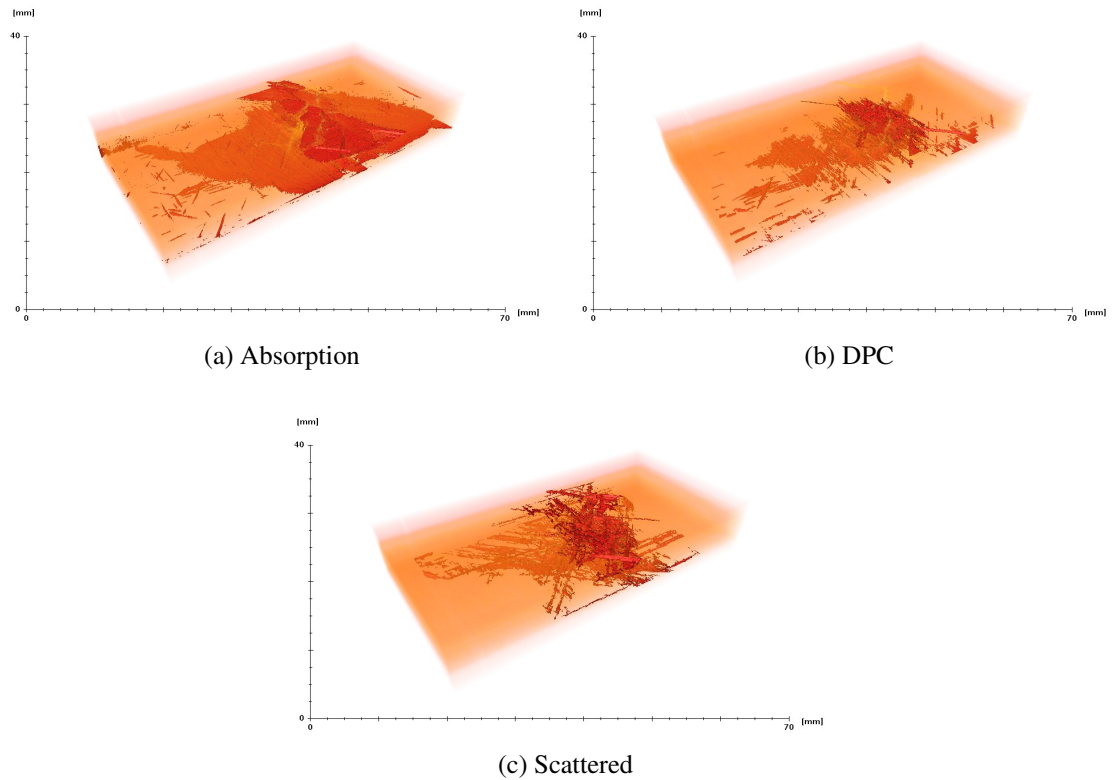


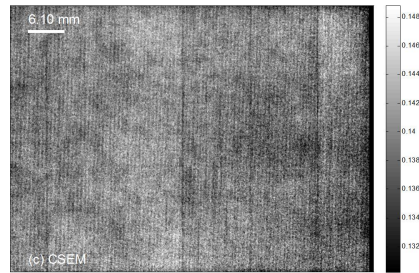
Figure 7.17: 3D renderings of impact damage using grating interferometer tomography.

### 7.4.3 Dark field imaging of CAI Samples

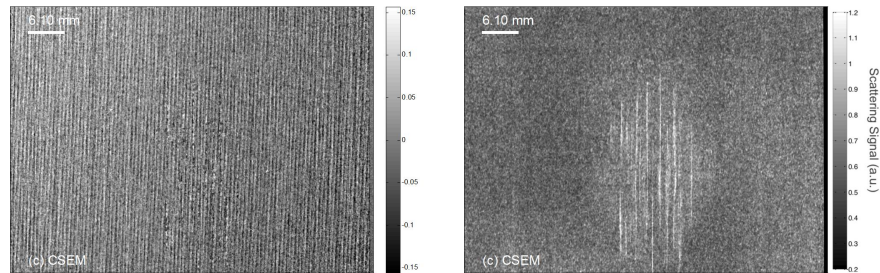
This section presents results of projection images taken on the CSEM system of three impacted samples. After the initial tomography experiment at CSEM, it was clear that the dark field imaging method could be used to identify impact damage in CFRP plates using only 2D projections. Three samples, B5, B10 and B15, were impacted at 5, 10 and 15 J respectively. These samples were sent back to CSEM for projection imaging to assess whether the increase in impact energy would cause an observable change in the dark field images.

**The images in this sub-section were acquired by Vincent Revol, a PhD student at CSEM. Data processing was performed by the author.**

Figure 7.18 shows absorption, DPC, and scattered images for the 15 J samples (B15). Damage is clearly visible in the scattered image, 7.18 (c), but not in the absorption or DPC images. Although some damage was observable from the absorption and DPC projections of sample Z1 in the previous section, the relative thickness of samples B5-B15 results in very little beam attenuation. Consequently, the absorption images show little damage and the path length available for refraction in the DPC image is limited. Furthermore, as a result of the reduced beam attenuation, the SNR in all the projections of samples B5-15 is reduced compared to the results from sample Z1.



(a) Absorption

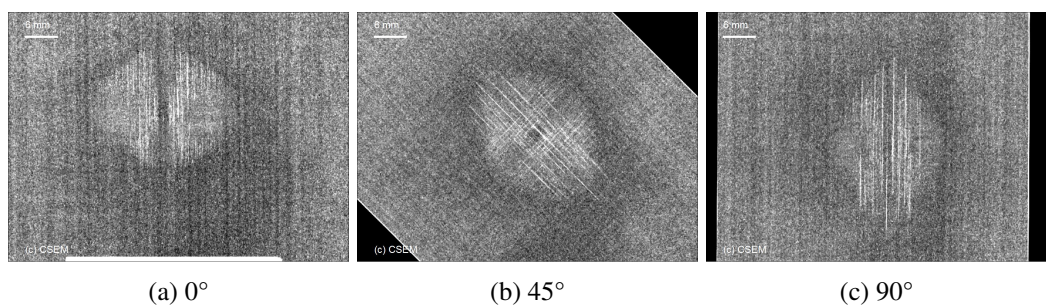


(b) DPC

(c) Scattered

Figure 7.18: Grating Interferometer Projection images of sample B15 which was impacted at 15 J.

The following figures, 7.19 to 7.21, show the dark field images of each impacted sample under various rotations about the optical axis (sample  $X$  axis). In figure 7.21, thresholded images for each damage are shown. These thresholds were achieved using semi-automatic methods, as the low SNR prevented automated thresholding. The "*brush within range*" tool in Avizo® was applied by selecting the lower threshold to 50% of the maximum brightness in each case.



(a) 0°

(b) 45°

(c) 90°

Figure 7.19: Dark field projections of 5 J impact sample rotated with respect to optical axis.

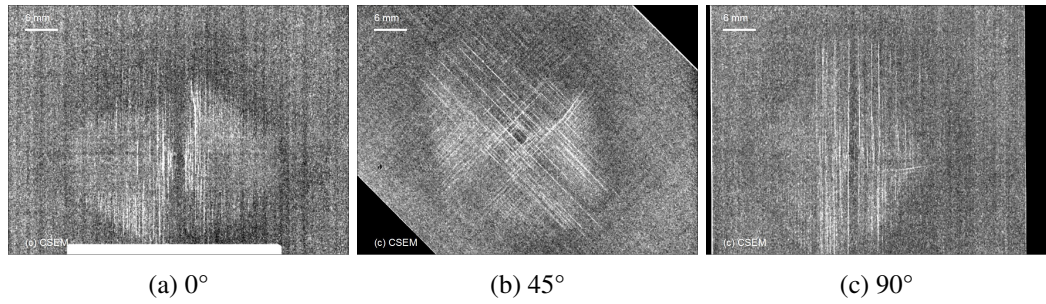


Figure 7.20: Dark field projections of 10 J impact sample rotated with respect to optical axis.

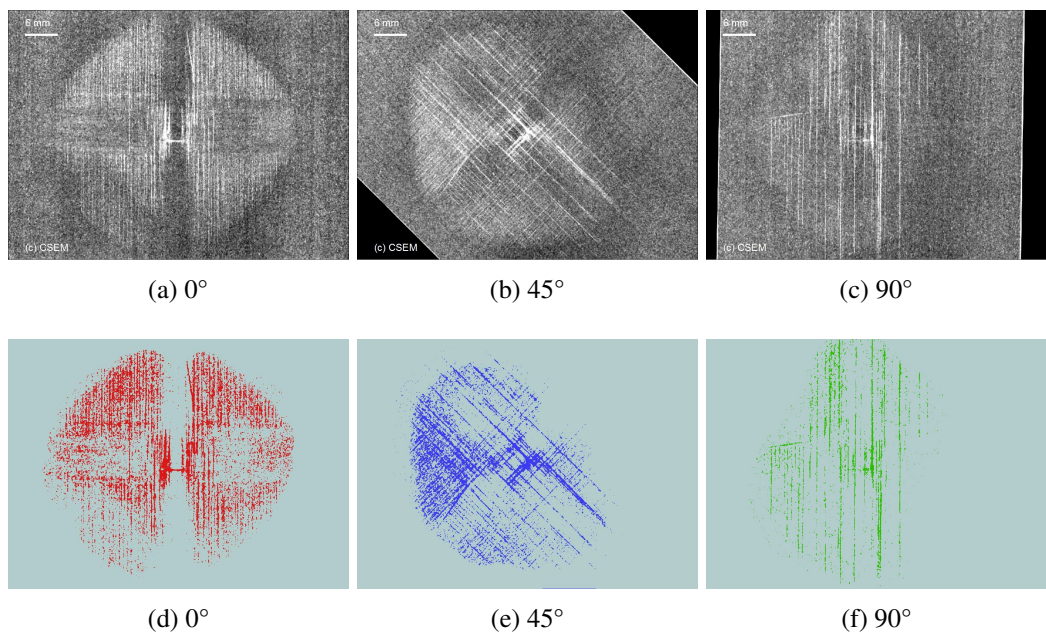


Figure 7.21: Dark field projections of 15 J impact sample rotated with respect to optical axis (a-c). Respective damage areas thresholded (d-f).

Similar to the results obtained from sample Z1, figures 7.19 to 7.21 show increasing signal intensity when the sample is rotated to  $0^\circ$  with respect to the optical axis. The projections also show two distinct orientations of damage. As samples B5-15 contain only  $0^\circ$  and  $90^\circ$  ply (fibre) orientations, the damage is clearly linked to the fibre orientation. This result was observed in sample Z1, and also in the micro-CT studies performed in Chapter 5, and as such must represent the general state of matrix cracking in the sample. Interestingly, the damage highlighted by the scattering projection outlines the typical pattern of delamination observed previously. This result suggests that scattered imaging could also be used to imply the delamination area. It is possible the delamination extent was not observed in projections of sample Z1 due to the coupons width being cut to within the delamination area.

Figure 7.22 shows the variation of measured damage area, based on the thresholded images, for each sample and orientation.

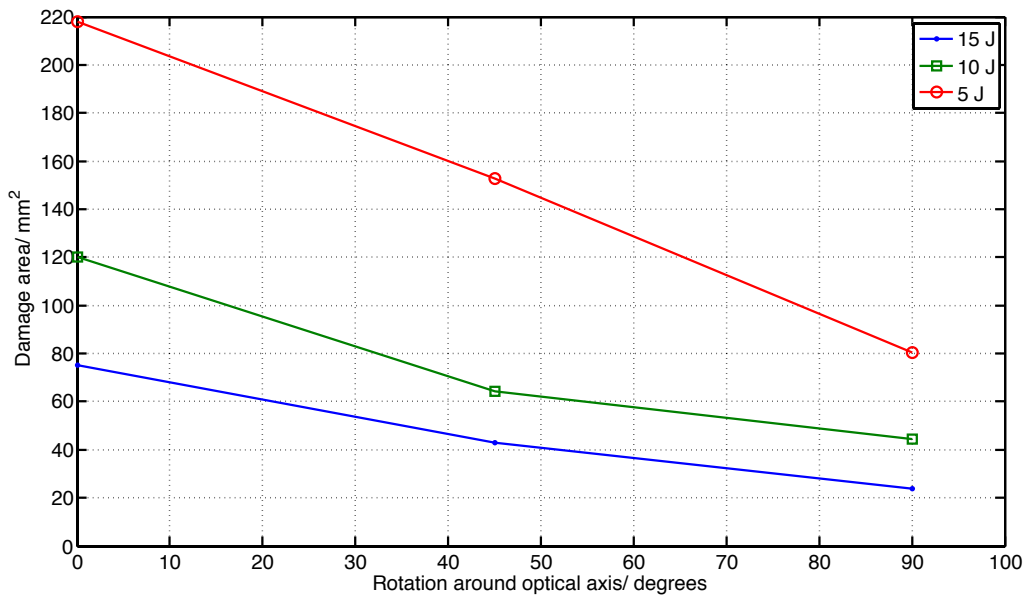


Figure 7.22: Variation of thresholded damage area with rotation about optical axis.

Figure 7.22 illustrates under all three impact conditions, the measured damage area from the scattered projections reduces as the angle between the  $0^\circ$  fibre orientation and the optical axis increases. The trends appear to be linear in all cases, but further work is needed to obtain any statistical significance. The trends do however, reflect those seen in Chapter 5 whereby damage area was seen to increase with increasing impact energy.

## 7.5 Chapter Summary and Conclusions

The work presented in this chapter has demonstrated the novel use of grating interferometer CT to characterise impact damage in a CFRP material containing uni-directional plies. The system was able to perform projection and full rotation tomographic imaging in absorption, differential phase, and scattering contrast modes.

Initial results revealed that the scattering projections were particularly sensitive to matrix cracking due to small angle X-Ray scattering. In contrast, the absorption and differential phase contrast images showed very little projection information.

Performing full tomographic imaging of a physically sectioned coupon showed typical results from the absorption contrast imaging mode. Shear cracking and delaminations were visible, comparable to the results obtained with the Nikon Metrology Custom Bay at the HMXIF. Unfortunately, the differential phase tomography contained significant edge and phase wrapping artefacts which degraded any damage signals from dominating the image. Although damage was more clearly visible in the plane of the laminate plies ( $YZ$  plane), the contrast was relatively low and horizontal artefacts in this cross section

prevented quantitative segmentation. Tomographic results from the scattered imaging mode proved to be more useful than from the DPC. Shear cracks were clearly visible in all planes, and matrix-micro cracking also have a strong signal. Some of these cracks were not visible even in the absorption images, suggesting that scattering may improve damage detection beyond the spatial resolution of the X-Ray detector. Significant in-plane artefacts, however, also prevented quantitative thresholding in the scattered volume. Overlap of bright signals from the matrix cracking also made segmentation difficult.

Projections of three plate samples impacted at 5, 10 and 15 J in scattering mode revealed an increase of measurable damage area with impact energy. The damage visible was mainly due to matrix cracking, but also outline the projected damage area to some extent. By rotating the sample around the optical axis, it was found that the intensity and direction of the damage signal varied. This result implies that the technique is also sensitive to damage direction, but more importantly, the ply direction in which the damage exists. The scattered projections in these impacted samples revealed two major damage directions, which did correspond to the ply directions used in the lay-up ( $0^\circ$  and  $90^\circ$ ).

Overall, CT using a grating interferometer has significant potential as a tool for characterising and quantifying damage in CFRP materials. There is scope for a large amount of further work, and indeed the technology is developing rapidly thanks to the group at CSEM. Of note is a paper recently published by the group concerning the removal of artefacts in the DPC images, which shows potential to improve the information which can be extracted from the reconstructed tomographic data (Jerjen *et al.*, 2011).

## GENERAL CONCLUSIONS AND FURTHER WORK

The work presented in this thesis has made several contributions to knowledge in the field of tomographic imaging of carbon-fibre reinforced plastics. It has also provided many more opportunities for further work.

Chapter 4 demonstrated a proof-of-concept for dual-energy imaging of high aspect ratio CFRP plates. Two cases were presented. Both were based on experimental determination of beam hardening coefficients, but differed in their image processing approach to generating the dual-energy data set. It was found that 'case 2', which used a weighting function dependant on signal-to-noise ratio, gave improved image quality and better contrast than a compromised scans. The method also gave a practical improvement in the ability to threshold damage using image segmentation techniques, due to improved SNR. Due to the degree of beam hardening which occurs at large material thicknesses, however, the technique failed to accurately reconstruct a large panel. The polynomials used to correct the beam hardening were poorly fitting at large thicknesses in all cases, and poorly fitting at low thicknesses for high voltages due to high beam transmission. To implement the dual-energy at these extremely high aspect ratios, where the X-Ray path length is large in absolute terms ( $>100$  mm), a better beam hardening correction needs to be developed. This could be performed using the same method as in this work, if a filtered beam is to be used. However, this would reduce the projection contrast due to removal of the low energy photons. Furthermore, a large number of experimental observations would need to be made for several filtration thicknesses. The time required to obtain the absorption data for all targets in this work by imaging the step-wedge was over 3 days. This process could perhaps be mitigated by modelling the beam hardening using the energy sensitive spectrum data which is shown in Appendix A.

The work in Chapter 5 applied the dual-energy imaging technique to the imaging and quantification of impact damage in two CFRP materials. Drop weight low velocity impact testing was used to introduce damage into small CFRP plates, which were imaged using CT and ultrasonic C-scan. The samples were then tested to failure using the compression after impact test. The work showed that CT was able to quantify projected damage area to

---

the same degree as ultrasonic C-scan in the uni-directional material when imaging the full geometrical extent of the samples. To achieve this result, a methodology for extracting the in-plane damage area from CT data was developed using image masks based on grey-scale thresholding. For the woven samples however, it was found that CT provided a lower measure of damage area when comparing CT and C-scan for the woven samples. It was proposed this difference was due to the low resolution and contrast achieved in imaging the full extent of the woven samples. Chapter 5 also demonstrated that CT could be used to visualise and quantify damage in 3D. A methodology for quantifying damage through the thickness of the laminates gave results which were in agreement with those found in the literature using other methods for determining damage. This included relating damage parameters such as area and extent from impact zone to be correlated with impact energy and CAI strength. CT also allowed the identification of damage mechanisms in both UD and woven materials.

Region of interest imaging techniques were applied in Chapter 6 to assess the practicalities of data completion methods. It was found that two data completion methods, namely level- and cosine-extensions, were effective at removing ring artefacts associated with ROI imaging. The cosine extension method was particularly useful as it allowed automatic centre of rotation calculations to be performed when reconstructing the data sets. The high aspect ratio of the CFRP test plate proved to be an advantage in the ROI case, as it meant that not all projections contained truncated data. It was still found, however, that increasing the number of projections past the number which would be required when imaging the sample within the detector FOV gave a significant improvement in image quality. ROI imaging of samples with increasing amounts of impact damage allowed further characterisation of damage in both the UD and woven materials. The higher resolution achieved under ROI conditions proved particularly useful in the case of the woven samples, whereby intra-tow cracking became observable. Matrix micro-cracking in the UD samples was also observed. Further work should focus on more detailed studies of the effect of aspect ratio on ROI image quality. The absolute amount of material outside the FOV should also be studied in more depth.

In the case of both full-object and ROI imaging, image segmentation is a particularly important area that requires further work. The geometrically complex nature of impact damage made it very difficult to perform accurate image thresholding. This was made more difficult by the generally low contrast achieved when image CFRP materials when compared with higher density materials. Other project work the author has been involved in at the Henry Moseley Image Facility has shown several opportunities for imaging projects to further quantify and understand damage mechanisms in CFRP. The use of dye penetrant significantly improves the contrast of delaminations and matrix cracking, when the dye fluid has a path into the damage. Figure 8.1 illustrates the use of iodine-based dye penetrant to image fatigue damage in a CFRP laminate manufactured from uni-directional plies. Figures 8.1 (b)-(d) shows 3D renderings of the damage visible

under fatigue at varying fractions of the ultimate tensile strength (UTS)

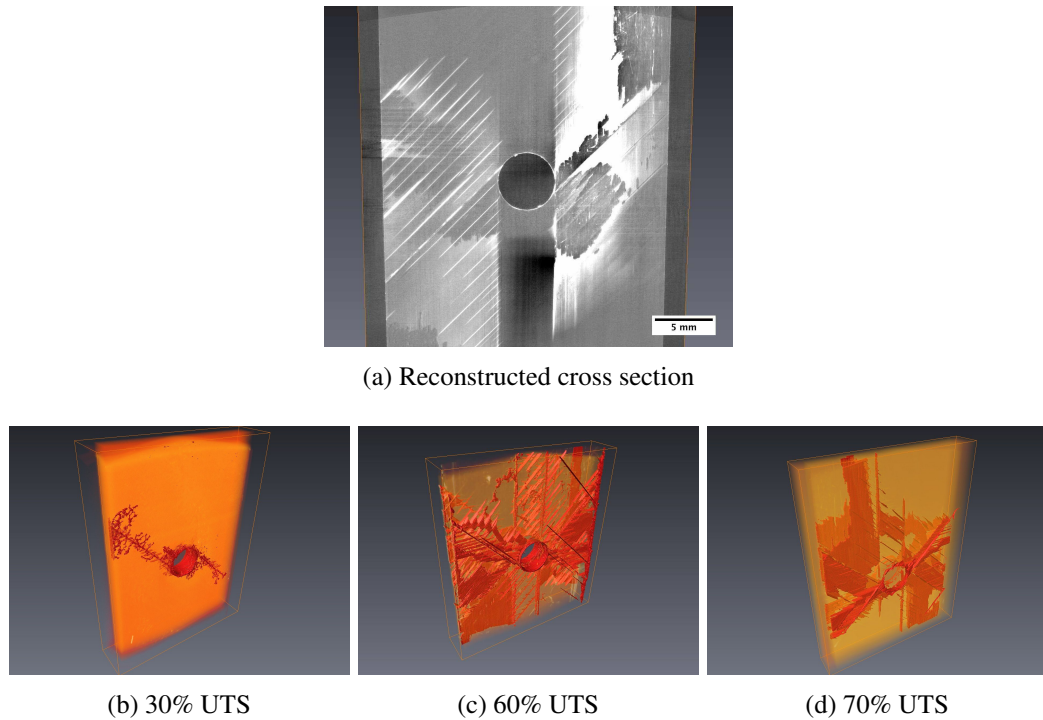


Figure 8.1: CT images of fatigue damage in CFRP containing dye penetrant. (a) is a reconstructed cross section, (b)-(d) 3D renderings highlighting the dye penetrant (red).

Chapter 7 demonstrated the first use of a laboratory grating interferometer CT set-up to image damage in CFRP. It was found that scattering (dark field) imaging was able to identify impact damage in a single projection, as opposed to performing a full CT scan. Furthermore, by rotating the sample around the optical axis, damage in different orientations became more or less visible in the signal. Although the tomographic images contained significant artefacts in both differential phase contrast (DPC) and scattering modes, the CT method shows future potential for damage characterisation. In particular, the dark field CT showed intense signals for shear cracking and matrix micro-cracking. Development of the system at CSEM is currently examining how to manufacture larger gratings to increase the field of view, and better detectors to allow increased resolution.

Although the differential phase contrast CT showed significant artefacts due to the physical set-up of the experiment, alternative phase contrast imaging techniques are becoming effective on laboratory CT systems. The HMXIF has a system manufactured by X-Radia which can image using 'propagation phase contrast'. This technique relies on the phase shift at material boundaries, and by allowing the refracted X-Rays to propagate over a long distance, the interference fringes at these boundaries can be imaged. In practise this relies on moving the detector a significant distance away from the sample, resulting in long CT acquisition times due to the reduced flux reaching the detector. The system can however, attain extremely high resolutions (sub-micron). Figure 8.2 shows examples of a matchstick sized CFRP sample which was imaged using the X-Radia micro-CT.

Individual fibres are clearly resolved, as well as the matrix between the fibres.

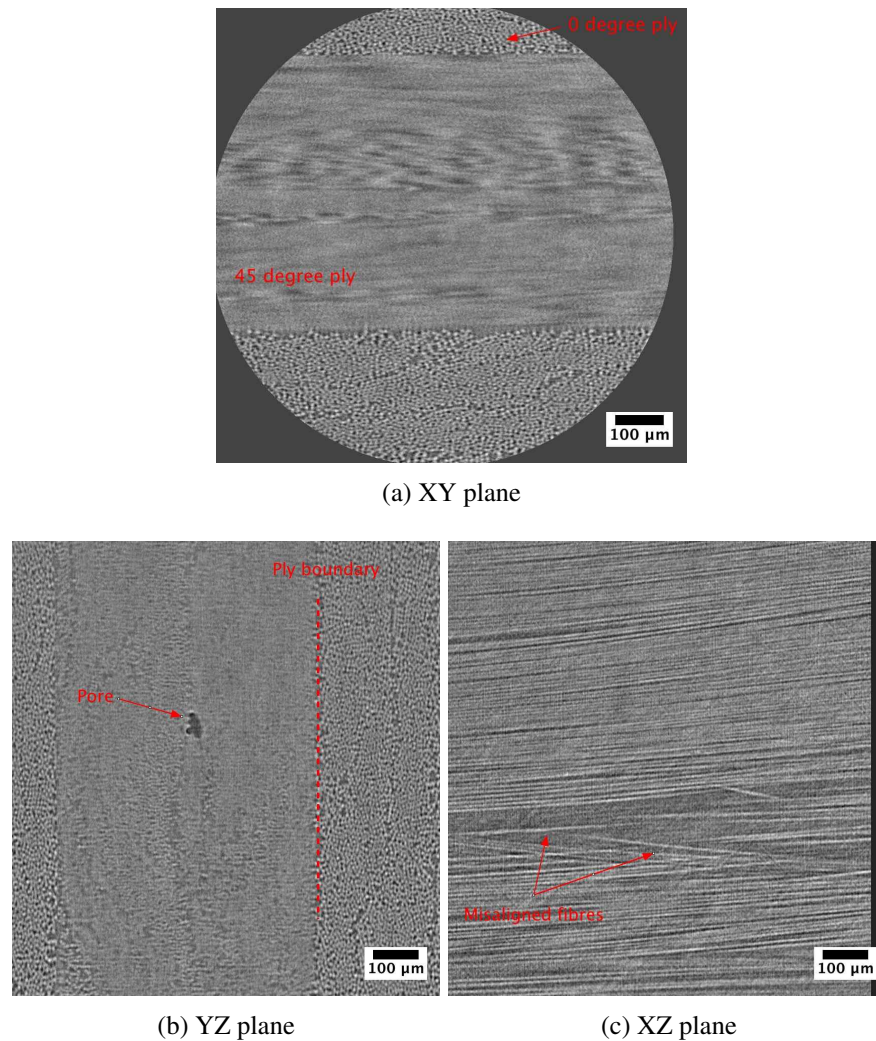


Figure 8.2: Propagation phase contrast image of a CFRP laminate with uni-directional plies.

As figure 8.2 shows, laboratory based propagation phase contrast can provide excellent high resolution images of CFRP. Fibres, micro-scale porosity and resin pockets can be identified in addition to fibre misalignment. This type of imaging would provide an excellent addition to the multi-scale imaging of impact damage in CFRP. Time constraints meant it was not possible to perform this investigation in the current work, but should be a priority for further work in the field.

Prior to performing the work in this thesis, very little work had been published in the literature concerning the characterisation of CFRP on laboratory based CT systems. The work has shown that CT has great potential as a non-destructive imaging tool for CFRP, but many more questions have been raised providing significant scope for further research.

## 8.1 Commercial Aspects

From a commercial perspective the work in this thesis has highlighted a specific area where X-Ray tomography can provide information on damage in composite materials. The resolution and three-dimensional nature of the data obtained using X-Ray CT is unmatched by any other single NDT technique. Obviously limitations still exist, such as the size of the object which can be imaged, the speed of data acquisition and data processing, and the cost. This final section discusses some of these issues in terms of their implications for industrial uptake of CT as an engineering tool.

CT has the potential to influence several areas of engineering, inclusive of virtually any engineering material. Figure 8.3 highlights the areas where CT is currently being applied.

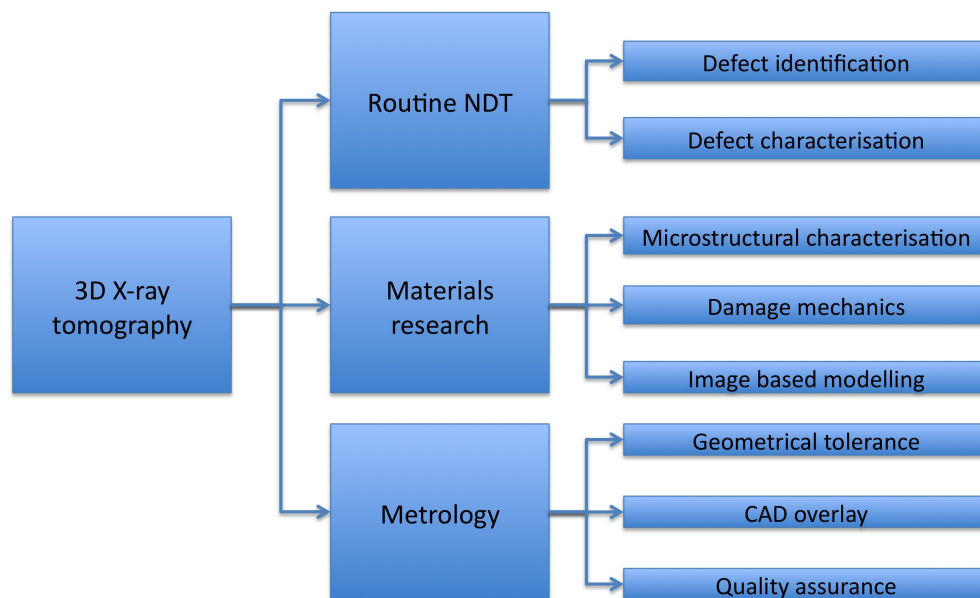


Figure 8.3: Commercial applications of computed tomography

### 8.1.1 Cost

Table 8.1 gives a general overview of the costs associated with the installation and use of an industrial CT system. The costs of associated equipment and staff are also given. This data is based on the X-Tek CT system which was used for the majority of the work in this thesis. From an industrial perspective, this system offers a good balance of resolution, scan duration and ease of operation. A relatively high source power also allows analysis of thick samples, giving the ability to scan CFRP samples up to 200mm thick with good resultant image quality. Table 8.2 gives the rates of access which are charged at the University of Manchester, which are based on market rates charged by

industrial NDT companies that currently own CT scanners.

Table 8.1: Costs associated with industrial tomography systems.

<b>Item</b>	<b>Cost/ £</b>
X-Tek CT system	700,000
Annual service charge	10,000
Technican/ Operator annual salary	50,000 (including employer contributions)
Avizo data processing software	10,000 (perpetual license)
Avizo annual support	5,000 (optional)
Computer workstation	10,000

Table 8.2: Rates to access CT equipment at University of Manchester.

<b>Access type</b>	<b>Cost/ £</b>
Academic	350/ day
Commercial	1500/ day
Commercial data processing	75/ hour

From the values in tables 8.1 and 8.2 it is apparent that to repay the investment in equipment (scanner and associated IT infrastructure) would require approximately 473 of scan days to be sold. This figure would be reduced by customers also purchasing data processing time at the 75/ hour rate. To cover the additional annual running costs (employee and licenses etc.) would require the sale of at least 43 days of scan time.

Overall, X-Ray tomography systems will have a significantly higher initial financial outlay than current standard systems, such as transmission C-scan. Annual running costs will also be higher considering the extra computational facilities required, but for appropriately sized objects can give a significant improve in defect detection capability. Assuming that there is a market need for this type of inspection system (evidenced by the number of businesses currently offering CT as a service), the cost-benefit ratio is reasonable considering the payback time being on the order of just a few years. This is especially true for the current generation of CT systems which will have design lives significantly in excess of the payback times, and are certainly capable of identifying defects smaller than the critical defect size for life predictions in most structures.

Due to the relative complexity of operation and data processing of CT systems, some thought should be given to staff retention and development. As with any difficult process, operator skill is often critical to the successful application of the technology. Investment in staff through training and development should be taken seriously in order to retain experienced staff, not forgetting fair remuneration to prevent high staff turnover.

### 8.1.2 Supply Chain Position

The current generation of industrial CT systems have been proliferated through the engineering supplying chain. Systems can be found in University research groups, aircraft OEM's (such as Rolls Royce), component manufacturers and NDT service companies. As a result, the particular applications of CT are also widespread.

In terms of Technology Readiness Levels (TRL), the current generation of industrial CT systems have far exceeded TRL 9 for certain applications. This TRL means the process has been applied to industrial problems in its final form. This is true, for example, in the electronics industry where routine inspection of high value circuit boards is performed by CT. Companies such as Nikon Metrology are manufacturing CT systems under continuous manufacturing conditions for the electronics industry. Contract/ service companies such as TWI and NDT Services Ltd, among others, are also offering CT inspection of components on a routine basis.

When considering composite components however, the specific TRL under which CT systems are being applied does vary. From the literature and industry conference proceedings, it is apparent that much of the CT work being performed on composite materials is taking place under a research context. Similarly, developments of CT hardware and associated reconstruction/ computational systems appear to be heavily research based (see section 2.4.1 for a related discussion).

To date, many of the applications of CT to composites within industry have been funded through the Technology Strategy Board (TSB), Engineering and Physical Sciences Research Council (EPSRC), or European Framework programmes. This funding has led to the implementation of CT within those tiers of the supply which are research led, such as the NDT Validation Centre at TWI Port Talbot (see Amos (2011); Amos *et al.* (2010)).

### 8.1.3 Current Limitations and Future Developments

In addition to cost barriers, several factors are currently limiting the increased uptake of CT systems as industrial tools for NDI/ NDT, metrology and research applications. This is particularly true for application to composite structures.

For aerospace applications, the size limitations imposed by CT systems presents a significant barrier to the routine NDT/ NDI of composite structures. Composite materials are routinely being used in large-scale structures where the use of 3D X-ray CT is simply not feasible. Although 2D radiographic inspections are commonplace, it is likely that ultrasonic inspection will remain the most widespread technology in this area. Current CT systems are providing larger area coverage with the use of moving detectors, but the requirement of a closed cabinet for radiation safety will eventually present a practical cost barrier to the size of objects which can be scanned. The inevitable trade-off between object size and resolution would also remove the advantage of CT over C-scan.

Nevertheless it is evident that CFRP materials are being increasingly used in substruc-

ture applications such as propellers, fan blades, and secondary structures. Inevitably this proliferation will increase due to the drive for lighter weight structures, the reducing cost of CFRP and the ability to manufacture net shape preforms using technologies such as 3D weaving. These components are easily within the scanning geometry and useful resolution range of CT. Therefore, similar to the electronics industry with the routine inspection of high value semiconductor devices, it may be the case that these expensive components are routinely inspected with CT.

Improvements to automated defect detection and characterisation also need to be made to allow greater industrial uptake of CT. The work in this thesis revealed the difficulty in processing CT data specific to high aspect ratio composite plates. The relatively low signal to noise ratio, complex damage characteristics and large data files make interpretation of useful data more complex than other NDT methods. Improvements in computational power, however, may remove many of the difficulties associated with data handling and processing. Considering the use of CT as a routine inspection tool, automated detection techniques are probably not a very distant ambition. This is because defects such as porosity or simple features such as cracks of a specific length could easily be identified and flagged. The complications with measuring and quantifying impact damage which were identified in this thesis may not be so prevalent under conditions of simply identifying whether a defect exists or not.

Several research projects at the University of Manchester are currently concerned with the use of CT as a metrology tool. In this respect, CT is used to geometrically define the object of interest. In turn, this information can be used to assess whether parts are out of tolerance. Using CT in this manner is particularly useful for objects with regions which are inaccessible for conventional metrology processes, such as CMM or laser scanners. This process can, for example, be used in acceptance testing or to provide information on manufacturing process errors. Additionally the data could inform downstream operations such as shimming, or jiggling adjustments to ensure correct assembly. Data can be overlaid with CAD models for visual comparisons and highlighting of out of tolerance regions. Figure 8.4 gives an example of CAD-CT data comparison of an aluminium valve block.

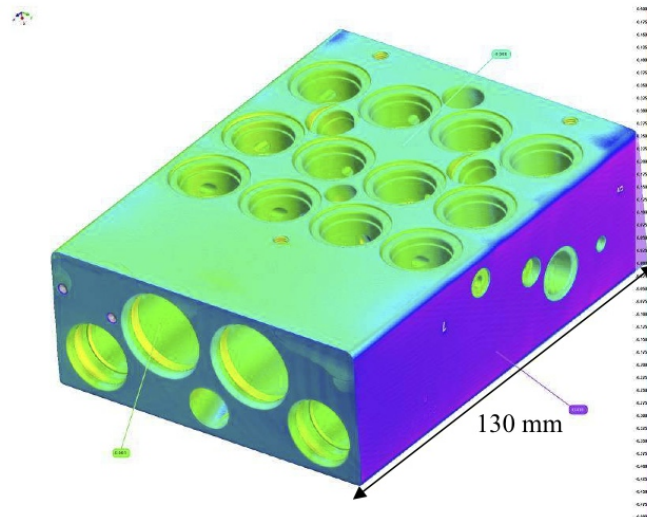


Figure 8.4: Nominal (CAD) actual (CT) comparison of an aluminum valve block (Brunke, 2010).

The use of CT in metrological applications is a relatively new, and therefore rapidly progressing field. Many papers are available in the relevant journals such as (Brunke, 2010; Carmignato, 2009; Kiekens, 2011; Kruth, 2011).

Possibly the most important issue facing the implementation of CT in a production environment is the lack of standards. Although a British Standard exists in draft form which explains the general principles and application of CT, no standards or good practise guides exist for its application in industrial/ production environments. This should be a major focus of efforts in order to ensure that CT is used effectively to give accurate and reliable results for any application.

Overall, the outlook for the uptake of CT in a commercial setting is clearly good. Although it will not replace well established techniques such as C-scan, there is room for it to be used alongside and in addition to current techniques. This is particularly true for high value components, and those situations where other techniques cannot give a definitive answer- for example where critically sized defects may be overlaid and require a 3D inspection technique.

---

## CHARACTERISATION OF COMPUTED TOMOGRAPHY SYSTEM

### A.1 Introduction

This chapter investigates the system characteristics and performance of the Nikon Metrology 225kV Custom Bay at the Henry Moseley X-Ray Imaging Facility, School of Materials, University of Manchester.

An overview of the system is given in terms of its specific operation and procedures which were followed to acquire data in subsequent experiments was given in Chapter 4. These procedures involve optimising the system operation at each use in terms of X-ray focus and beam stability.

Experiments to determine the maximum spatial resolution of the system were performed, which allows specifications to be made on the smallest features which are detectable under known imaging conditions.

Characterisation of the X-ray spectra of a multi-metal target is presented. The CT system under investigation is fitted with a multi-metal target in order that the X-ray spectrum can be tuned to optimise imaging of the material under investigation. This experiment was performed using a Cadmium Telluride photon counting detector, which allows characterisation of the spectrum in terms of beam energy and X-ray counts at each energy. Spectrum characterisation allowed subsequent decisions on imaging parameters to be made when imaging the materials studied in chapters 3 and 4.

### A.2 Objectives

The objectives of the work presented in this chapter were to:

1. Quantify the maximum resolution of the CT system by radiographic and tomographic methods
2. Quantify the X-ray spectra produced by a multi-metal target

## A.3 Determination of System Resolution

The smallest features that can be identified in a sample are determined by the resolution of the CT imaging system. Because the system being used employs cone beam geometry, magnification is determined by the sample-to-object and object-to-detector distance. Hence, very high resolutions can be obtained by projecting a magnified image onto the detector, despite the pixel size only being 200 $\mu\text{m}$ . Physical limitations on the system (i.e how close an object can be placed to the X-ray source) determine the maximum resolution, but in all cases this cannot exceed the spot size of the X-ray source. Therefore to determine the maximum resolution of the Nikon Metrology Custom Bay, several experiments were performed to measure the size of the X-Ray spot. These experiments involved the use of a resolution plate as well as measurement of the penumbra formed on an image of a wire at high magnifications. As the spot size will determine the maximum resolution in a radiograph, a further experiment was performed to assess the maximum resolution of a reconstructed object at high magnification.

### A.3.1 Resolution Target

In order to make a direct measurement of the resolution of the imaging system in a projection, a resolution target was imaged.

The resolution target was imaged in the Nikon Custom Bay under the conditions prescribed in table A.1.

Table A.1: Image conditions for radiograph of resolution target

<b>Image Variable</b>	<b>Condition</b>
Target Material	Molybdenum
Accelerating voltage	50kV
Filament current	200mA
Frame exposure time	2000ms
Number of frames averaged	256
Magnification	120X

Due to the low thickness of the resolution plate, a very low accelerating voltage was used in order to obtain significant attenuation of the X-ray beam. The molybdenum target was chosen as it generates a beam with a relatively low mean beam energy, but retains a relatively high flux (see section A.5). Still, due to the low flux in absolute terms, an averaging of 256 frames was performed to reduce noise in the image to an acceptable level. The image was acquired with the detector corrections turned off. White and black references were then acquired to correct the radiograph. A white reference ( $I_w$ ) was taken by acquiring a radiograph under the conditions prescribed in table A.1, but without the sample in the field of view. The black reference ( $I_b$ ) was then acquired by acquiring a

radiograph with no X-rays being generated, again under the conditions prescribed in table A.1.

The radiograph can then be corrected ( $I_{corr}$  for defective pixels, gain and intensity variations by equation (A.1). This correction method is known as 'flat field correction'.

$$I_{corr} = \frac{I - I_b}{I_w - I_b} \quad (\text{A.1})$$

Figure A.1 shows the radiograph of the resolution plate.

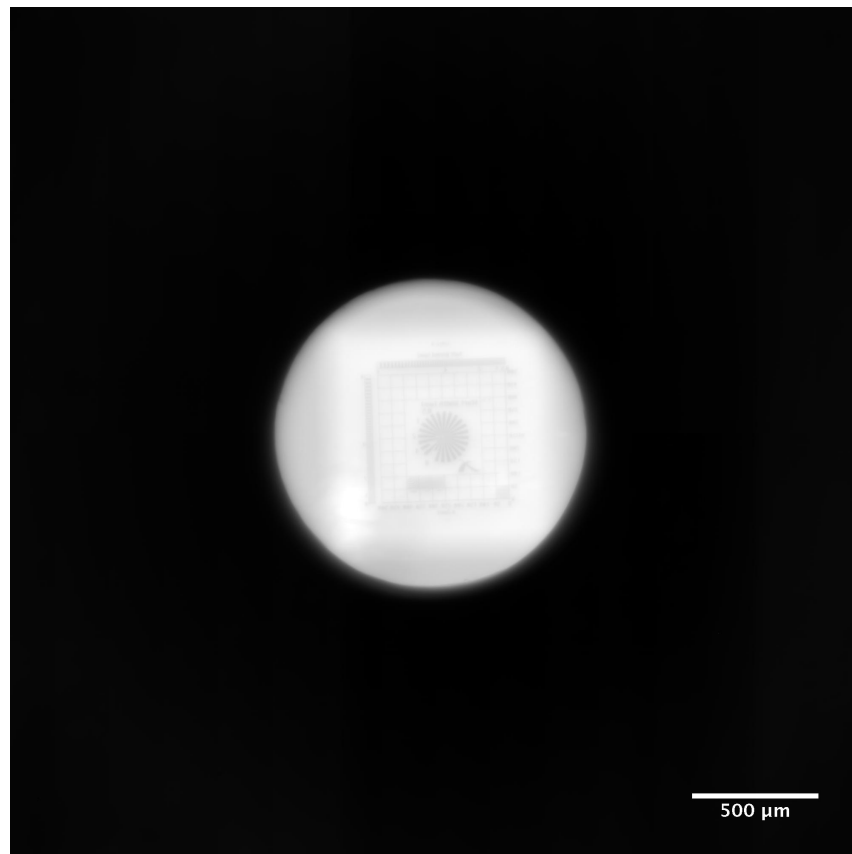


Figure A.1: Flat field corrected radiograph of resolution plate at 120X magnification

To assess the radiographic resolution using the resolution plate, image processing software ImageJ was used to plot intensity line profiles across the various resolution scales on the radiograph shown in figure A.1. The line intensity profiles could then be analysed to infer the resolution, according to the smallest visible resolution marker.

#### A.3.1.1 Results and Discussion

Figure A.2 shows the positions of the line profiles taken on vertical and horizontal scale bars of the resolution target which consist of black and white stripes (line pairs) having spacings which increase from  $0.5\mu\text{m}$  to  $8\mu\text{m}$ . The image has been cropped and contrast enhanced for illustration. Actual profiles were averaged over a width of 6 pixels

to smooth out noise, yet remain within the boundaries of the resolution markers. The line profiles for AA' and BB' are shown in figure ??

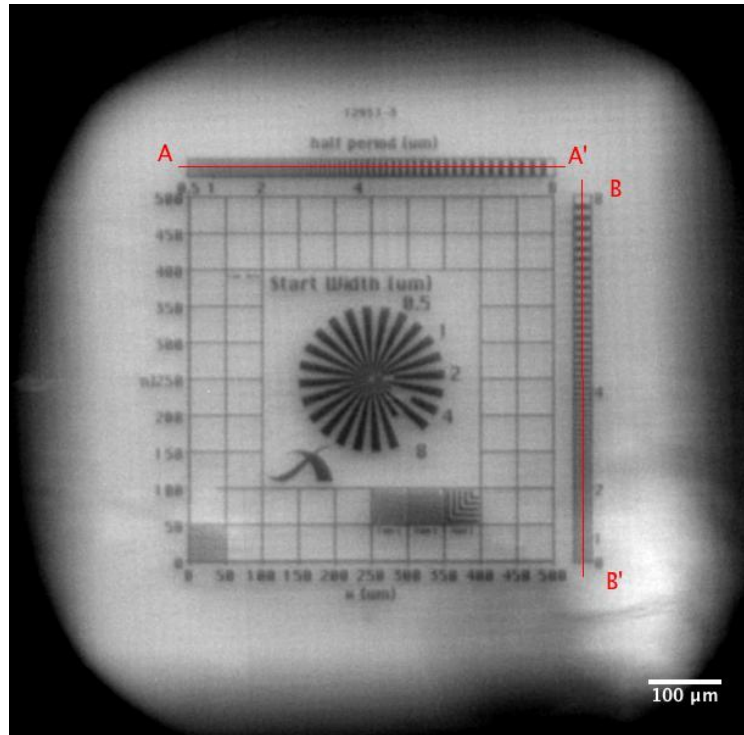
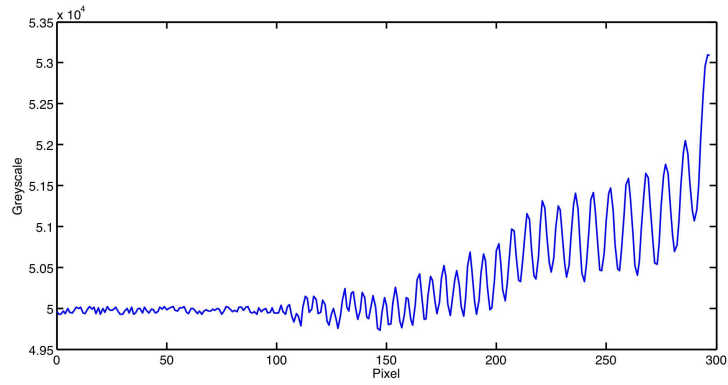
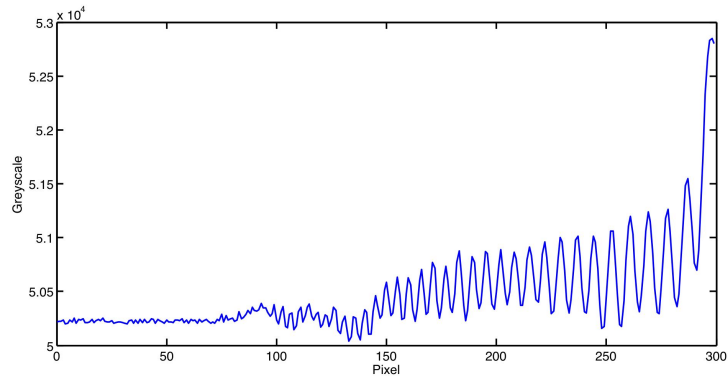


Figure A.2: Cropped and enhanced view of resolution target illustrating line profiles take across resolution markings.



(a)



(b)

Figure A.3: Line profiles across resolution scale bars at (a) AA' and (b) BB' from figure A.2.

From figure A.3 it can be seen that peaks and troughs in the greyscale occur at bright and dark points respectively in the resolution scale bars. These variations become reduced to the point where peaks and troughs are no longer distinguishable. At this point the line pairs can no longer be resolved and the resolution limit has been reached. Taking the resolution limit to be the point at which the greyscale difference between a peak and a trough is equal to the standard deviation (i.e image noise), gives a distance in pixels along the line at which the resolution is limited. For the line profiles in figure A.3 this gives values of approximately 100 pixels for both horizontal and vertical resolution scales. Knowing that the effective pixel size at 120X magnification is  $1.6\mu\text{m}$  and that the spacing of the peaks at this point is 2 pixels, this measurement equates to a resolution of  $3.2\mu\text{m}$ . This value is at the lower end of the manufacturers spot size range of  $3\text{-}5\mu\text{m}$ .

### A.3.2 Spot Size Measurement by Radiography of a Tungsten Wire

An alternative method estimate the maximum resolution was performed by estimating the focal spot size. This was achieved by taking radiographs of a 1mm diameter tungsten wire, and measuring the pixel intensities across the edge of object, according to (British Standards, 1999). Due to the penumbra effect, which was illustrated in figure 4.3, the spot size can be implied from the image blur at the object edges.

#### A.3.2.1 Methodology

A tungsten wire was radiographed at a geometrical magnification of 300 times, giving an equivalent pixel size of  $0.66\mu\text{m}$ . The manufacturer's specification states a focal spot size of  $3\text{-}5\mu\text{m}$ , hence at this magnification the effective pixel size is smaller than the spot size, so the penumbra would be expected to cause blurring on the order of 5-8 pixels. As the geometry of the system is known, equation (4.2) can be used to imply the spot size by measuring the size of the penumbra. This was performed using the method described in British Standard BS EN 12543-4 (British Standards, 1999). The imaging conditions used to image the wire at give in table A.2.

Table A.2: Image conditions for radiograph of tungsten wire

Image Variable	Condition
Target Material	Molybdenum
Accelerating voltage	100kV
Filament current	200mA
Frame exposure time	2000ms
Number of frames averaged	256
Magnification	300X

#### A.3.2.2 Results and Discussion

As shown in figure A.4 a line profile was drawn across the object edge in a flat-field corrected radiograph, and  $x$ -intercepts at 5% and 95% of the maximum greyscale projected onto an axis representing the distance across the edge. The associated line profile plot is shown in figure A.5.

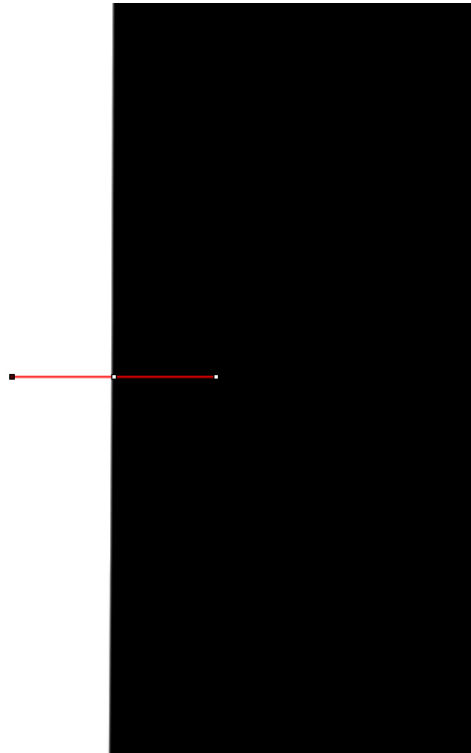
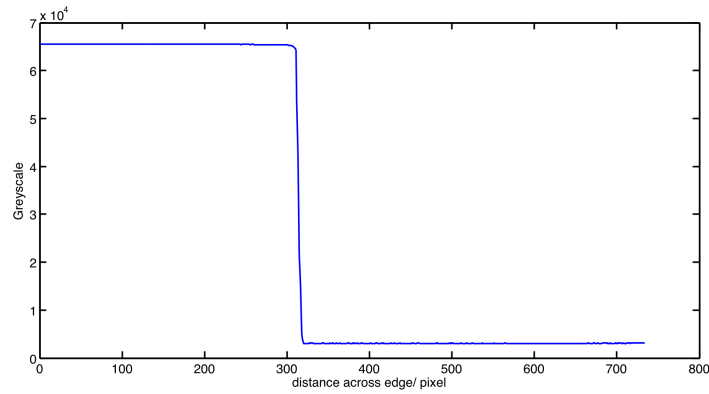
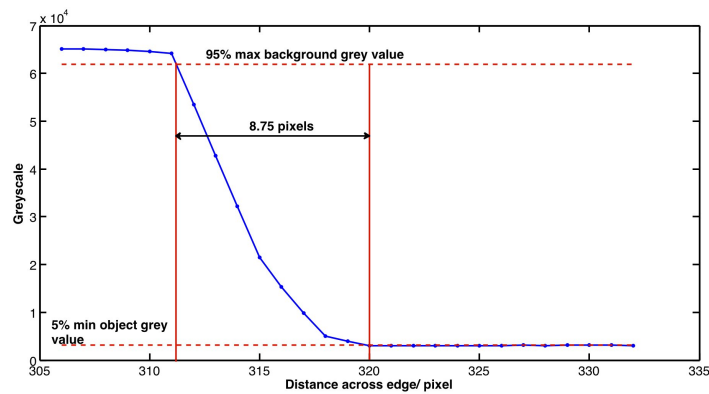


Figure A.4: Radiograph of tungsten wire, showing line profile.



(a)



(b)

Figure A.5: (a) Line profile across edge of tungsten wire (b) Close-up view of profile across edge, illustrating edge blur due to penumbra effect.

The penumbra blur is seen to be spread across approximately 8.75 pixels, which equates to a spot size of  $5.8\mu\text{m}$ . This is higher than the expected value by  $0.8\mu\text{m}$ . However, due to the use of such a small diameter cylinder to achieve the necessary magnification, it is likely that penetration of the object near the edge has occurred. This penetration would give elevated grey values within the object, reducing the edge gradient and extending the number of pixels over which the edge is blurred, in this case by only 1-2 pixels.

### A.3.3 Reconstructed Volume Resolution

To assess the maximum resolution of the imaging system under CT scan conditions, the tungsten wire imaged in section A.3.2 was tomographed. Again, the tungsten wire was chosen because the high density gives a sharp edge in each projection. The small diameter allows high magnification, approaching the limit of the system, and the circular cross section give even beam attenuation at each projection angle. The imaging conditions used in the scan were as shown in table A.3.

Slices of the object were reconstructed at various heights in the sample. Relative to the pixel height of the detector, slices were reconstructed at 250, 500, 750, 1000 (central

Table A.3: Image conditions for CT scan of tungsten Wire

Image Variable	Condition
Target Material	Tungsten
Accelerating voltage	180kV
Filament current	200mA
Number of projections	3142
Angular increment between projections	3142
Frame exposure time	2000ms
Number of frames frames averaged per projection	2
Magnification	120X

slice), 1250, 1500 and 1750 pixels. The reconstructed slices were saved as 16 bit TIFF images, and then processed using Matlab. The resolution was then estimated using an edge profile method.

#### A.3.3.1 Measurement of Edge Profiles

The 16 bit reconstructed slices of the tungsten wire were processed using Matlab to measure the resolution of the image from edge sharpness values. The following steps were performed;

1. Differentiation of the image in the  $x$  cartesian direction, by using the ‘gradient’ function in Matlab.
2. Plotting a line profile across the differentiated image to give a Line Response Function (LRF) which is characteristic of the sharpness of an edge. A peak is found at the position of the edge.
3. Applying a Full Width Half Maximum Height (FWHM) measurement to attain a resolution value

#### A.3.3.2 Results and Discussion

Figure A.6 shows the central reconstructed slice from a CT scan of the tungsten wire, and associated gradient image. Taking a line profile across the bright (left) edge of the gradient image results in the LRF, as shown in figure ???. Measuring the FWHM gives the number of pixels across which the edge is blurred. In this case, it can be seen that the width of the peak is 2.6 pixels. As the reconstructed voxel size at this magnification (120) is  $1.66\mu\text{m}$ , it equates that the edge resolution is  $4.3\mu\text{m}$ .

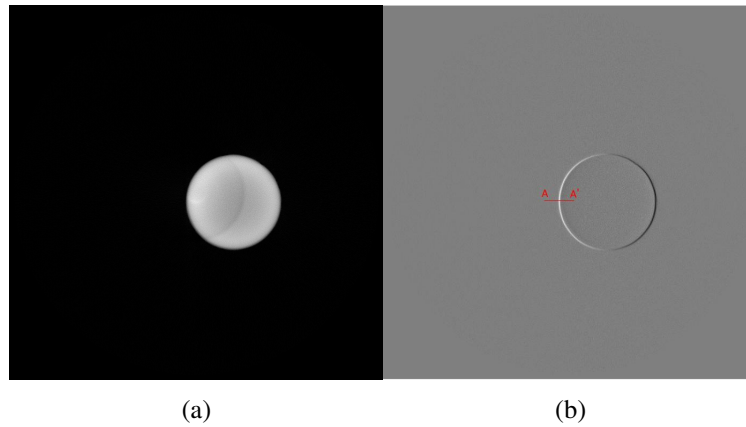


Figure A.6: (a) Reconstructed central slice of tungsten wire (b) Differential image of central slice.

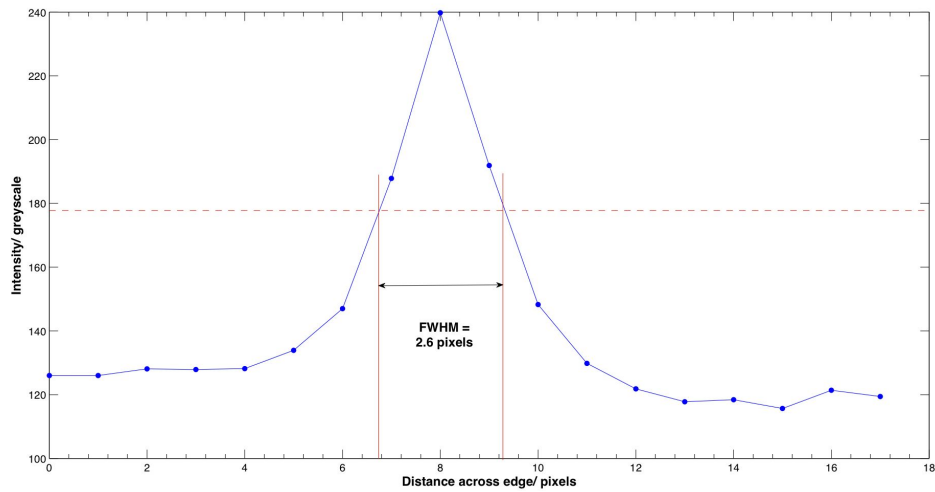


Figure A.7: Line Response Function of the edge of the central reconstructed slice of tungsten wire. The LRF is taken over the line AA' in figure A.6(b).

The edge measurement procedure was applied to all the reconstructed slices to give resolution values throughout the height of the reconstructed volume. The values are shown in figure A.8.

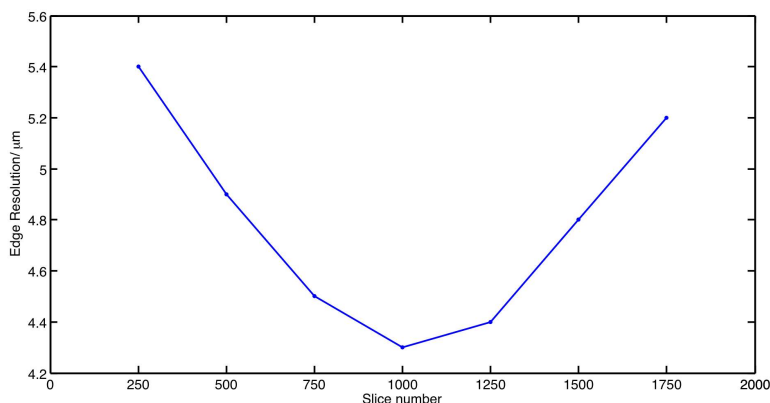


Figure A.8: Edge resolution vs. slice number for the reconstructed tungsten wire volume. Slices are numbered from the bottom of the volume upwards relative to the detector.

As illustrated in figure A.8, the edge resolution is reduced moving away from the central slice. This observation is consistent with the fact that the cone-beam reconstruction algorithm is most accurate at the central slice. However, it is also apparent that the resolution values remain more accurate in slices 1250-1750. This would imply that the system was slightly misaligned relative to the  $z$ -axis, and that the beam is perpendicular to the detector at a very small offset from the centre of the detector.

Overall, it has been shown that the various methods used to infer the system resolution have given consistent results that are within, or very close to, the manufacturer's specification. This gives confidence to the CT measurements obtained in later chapters.

## A.4 Effect of Projection Number on Image Quality

Figure A.9 shows how the image quality, in terms of signal to noise ratio, varies with the number of projections taken during CT imaging of a CFRP sample. The sample was a coupon cut from a plate of woven MTM-45, with a cross section of 28 x 2.2 mm. Figure A.10 shows cropped sections of the reconstructed data at 500, 1000, 2000 and 8000 projections.

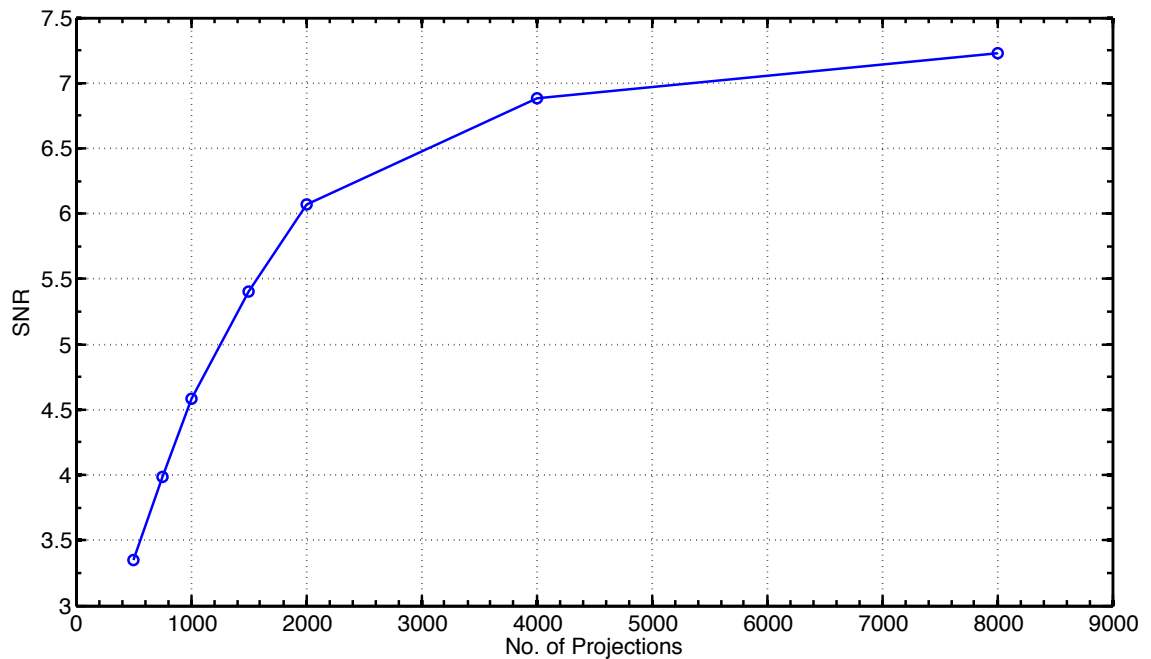


Figure A.9: Variation of SNR with no of projections for a CFRP which fits inside the detector field of view.

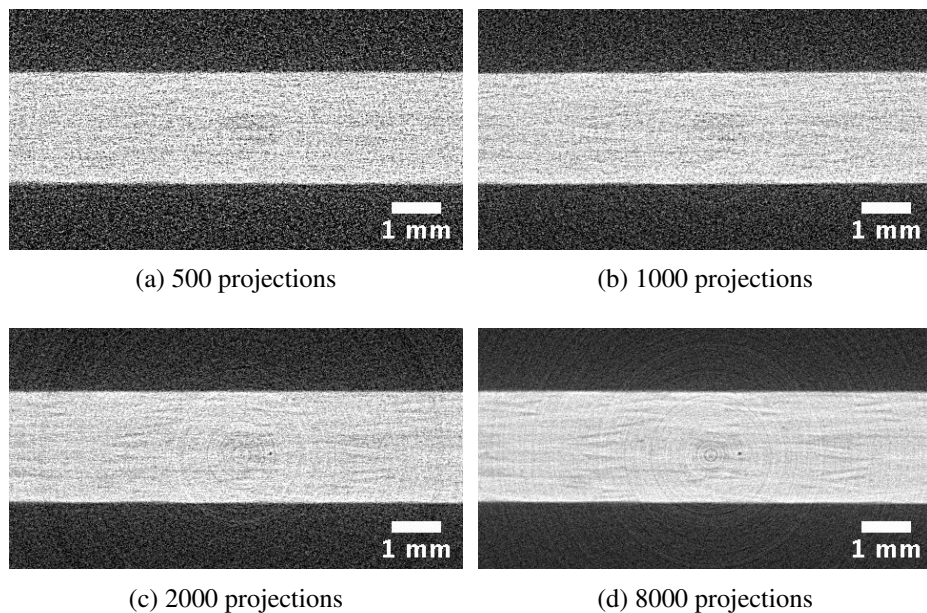


Figure A.10: Reconstructed cross sections of woven MTM-45 coupon with varying numbers of CT projections.

Figures A.9 and A.10 show a rapid increase in the image quality when increasing from 500 to 2000 projections. After this point, the increase in SNR becomes less pronounced with increasing projections, which is in agreement with the general consensus that the optimum trade off between image quality and the number of projections occurs between  $\frac{q\pi}{2}$  and  $\frac{q\pi}{4}$  where  $q$  is the maximum width of the object in pixels.

## **A.5 Characterisation of Spectral Emission from a Multi-Metal Target**

The Nikon Metrology Custom Bay is fitted with a multi-metal target (MMT) to provide the user with a choice of characteristic X-ray spectra. The MMT consists of a circular threaded holder, into which a cylinder of four target materials is screwed. The target materials are Copper, Molybdenum, Silver and Tungsten.

Each target material emits a characteristic X-ray spectrum, with varying mean energies and characteristic fluorescence lines etc. As discussed in Chapter 2, the attenuation coefficient of a material is a function of the incident beam energy. Therefore, the degree to which an X-ray beam is attenuated by object during a CT scan can be tuned by choosing a particular target material and accelerating voltage.

In order to optimise imaging of the CFRP samples in the damage tolerance study, the spectra of all target materials were characterised using an Amptek XR-100T cadmium telluride (CdTe) energy sensitive detector. The spectra were measured at various accelerating voltages and currents.

The long and short term stability of the X-ray source were also measured, in addition to a maximum flux prediction.

### **A.5.1 Experimental Method**

The Amptek XR-100T CdTe detector was mounted 430mm in front of the exit window of the 225 kV source. The detector plane was perpendicular to the beam propagation axis at the centre of the cone beam. A 50 $\mu$ m tungsten collimator was attached to the front of the detector housing, approximately 10mm in front of the detector plane. This was used to prevent saturation of the detector. 1024 channels were used, with the peak shaping time optimised automatically by the ADMCA acquisition software. Setting a detector gain of 33.34 gave a maximum energy cut-off at 257 keV, with a low energy cut off at 7 keV. Acquisition times of 300s were used for all measurements except for the source stability measurements. Figure A.11 shows the Amptek detector.

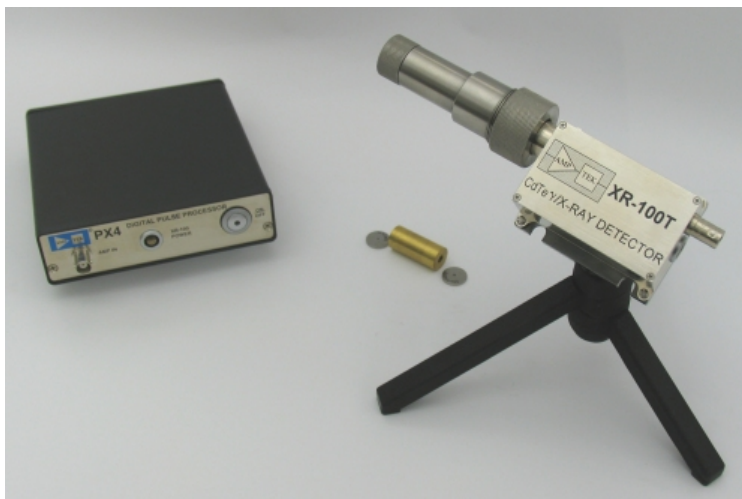


Figure A.11: Amptek XR-100T CdTe detector system. Amplifier (left), detector housing fitted with collimator (right).(Amptek, 2011).

The Amptek detector was first calibrated using an americium-241 dial source and known peaks from the W source on the 225kV CT system. This allows photon energies for each detector channel to be deduced, resulting in the linear calibration plot shown in figure A.12. The relationship between channel number and photon energy (in keV) is given by:

$$Energy = channel; , no. \times 0.154 - 0.267 \quad (A.2)$$

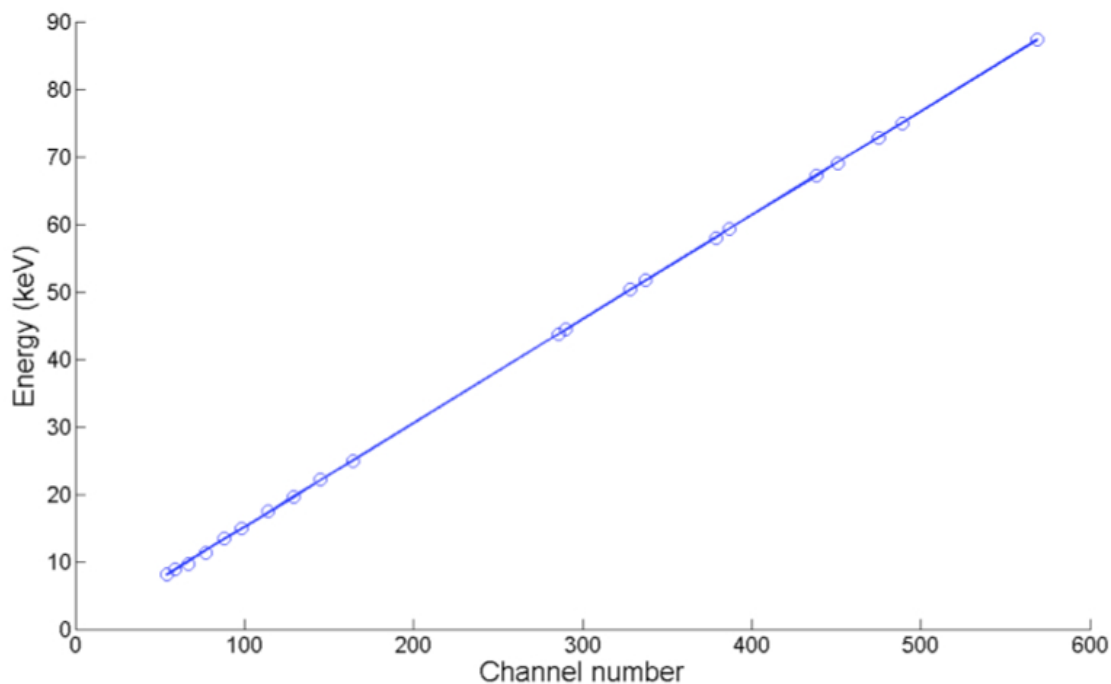


Figure A.12: Linear calibration obtained using a dial source and W spectra peaks.

## A.5.2 Spectra Results

The four target material spectra Ag, Cu, Mo, and W were collected over a period of 300 seconds at 50kV, 150kV and 225kV with a fixed current of 50 $\mu$ A. The spectra were also collected at a fixed voltage of 100kV with varying currents of 50, 100 and 200 $\mu$ A. The following figures show the data from each spectra collection.

### A.5.2.1 Cu target

Figure A.13 shows a typical spectrum for the copper target, measured at 225kV and 50 $\mu$ A. The Cu K $\alpha$  and K $\beta$  fluorescence peaks are observed at 8 keV and 8.9 keV respectively. The very small peaks at higher energies originate from the tungsten collimator. The fluorescence are superimposed on a bremsstrahlung background which is relatively weak.

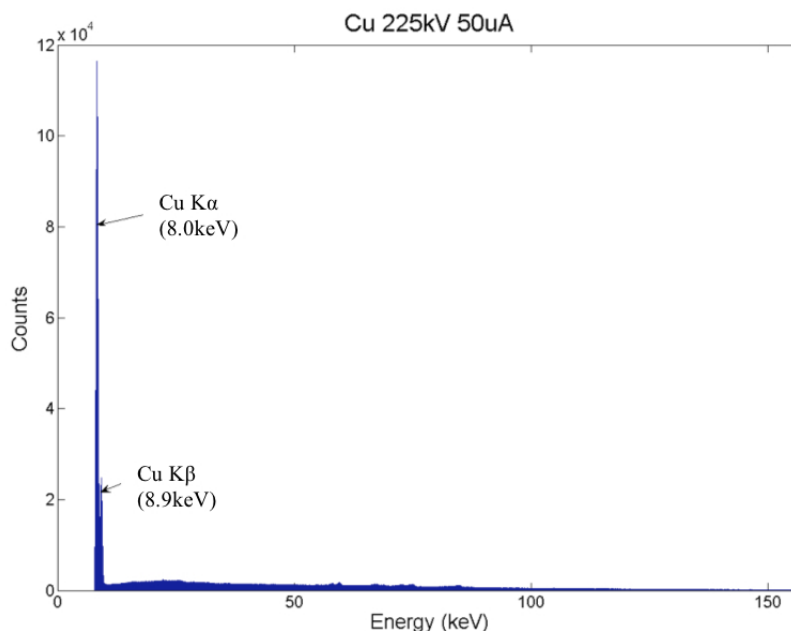


Figure A.13: Cu target spectrum at 225kV at 50 $\mu$ A

The following figures show the variation of the Cu spectra with voltage and current, along with the total photon count variation with voltage and current.

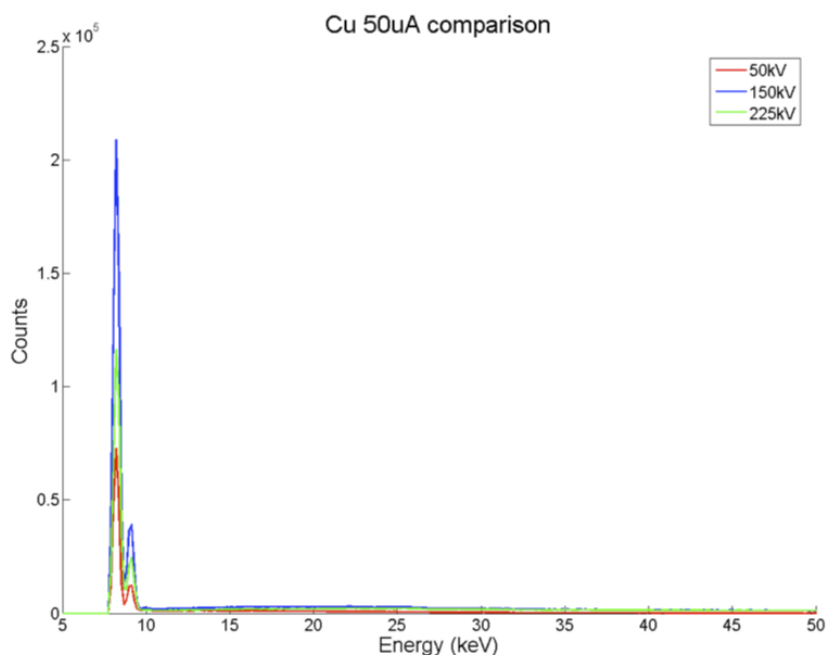


Figure A.14: Cu target spectrum at 50kV, 100kV and 225kV at 50 $\mu$ A

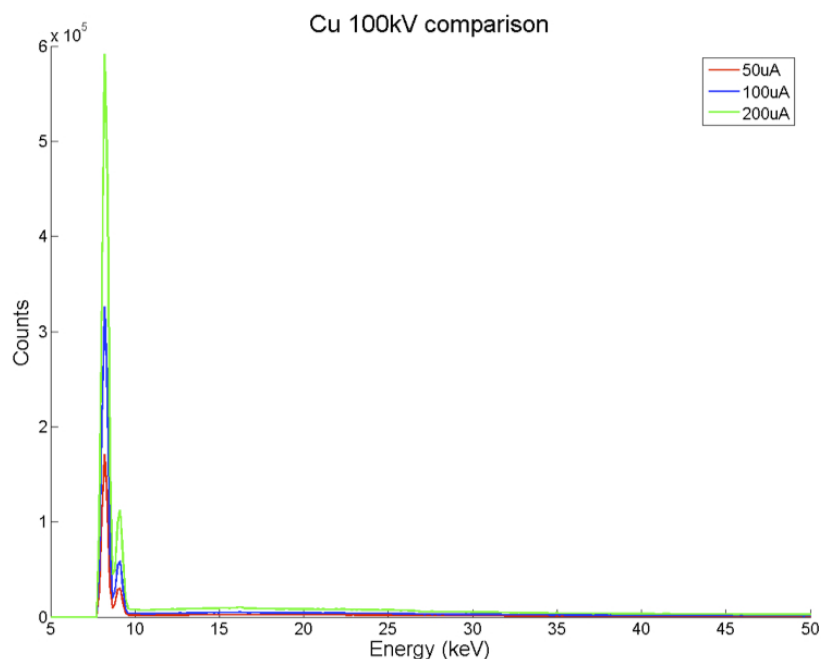


Figure A.15: Cu target spectrum at 50 $\mu$ A, 100 $\mu$ A and 200 $\mu$ A at 100kV

### A.5.2.2 Mo Target

Figure A.16 shows a typical spectrum for the molybdenum target, measured at 225kV and 50 $\mu$ A. The Mo  $K\alpha$  and  $K\beta$  fluorescence peaks are observed at 17.4 keV and 19.6 keV respectively. As with the Cu target, the peaks are superimposed on a relatively weak bremsstrahlung background.

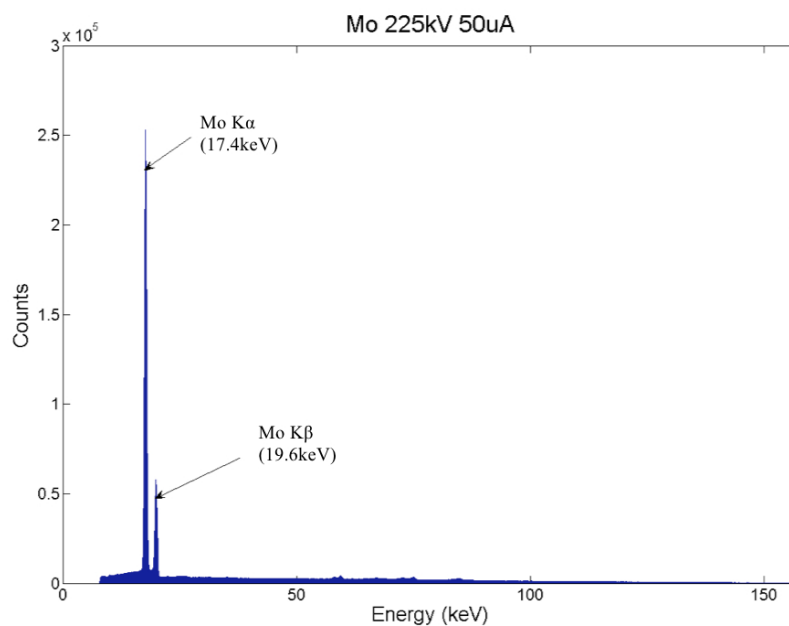


Figure A.16: Mo target spectrum at 225kV at 50 $\mu$ A

The following figures show the variation of the Mo spectra with voltage and current, along with the total photon count variation with voltage and current.

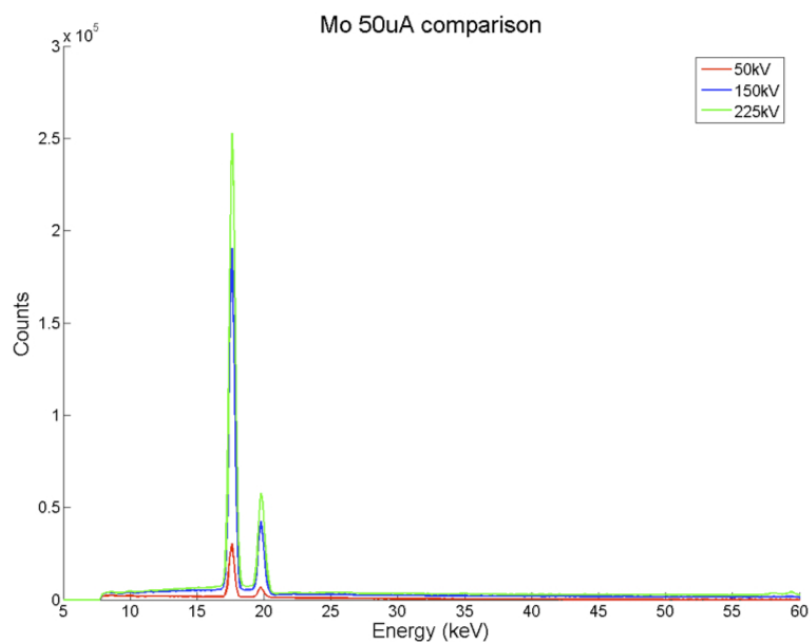


Figure A.17: Mo target spectrum at 50kV, 100kV and 225kV at 50 $\mu$ A

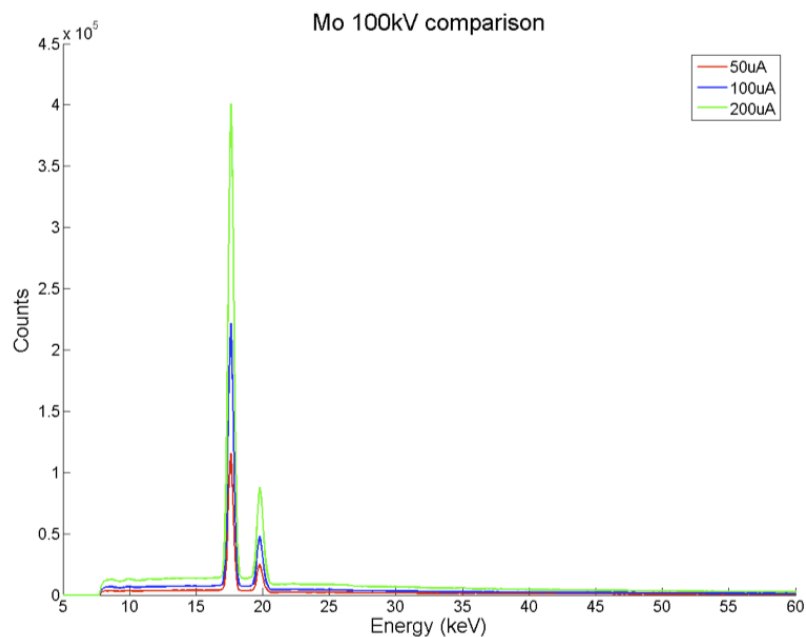


Figure A.18: Mo target spectrum at 50µA, 100µA and 200µA at 100kV

### A.5.2.3 Ag Target

Figure A.19 shows a typical spectrum for the molybdenum target, measured at 225kV and 50µA. The Ag K $\alpha$  and K $\beta$  fluorescence peaks are observed at 22.2 keV and 24.9 keV respectively. Also visible are the W fluorescence (59.3 keV) from the collimator and Pb fluorescence (74.9 keV and 84.9 keV) from the shielding surrounding the detector.

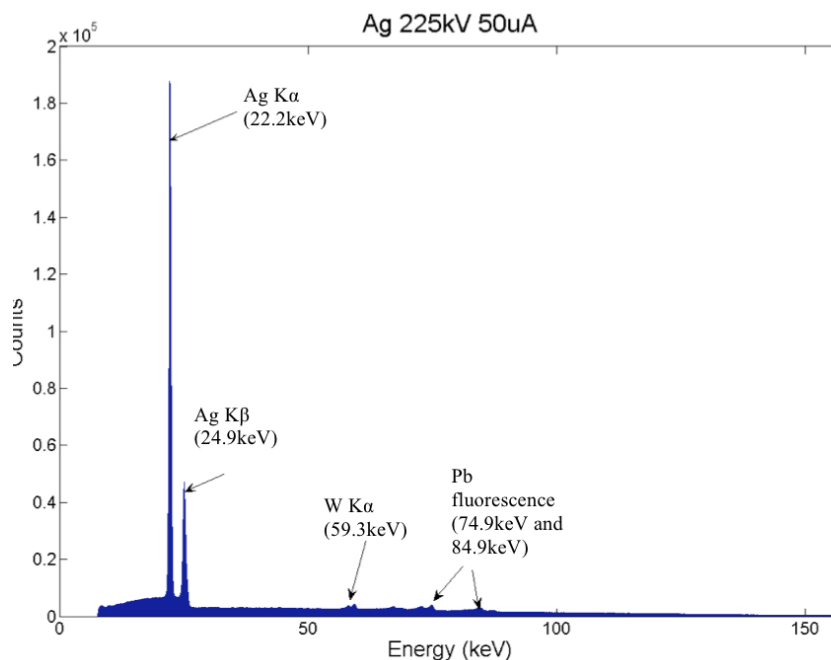


Figure A.19: Ag target spectrum at 225kV at 50µA

The following figures show the variation of the Ag spectra with voltage and current,

along with the total photon count variation with voltage and current.

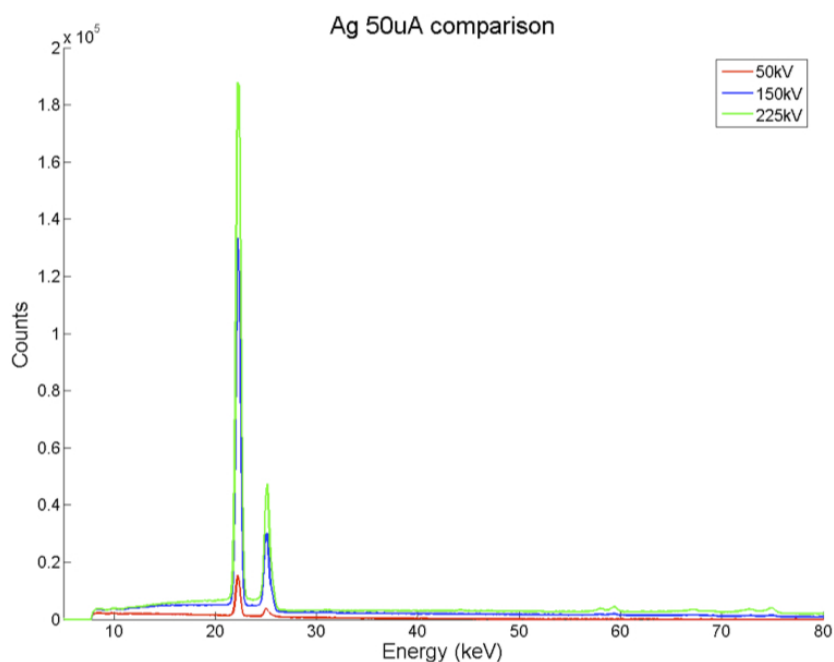


Figure A.20: Ag target spectrum at 50kV, 100kV and 225kV at 50 $\mu$ A

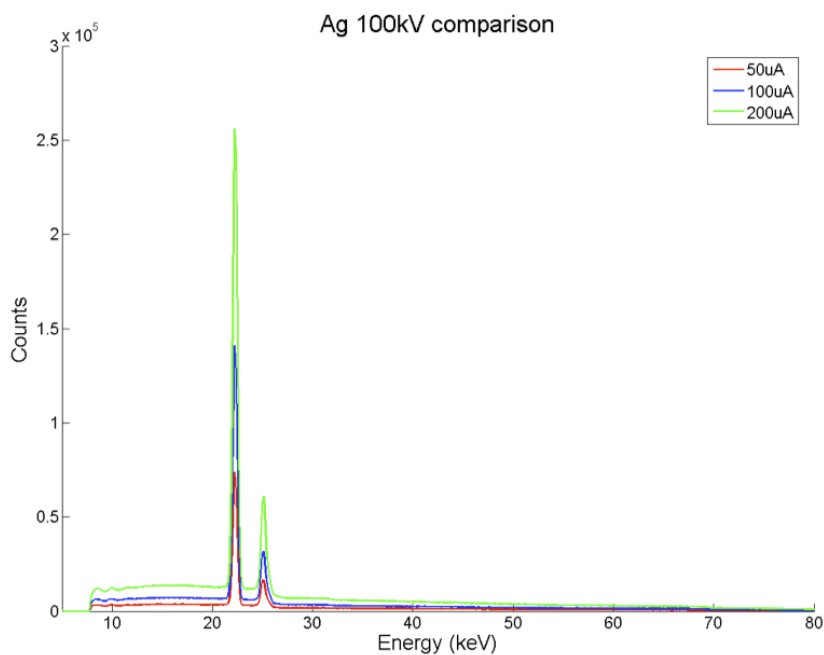


Figure A.21: Ag target spectrum at 50 $\mu$ A, 100 $\mu$ A and 200 $\mu$ A at 100kV

#### A.5.2.4 W Target

Figure A.22 shows the spectrum obtained using the W target at 225 kV and 50  $\mu$ A. There are a number W lines visible  $\text{\textcircled{D}}$  the L lines (8  $\text{\textcircled{D}}$  11 keV), the  $K\alpha_1$  (59.3 keV) and  $K\alpha_2$  (57.98 keV) lines and the  $K\beta_1$  (67.2 keV) and  $K\beta_2$  (69.1 keV) lines. There are also a

number of Cd and Te escape peaks caused by secondary X-rays, produced in the detector, escaping the detection medium. An escaping photon carries away some of the energy deposited by the incident X ray, so a lower energy event is registered. Also visible is the Cd K absorption edge (26.7 keV). There is a discontinuity here as this is the energy at which the Cd atoms begin producing the secondary X-rays. Furthermore, the W target shows a very strong bremsstrahlung background compared to the other targets.

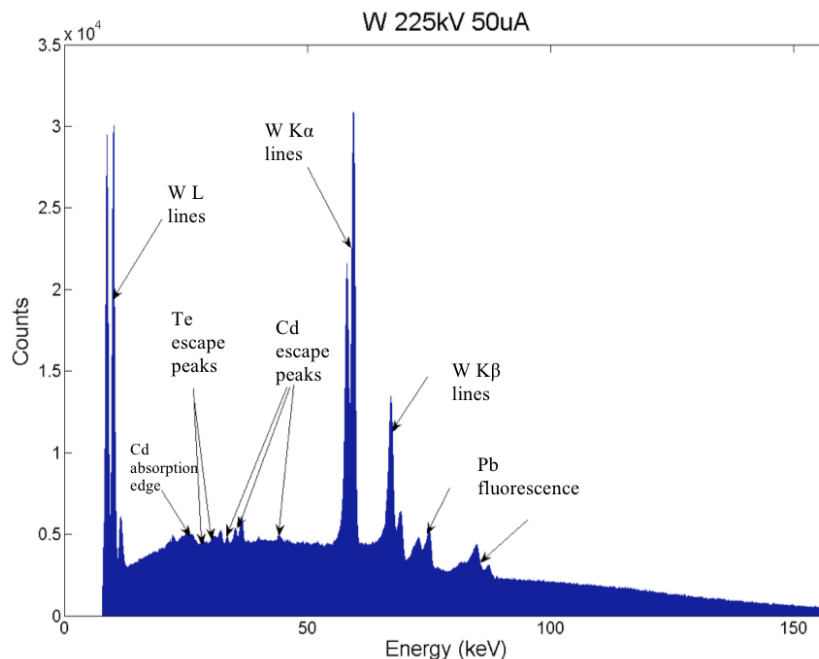


Figure A.22: W target spectrum at 225kV at 50µA

The following figures show the variation of the Ag spectra with voltage and current, along with the total photon count variation with voltage and current.

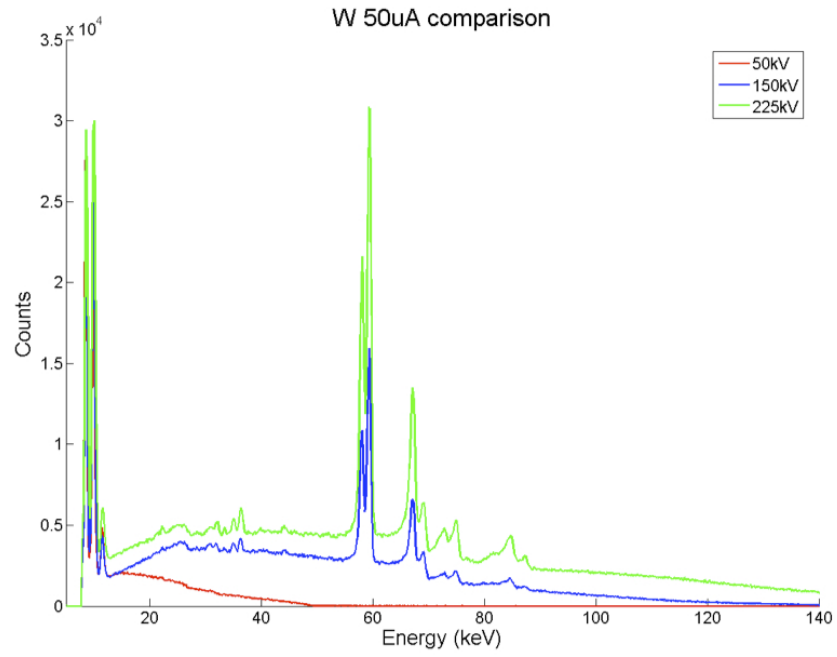


Figure A.23: W target spectrum at 50kV, 100kV and 225kV at 50 $\mu$ A

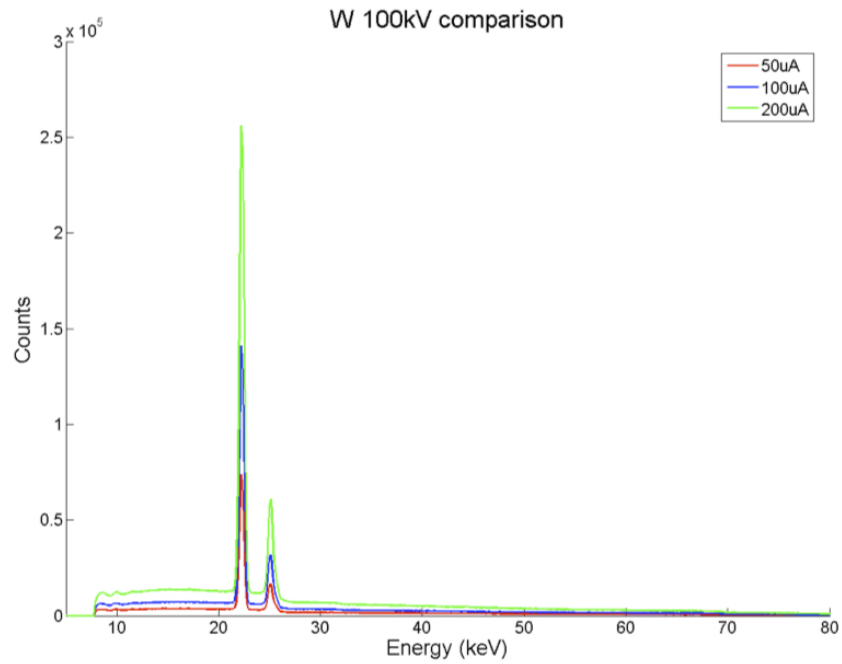


Figure A.24: W target spectrum at 50 $\mu$ A, 100 $\mu$ A and 200 $\mu$ A at 100kV

### A.5.2.5 Comparison of Targets

Overlaying the spectra measurements illustrates how the spectra produced from each target compare to each other in terms of photon energies and total counts, as shown in figure A.25 and A.26.

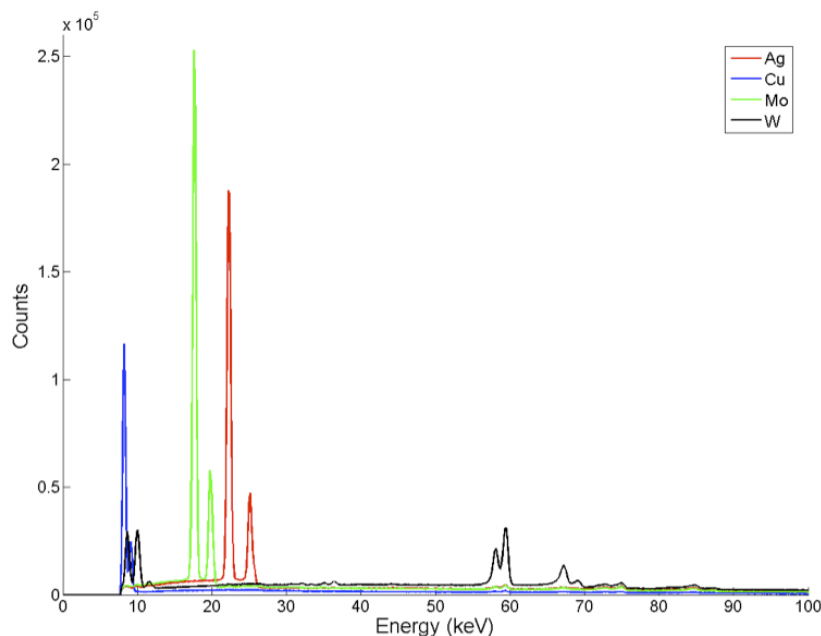


Figure A.25: Comparison of spectra produced with each target at 225kV and 50µA.

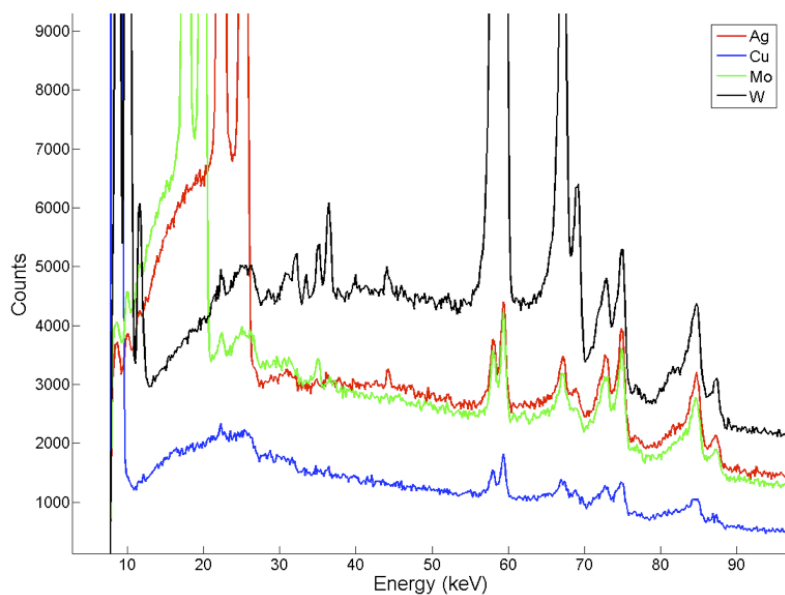


Figure A.26: Comparison of spectra produced with each target at 225kV and 50µA, magnified to show relative bremsstrahlung backgrounds.

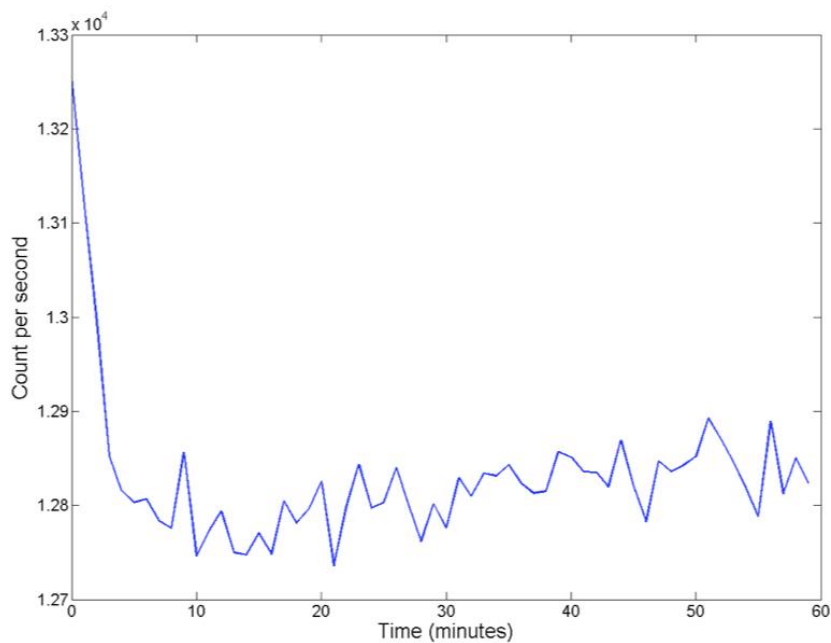
Table A.4: Comparison of total counts, and percentage of total counts in fluorescence peaks for each target material at 225kV

Target Material	Total Count	% of Counts in Fluorescence Peaks
Cu	1246618	29
Mo	3045767	33
Ag	3051990	33
W	3344953	17

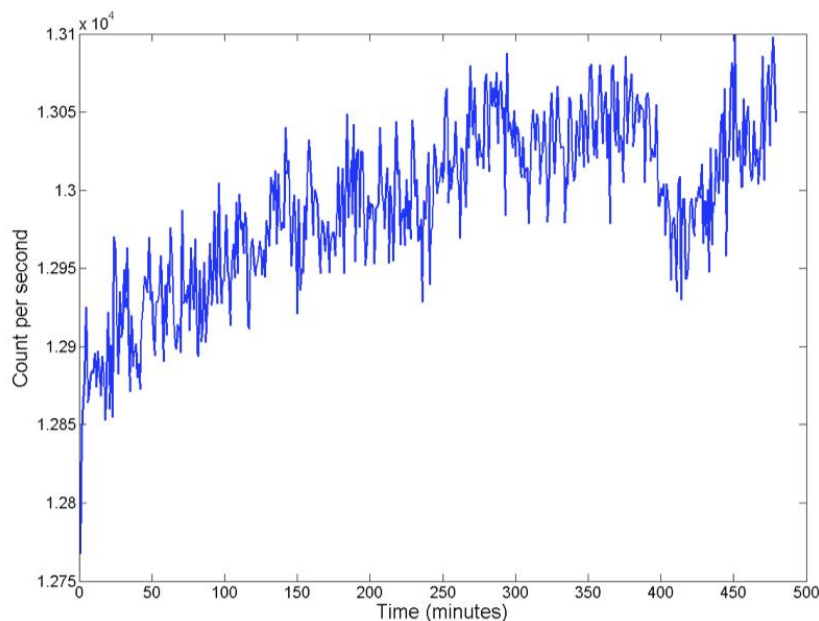
From the previous figures it can be seen that the X-ray flux increases across all voltages as the atomic number of the target material increases, which is in agreement with the theoretical background. The targets display increasing photon counts at higher energies moving from the Cu to the W tungsten, with the lower atomic number targets having a significant proportion of their flux in the low energy fluorescence peaks. This implies that the Cu or Mo targets would be more effective for CT imaging of low density materials such as CFRP due the increased absorption at these energies, resulting in better contrast and higher signal-to-noise ratio projections. This principal is demonstrated and discussed further in Chapter 4.

### **A.5.3 X-ray Source Stability**

In order to assess the ability of the CT system to perform long duration scans, the stability of the 225kV source was measured under short- and long-term conditions. The W target was used to generate a beam at 225kV and 60 $\mu$ A. Data acquisition was performed by taking 20s exposures spaced at 60s intervals. The short term stability was measured over a period of 1 hour, compared to 8 hours for the long-term stability measurement. Figures A.27 shows the stability of the source in terms of the number of photons detected per second over the respective measurement periods.



(a)



(b)

Figure A.27: Stability of 225kV X-ray source. (a) Short term stability (b) long term stability.

Figure A.27(a) shows that the source takes approximately 10 minutes to stabilise, before which the flux drops by approximately 3% from an initial maximum of  $1.325 \times 10^4$  counts per second. Figure A.27(b)

### A.5.4 Beam Transmission Through CFRP

To examine the absorption characteristics of the CFRP materials under investigation in chapters 4 and 5, transmission spectra were acquired using the Amptek detector. Figure A.28 shows a spectra acquired at 100kV and 80 $\mu$ A with and without a 2mm thick sample of MTM-45 (woven) CFRP obstructing the beam. The difference in the spectrum is also shown. Most of the absorption occurs at low voltages.

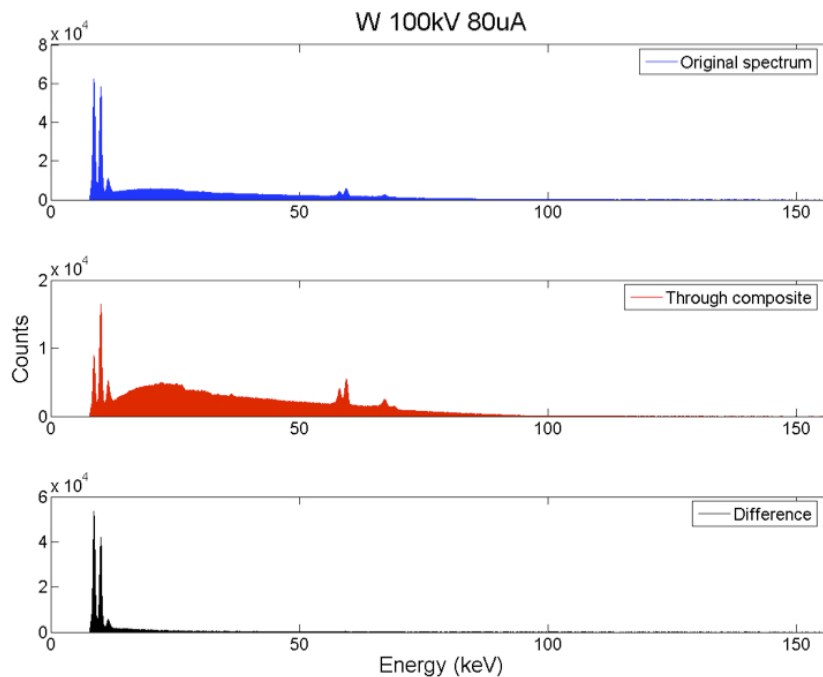


Figure A.28: Spectra obtained with and without a CFRP sample obstructing the X-ray beam, and difference between the spectra.

A transmission profile was calculated by dividing the obstructed spectrum by the unobstructed spectrum to give the result shown in figure A.29. This transmission profile shows that almost 90% of X-rays are transmitted above 20kV.

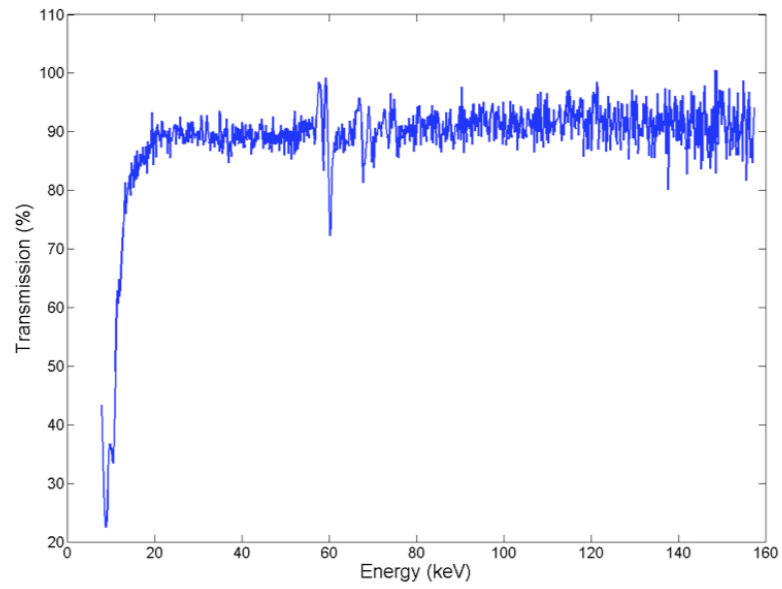


Figure A.29: Transmission profile of a CFRP sample at 225kV and 80 $\mu$ A

## A.6 Appendix Summary and Conclusions

This chapter has demonstrated that the CT system which is used for imaging of CFRP materials has a maximum resolution which is close to the manufacturer specified focal spot size of 3-5 $\mu\text{m}$ . Values ranging from 3.2- 5.8 $\mu\text{m}$  were measured from the central region of the detector, using spot size estimation and reconstruction methods.

The X-ray spectra for a multi-metal target were characterised and it was shown that increasing the atomic number of the target material produced a higher flux, as predicted from theory. Furthermore, it was shown that the lower atomic number targets have a significant proportion (up to 33%) of their flux in fluorescence peaks. Measuring the transmission of X-rays through a CFRP sample showed most of the absorption to take place at low (<20kV energies). These measurements have implications for the work performed in later sections in terms of target material choices and image acquisition parameters such as accelerating voltage.

---



---

## MATLAB CODE FOR DUAL ENERGY CT

```

Matlab code for dual energy CT

function output= xtekidualenergy(file1,file2,bh1,bh2)
output = [];

if nargin==0

    file1 = [];
    file2 = [];
    bh1 = [];
    bh2 = [];

end

{\color{red} \%selects xtekct files}
if isempty(file1)
    [FileName,PathName] = uigetfile({'*.xtekct','XTekCT files (*.xtekct)';...
    '*.*', 'All files (*.*)'},...
    'Select first xtekct file', 'MultiSelect', 'off');

    file1 = [PathName FileName];

end

if isempty(file2)
    [FileName,PathName] = uigetfile({'*.xtekct','XTekCT files (*.xtekct)';...
    '*.*', 'All files (*.*)'},...
    'Select second xtekct file', 'MultiSelect', 'off');

    file2 = [PathName FileName];

end

if isempty(bh1)
    answer = inputdlg('Enter beam-hardening polynomial coefficients for file 1', 'BH correction');
    bh1 = str2num(answer{1});
end
if isempty(bh2)
    answer = inputdlg('Enter beam-hardening polynomial coefficients for file 2', 'BH correction');
    bh2 = str2num(answer{1});
end

{\color{red} \%reads information from two xtekct files}
header1 = xtekct_read(file1);
header2= xtekct_read(file2);

{\color{red} \%reads no. of images from _ctdata.txt}
nimages1 = header1.CTData.NoOfProjections;
nimages2 = header2.CTData.NoOfProjections;

{\color{red} \%directory to look in for images}
directory1 = fileparts(header1.File);
directory2 = fileparts(header2.File);

{\color{red} \%gets root name for all images in dir1 e.g JR_32mm40kV_)

```

---

```

dirlimagerootname = [directory1 '\ ' header1.XTekCT.Name];
dir2imagerootname = [directory2 '\ ' header2.XTekCT.Name];

outputdir1 = [directory1 '\dualenergy\' header1.XTekCT.Name];

{\color{red} \%to write correct tiff file size}
tagstruct.ImageLength = header1.XTekCT.DetectorPixelsY;
tagstruct.ImageWidth = header1.XTekCT.DetectorPixelsX;
tagstruct.Photometric = 1;
tagstruct.Compression = 1;
tagstruct.Software = 'xtekualenergy';
tagstruct.PlanarConfiguration = 1;
tagstruct.Orientation = 5;
tagstruct.BitsPerSample = 16;
tagstruct.SamplesPerPixel = 1;

for n = 1:nimages1
    {\color{red} \%progress monitor}
    fprintf(1, ['Processing image ' num2str(n) '....']);
    tic

    {\color{red} \%concatenated directory with root name and image no. and file extension}
    dir1imagename = [dirlimagerootname sprintf('\%#04i',n) '.tif'];
    img1 = imread(dir1imagename);

    {\color{red} \%converts to double (64bit floating point) then divides to normalise}
    {\color{red} \%grey values between 0 and 1 to allow neg log to be taken}
    img1 = double(img1)/65535;
    abs1 = -log(img1);

    {\color{red} \%concatenated directory with root name and image no. and file extension}
    dir2imagename = [dir2imagerootname sprintf('\%#04i',n) '.tif'];
    img2 = imread(dir2imagename);

    {\color{red} \%converts to double (64bit floating point) then divides to normalise}
    {\color{red} \%grey values between 0 and 1 to allow neg log to be taken}
    img2 = double(img2)/65535;
    abs2 = -log(img2);

    {\color{red} \%correcting absorbance image for beam hardening}
    \%generates a matrix of all zeros of size 'abs1' then adds value of constant from bh1 (i.e first term in bh1)

    bhcorrected1 = zeros(size(abs1))+ (bh1(1)) {\color{red} bhcorrected2 = zeros(size(abs2)) + (bh2(1));

    for D=1: numel(bh1)-1 {\color{red} \%loops over user inputted bh terms}

    bhcorrected1 = bhcorrected1 + (bh1(D+1))*abs1.^D ;

    end

    for D=1: numel(bh2)-1 {\color{red} \%loops over user inputted bh terms}
    bhcorrected2 = bhcorrected2 + (bh2(D+1))*abs2.^D;

    end

    {\color{red} \%calculate STD to weight radiographs}
    noiseratio = 0.1;
    sigmaA_bhcorrected1 = ((1./img1)+(1/64)+ noiseratio*(img1.^-2+(1/64)));

    sigma1 = zeros(size(abs1))+ (bh1(1)^2);

    for D=1: numel(bh1)-1 {\color{red} \%loops over user inputted bh terms}

    sigma1 = sigma1 + (bh1(D+1)^2)*(D+1)^2*(abs1.^(2*(D+1)-2));

    end

    sigma1 = sigma1.*sigmaA_bhcorrected1;

    sigmaA_bhcorrected2 = ((1./img2)+(1/64)+ noiseratio*(img2.^-2+(1/64)));

    sigma2 = zeros(size(abs2))+ (bh2(1)^2);

    for D=1: numel(bh2)-1 {\color{red} \%loops over user inputted bh terms}

    sigma2 = sigma2 + (bh2(D+1)^2)*(D+1)^2*(abs2.^(2*(D+1)-2)) ;

    end

    sigma2 = sigma2.*sigmaA_bhcorrected2;

```

---

```

{\color{red}\%weights absorbance images according to optimum SNR }

sigma_optimum = sigma2./(sigma2+sigma1);

sigma_optimum(sigma_optimum > 0.9)=1;
sigma_optimum(sigma_optimum < 0.1) = 0;

combinedA = sigma_optimum.*bhcorrected1 + (1-sigma_optimum).*bhcorrected2;

{\color{red} \%convert back to corrected radiograph (Transmittance) and original 16bit}
{\color{red} \%greyscale range}
combinedT = exp(-combinedA)*65535;
bhcorrected16bit = uint16(combinedT);

    outputfilename = [outputdir1 sprintf('\%#04i',n) '.tif'];

tiff_file = Tiff(outputfilename, 'w');
    tiff_file.setTag(tagstruct);

    {\color{red} \%Write image}
    tiff_file.write(bhcorrected16bit);
    tiff_file.close();

t = toc;
fprintf(1, ['Done in ' num2str(t) 's\n']);

end

end

```

## BIBLIOGRAPHY

- Donald F. Adams and A.Keith Miller. An analysis of the impact behavior of hybrid composite materials. *Materials Science and Engineering*, 19(2):245 – 260, 1975. ISSN 0025-5416. doi: DOI:10.1016/0025-5416(75)90112-3. URL <http://www.sciencedirect.com/science/article/pii/0025541675901123>.
- D.J. Schneberk adn S.G. Azevedo, H.E. Martz, and M.F. Skeate. Sources of error in industrial tomographic reconstruction. *Materials Evaluation*, (48):609–617, 1990.
- A.M. Ali, Z. Melegy, M. Morsy, R.M. Megahid, T. Bucherl, and E.H. Lehmann. Image reconstruction techniques using projection data from transmission method. *Annals of Nuclear Energy*, 31(12):1415 – 1428, 2004. ISSN 0306-4549. doi: 10.1016/j.anucene.2004.03.006. URL <http://www.sciencedirect.com/science/article/pii/S0306454904000568>.
- R E Alvarez and A Macovski. Energy-selective reconstructions in x-ray computerised tomography. *Physics in Medicine and Biology*, 21(5):733, 1976. URL <http://stacks.iop.org/0031-9155/21/i=5/a=002>.
- R. Ambu, F. Aymerich, F. Ginesu, and P. Priolo. Assessment of ndt interferometric techniques for impact damage detection in composite laminates. *Composites Science and Technology*, 66(2):199 – 205, 2006. ISSN 0266-3538. doi: 10.1016/j.compscitech.2005.04.027. URL <http://www.sciencedirect.com/science/article/pii/S0266353805001387>. <ce:title>Experimental Techniques and Design in Composite Materials</ce:title> <xocs:full-name>Experimental Techniques and Design in Composite Materials</xocs:full-name>.
- M. Amos. *Advanced Industrial X-Ray Computed Tomography for Defect Detection and Characterisation in Composite Structures*. PhD thesis, University of Manchester, 2011.
- M. Amos, S. Woods, P.J. Withers, and P. Wallace. An roi x-ray ct technique for defect characterisation in carbon-fibre-reinforced-plastic laminates. In *Proceedings of the 37th International Conference on Quantitative Non-Destructive Evaluation, San Diego, USA, July 2010* 2010.
- Amptek. Exvc collimator kit technical documentation. Technical report, Amptek Inc., July 2011. URL <http://www.amptek.com/xrcol.html>.
- M.A. Anastasio, Y. Zou, E.Y. Sidky, and X. Pan. Local cone-beam tomography image reconstruction on chords. *JOSA A*, 24(6):1569–1579, 2007.

- A.H. Andersen and A.C. Kak. Simultaneous algebraic reconstruction technique (sart): A superior implementation of the art algorithm. *Ultrasonic Imaging*, 6(1):81 – 94, 1984. ISSN 0161-7346. doi: 10.1016/0161-7346(84)90008-7. URL <http://www.sciencedirect.com/science/article/pii/0161734684900087>.
- J.G. Avery. Design manual for impact damage tolerant aircraft structures. Technical report, NATO, 1981.
- M.G. Bader and R.M. Ellis. The effect of notches and specimen geometry on the pendulum impact strength of uniaxial cfrp. *Composites*, 5(6):253 – 258, 1974. ISSN 0010-4361. doi: DOI: 10.1016/0010-4361(74)90365-6. URL <http://www.sciencedirect.com/science/article/pii/0010436174903656>.
- J. Banhart. *Advanced tomographic methods in materials research and engineering*, volume 66. Oxford University Press, USA, 2008.
- W. Bascom, R. Ting, R. Moulton, C. Riew, and A. Siebert. The fracture of an epoxy polymer containing elastomeric modifiers. *Journal of Materials Science*, 16:2657–2664, 1981. ISSN 0022-2461. URL <http://dx.doi.org/10.1007/BF02402827>. 10.1007/BF02402827.
- P.W.R. Beaumont. Fracture mechanisms in fibrous composites. In *The Symposium on Fracture Mechanics - Current Status, Future Prospects*, 1979.
- P.W.R. Beaumont, P.G. Riewald, and C. Zweben. Methods for improving the impact resistance of composite materials. *ASTM Special Technical Publication*, pages 134–138, 1974.
- Hans-Christoph Becker and Thorsten Johnson. Cardiac ct for the assessment of chest pain: Imaging techniques and clinical results. *European Journal of Radiology*, (0):–, 2011. ISSN 0720-048X. doi: 10.1016/j.ejrad.2011.05.038. URL <http://www.sciencedirect.com/science/article/pii/S0720048X1100595X>.
- B. Bednarczyk, J. Aboudi, and P. Yarrington. Determination of the shear stress distribution in a laminate from the applied shear resultant—a simplified shear solution. Technical report, NASA, 2007.
- P. Berbinau, C. Soutis, and I. A. Guz. Compressive failure of 0°unidirectional carbon-fibre-reinforced plastic (cfrp) laminates by fibre microbuckling. *Composites Science and Technology*, 59(9):1451 – 1455, 1999. ISSN 0266-3538. doi: DOI:10.1016/S0266-3538(98)00181-X. URL <http://www.sciencedirect.com/science/article/pii/S026635389800181X>.
- Junguo Bian, Dan Xia, Emil Y Sidky, and Xiaochuan Pan. Region of interest imaging for a general trajectory with the rebinned bpf algorithm. *Tsinghua Science and Technology*, 15(1):68 – 73, 2010. ISSN 1007-0214. doi: 10.1016/S1007-0214(10)70011-0. URL <http://www.sciencedirect.com/science/article/pii/S1007021410700110>.

- Rikard Borg, Larsgunnar Nilsson, and Kjell Simonsson. Simulation of low velocity impact on fiber laminates using a cohesive zone based delamination model. *Composites Science and Technology*, 64(2):279 – 288, 2004. ISSN 0266-3538. doi: 10.1016/S0266-3538(03)00256-2. URL <http://www.sciencedirect.com/science/article/pii/S0266353803002562>.
- Christophe Bouvet, Bruno Castanié, Matthieu Bizeul, and Jean-Jacques Barrau. Low velocity impact modelling in laminate composite panels with discrete interface elements. *International Journal of Solids and Structures*, 46(14–15):2809 – 2821, 2009. ISSN 0020-7683. doi: 10.1016/j.ijsolstr.2009.03.010. URL <http://www.sciencedirect.com/science/article/pii/S002076830900136X>.
- F.J. Bradshaw, G. Dorey, and G.R. Sidey. Impact resistance of carbon fibre reinforced plastics. Technical report, Royal Aircraft Establishment, 1973.
- Torsten Brandmüller. Investigation of casting defects by x-ray ct. *online article* <http://www.chemie.uni-erlangen.de/>, 2008.
- British Standards. Non-destructive testing, Characteristics of focal spots in industrial X-ray systems for use in non-destructive testing Part 4: Edge method. Technical report, British Standards, 1999.
- British Standards. Bs iso 1268-1:2001 fibre-reinforced plastics — methods of producing test plates — part 1: General conditions. Technical report, British Standards, December 2001.
- British Standards. BS ISO 1268-4:2005 Fibre-reinforced plastics — Methods of producing test plates — part 4: Moulding of prepregs. Technical report, British Standards, March 2005.
- British Standards. BS ISO 16016-1 Non destructive testing. Radiation method. Computed tomography. Part 2. Principle, equipment and samples. Technical report, British Standards, November 2009a.
- British Standards. BS ISO 16016-1 Non destructive testing. Radiation method. Computed tomography. Part 3. Operation and interpretation. Technical report, British Standards, November 2009b.
- Santillan J. Suppes A. Brunke, O. Precise 3d dimensional metrology using high-resolution x-ray computed tomography (Îijct). volume 7804, 2010. URL <http://www.scopus.com/inward/record.url?eid=2-s2.0-78649426765&partnerID=40&md5=1b5e4c68ae4de89f593a48e97e77ff56>. cited By (since 1996) 1.
- W. Cantwell, P. Curtis, and J. Morton. Post-impact fatigue performance of carbon fibre laminates with non-woven and mixed-woven layers. *Composites*, 14(3):301 – 305, 1983. ISSN 0010-4361. doi: DOI:10.1016/0010-4361(83)90020-4. URL <http://www.sciencedirect.com/science/article/pii/0010436183900204>.
- W.J. Cantwell. The influence of target geometry on the high velocity impact response of CFRP. *Composite Structures*, 10(3):247 – 265, 1988. ISSN 0263-8223. doi: DOI:10.

- 1016/0263-8223(88)90022-0. URL <http://www.sciencedirect.com/science/article/pii/0263822388900220>.
- W.J. Cantwell and J. Morton. Geometrical effects in the low velocity impact response of CFRP. *Composite Structures*, 12(1):39 – 59, 1989. ISSN 0263-8223. doi: DOI:10.1016/0263-8223(89)90043-3. URL <http://www.sciencedirect.com/science/article/pii/0263822389900433>.
- W.J. Cantwell and J. Morton. An assessment of the residual strength of an impact-damaged carbon fibre reinforced epoxy. *Composite Structures*, 14(4):303 – 317, 1990. ISSN 0263-8223. doi: DOI:10.1016/0263-8223(90)90012-4. URL <http://www.sciencedirect.com/science/article/pii/0263822390900124>.
- W.J. Cantwell and J. Morton. The impact resistance of composite materials – a review. *Composites*, 22(5):347 – 362, 1991. ISSN 0010-4361. doi: DOI:10.1016/0010-4361(91)90549-V. URL <http://www.sciencedirect.com/science/article/pii/001043619190549V>.
- G. Caprino, V. Lopresto, and D. Santoro. Ballistic impact behaviour of stitched graphite/epoxy laminates. *Composites Science and Technology*, 67(3-4):325 – 335, 2007. ISSN 0266-3538. doi: DOI:10.1016/j.compscitech.2006.04.015. URL <http://www.sciencedirect.com/science/article/pii/S0266353806001588>.
- Dreossi D. Mancini L. Marinello F. Tromba G. Savio E. Carmignato, S. Testing of x-ray microtomography systems using a traceable geometrical standard. *Measurement Science and Technology*, 20(8), 2009. URL <http://www.scopus.com/inward/record.url?eid=2-s2.0-70350643584&partnerID=40&md5=17396f5cb0efbda41bc04e0dbab45e48>. cited By (since 1996) 8.
- T. Centea and P. Hubert. Measuring the impregnation of an out-of-autoclave prepreg by micro-ct. *Composites Science and Technology*, 71(5):593 – 599, 2011. ISSN 0266-3538. doi: DOI:10.1016/j.compscitech.2010.12.009. URL <http://www.sciencedirect.com/science/article/pii/S026635381000477X>.
- C. Chamis, M.P. Hanson, and T.T. Serafini. Impact resistance of unidirectional fibre composites. *Composite materials: testing and design (2nd conf)*, ASTM STP 497, pages 324–349, 1972.
- David A. Chesler, Stephen J. Riederer, and Norbert J. Pelc. Noise due to photon counting statistics in computed x-ray tomography. *Journal of Computer Assisted Tomography*, 1(1), 1977.
- Seungryong Cho, Lifeng Yu, C.A. Pelizzari, and Xiaochuan Pan. Circular cone-beam micro-ct for small animal imaging with truncated data. In *Nuclear Science Symposium Conference Record, 2006. IEEE*, volume 5, pages 2889 –2891, 29 2006-nov. 1 2006. doi: 10.1109/NSSMIC.2006.356480.
- Hyung Yun Choi, R. J. Downs, and Fu-Kuo Chang. A new approach toward understanding damage mechanisms and mechanics of laminated composites due to low-velocity impact: Part i—experiments. *Journal of Composite Materials*, 25(8):992–1011, 1991a. doi:

- 10.1177/002199839102500803. URL <http://jcm.sagepub.com/content/25/8/992.abstract>.
- Hyung Yun Choi, Hsi-Yung T. Wu, and Fu-Kuo Chang. A new approach toward understanding damage mechanisms and mechanics of laminated composites due to low-velocity impact: Part ii—analysis. *Journal of Composite Materials*, 25(8):1012–1038, 1991b. doi: 10.1177/002199839102500804. URL <http://jcm.sagepub.com/content/25/8/1012.abstract>.
- R. Choudhry. *Characterisation and modelling of impact damage in bonded joints of woven fibre polymeric composites*. PhD thesis, University of Manchester, 2009.
- I.K. Chun, M.H. Cho, S.C. Lee, M.H. Cho, and S.Y. Lee. X-ray micro-tomography system for small-animal imaging with zoom-in imaging capability. *Physics in medicine and biology*, 49: 3889, 2004.
- T. W. Clyne and P. J. Withers. *An introduction to metal matrix composites / T.W. Clyne, P.J. Withers*. New York, NY, USA : Cambridge University Press, Cambridge [England] ;, 1993. ISBN 0521418089.
- V. Coenen. *Auxetic Composite Laminates with Enhanced Impact Resistance*. PhD thesis, Bolton Institute of Higher Education, 2003.
- Robert Crane, Donald Hagemaijer, and Robert Fassbender. Radiographic inspection of composites. In Anthony Kelly and Carl Zweben, editors, *Comprehensive Composite Materials*, pages 321 – 344. Pergamon, Oxford, 2000. ISBN 978-0-08-042993-9. doi: 10.1016/B0-08-042993-9/00078-4. URL <http://www.sciencedirect.com/science/article/pii/B0080429939000784>.
- C.Ruiz and Y. R. Xia. Significance of interfaces in impact response of laminated composites. Technical report, American Society of Mechanical Engineers, Petroleum Division (Publication), 1991.
- J. C. Dainty and Rodney Shaw. *Image science : principles, analysis and evaluation of photographic-type imaging processes / J. C. Dainty and R. Shaw*. Academic Press, London ; New York ;, 1974. ISBN 0122008502.
- J.C. Dainty, R. Shaw, and LJ Cutrona. Image science: principles, analysis and evaluation of photographic-type imaging processes. *Physics Today*, 29:71, 1976.
- M. de Freitas and L. Reis. Failure mechanisms on composite specimens subjected to compression after impact. *Composite Structures*, 42(4):365 – 373, 1998. ISSN 0263-8223. doi: 10.1016/S0263-8223(98)00081-6. URL <http://www.sciencedirect.com/science/article/pii/S0263822398000816>. <ce:title>International Workshop on Experimental Techniques in the Analysis of Composite Structures</ce:title>.

- John P. Dear and Samuel A. Brown. Impact damage processes in reinforced polymeric materials. *Composites Part A: Applied Science and Manufacturing*, 34(5):411 – 420, 2003. ISSN 1359-835X. doi: 10.1016/S1359-835X(03)00082-4. URL <http://www.sciencedirect.com/science/article/pii/S1359835X03000824>.
- Michel Defrise, Frédéric Noo, Rolf Clackdoyle, and Hiroyuki Kudo. Truncated hilbert transform and image reconstruction from limited tomographic data. *Inverse Problems*, 22(3):1037, 2006. URL <http://stacks.iop.org/0266-5611/22/i=3/a=019>.
- Luke P. Djukic, Israel Herszberg, William R. Walsh, Gregory A. Schoeppner, and B. Gangadhara Prusty. Contrast enhancement in visualisation of woven composite architecture using a microct scanner. part 2: Tow and preform coatings. *Composites Part A: Applied Science and Manufacturing*, 40(12):1870 – 1879, 2009a. ISSN 1359-835X. doi: DOI:10.1016/j.compositesa.2009.04.002. URL <http://www.sciencedirect.com/science/article/pii/S1359835X09000839>. Special Issue: CompTest 2008.
- Luke P. Djukic, Israel Herszberg, William R. Walsh, Gregory A. Schoeppner, B. Gangadhara Prusty, and Don W. Kelly. Contrast enhancement in visualisation of woven composite tow architecture using a microct scanner. part 1: Fabric coating and resin additives. *Composites Part A: Applied Science and Manufacturing*, 40(5):553 – 565, 2009b. ISSN 1359-835X. doi: DOI:10.1016/j.compositesa.2008.12.016. URL <http://www.sciencedirect.com/science/article/pii/S1359835X09000074>.
- G. Dorey. Fracture behaviour and residual strength of carbon fibre composites subjected to impact loads. *1975. 12*, 1975.
- G. Dorey. Relationships between impact resistance and fracture toughness in advanced composite materials. *AGARD Effects of Serv. Environ. on Composite Mater. 11 p(SEE N 81-11128 02-24)*, 1980.
- G. Dorey. Fracture of composites and damage tolerance. *AGARD Pract. Considerations of Design, Fabric. and Tests for Composite Mater. 12 p(SEE N 83-17609 08-24)*, 1982.
- G. Dorey. Impact damage in composites- development, consequences and prevention. *Proc. 6th Int Conf on Composite Materials*, 1988.
- G. Dorey, S.M. Bishop, and P.T. Curtis. On the impact performance of carbon fibre laminates with epoxy and peek matrices. *Composites Science and Technology*, 23(3):221 – 237, 1985. ISSN 0266-3538. doi: DOI:10.1016/0266-3538(85)90019-3. URL <http://www.sciencedirect.com/science/article/pii/0266353885900193>.
- N. Douarche, D. Rouby, G. Peix, and J. M. Jouin. Relations between x-ray tomography, density and mechanical properties in carbon-carbon composites. *Carbon*, 39(10):1455 – 1465, 2001. ISSN 0008-6223. doi: DOI:10.1016/S0008-6223(00)00196-2. URL <http://www.sciencedirect.com/science/article/pii/S0008622300001962>.

- A. Enfedaque, J.M. Molina-Aldareguía, F. Gálvez, C. González, and J. LLorca. Effect of glass fiber hybridization on the behavior under impact of woven carbon fiber/epoxy laminates. *Journal of Composite Materials*, 44(25):3051–3068, 2010. doi: 10.1177/0021998310369602. URL <http://jcm.sagepub.com/content/44/25/3051.abstract>.
- Finch D.V. Ritman E.L. Smith K.T. Faridani, A. Local tomography ii. *SIAM Journal on Applied Mathematics*, 57(4):1095–1127, 1997. URL <http://www.scopus.com/inward/record.url?eid=2-s2.0-0031206990&partnerID=40&md5=c86600b80b6409775a47962760ade6fa>. cited By (since 1996) 72.
- Ritman E.L. Faridani, A. High-resolution computed tomography from efficient sampling. *Inverse Problems*, 16(3):635–650, 2000. URL <http://www.scopus.com/inward/record.url?eid=2-s2.0-0042643442&partnerID=40&md5=d6ec865cc981a3358e6d384979b4b3ca>. cited By (since 1996) 10.
- Ritman Erik L. Smith Kennan T. Faridani, Adel. Examples of local tomography. *SIAM Journal on Applied Mathematics*, 52(4):1193–1198, 1992a. URL <http://www.scopus.com/inward/record.url?eid=2-s2.0-0026909276&partnerID=40&md5=b48f862ad4374a0adc1fdb8fb70d1a39>. cited By (since 1996) 14.
- Ritman Erik L. Smith Kennan T. Faridani, Adel. Local tomography. *SIAM Journal on Applied Mathematics*, 52(2):459–484, 1992b. URL <http://www.scopus.com/inward/record.url?eid=2-s2.0-0026846049&partnerID=40&md5=e11bbed4369212c4f70356823e937188>. cited By (since 1996) 85.
- L. A. Feldkamp, L. C. Davis, and J. W. Kress. Practical cone-beam algorithm. *Journal of the Optical Society of America A*, 1:612–619, June 1984. doi: 10.1364/JOSAA.1.000612.
- Rosalind Franklin. Photo 51. 1952.
- Jian Fu, BaiHong Jiang, and Bin Li. Large field of view computed laminography with the asymmetric rotational scanning geometry. *SCIENCE CHINA Technological Sciences*, 53:2261–2271, 2010. ISSN 1674-7321. URL <http://dx.doi.org/10.1007/s11431-010-4012-6>. 10.1007/s11431-010-4012-6.
- Hwei Gao, Li Zhang, Zhiqiang Chen, Yuxiang Xing, and Shuanglei Li. Beam hardening correction for middle-energy industrial computerized tomography. *Nuclear Science, IEEE Transactions on*, 53(5):2796–2807, oct. 2006. ISSN 0018-9499. doi: 10.1109/TNS.2006.879825.
- Spyrou N.M. Gentle, D.J. Region of interest tomography in industrial applications. *Nuclear Inst. and Methods in Physics Research, A*, 299(1-3):534–537, 1990. URL <http://www.scopus.com/inward/record.url?eid=2-s2.0-38249016294&partnerID=40&md5=344184aba590f81df9936936a4260a88>. cited By (since 1996) 4.
- Peter Gilbert. Iterative methods for the three-dimensional reconstruction of an object from projections. *Journal of Theoretical Biology*, 36(1):105 – 117, 1972. ISSN 0022-5193. doi: 10.1016/0022-5193(72)90180-4. URL <http://www.sciencedirect.com/science/article/pii/0022519372901804>.

- E.L. Gingold and B.H. Hasegawa. Systematic bias in material decomposition applied to quantitative dual-energy x-ray imaging. *Medical Physics*, (19):35–33, 1992.
- S. Gondrom, J. Zhou, M. Maisl, H. Reiter, M. Kr Ening, and W. Arnold. X-ray computed laminography: an approach of computed tomography for applications with limited access. *Nuclear Engineering and Design*, 190(1-2):141 – 147, 1999. ISSN 0029-5493. doi: DOI:10.1016/S0029-5493(98)00319-7. URL <http://www.sciencedirect.com/science/article/pii/S0029549398003197>.
- R. Gordon, R. Bender, and G. T. Herman. Algebraic reconstruction techniques (ART) for three-dimensional electron microscopy and x-ray photography. *Journal of theoretical biology*, 29(3): 471–481, December 1970. ISSN 0022-5193. URL <http://view.ncbi.nlm.nih.gov/pubmed/5492997>.
- Donald T. Graham and P.J. Cloke. *Principles of radiological physics*. Churchill Livingstone, 2003. ISBN 9780443070730. URL <http://books.google.com/books?id=Tah1RHFa0ZsC>.
- Huaiqun Guan and Richard Gordon. Computed tomography using algebraic reconstruction techniques (arts) with different projection access schemes: a comparison study under practical situations. *Physics in Medicine and Biology*, 41(9):1727, 1996. URL <http://stacks.iop.org/0031-9155/41/i=9/a=012>.
- F.J. Guild, P.J. Hogg, and J.C. Prichard. A model for the reduction in compression strength of continuous fibre composites after impact damage. *Composites*, 24(4):333 – 339, 1993. ISSN 0010-4361. doi: DOI:10.1016/0010-4361(93)90043-8. URL <http://www.sciencedirect.com/science/article/pii/0010436193900438>.
- P. Hammersberg and M. Mangard. Correction for beam hardening artefacts in computerised tomography. *Journal of X-ray Science and Technology*, 8(1):75, 1998.
- P. Hammersberg and M. Mangard. Optimal computerized tomography performance. In *Computerized Tomography for Industrial Applications and Image Processing in Radiology*, March 1999.
- N.L. Hancox and H. Wells. Izod impact properties of carbon-fibre/glass-fibre sandwich structures. *Composites*, 4(1):26 – 30, 1973. ISSN 0010-4361. doi: DOI:10.1016/0010-4361(73)90292-9. URL <http://www.sciencedirect.com/science/article/pii/0010436173902929>.
- G. Harding, J. Kosanetzky, and U. Neitzel. X-ray diffraction computed tomography. *Medical Physics*, 14(4):515–525, 1987. doi: 10.1118/1.596063. URL <http://link.aip.org/link/?MPH/14/515/1>.
- Z. Hashin. Failure criteria for unidirectional fiber composites. *Failure Criteria for Unidirectional Fiber Composites*, 47:329–334, 1980.

- B. J. Heismann, J. Leppert, and K. Stierstorfer. Density and atomic number measurements with spectral x-ray attenuation method. *Journal of Applied Physics*, 94(3):2073–2079, 2003. doi: 10.1063/1.1586963. URL <http://link.aip.org/link/?JAP/94/2073/1>.
- Baumbach T. Mikulík P. Kiel D. Pernot P. Cloetens P.-Baruchel J. Helfen, L. High-resolution three-dimensional imaging of flat objects by synchrotron-radiation computed laminography. *Applied Physics Letters*, 86(7):1–3, 2005. URL <http://www.scopus.com/inward/record.url?eid=2-s2.0-17044385027&partnerID=40&md5=1b8def905b967223706fa4e62ae32df1>. cited By (since 1996) 15.
- L. Helfen, A. Myagotin, P. Pernot, M. DiMichiel, P. Mikulík, A. Berthold, and T. Baumbach. Investigation of hybrid pixel detector arrays by synchrotron-radiation imaging. *Nuclear Instruments and Methods in Physics Research Section A: Accelerators, Spectrometers, Detectors and Associated Equipment*, 563(1):163 – 166, 2006. ISSN 0168-9002. doi: DOI:10.1016/j.nima.2006.01.085. URL <http://www.sciencedirect.com/science/article/pii/S016890020600194X>. Proceedings of the 7th International Workshop on Radiation Imaging Detectors - IWORID 2005.
- Myagotin A. Rack A. Pernot P. Mikulík P. Di Michiel-M. Baumbach T. Helfen, L. Synchrotron-radiation computed laminography for high-resolution three-dimensional imaging of flat devices. *Physica Status Solidi (A) Applications and Materials*, 204(8):2760–2765, 2007. URL <http://www.scopus.com/inward/record.url?eid=2-s2.0-34548288936&partnerID=40&md5=43056222f7b7398a54fb2a881f9eed3f>. cited By (since 1996) 6.
- G.T. Herman. *Fundamentals of Computerized Tomography: Image Reconstruction from Projections*. Springer Verlag, 2009.
- M.J. Hinton, P.D. Soden, and A.S. Kaddour. Preface. In M.J. Hinton, A.S. Kaddour, and P.D. Soden, editors, *Failure Criteria in Fibre-Reinforced-Polymer Composites*, pages v – vi. Elsevier, Oxford, 2004. ISBN 978-0-08-044475-8. doi: 10.1016/B978-008044475-8/50000-7. URL <http://www.sciencedirect.com/science/article/pii/B9780080444758500007>.
- S.A. Hitchen and R.M.J. Kemp. The effect of stacking sequence on impact damage in a carbon fibre/epoxy composite. *Composites*, 26(3):207 – 214, 1995. ISSN 0010-4361. doi: DOI:10.1016/0010-4361(95)91384-H. URL <http://www.sciencedirect.com/science/article/pii/001043619591384H>.
- G. N. Hounsfield. Computerized transverse axial scanning (tomography): Part 1. description of system. *Br J Radiol*, 46(552):1016–1022, 1973. doi: 10.1259/0007-1285-46-552-1016. URL <http://bjr.birjournals.org/cgi/content/abstract/46/552/1016>.
- J. Hsieh. *Computed tomography: principles, design, artifacts, and recent advances*, volume 114. Society of Photo Optical, 2003.

- Hongli Hu and Jianzhou Zhang. Exact weighted-fbp algorithm for three-orthogonal-circular scanning reconstruction. *Sensors*, 9(6):4606–4614, 2009. ISSN 1424-8220. doi: 10.3390/s90604606. URL <http://www.mdpi.com/1424-8220/9/6/4606/>.
- Harold K. Hughes. Beer's law and the optimum transmittance in absorption measurements. *Appl. Opt.*, 2(9):937–945, Sep 1963. doi: 10.1364/AO.2.000937. URL <http://ao.osa.org/abstract.cfm?URI=ao-2-9-937>.
- Derek. Hull and T. W. Clyne. *An introduction to composite materials*. Cambridge solid state science series. Cambridge University Press., Cambridge :, 2nd ed. edition, 1996. ISBN ISBN: 9780521388559. Includes bibliographical references and indexes.
- L. Iannucci and M.L. Willows. An energy based damage mechanics approach to modelling impact onto woven composite materials—part i: Numerical models. *Composites Part A: Applied Science and Manufacturing*, 37(11):2041 – 2056, 2006. ISSN 1359-835X. doi: 10.1016/j.compositesa.2005.12.013. URL <http://www.sciencedirect.com/science/article/pii/S1359835X05004318>.
- Daphne F. Jackson and D. J. Hawkes. X-ray attenuation coefficients of elements and mixtures. *Physics Reports*, 70(3):169 – 233, 1981. ISSN 0370-1573. doi: DOI:10.1016/0370-1573(81)90014-4. URL <http://www.sciencedirect.com/science/article/pii/0370157381900144>.
- Iwan Jerjen, Vincent Revol, Philipp Schuetz, Christian Kottler, Rolf Kaufmann, Thomas Luethi, Konstantins Jefimovs, Claus Urban, and Urs Sennhauser. Reduction of phase artifacts in differential phase contrast computed tomography. *Opt. Express*, 19(14):13604–13611, Jul 2011. doi: 10.1364/OE.19.013604. URL <http://www.opticsexpress.org/abstract.cfm?URI=oe-19-14-13604>.
- C.J. Jih and C.T. Sun. Prediction of delamination in composite laminates subjected to low velocity impact. *Journal of Composite Materials*, 27(7):684–701, 1993. doi: 10.1177/002199839302700703. URL <http://jcm.sagepub.com/content/27/7/684.abstract>.
- T.S. Jones, D. Polansky, and H. Berger. Radiation inspection methods for composites. *NDT International*, 21(4):277 – 282, 1988. ISSN 0308-9126. doi: DOI:10.1016/0308-9126(88)90341-0. URL <http://www.sciencedirect.com/science/article/pii/0308912688903410>.
- S.P. Joshi and C.T. Sun. Impact induced fracture in a laminated composite. *Journal of Composite Materials*, 19(1):51–66, 1985. doi: 10.1177/002199838501900104. URL <http://jcm.sagepub.com/content/19/1/51.abstract>.
- A.C. Kak and M. Slaney. Principles of computerized tomographic imaging. 1988.
- W A Kalender, W Seissler, E Klotz, and P Vock. Spiral volumetric ct with single-breath-hold technique, continuous transport, and continuous scanner rotation. *Radiology*, 176(1):181–183, 1990. URL <http://www.ncbi.nlm.nih.gov/pubmed/2353088>.

- Welkenhuyzen F. Tan Y. Bleys P. Voet A. Kruth J.-P. Dewulf W. Kiekens, K. A test object with parallel grooves for calibration and accuracy assessment of industrial computed tomography (ct) metrology. *Measurement Science and Technology*, 22(11), 2011. URL <http://www.scopus.com/inward/record.url?eid=2-s2.0-80054739817&partnerID=40&md5=f876d8cf0d97bb7deeac90ecfbe49b00>. cited By (since 1996) 0.
- C. Kottler, F. Pfeiffer, O. Bunk, C. Grunzweig, and C. David. Grating interferometer based scanning setup for hard x-ray phase contrast imaging. *REVIEW OF SCIENTIFIC INSTRUMENTS*, 78, 2007.
- R. Krueger, J. Ratcliffe, and P. Minguet. Panel stiffener debonding analysis using a shell/3d modeling technique. *Composites Science and Technology*, 69:2352–2362, 2009.
- Bartscher M. Carmignato S. Schmitt R. De Chiffre L. Weckenmann-A. Kruth, J.P. Computed tomography for dimensional metrology. *CIRP Annals - Manufacturing Technology*, 60(2):821–842, 2011. URL <http://www.scopus.com/inward/record.url?eid=2-s2.0-80051668123&partnerID=40&md5=53826631c61dcbdfb21cb11f28e4876>. cited By (since 1996) 1.
- A. Kyrieleis, V. Titarenko, M. Ibison, T. Connolley, and P.J. Withers. Region-of-interest tomography using filtered backprojection: Assessing the practical limits. *Journal of Microscopy*, 241(1):69–82, 2010. URL <http://www.scopus.com/inward/record.url?eid=2-s2.0-78650058535&partnerID=40&md5=0b4b1a7543fc24a3e425e0175240d88c>. cited By (since 1996) 1.
- S-W. R. Lee and C.T. Sun. A quasi-static penetration model for composite laminates. *Journal of Composite Materials*, 27(3):251–271, 1993. doi: 10.1177/002199839302700302. URL <http://jcm.sagepub.com/content/27/3/251.abstract>.
- S.M. Lee. *Dictionary of composite materials technology*. CRC, 1989.
- L.A. Lehmann, R.E. Alvarez, A. Macovski, W.R. Brody, N.J. Pelc, S.J. Riederer, and A.L. Hall. Generalized image combinations in dual kvp digital radiography. *Medical Physics*, (8):659–667, 1981.
- Megerdigian Cindy Papalia Rocco Lehmann, Stan. Carbon fiber/resin matrix interphase: Effect of carbon fiber surface treatment on composite performance. *S.A.M.P.E. quarterly*, 16(3): 7–13, 1985. URL <http://www.scopus.com/inward/record.url?eid=2-s2.0-0022045709&partnerID=40&md5=2bc0ed3ca49f3f507501c938060909ae>. cited By (since 1996) 5.
- B. Li and J. Hsieh. Comparison of reconstruction algorithms to extend ct reconstruction field-of-view. In *Nuclear Science Symposium Conference Record, 2007. NSS'07. IEEE*, volume 5, pages 3912–3914. IEEE, 2007.
- Dahsin Liu. Impact-induced delamination—a view of bending stiffness mismatching. *Journal of Composite Materials*, 22(7):674–692, 1988. doi: 10.1177/002199838802200706. URL <http://jcm.sagepub.com/content/22/7/674.abstract>.

- Dahsin Liu and Lawrence E. Malvern. Matrix cracking in impacted glass/epoxy plates. *Journal of Composite Materials*, 21(7):594–609, 1987. doi: 10.1177/002199838702100701. URL <http://jcm.sagepub.com/content/21/7/594.abstract>.
- Mangard Maans. *Optimised performance of industrial high resolution computerised tomography*. PhD thesis, Linköping University, The Institute of Technology, Engineering Materials, 2000. 2000.
- P. Maimi, P. Camanho, and J. Mayugo. A thermodynamically consistent damage model for advanced composites. In *NASA TM 2006 214282*, pages 1–42. NASA Langley Research Centre, 2006.
- George Marsh. Airframers exploit composites in battle for supremacy. *Reinforced Plastics*, 49(3): 26 – 32, 2005. ISSN 0034-3617. doi: DOI:10.1016/S0034-3617(05)00577-1. URL <http://www.sciencedirect.com/science/article/pii/S0034361705005771>.
- J. Martín-Herrero and Ch. Germain. Microstructure reconstruction of fibrous c/c composites from x-ray microtomography. *Carbon*, 45(6):1242 – 1253, 2007. ISSN 0008-6223. doi: DOI:10.1016/j.carbon.2007.01.021. URL <http://www.sciencedirect.com/science/article/pii/S0008622307000589>.
- A. McNeil. 3d rendering of a huntsman spider from x-ray phase contrast ct. *available online at <http://xray-imaging.org.uk/>*.
- Leon Mishnaevsky and Povl Brøndsted. Micromechanical modeling of damage and fracture of unidirectional fiber reinforced composites: A review. *Computational Materials Science*, 44(4): 1351 – 1359, 2009. ISSN 0927-0256. doi: 10.1016/j.commatsci.2008.09.004. URL <http://www.sciencedirect.com/science/article/pii/S0927025608004114>.
- A.J. Moffat, P. Wright, L. Helfen, T. Baumbach, G. Johnson, S.M. Spearing, and I. Sinclair. In situ synchrotron computed laminography of damage in carbon fibre-epoxy [90/0]s laminates. *Scripta Materialia*, 62(2):97 – 100, 2010. ISSN 1359-6462. doi: DOI:10.1016/j.scriptamat.2009.09.027. URL <http://www.sciencedirect.com/science/article/pii/S1359646209005983>.
- J. Morton and E.W. Godwin. Impact response of tough carbon fibre composites. *Composite Structures*, 13(1):1 – 19, 1989. ISSN 0263-8223. doi: DOI:10.1016/0263-8223(89)90069-X. URL <http://www.sciencedirect.com/science/article/pii/026382238990069X>.
- Klaus Mueller, Roni Yagel, and John J. Wheller. Fast implementations of algebraic methods for 3d reconstruction from cone-beam data. *IEEE Transactions on Medical Imaging*, 18:538–547, 1998.
- F. Nachtrab, S. Weis, P. Keßling, F. Sukowski, U. Haßler, T. Fuchs, N. Uhlmann, and R. Hanke. Quantitative material analysis by dual-energy computed tomography for industrial ndt applications. *Nuclear Instruments and Methods in Physics Research Section A: Accelerators, Spectrometers, Detectors and Associated Equipment*,

- 633, Supplement 1(0):S159 – S162, 2011. ISSN 0168-9002. doi: 10.1016/j.nima.2010.06.154. URL <http://www.sciencedirect.com/science/article/pii/S0168900210013446>. <ce:title>11th International Workshop on Radiation Imaging Detectors (IWORID)</ce:title>.
- NASA. False colour x-ray image of sun. 2000.
- Frédéric Noo, Rolf Clackdoyle, and Jed D Pack. A two-step hilbert transform method for 2d image reconstruction. *Physics in Medicine and Biology*, 49(17):3903, 2004. URL <http://stacks.iop.org/0031-9155/49/i=17/a=006>.
- A.C. Orifici, I. Herszberg, and R.S. Thomson. Review of methodologies for composite material modelling incorporating failure. *Composite Structures*, 86(1–3):194 – 210, 2008. ISSN 0263-8223. doi: 10.1016/j.compstruct.2008.03.007. URL <http://www.sciencedirect.com/science/article/pii/S0263822308000810>. <ce:title>Fourteenth International Conference on Composite Structures</ce:title> <ce:subtitle>ICCS/14</ce:subtitle>.
- N. J. Pagano and G. A. Schoeppner. Delamination of polymer matrix composites: Problems and assessment. In Anthony Kelly and Carl Zweben, editors, *Comprehensive Composite Materials*, pages 433 – 528. Pergamon, Oxford, 2000. ISBN 978-0-08-042993-9. doi: 10.1016/B0-08-042993-9/00073-5. URL <http://www.sciencedirect.com/science/article/pii/B0080429939000735>.
- S. Pan and A. Kak. A computational study of reconstruction algorithms for diffraction tomography: Interpolation versus filtered-backpropagation. *Acoustics, Speech and Signal Processing, IEEE Transactions on*, 31(5):1262 – 1275, oct 1983. ISSN 0096-3518. doi: 10.1109/TASSP.1983.1164196.
- Xiaochuan Pan, Emil Y Sidky, and Michael Vannier. Why do commercial ct scanners still employ traditional, filtered back-projection for image reconstruction? *Inverse Problems*, 25(12):123009, 2009a. URL <http://stacks.iop.org/0266-5611/25/i=12/a=123009>.
- Yongsheng Pan, Ross Whitaker, Arvi Cheryauka, and Dave Ferguson. Feasibility of gpu-assisted iterative image reconstruction for mobile c-arm ct. volume 7258, page 72585J. SPIE, 2009b. doi: 10.1117/12.812162. URL <http://link.aip.org/link/?PSI/7258/72585J/1>.
- Martin Petersilka, Herbert Bruder, Bernhard Krauss, Karl Stierstorfer, and Thomas G. Flohr. Technical principles of dual source ct. *European Journal of Radiology*, 68(3):362 – 368, 2008. ISSN 0720-048X. doi: 10.1016/j.ejrad.2008.08.013. URL <http://www.sciencedirect.com/science/article/pii/S0720048X08004713>. <ce:title>Definition - Dual Source Imaging</ce:title>.
- F. Pfeiffer, O. Bunk, C. Kottler, and C. David. Tomographic reconstruction of three-dimensional objects from hard X-ray differential phase contrast projection images. *Nuclear Instruments and Methods in Physics Research A : Accelerators, Spectrometers, Detectors and Associated Equipment*, 580(2):925–928, 2007. doi: 10.1016/j.nima.2007.06.104.

- F. Pfeiffer, M. Bech, O. Bunk, P. Kraft, E. F. Eikenberry, Ch. Bronnimann, C. Grunzweig, and C. David. Hard-x-ray dark-field imaging using a grating interferometer. *Nat Mater*, 7(2):134–137, 02 2008. URL <http://dx.doi.org/10.1038/nmat2096>.
- Franz Pfeiffer, Timm Weitkamp, Oliver Bunk, and Christian David. Phase retrieval and differential phase-contrast imaging with low-brilliance x-ray sources. *Nat Phys*, 2(4):258–261, 04 2006. URL <http://dx.doi.org/10.1038/nphys265>.
- S.T. Pinho, C.G Davila, and P.P Camanho. Failure models and criteria for frp under in-plane or three dimensional stress states including shear non-linearity. In *NASA TM 2005 213530*. NASA Langley Research Centre, 2005.
- R. Prakash. Non-destructive testing of composites. *Composites*, 11(4):217 – 224, 1980. ISSN 0010-4361. doi: DOI:10.1016/0010-4361(80)90428-0. URL <http://www.sciencedirect.com/science/article/pii/0010436180904280>.
- J.C. Prichard and P.J. Hogg. The role of impact damage in post-impact compression testing. *Composites*, 21(6):503 – 511, 1990. ISSN 0010-4361. doi: DOI:10.1016/0010-4361(90)90423-T. URL <http://www.sciencedirect.com/science/article/pii/001043619090423T>.
- A. Puck and H. Schürmann. Failure analysis of frp laminates by means of physically based phenomenological models. *Composites Science and Technology*, 62(12–13):1633 – 1662, 2002. ISSN 0266-3538. doi: 10.1016/S0266-3538(01)00208-1. URL <http://www.sciencedirect.com/science/article/pii/S0266353801002081>.
- Johann Radon. Über die bestimmung von funktionen durch ihre integralwerte längs gewisser mannigfaltigkeiten. *Berichte über die Verhandlungen der Sächsische Akademie der Wissenschaften (Reports on the proceedings of the Saxony Academy of Science)*, 69:262–277, 1917.
- Johann Radon. On the Determination of Functions from Their Integral Values along Certain Manifolds. *IEEE Transactions on Medical Imaging*, 5(4):170–176, 1986. ISSN 0278-0062. doi: 10.1109/TMI.1986.4307775. URL <http://dx.doi.org/10.1109/TMI.1986.4307775>.
- K. Remeysen and R. Swennen. Beam hardening artifact reduction in microfocus computed tomography for improved quantitative coal characterization. *International Journal of Coal Geology*, 67(1-2):101 – 111, 2006. ISSN 0166-5162. doi: 10.1016/j.coal.2005.10.001. URL <http://www.sciencedirect.com/science/article/pii/S0166516205001862>.
- V. Revol, C. Kottler, R. Kaufmann, I. Jerjen, T. Luthi, F. Cardot, Ph. Niedermann, U. Sennhauser, U. Straumann, and C. Urban. Application-oriented x-ray grating interferometer. *AIP Conference Proceedings*, 1236(1):221–226, 2010. doi: 10.1063/1.3426117. URL <http://link.aip.org/link/?APC/1236/221/1>.
- V. Revol, C. Kottler, R. Kaufmann, U. Straumann, and C. Urban. Noise analysis of grating-based x-ray differential phase contrast imaging. *REVIEW OF SCIENTIFIC INSTRUMENTS*, 81, 2010.

- V. Revol, I. Jerjen, C. Kottler, P. Schutz, R. Kaufmann, T. Lüthi, U. Sennhauser, U. Straumann, and C. Urban. Sub-pixel porosity revealed by x-ray scatter dark field imaging. *Journal of Applied Physics*, (110), 2011a.
- V. Revol, C. Kottler, R. Kaufmann, I. Jerjen, T. Lüthi, F. Cardot, P. Niedermann, U. Straumann, U. Sennhauser, and C. Urban. X-ray interferometer with bent gratings: Towards larger fields of view. *Nuclear Instruments and Methods in Physics Research A*, 648:302–+, August 2011b. doi: 10.1016/j.nima.2010.11.040.
- Vincent Revol, Christian Kottler, Rolf Kaufmann, Iwan Jerjen, Thomas Lüthi, Francis Cardot, Philippe Niedermann, Ulrich Straumann, Urs Sennhauser, and Claus Urban. X-ray interferometer with bent gratings: Towards larger fields of view. *Nuclear Instruments and Methods in Physics Research Section A: Accelerators, Spectrometers, Detectors and Associated Equipment*, 648, Supplement 1(0):S302 – S305, 2011. ISSN 0168-9002. doi: 10.1016/j.nima.2010.11.040. URL <http://www.sciencedirect.com/science/article/pii/S0168900210025027>. NIMA 4th International Conference on Imaging techniques in Subatomic Physics, Astrophysics, Medicine, Biology and Industry</ce:title>.
- M. O. W. Richardson and M. J. Wisheart. Review of low-velocity impact properties of composite materials. *Composites Part A: Applied Science and Manufacturing*, 27(12):1123 – 1131, 1996. ISSN 1359-835X. doi: DOI:10.1016/1359-835X(96)00074-7. URL <http://www.sciencedirect.com/science/article/pii/1359835X96000747>.
- Sidey G.R. Kingston-Lee D.M. Rogers, K.F. Ballistic impact resistance of carbon-fibre laminates. *Composites*, 2(4):237–241, 1971. URL <http://www.scopus.com/inward/record.url?eid=2-s2.0-0015204135&partnerID=40&md5=a92216b00858e7545194124382800121>. cited By (since 1996) 9.
- W. Röntgen. Hand mit ringen. 1895.
- A. Rosenfeld and A.C. Kak. *Digital Imaging Processing*. Academic Press, New York, 1982.
- A. Rotem. Residual flexural strength of frp composite specimens subjected to transverse impact loading. *SAMPE Journal*, 24(2):19–25, 1988. URL <http://www.scopus.com/inward/record.url?eid=2-s2.0-0023983012&partnerID=40&md5=7b6efad0f869598646749b8827c13d0a>. cited By (since 1996) 8.
- J.C. Russ. *The Image Processing Handbook*. CRC Press, 2007.
- E.F. Rybicki and M.F. Kanninen. A finite element calculation of stress intensity factors by a modified crack closure integral. *Engineering Fracture Mechanics*, 9(4):931 – 938, 1977. ISSN 0013-7944. doi: 10.1016/0013-7944(77)90013-3. URL <http://www.sciencedirect.com/science/article/pii/0013794477900133>.
- J. Degrieck J. Xu b S.V. Lomov-I. Verpoest S. Daggumati, W. Van Paepegem. Local damage in a 5-harness satin weave composite under static tension: Part ii – meso-fe modelling. *Composites Science and Technology*, 70:1934–1941, 2010.

- M.J. Salkind. Early detection of fatigue damage in composite materials. *Journal of Aircraft*, 13(10):764–769, 1976. URL <http://www.scopus.com/inward/record.url?eid=2-s2.0-0017014083&partnerID=40&md5=e55626b2582843e2b0df386853b6a725>. cited By (since 1996) 2.
- G. A. Schoeppner and S. Abrate. Delamination threshold loads for low velocity impact on composite laminates. *Composites Part A: Applied Science and Manufacturing*, 31(9):903 – 915, 2000. ISSN 1359-835X. doi: DOI:10.1016/S1359-835X(00)00061-0. URL <http://www.sciencedirect.com/science/article/pii/S1359835X00000610>.
- I.G. Scott and C.M. Scala. A review of non-destructive testing of composite materials. *NDT International*, 15(2):75 – 86, 1982. ISSN 0308-9126. doi: DOI:10.1016/0308-9126(82)90001-3. URL <http://www.sciencedirect.com/science/article/pii/0308912682900013>.
- N. Sela and O. Ishai. Interlaminar fracture toughness and toughening of laminated composite materials: a review. *Composites*, 20(5):423 – 435, 1989. ISSN 0010-4361. doi: DOI:10.1016/0010-4361(89)90211-5. URL <http://www.sciencedirect.com/science/article/pii/0010436189902115>.
- R.J. Shadbolt, R.S.J. Corran, and C.Ruiz. A preliminary investigation of plate perforation in the sub-ordnance range. Technical report, University of Oxford, 1981.
- R. Sia, S. Kleinfelder, and V.V. Nagarkar. Solid-state photon-counting hybrid detector array for high-resolution multi-energy x-ray imaging. *Nuclear Instruments and Methods in Physics Research Section A: Accelerators, Spectrometers, Detectors and Associated Equipment*, 652(1):470 – 473, 2011. ISSN 0168-9002. doi: 10.1016/j.nima.2011.01.135. URL <http://www.sciencedirect.com/science/article/pii/S0168900211002373>. <ce:title>Symposium on Radiation Measurements and Applications (SORMA) XII 2010</ce:title>.
- Sameer Singh and Maneesha Singh. Explosives detection systems (eds) for aviation security. *Signal Process.*, 83(1):31–55, January 2003. ISSN 0165-1684. doi: 10.1016/S0165-1684(02)00391-2. URL [http://dx.doi.org/10.1016/S0165-1684\(02\)00391-2](http://dx.doi.org/10.1016/S0165-1684(02)00391-2).
- David Sizer. Boeing 787 photograph. 2009.
- A. Snigirev, I. Snigireva, V. Kohn, S. Kuznetsov, and I. Schelokov. On the possibilities of x-ray phase contrast microimaging by coherent high-energy synchrotron radiation. *Review of Scientific Instruments*, 66(12):5486–5492, 1995. doi: 10.1063/1.1146073. URL <http://link.aip.org/link/?RSI/66/5486/1>.
- Delia Soimu, Ivan Buliev, and Nicolas Pallikarakis. Studies on circular isocentric cone-beam trajectories for 3d image reconstructions using fdk algorithm. *Computerized Medical Imaging and Graphics*, 32(3):210 – 220, 2008. ISSN 0895-6111. doi: 10.1016/j.compmedimag.2007.12.005. URL <http://www.sciencedirect.com/science/article/pii/S0895611107001711>.

- C. Soutis. Measurement of the static compressive strength of carbon-fibre/epoxy laminates. *Composites Science and Technology*, 42(4):373 – 392, 1991. ISSN 0266-3538. doi: DOI:10.1016/0266-3538(91)90064-V. URL <http://www.sciencedirect.com/science/article/pii/026635389190064V>.
- C. Soutis. Compressive strength of unidirectional composites: measurement and prediction. *Composite materials: testing and design (thirteenth volume)*, page 168, 1997.
- C. Soutis. Fibre reinforced composites in aircraft construction. *Progress in Aerospace Sciences*, 41(2):143 – 151, 2005. ISSN 0376-0421. doi: DOI:10.1016/j.paerosci.2005.02.004. URL <http://www.sciencedirect.com/science/article/pii/S0376042105000448>.
- C. Soutis and P. T. Curtis. Prediction of the post-impact compressive strength of cfrp laminated composites. *Composites Science and Technology*, 56(6):677 – 684, 1996. ISSN 0266-3538. doi: DOI:10.1016/0266-3538(96)00050-4. URL <http://www.sciencedirect.com/science/article/pii/0266353896000504>.
- British Standards. Bs en 2563:1997 carbon fibre reinforced plastics — unidirectional laminates — determination of the apparent interlaminar shear strength. Technical report, British Standards, January 1997.
- M. Stenstrom. *Computerised Microtomography: Non-invasive imaging and analysis of biological samples, with special reference to monitoring development of osteoporosis in small animals*. PhD thesis, Linköpings universitet Institutionen för medicin och hälsa. Medicinsk radiofysik., 2001.
- J. Peter Stonestrom, Robert E. Alvarez, and Albert Macovski. A framework for spectral artifact corrections in x-ray ct. *Biomedical Engineering, IEEE Transactions on*, BME-28(2):128 –141, feb. 1981. ISSN 0018-9294. doi: 10.1109/TBME.1981.324786.
- P.M.V. Subbarao, P. Munshi, and K. Muralidhar. Performance of iterative tomographic algorithms applied to non-destructive evaluation with limited data. *NDT & E International*, 30(6):359 – 370, 1997. ISSN 0963-8695. doi: 10.1016/S0963-8695(97)00005-4. URL <http://www.sciencedirect.com/science/article/pii/S0963869597000054>.
- C.T. Sun and S.Rechak. Effect of adhesive layers on impact damage in composite laminates. *Composite Materials: Testing and design (8th conference)*, ASTM STP 972:97–123, 1988.
- D.D. Symons. Characterisation of indentation damage in 0/90 lay-up t300/914 cfrp. *Composites Science and Technology*, 60(3):391–401, 2000. URL <http://www.scopus.com/inward/record.url?eid=2-s2.0-0033627002&partnerID=40&md5=9968d71f9e647948ef98907a5be860b1>. cited By (since 1996) 15.
- K.T. Tan, N. Watanabe, and Y. Iwahori. X-ray radiography and micro-computed tomography examination of damage characteristics in stitched composites subjected to impact loading. *Composites Part B: Engineering*, 42(4):874 – 884, 2011a. ISSN 1359-8368. doi: DOI:10.1016/j.compositesb.2011.01.011. URL <http://www.sciencedirect.com/science/article/pii/S1359836811000394>.

- KT Tan, N. Watanabe, and Y. Iwahori. Impact damage resistance, response, and mechanisms of laminated composites reinforced by through-thickness stitching. *International Journal of Damage Mechanics*, 2011b.
- Ion Tiseanu, Emanuelle Tsitrone, Arkadi Kreter, Teddy Craciunescu, Thierry Loarer, Bernard PÈgouriÈ, and Timo Dittmar. X-ray micro-tomography studies on carbon based composite materials for porosity network characterization. *Fusion Engineering and Design*, In Press, Corrected Proof:–, 2011. ISSN 0920-3796. doi: DOI:10.1016/j.fusengdes.2011.04.079. URL <http://www.sciencedirect.com/science/article/pii/S0920379611004777>.
- Stephen W. Tsai and Edward M. Wu. A general theory of strength for anisotropic materials. *Journal of Composite Materials*, 5(1):58–80, 1971. doi: 10.1177/002199837100500106. URL <http://jcm.sagepub.com/content/5/1/58.abstract>.
- SW. Tsai. *Theory of Composites Design*. Think Composites, 1992.
- Heang K. Tuy. An inversion formula for cone-beam reconstruction. *SIAM Journal on Applied Mathematics*, 43(3):546–552, 1983. URL <http://scitation.aip.org/getabs/servlet/GetabsServlet?prog=normal&id=SMJMAP000043000003000546000001&idtype=cvips&gifs=yes>.
- E. Van de Casteele, D. Van Dyck, J. Sijbers, and E. Raman. A model-based correction method for beam hardening artefacts in x-ray microtomography. *Journal of X-ray Science and Technology*, 12(1):43–57, 2004.
- S.S. Wang. Delamination crack growth in unidirectional fibre-reinforced composites under static and cyclic loading. *Composite materials: testing and design (5th conf)*, ASTM STP 674, 1979.
- E. Weber, M. Fernandez, P. Wapner, and W. Hoffman. Comparison of x-ray micro-tomography measurements of densities and porosity principally to values measured by mercury porosimetry for carbon-carbon composites. *Carbon*, 48(8):2151 – 2158, 2010. ISSN 0008-6223. doi: DOI: 10.1016/j.carbon.2009.11.047. URL <http://www.sciencedirect.com/science/article/pii/S0008622309007829>.
- Timm Weitkamp, Ana Diaz, Christian David, Franz Pfeiffer, Marco Stampanoni, Peter Cloetens, and Eric Ziegler. X-ray phase imaging with a grating interferometer. *Opt. Express*, 13(16):6296–6304, Aug 2005. doi: 10.1364/OPEX.13.006296. URL <http://www.opticsexpress.org/abstract.cfm?URI=oe-13-16-6296>.
- Jens Wiegert, Matthias Bertram, Jörg Wulff, Dirk Schäfer, Jürgen Weese, Thomas Netsch, Hermann Schomberg, and Georg Rose. 3d roi imaging for cone-beam computed tomography. In Heinz U. Lemke, Kiyonari Inamura, Kunio Doi, Michael W. Vannier, Allan G. Farman, and Johan H. C. Reiber, editors, *CARS*, volume 1268 of *International Congress Series*, pages 7–12. Elsevier, 2004. ISBN 0-444-51731-6. URL <http://dblp.uni-trier.de/db/conf/cars/cars2004.html#WiegertBWSWNSR04>.

- S. W. Wilkins, T. E. Gureyev, D. Gao, A. Pogany, and A. W. Stevenson. Phase-contrast imaging using polychromatic hard x-rays. *Nature*, 384(6607):335–338, 11 1996. URL <http://dx.doi.org/10.1038/384335a0>.
- J.G. Williams and M.D. Rhodes. Effect of resin on impact damage tolerance of graphite/epoxy composites. Technical report, ASTM Special Technical Publication, 1982.
- M.R. Wisnom. Modelling discrete failures in composites with interface elements. *Composites Part A: Applied Science and Manufacturing*, 41(7):795 – 805, 2010. ISSN 1359-835X. doi: 10.1016/j.compositesa.2010.02.011. URL <http://www.sciencedirect.com/science/article/pii/S1359835X10000680>.
- Y. Woong-Ryeol, Philip Harrison, and Andrew Long. Finite element forming simulation for non-crimp fabrics using a non-orthogonal constitutive equation. *Composites Part A: Applied Science and Manufacturing*, 36:1079–1093, 2005.
- Feng Xu, Lukas Helfen, Andrew J. Moffat, Gregory Johnson, Ian Sinclair, and Tilo Baumbach. Synchrotron radiation computed laminography for polymer composite failure studies. *Journal of Synchrotron Radiation*, 17(2):222–226, 2010. ISSN 1600-5775. doi: 10.1107/S0909049510001512. URL <http://dx.doi.org/10.1107/S0909049510001512>.
- Hao Yan, Caglar Oskay, Arun Krishnan, and Luoyu Roy Xu. Compression-after-impact response of woven fiber-reinforced composites. *Composites Science and Technology*, 70(14):2128 – 2136, 2010. ISSN 0266-3538. doi: 10.1016/j.compscitech.2010.08.012. URL <http://www.sciencedirect.com/science/article/pii/S0266353810003209>.
- F.J. Yang and W.J. Cantwell. Impact damage initiation in composite materials. *Composites Science and Technology*, 70(2):336 – 342, 2010. ISSN 0266-3538. doi: DOI:10.1016/j.compscitech.2009.11.004. URL <http://www.sciencedirect.com/science/article/pii/S026635380900390X>.
- Qingda Yang and Brian Cox. Cohesive models for damage evolution in laminated composites. *International Journal of Fracture*, 133:107–137, 2005. ISSN 0376-9429. URL <http://dx.doi.org/10.1007/s10704-005-4729-6>. 10.1007/s10704-005-4729-6.
- W. Yashiro, Y. Terui, K. Kawabata, and A. Momose. On the origin of visibility contrast in x-ray talbot interferometry. *Opt. Express*, 18(16), 2010.
- Zhengrong Ying, R. Naidu, K. Guilbert, D. Schafer, and C.R. Crawford. Dual energy volumetric x-ray tomographic sensor for luggage screening. In *Sensors Applications Symposium, 2007. SAS '07. IEEE*, pages 1 –6, feb. 2007. doi: 10.1109/SAS.2007.374371.
- Shu-Ang Zhou and Anders Brahme. Development of phase-contrast x-ray imaging techniques and potential medical applications. *Physica Medica*, 24(3):129 – 148, 2008. ISSN 1120-1797. doi: 10.1016/j.ejmp.2008.05.006. URL <http://www.sciencedirect.com/science/article/pii/S1120179708000689>.

Yu Zou and Xiaochuan Pan. Image reconstruction on pi-lines by use of filtered backprojection in helical cone-beam ct. *Physics in Medicine and Biology*, 49(12):2717, 2004. URL <http://stacks.iop.org/0031-9155/49/i=12/a=017>.

Carl Zwebel. *Handbook of Materials Selection*, chapter 12 Composite Materials. John Wiley and Sons, 2002.